UNIVERSITY OF SOUTHAMPTON

FACULTY OF MEDICINE

Clinical and Experimental Science

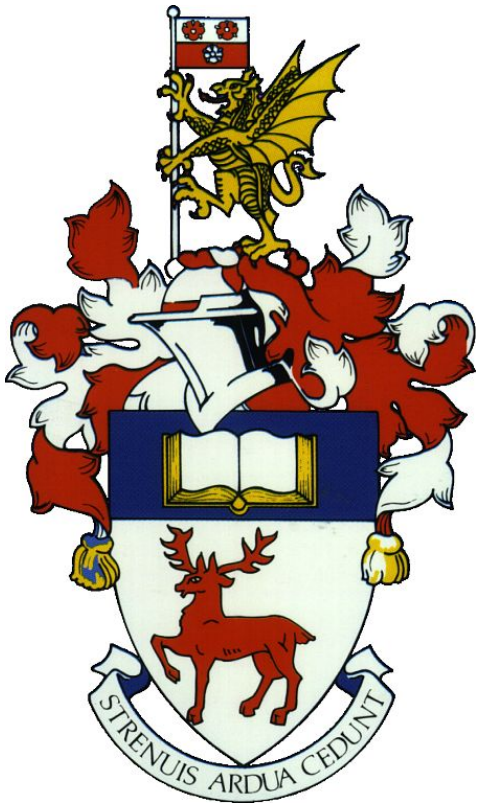

The role of high-fat diet and oxidative stress in driving the structural and functional deficits associated with Age-related Macular Degeneration

By

Eloise Elizabeth Keeling, BSc (Hons)

Thesis for the degree of Doctor of Philosophy

February 2019

University of Southampton

ABSTRACT

FACULTY OF MEDICINE

Clinical and Experimental Sciences

Thesis for the degree of Doctor of Philosophy

The role of high-fat diet and oxidative stress in driving the structural and functional deficits associated with Age-related Macular Degeneration

Eloise Elizabeth Keeling

Age-related Macular Degeneration (AMD) is the leading cause of irreversible blindness in the developed world. Current treatments are only suitable for a proportion of patients and are usually ineffective in the long-term. This is partially due to an incomplete understanding of the underlying aetiologies that drive pathology in the Retinal Pigment Epithelium (RPE) and adjacent tissues of the outer retina. Many risk factors for AMD, including consumption of a high fat diet (HFD), increase oxidative stress in the retina. I studied the link between a HFD and structural changes to the tissues in the outer retina. Next, I investigated how these pathogenic changes could cause disease phenotypes in the RPE at a single cell resolution.

To achieve these objectives, I used serial block-face scanning electron microscopy (SBSEM) to study healthy tissues in the mouse outer retina. An entire patch of RPE and overlying photoreceptors were reconstructed in 3D, and comparisons were made between mono-nucleate and bi-nucleate RPE cells, of which the latter is associated with early AMD. This novel approach provided new data on the structure and arrangement of RPE and photoreceptors, as well as their relationship to each other. 3D approaches have not been extensively used before, thus we have gained new types of structural information on these tissues. In mice fed a HFD, I used conventional TEM alongside confocal immunofluorescence imaging to study the pathogenic changes in tissues of the outer retina. Detailed studies of HFD mouse eyes have not been carried out to this extent before. My findings revealed HFD-induced changes to the structure of outer retinal tissues, showing the effects of an unhealthy diet and oxidative stress in living eyes. Next, my work delved into these pathogenic mechanisms at single-cell resolution. A HFD is associated with oxidative stress and impaired acidification of intracellular compartments in the lysosomal-autophagy pathway. Using confocal-immunofluorescence microscopy and conventional TEM, I studied how these insults impaired the trafficking of photoreceptor outer segments (POS) in cultured RPE cells. My discoveries reveal the trafficking and breakdown of POS cargos in early and late endosomes/ phagosomes, and their eventual transport to lysosomes and autophagy bodies in healthy RPE cells. My data also provides novel mechanistic insights into how HFD associated oxidative stress and impaired acidification alters POS trafficking, potentially contributing to early stages of RPE pathology. Notably, it appears that damage may be confined to only a proportion of RPE lysosomes, suggesting that at least some compartments in the endo-lysosomal pathway remains functional, even in diseased cells.

Collectively, my work has revealed novel structural and functional insights into pathogenic mechanism in the RPE and adjacent tissues of the outer retina, which could significantly influence the way in which disease processes in the aging retina are understood. Such insights are critical if effective treatments against AMD are to be devised in the future

Table of Contents

Table of Tables

Table of Figures

Publications of work

Peer-reviewed papers

1. George Taylor-Walker, Savannah A Lynn, **Eloise Keeling**, Rosie Munday, David A Johnston, Anton Page, Jennifer A Scott, Srini Goverdhan, Andrew J Lotery, J Arjuna Ratnayaka (2016). The Alzheimer's-related amyloid beta peptide is internalised by R28 neuroretinal cells and disrupts the microtubule associated protein 2. *Experimental Eye Research*, 153:110-121.

2. Savannah A Lynn, Gareth Ward, **Eloise Keeling**, Jennifer A Scott, Angela J Cree, David A Johnston, Anton Page, Enrique Cuan-Urquizo, Atul Bhaskar, Martin C Grossel, David A Tumbarello, Tracey A Newman, Andrew J Lotery, J Arjuna Ratnayaka (2017). Ex-vivo models of the Retinal Pigment Epithelium (RPE) in long-term culture faithfully recapitulate key structural and physiological features of native RPE. *Tissue and Cell*, 49(4):447-460.

3. Savannah A Lynn, **Eloise Keeling,** Rosie Munday, Gagandeep Gabha, Helen Griffiths, Andrew J Lotery, J Arjuna Ratnayaka (2017). The complexities underlying age-related macular degeneration: could amyloid beta play an important role? *Neural Regeneration Research*, 12(4):538-548.

4. Savannah A Lynn, **Eloise Keeling**, Jennifer M Dewing, David A Johnston, Anton Page , Angela J Cree , David A Tumbarello, Tracey A Newman, Andrew J Lotery, J Arjuna Ratnayaka (2018). A convenient protocol for establishing a human cell culture model of the outer retina. F1000 Research, 7:1107.

5. **Eloise Keeling**, Andrew J Lotery, David A Tumbarello, J Arjuna Ratnayaka (2018). Impaired Cargo Clearance in the Retinal Pigment Epithelium (RPE) Underlies Irreversible Blinding Diseases. Cells. 7(2):16.

6. **Eloise Keeling**, David S. Chatelet, David A. Johnston, Anton Page, David A. Tumbarello, Andrew J. Lotery, J. Arjuna Ratnayaka. Oxidative stress and dysfunctional intracellular traffic linked to an unhealthy diet results in impaired cargo transport in the Retinal Pigment Epithelium (RPE). Molecular Nutrition and Food Research.

7. Paul Ibbett, Srinivas. V Goverdhan, Elena Pipi, Joseph Chouhan, **Eloise Keeling**, Elizabeth. M Angus, Jenny A. Scott, Maureen Gatherer, Anton Page, Jessica Teeling, Andrew Lotery, and J. Arjuna Ratnayaka. A lasered mouse model of retinal degeneration displays progressive outer retinal pathology providing insights into early geographic atrophy. Scientific Reports

Book chapters

1. J. Arjuna Ratnayaka, **Eloise Keeling**, David S. Chatelet (2019). Study of intracellular cargo trafficking and co-localisation in the phagosome and autophagy-lysosomal pathways of RPE cells. Springer Methods in Molecular Biology

Presentations of work

Oral Presentations

Southampton Neuroscience Group (SoNG) seminar, Southampton, November 2016, *"A murine outer retina ultrastructural study; exploiting novel 3D imaging technology."*

SEMT, London, December 2016 *"Murine outer retina ultrastructural study- exploiting novel 3D imaging technology."*

Oxford Bristol Cardiff Southampton Vision Alliance Conference, Southampton, June 2017, *"Developing a model to study lysosomal impairment in the retinal pigment epithelium; insights into AMD."*

SoNG symposium, Southampton, September 2017 *"3D imaging of the mammalian outer retina"*

Macular society trustees and donors, Southampton, November 2017, *"The importance of RPE dysfunction in driving an early AMD phenotype."*

Gift of Sight donors, Southampton, October 2018*, "The role of oxidative stress in the structural and functional deficits associated with retinal disease."*

Poster Presentations

Alzheimer's Research UK (ARUK) conference, Aberdeen, March 2017, *"Lysosomal impairment in the Retinal Pigment Epithelium – common pathways of damage in the ageing retina and brain."*

Faculty of Medicine conference, Southampton, June 2017 *"Exploiting novel 3D imaging technology to study the ultrastructure of the outer retina; insights into AMD."*

SoNG Symposium, Southampton, September 2017, *"Exploiting novel 3D imaging technology to study the ultrastructure of the outer retina; insights into AMD."*

Association of Research in Vision and Ophthalmology, Hawaii, 2018, *"Lysosomal impairment in the Retinal Pigment Epithelium – a pathway of damage in the aging retina."*

Keeling, E., Johnston, D., Chatelet, D., Tumbarello, D., Lotery, A., & Ratnayaka, J. A. (2018). Lysosomal impairment in the Retinal Pigment Epithelium (RPE) - a pathway of damage in the ageing retina. *Investigative Ophthalmology & Visual Science*, *59* , 4487.

Scientific Cafes

ARUK South Coast Network Day, January 2016, 2017, 2018 and 2019 – "*Why do cells die in the ageing brain and retina?*

List of accompanying materials

Electronic appendices are including on the USB stick provided. The materials on this drive include an interactive 3D PDF of the reconstructed patch of RPE. Use the buttons at the bottom of the PDF to view the cells in different orientations, and change each structure opaque, translucent or transparent. Scroll and Pan features can also be used to move around the patch manually, and zoom can be used to view areas in more detail.

Research Thesis: Declaration of Authorship

Print name:	Eloise Keeling

Title of thesis:	The role of high fat diet and oxidative stress in driving the structural and functional deficits associated with Age-related Macular Degeneration

I declare that this thesis and the work presented in it are my own and has been generated by me as the result of my own original research.

I confirm that:

1. This work was done wholly or mainly while in candidature for a research degree at this University;
2. Where any part of this thesis has previously been submitted for a degree or any other qualification at this University or any other institution, this has been clearly stated;
3. Where I have consulted the published work of others, this is always clearly attributed;
4. Where I have quoted from the work of others, the source is always given. With the exception of such quotations, this thesis is entirely my own work;
5. I have acknowledged all main sources of help;
6. Where the thesis is based on work done by myself jointly with others, I have made clear exactly what was done by others and what I have contributed myself;
7. Parts of this work have been published as:

Savannah A Lynn, Gareth Ward, **Eloise Keeling**, Jennifer A Scott, Angela J Cree, David A Johnston, Anton Page, Enrique Cuan-Urquizo, Atul Bhaskar, Martin C Grossel, David A Tumbarello, Tracey A Newman, Andrew J Lotery, J Arjuna Ratnayaka (2017). Ex-vivo models of the Retinal Pigment Epithelium (RPE) in long-term culture faithfully recapitulate key structural and physiological features of native RPE. *Tissue and Cell*, 49(4):447-460

Savannah A Lynn, **Eloise Keeling**, Jennifer M Dewing, David A Johnston, Anton Page , Angela J Cree , David A Tumbarello, Tracey A Newman, Andrew J Lotery, J Arjuna Ratnayaka (2018). A convenient protocol for establishing a human cell culture model of the outer retina. F1000 Research, 7:1107

Eloise Keeling, Andrew J Lotery, David A Tumbarello, J Arjuna Ratnayaka (2018). Impaired Cargo Clearance in the Retinal Pigment Epithelium (RPE) Underlies Irreversible Blinding Diseases. Cells. 7(2):16.

J. Arjuna Ratnayaka, **Eloise Keeling**, David S. Chatelet (2019). Study of intracellular cargo trafficking and co-localisation in the phagosome and autophagy-lysosomal pathways of RPE cells. Springer Methods in Molecular Biology.

Signature:		Date:	

Acknowledgements

This research project would not have been possible without the guidance of my supervisory team: Dr Arjuna Ratnayaka, Dr David Tumbarello and Professor Andrew Lotery. They have offered support and encouragement throughout the past three years and have ensured that this PhD was as productive and enjoyable as possible. I would also like to say a particular thank you to Arjuna for being so generous with his time and ensuring my personal and scientific development throughout the project. He has helped with all aspects of this work- from experimental design to publishing manuscripts. I am eternally grateful for all he has done.

I would like to express my deepest gratitude to Dr David Chatelet who has been pivotal in devising the best methods of segmentation and image analysis. He is always on hand when problems arise, and has been extremely supportive throughout. I would also like to thank Dr David Johnston for his help with confocal microscopy and Patricia Goggin for helping to set up the SBSEM. A special mention must also go to Angela Cree who, despite not being a supervisor, has been supportive since day one. She always offers constructive feedback and is not hesitant to praise or compliment good work; something I have found tremendously encouraging. I would also like to express my deepest appreciation to the Macular Society for providing the generous funding for this project.

Two of the biggest thank yous have to go to my hospital support network. Katie Askew, Matt Morton and Chelsea Norman (aka the Biscuit club) – the past three years would have been significantly less fun without you. I will miss our breaks (moans) – you have kept me going through the dark times. I can't believe we made it! Chelsea, thanks for always agreeing to my crazy ideas, my PhD experience would have been very different without you by my side. Also to my "work-place proximity associates" as Ben would say. Ben Coles, Janice Sutton, Tutte Newall and Jenny Scott; thank you for providing me with endless entertainment. I am very happy to be one of Ben's memorable PhD students. A special thank you has to go to Janice. Thanks for being my biggest cheerleader! You've always been on hand to be a shoulder to cry on, and to whisk me away for a Hot Chocolate when it's most needed. The next one's definitely on me!

My family have been so supportive of everything I have ever done, and my PhD was no exception. To my mum and dad, thank you for your endless belief in my abilities. Thanks for always having a warm meal and a comfy bed when I most need it, and for picking up the pieces whenever things go wrong. To my brother and sister, thank you for pushing me to do my best and for teaching me to dance in the rain.

Finally, a massive thank you to Hayden Foster. You have been my rock over the past three years. It probably would have been possible without you, but it definitely would have been much worse. Thank you for listening to me at the end of a hard day, and for motivating me to carry on. You always believe in me and show enormous patience and positivity. I could not ask for a more supportive partner, and I am deeply grateful for all the encouragement you have given me.

All data collected in this thesis was conducted by myself, except in the following instances. Here, help was given by colleagues or project students who I supervised. Their help is formally acknowledged below:

- Nicole Tan performed the segmentation of Cell 2, Chapter 3.
- Thibana Thisanathan prepared and stained the flat mounts in section 3.3.1.
- Yen Min Koh performed all cryosectioning, H&E staining and immunofluorescence staining in Chapter 4.
- Matt MacGregor Sharp perfuse fixed all mice used in Chapter 4.
- Katie Askew perfuse fixed all mice used in Chapter 3.

Definitions and Abbreviations

A2E	N-retinylidene-N-retinylethanolamine
AD	Alzheimer's disease
AGE	Advanced Glycation End Products
ALE	Advanced Lipid Peroxidation End Products
AMD	Age-related Macular Degeneration
AMPK	AMP-activated Protein Kinase
ApoE	Apolipoprotein E
APP	Amyloid Precursor Protein
AREDS	Age-related Eye Disease Study
Aβ	Amyloid-beta
BCA	Bicinchoninic Acid
BBB	Blood-brain Barrier
BRB	Blood-retina Barrier
BrM	Bruch's Membrane
BSA	Bovine Serum Albumin
CFH	Complement Factor H
CNS	Central Nervous System
CNV	Choroidal Neovascularisation
DAPI	4',6'-diamino-2-phenylindole
ddH_2O	double distilled water
DHA	Docosahexaenoic acid
DMEM	Dulbecco's Modified Eagle's Medium
DMSO	Dimethylsulfoxide
ECM	Extracellular Matrix
EDCCS	Eye Disease Case-Control Study
EE	Early Endosome
EL	Elastin Layer
ESCRT	Endosomal Sorting Complex Required for Transport
FAD(2H)	Flavin Adenine Dinucleotide-(2-Hydrogen)
FCS	Foetal Calf Serum
FITC	Fluorescein isothiocyanate
FITC-POS	Fluorescein isothiocyanate-conjugated photoreceptor outer segments
GA	Geographic Atrophy
HBSS	Hank's Buffered Saline Solution
HFD	High-fat Diet
HLA	Human Leukocyte Antigen
HO-1	Heme Oxygenase-1
H&E	Haemotoxylin & Eoisin
H_2O_2	Hydrogen Peroxide
ICL	Inner Collagenous Layer
ILV	Intraluminal Vesicle
INL	Inner Nuclear Layer
IPL	Inner Plexiform Layer
LAMP	Lysosome Associated Membrane Protein
LAP	LC3-associated Phagocytosis
LE	Late Endosome
LSD	Lysosomal Storage Disease
mAb	Monoclonal Antibody
MerTK	Tyrosine Kinase c-mer
mTORC	Mechanistic Target of Rapamycin Complex
MVB	Multi-vesicular Bodies
NADH	Nicotinamide Adenine Dinucleotide
OCL	Outer Collagenous Layer

OCT	Optical Coherence Tomography
OCT	Optimal Cutting Temperature Medium
ONL	Outer Nuclear Layer
OPL	Outer Plexiform Layer
P	Passage Number
pAb	Polyclonal Antibody
PBS	Phosphate Buffered Solution
PD	Parkinson's Disease
PEDF	Pigment Epithelium-Derived Factor
PFA	Paraformaldehyde
PIPES	Piperazine-N, N'-bis
PI3 Kinase	Phosphoinositide-3-Kinase
POS	Photoreceptor Outer Segments
PR	Photoreceptors
RGC	Retinal Ganglion Cells
ROI	Region of Interest
ROS	Reactive Oxygen Species
RPE	Retinal Pigment Epithelium
SBSEM	Serial Block-face Scanning Electron Microscope
SD	Standard Deviation
SEM	Scanning Electron Microscope
SFD	Sorsby's Fundus Dystrophy
TCA	Tricarboxylic Acid
TEM	Transmission Electron Microscopy
TIMP-3	Tissue Inhibitor of Metalloproteinase-3
UP	Ubiquitin Proteasome
VEGF	Vascular Endothelial Growth Factor
WT	Wild-type
ZO	Zonula Occludens
2D	Two dimensional
3D	Three dimensional

Chapter 1 Introduction

1.1 General Introduction

The visual system is an extraordinary evolutionary adaptation. Much of what we learn about the world is learnt through seeing. A single glance is sufficient to describe the location, size, shape, colour, and texture of objects and, if objects are moving, their direction and speed. Remarkably this complex sensory process allows for sight across a wide range of stimulus intensities, from the faint light of stars at night through to vision in bright sunlight. Sight is common to most animals: from the simple pit eye of a flatworm to the highly sophisticated arthropod compound eye, and the single-chambered eyes of vertebrates[1].

Interestingly, ocular structures are conserved across distinct phylogenetic lineages despite phenotypic, genetic and behavioural differences[2]. This highlights the obvious evolutionary advantage that vision provides. This is further illustrated by species-specialised visionary adaptations to suit an animals' specific environment. For example, herbivores exhibit a large field of view to increase predatory awareness[3], while birds possess a dual fovea as well as a thicker lens to detect prey from high altitudes[4]. Even 'blind' animals such as the mole rat whose eyes are thought to be non-functional, rely on light detection for circadian rhythm regulation[5]. Such diversity in the visual system highlights its plasticity and importance for survival.

Of all the senses, vision is the most versatile, allowing animals to navigate through their environment, find food, and increase awareness of danger. Eyesight allows for recognition of other individuals and communication by gesture and expression. Given this, the visual ability has become essential for basic human behaviour and social interaction. It is therefore unsurprising that blindness and impaired vision are among the most feared medical conditions after cancer and cardiovascular disease[6]. This is particularly concerning for patients with Age-related Macular Degeneration (AMD), the most common cause of irreversible blindness in the developed world[7]. This chronic blinding disease causes the loss of central vision and impairs the performance of routine daily tasks such as recognising faces, reading and driving. It also imposes a significant burden, both financially and emotionally, on the patient and their families. Despite the high prevalence of AMD, there is currently no effective treatment for this debilitating disease. This is largely due to an incomplete understanding of the molecular mechanisms underlying this complex disease.

Gradual degeneration and atrophy of a monolayer of cells in the retina called the Retinal Pigment Epithelium (RPE) appears to be integral to the disease process. In AMD, RPE pathology is focused within the macula, the region of the retina responsible for high visual

acuity. The degradation of the RPE layer appears to result in secondary deterioration of photoreceptors, ultimately leading to vision loss. As mentioned previously, AMD is a multifactorial disease driven by genetic and non-genetic risk factors. Recent advances have led to a better understanding of genetic risk factors. Other risk factors, which are less well studied, include the consumption of an unhealthy high fat and cholesterol enriched diet (commonly referred to as a western style diet).

Current knowledge of retinal structure is derived from 2D imaging techniques which were utilised in studies as far back as 1931[8]. More recently, advances in imaging technologies have allowed cells to be imaged in 3D for the first time, which has led to some exciting discoveries[9]. However 3D imaging techniques have not been performed wholescale on the delicate tissue of the outer retina, and therefore there is a lack of understanding of the 3D ultrastructure of these layers, including the RPE.

The themes explored in this thesis include the novel use of 3D imaging technology to study the tissues of the outer retina, and in particular the RPE monolayer. We also studied how an unhealthy diet rich in high-fat could trigger pathology in mouse eyes. Finally, we delved into studying AMD disease pathways at the level of single cells. We explored how oxidative stress and impaired acidification of intracellular compartments, which are caused by a high fat diet (HFD), could bring about early RPE pathology. In order to provide a context for this work, we first discuss the anatomy of the eye, retinal function as well as structures affected by AMD.

.

1.2 Structure of the Eye

The eye is a spherical fluid filled outgrowth of the brain enclosed by three layers of tissue, as shown in Figure 1. The outermost layer is known as the sclera which is composed of tough white fibrous tissue[10]. Towards the front of the eye, this outer layer merges into the cornea; a specialised and transparent tissue that permits entry of light into the eye[11]. After the light passes through the cornea, it travels through two distinct fluid compartments before reaching the retina. The first fluid compartment lies immediately behind the cornea. The aqueous humour is a clear, watery liquid which supplies nutrients to both the cornea and the underlying lens. Behind the lens lies the vitreous humour, which accounts for approximately 80% of eye volume. The vitreous is typically thick and gelatinous in the young and is responsible for maintaining the shape of the eye, as well as removing blood or debris that might interfere with the efficient transmission of light[12]. The inner layer is the retina, which detects light from external sources and converts it into a neural signal. These electrical messengers are transmitted via the optic nerve to the visual cortex in the brain where it is processed. The middle layer, which lies between the sensory neuroretina and the sclera, is the vascular choroid[13]; a rich capillary bed that nourishes tissues of the outer retina with nutrients and oxygen whilst removing metabolic waste[14] [Fig. 1]. Extending from the choroid is the ciliary body which structurally encircles the lens and adjusts its refractive power. The iris, visible through the cornea, is attached to the ciliary body and has an opening in its centre known as the pupil [Fig. 1], the size of which can be adjusted to compensate for differing light levels[11].

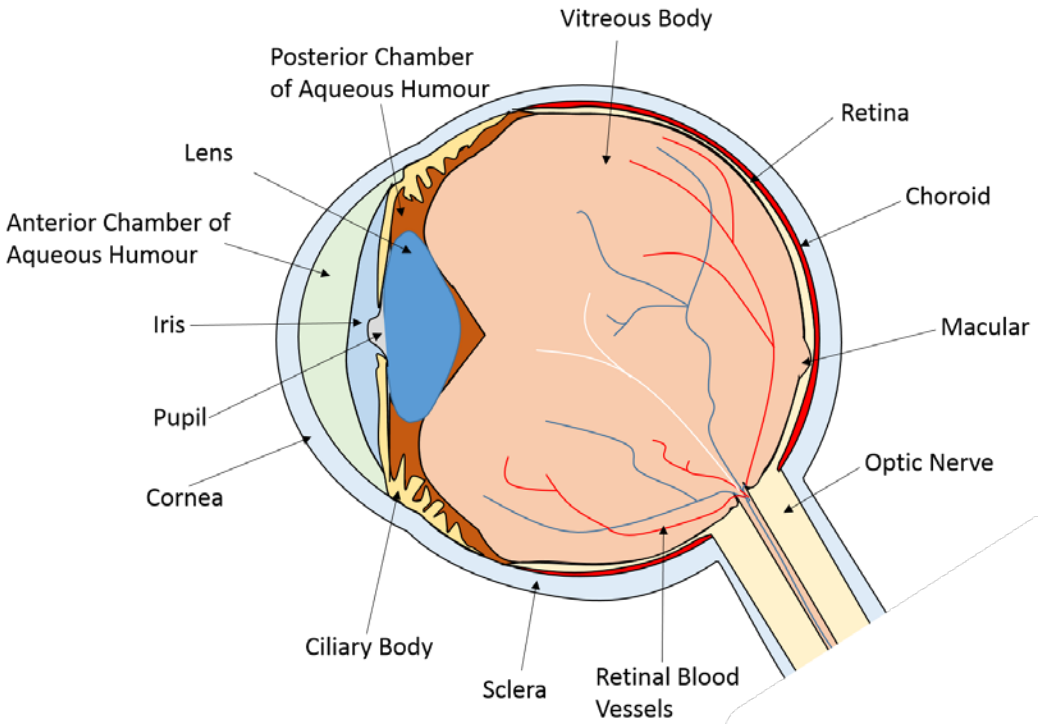

Figure 1: The anatomy of the human eye.
A diagram showing the anatomical structure of the human eye. The cornea and the sclera form the outer most layers of the eye and maintain the structural architecture in conjunction with the aqueous and vitreous humour. The choroid overlies the sclera and supplies the overlying neural retina with blood and nutrients that are essential to maintaining its health and function. The pupil and lens lie at the front of the eye and focus the light onto the retina. This can be finely tuned by the iris and ciliary body which contain muscles that are capable of controlling the pupil diameter, lens shape and refractive index. The retina converts the visual signal into a neural signal which is transmitted to the visual cortex via the optic nerve.

1.3 Structure of the Retina

The only part of the eye to contain neurons capable of converting light into electrical signals and transmit them to the brain is the retina [Figure 2]. The retina is composed of 3 layers of neurons, the innermost of which are the retinal ganglion cells (RGCs) followed by bipolar cells and finally the photoreceptor layer which constitute part of the outer retina. Amacrine cells lie between the RGCs and bipolar cells, where the inner plexiform layer is found. The outer plexiform layer, between the bipolar cells and photoreceptors, is the site of horizontal cells[11]. Light sensitive pigments in the photoreceptors, referred to as rhodopsin and opsin, detect light from external sources. Light is converted from graded electrical signals into an action potential by the bipolar and ganglion cells. The neural signal travels via axons in the optic nerve to the visual cortex, located in the occipital cortex of the brain[13], where they are processed. The primary role of the amacrine cells is to mediate the transmission of neural signals between the RGCs and bipolar cells, whilst the bipolar cells and photoreceptors are mediated by the horizontal cells[11].

There are two types of photoreceptors, known as rods and cones, which have separate and distinct roles. In humans, rod photoreceptors contribute 95% of entire photoreceptor numbers[15]. Rods express the photo-pigment rhodopsin and are responsible for low light visibility (scotopic vision) which can be activated by just a single photon of light[15-18]. Cones, which constitute the remaining 5%[15], have a larger surface area allowing for more efficient photo-transduction and are thus responsible for high acuity photopic vision under high or normal light levels[11]. Cones, by contrast, express the photopigment opsin which confers sensitivity to different wavelengths to allow perception of colour[11].

Both types of photoreceptors are comprised of inner and outer segments. The inner segments are composed of the nucleus and the cell cytoplasm. whilst the outer segments are made up of discs which contain the light-sensitive photopigment[11,15]. Due to constant light exposure, the visual pigment in the photoreceptor outer segments (POS) are rapidly consumed, and therefore the distal 10% of POS are phagocytosed and renewed daily by the underlying Retinal Pigment Epithelium (RPE)[19] (see section 1.9.5). The RPE is a monolayer of post-mitotic cells derived from the neuroectoderm and lies intimately associated with the overlying photoreceptors [Fig. 2]. Located directly beneath and supporting the RPE is a pentalaminar structure known as Bruch's membrane (BrM). Together RPE and BrM form the outer blood-retinal-barrier (BRB), equivalent to the blood-brain-barrier (BBB), which helps to maintain the immune-privileged state of the retina[20]. Underlying BrM is the choroid which supplies the overlying neural retina with blood and nutrients[13] (discussed in Chapter 1.2).

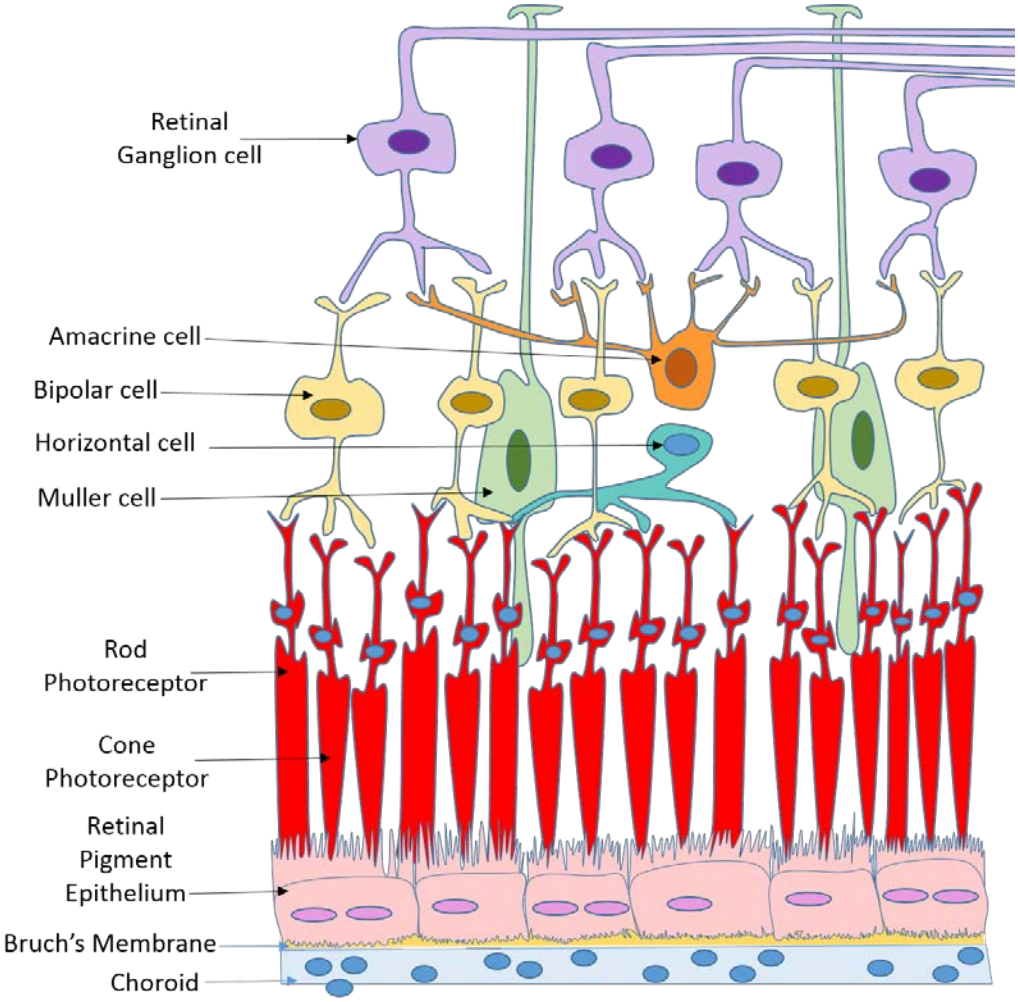

Figure 2: Structure of the retina.
A diagram showing the anatomical structure of the retina. The most direct route of transmission of visual signals occurs along a three-neuron chain comprising of the photoreceptors, bipolar cells and retinal ganglion cells. The amacrine, muller, and horizontal cells mediate the interactions of this chain to allow for more efficient processing of visual signals.

1.4 The Macula

The macula is an area of 3mm in diameter located in the centre of the retina where it is responsible for high acuity vision[13] (i.e. the ability to resolve fine details). In the centre of the macular lies the fovea, a small pit in the retina which is the only part of the eye able to provide 20/20 vision[21]– the highest acuity possible. This is largely due to the fovea having a high density of cones compared to the rest of the eye[13], with the central 300µm of this depression exhibiting a complete absence of rods[11]. To achieve this higher density, the diameter of the cones is reduced in comparison to those found in the peripheral eye[16,22]. Displacement of the inner retina within the fovea, causing the foveal pit, ensures minimal obstruction to create a clear image from the fovea[11]. There is an absence of inner retinal blood vessels, which causes the retina within the macular to be highly reliant on the choroid and RPE for the supply of nutrients and oxygen[11]. In this region, RPE cells are reported to be at their highest density[23]. This is the region of the retina that is affected by degenerative diseases such as AMD.

1.5 Age-related Macular Degeneration

AMD is the leading cause of irreversible blindness in the developed world[13], affecting over half a million individuals in the UK alone (Source: Macular Society) and 50 million people worldwide[24]. It is a late-onset neurodegenerative disease of the macula, leading to profound and debilitating central vision loss[13,25]; causing patients to become unable to perform simple daily activities such as reading, driving or recognising faces. The vision of someone with AMD is represented in Figure 3. AMD is associated with a loss of independence[26], decreased quality of life[27] and often leads to depression[28]. There are high incidence rates of AMD, where 1/3 individuals show symptoms by their 7th decade of life[29]. Due to this, there is a significant health burden involved with global costs reaching US$255billion per annum[13]. The disease incidence, as well as the associated costs of treatments and care of patients, will inevitably rise given the world's ageing demographics. Current trends predict a three-fold increase in global AMD cases within the next 20 years[29]. A number of studies have shown that AMD has a higher prevalence in Caucasian populations compared to individuals with African, Asian or Hispanic origin[13,30]. Some studies have also shown that women have a higher risk of developing AMD[13]. However this could be explained by an increase in average life expectancy compared to men.

1.5.1 Phenotypes of AMD

Since it was first described by Nettleship in 1884[25], AMD has been well characterised clinically and can be categorised into early and late stage disease. Clinical symptoms and different pathologies are used to classify disease stages using one of many grading systems including Wisconsin Age-related Maculopathy, Chesapeake Bay Waterlam and Age-related eye disease study (AREDS) scales[31]. The most commonly used is AREDS grading system which categorises patients into a nine-step severity scale upon visual examination of fundus images taken in clinics[32], examples of which are shown in Figure 4. Early stage AMD is often asymptomatic[13] and thus hard to diagnose. Occasionally AMD is detected as an incidental finding on a routine optometrist check-up, whilst the majority of diagnoses come from self-reported vision loss, by which point disease may have progressed to more advanced stages. This means that AMD is frequently under diagnosed[13]. Occasionally macular degeneration occurs in much younger individuals. The most common form of juvenile macular degeneration is the autosomal recessive disease known as Stargardt disease. Patients are usually diagnosed before they reach 20, and are often registered as legally blind before they reach 50. Genetic risk factors, such as a mutation in TIMP3 in Stargardt's disease are powerful drivers of disease phenotypes.

Figure 3: Visual impairment in Age-related macular degeneration.
Diagram representing the characteristic appearance of the visual field of healthy eyes with normal vision and eyes with age-related macular degeneration. The blurred region in the centre of the image is caused by RPE and photoreceptor loss in the macular region. Image source: http://thelensmen.squarespace.com/whats-new/2015/9/3/blue-light-may-cost-you-your-sight.

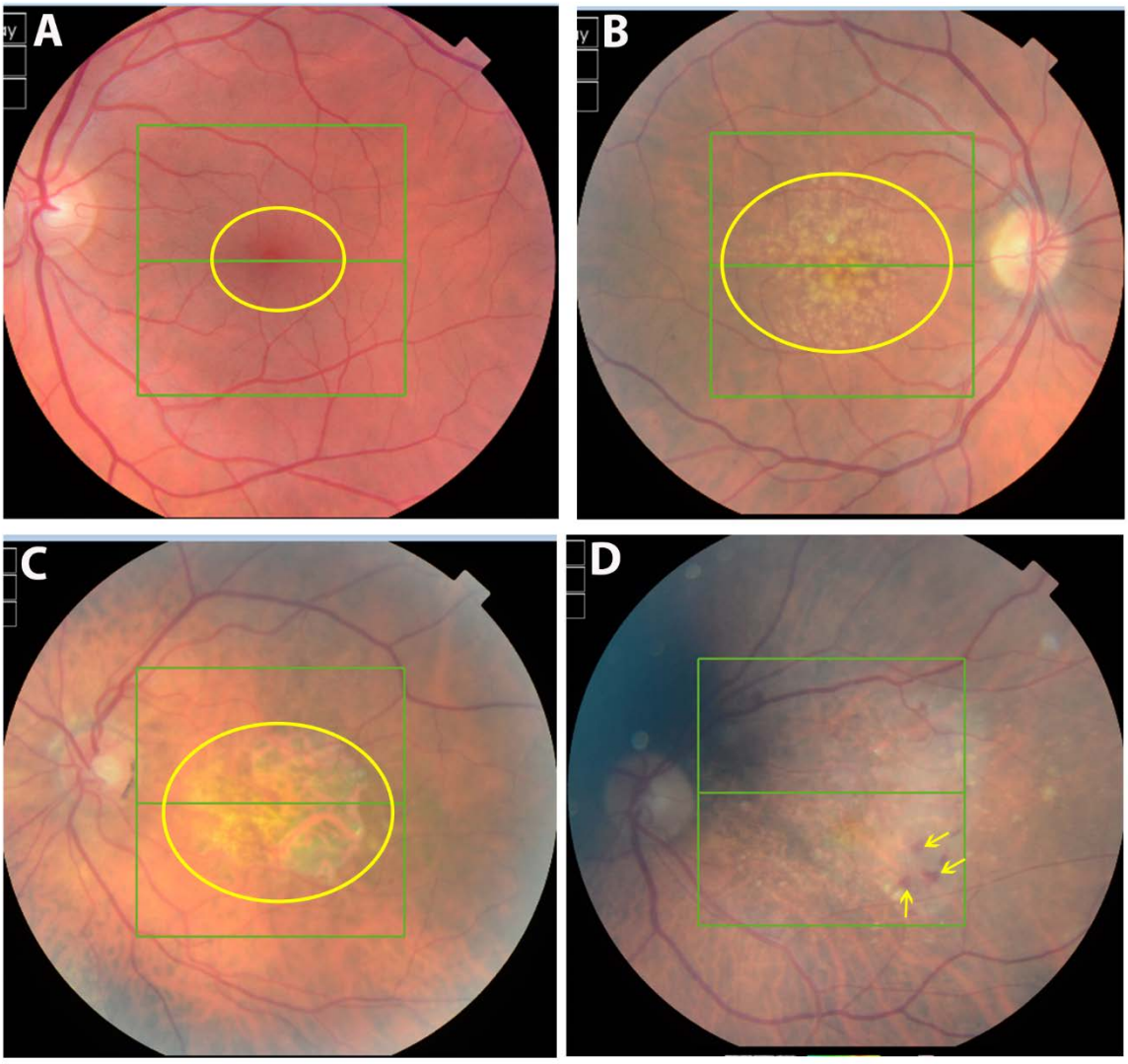

Figure 4: Fundus images showing different AMD stages.
[A] Funduscopy image of a representative healthy retina as viewed through an ophthalmoscope. The macula is denoted by a yellow circle. [B] The appearance of macular drusen (yellow-white spots) is considered to be the first clinical hallmark of AMD. [C] Disease may progress to Geographic Atrophy (GA) AMD in which there is atrophy of RPE and overlying photoreceptors resulting in a macular lesion (yellow circle), or [D] neovascular (nv) AMD in which invasive/leaky choroidal vessels cause a haemorrhage (yellow arrows) which results in retinal damage. Adapted from Lynn SA et al. Neural Regeneration Research 2017;12(4):538.

1.5.1.1 Late AMD

Late stages of AMD are subcategorised into geographic atrophy (GA), or dry AMD, and neovascular (NV) AMD, which is more commonly known as wet AMD. GA AMD develops more gradually to NV AMD and is often quoted as being the most prevalent form of late-stage AMD, reaching an incidence of 90% of all cases[13]. However, this estimate is based on combining all early AMD cases with the number of GA patients. When only sight-threatening late-stage forms are considered, GA AMD and NV AMD have comparable frequencies of incidence[7].

1.5.1.2 Geographic atrophy AMD

The progressive loss of RPE cells eventually leads to large areas of atrophy known as a GA lesion. These lesions are easily distinguishable, and appear as large, pale areas on a fundoscopy image[31] [Fig. 4C]. In these regions, the underlying choroid may be more visible due to death of the overlying RPE and photoreceptors. Gradual damage to patches of RPE cells in the macula results in compromised functions, including incomplete degradation of overlying POS (discussed in section 1.9.7.4). Other hallmarks of GA include RPE hypopigmentation, hypertrophy and hyperpigmentation. These insults to the RPE monolayer progress to cause RPE atrophy and irreversible damage to overlying photoreceptors, as well as choroidal atrophy in some instances[34]. RPE cells may also proliferate in areas adjacent to RPE and photoreceptor damage or atrophy[35]. Some patients with GA AMD can retain normal vision, however severe cases of GA often lead to registered blindness[31]. There are currently no available treatments for GA AMD, which reflects our limited understanding of disease mechanisms at the tissue and cellular levels.

1.5.1.3 Neovascular AMD

Neovascular AMD, also known as choroidal neovascularisation (CNV) is characterised by the formation of abnormal and leaky blood vessels from the choroid. These new blood vessels grow through the blood-retinal barrier (BRB) extending into subretinal space[13], a process which compromises the immune-privileged retinal environment. These nascent vessels leak exudates underneath the RPE, resulting in swelling and scarring of the macular[31]. The activities of new/leaky vessels appear to be regulated by the vascular endothelial growth factor (VEGF), the upregulation of which is typical in NV AMD[13]. Hence the use of intravitreally delivered anti-VEGF injections as the mainstay of current treatment for vascular AMD patients. Anti-VEGF injections available on the National Health Service include ranibizumab (Lucentis) and aflibercept (Eylea)[36]. Ranibizumab is a recombinant human monoclonal antibody fragment which targets the VEGFA receptor binding site. Aflibercept, a human recombinant fusion protein, binds to both the VEGF receptor 1 and 2. Both function to sequester endogenous VEGF activity by binding with high affinity to the

VEGF receptors, alleviating VEGF-driven pathologies[37]. However, treatment involves multiple injections to the eye which in themselves are unpleasant, and are also associated with a number of side effects including increased intraocular pressure, bleeding and inflammation within the eye[38,39]. Furthermore, initial visual gains are almost impossible to maintain. Prolonged treatment with anti-VEGF injections can cause damage to the remaining retina, which results in an unexpected switch to the GA form of the disease[40,41]. This highlights the importance of understanding disease aetiology to develop more effective treatments that prevent or arrest disease in earlier stages.

1.5.2 **Pathology of AMD**

AMD is a complex, multi-factorial disease which develops after a number of risk factors cause a 'disease threshold' to be exceeded. This may also be based on an individual's repair and regenerative capabilities[13]. Risks include age[42], genetics[6], environmental factors such as smoking[43] and an unhealthy 'western-style' diet[44-46], and biological factors such as drusen formation[14,47-50], oxidative damage[51-56], and lipofuscin accumulation[13,57-61]. Drusen is a key hallmark of AMD and will be discussed in more detail in subsequent chapters. The role of genetics in AMD has been well studied. Rare as well as common genetic risk factors have now been largely identified to which work carried out in Southampton has contributed substantially[62,63]. One of the most common genes associated with AMD is the coding variant Y402H in the complement factor H (CFH) gene which is thought to increase the risk of AMD by 5 fold[64]. This highlights the important role of the complement pathway in AMD pathology. Other genetic risk factors such as mutations in fibrillin which alter the barrier properties of BrM[65], and human leukocyte antigen (HLA) which alters the immune properties of the choroid[66] have also been identified. Thus far, however, the molecular and biochemical consequences of many risk genes and how they alter tissues of the outer retina are yet to be fully understood. As previously mentioned, non-genetic and environmental risk factors such as smoking, and nutrition can also drive disease pathologies in a senescent retina. However, the extent to which these exogenous factors influence retinal damage also remains to be established. These external risks may influence disease in conjunction with an individual's genetic background to add a further level of complexity to AMD. For example, some genes such as CETP, ABCA1 and ApoE cause deposition of cholesterol in the retinas. These genes correlate with disease progression but not the exact amounts of cholesterol deposited in the retina of an individual carrying one of these mutations. Therefore the genetic influences of cholesterol deposition may be modified by the individual's diet [67]. The accumulation of Amyloid-beta (Aβ) is another risk factor and is the focus of much research in our lab[67,68]. Aβ is a family of misfolded proteins associated with many neurodegenerative diseases including Alzheimer's Disease (AD)[42,69]. Aβ is secreted extracellularly from neurons after being sequentially cleaved from the ubiquitously expressed amyloid precursor

protein (APP)[70,71]. The healthy retina is constitutively exposed to Aβ, which has been shown to be synthesised within the retinal environment, namely in the RPE and RGCs[72,73]. The highly phototoxic environment of the human retina provides ideal conditions for Aβ accumulation. Hence Aβ deposition is a part of the normal ageing process in both humans and in laboratory animal models[74-76]. In AMD, Aβ is deposited in multiple locations throughout the retina, including in POS and as a major component of drusen where it accumulates as amyloid vesicles[75]. The mechanisms by which Aβ exerts its effects are largely unknown. One hypothesis is that other risk factors exacerbate Aβ pathology in the eye. These risk factors may be genetic as well as epigenetic, such as diet. This apparent increase in Aβ exposure and deposition with aging and disease are likely to exert toxic effects on the RPE and the photoreceptors[42].

1.6 High-fat diet as a risk factor for AMD

There is a growing awareness of the importance of nutrition and its links with AMD. In the western world it is reported that males and females consume 30% more fat than is recommended[77]. A diet containing high levels of particular fats including trans-fatty acid, saturated fats and omega six fatty acids cause a two-fold increase in AMD prevalence, whereas consumption of monosaturated fats has been shown to be protective of AMD[78]. Three different studies have identified positive associations with some dietary fats and AMD[46,79,80]. Dietary information from the Eye Disease Case-Control Study (EDCCS) showed higher intake of specific fats, including vegetable monounsaturated and polyunsaturated fats, and linoleic acid were positively associated with NV-AMD. However, diets high in omega three fatty acid and fish were protective[44]. Analysis of longitudinal studies shows total fat intake positively correlated with AMD risk and further corroborated that fish consumption was beneficial in protecting against AMD[46]. These findings suggest there is a relationship between the intake of a high fat diet (HFD) and risk of AMD. This link is also consistent with a correlation between cardiovascular disease and AMD[80]. Studies have shown that individuals consuming lower macronutrients, including DHA, lutein, zeaxanthin carotenoids and zinc are also more at risk of developing AMD compared to those consuming higher amounts of these trace nutrients[81]. Hence, some AMD patients are prescribed anti-oxidants and zinc supplements[82].Nonetheless, how lack of macronutrients trigger disease at the molecular level is still poorly understood[83]. Intake of a western style diet is associated with the increased accumulation and deposition of lipids and cholesterol, as well as dysfunctional clearance mechanisms and chronic inflammation[84]. The consumption of such fats is also thought to increase AMD risk via the oxidative stress pathway[85,86] by directly enhancing ROS generation[87]. In addition, a high-fat diet causes more substrates to enter into mitochondrial respiration. Subsequently, the number of electrons moving into the electron transport chain will increase. This causes an excess of electrons to be produced, which are free to react with molecular oxygen producing high levels of superoxide[88].

1.6.1 Oxidative stress and damage to the RPE and associated tissues of the outer retina

Oxidative stress was first defined by Helmut Sies as being an imbalance between the anti-oxidant defence system of the cell and the intracellular levels of harmful reactive oxygen species (ROS)[89,90]. Since then it has gained increasing recognition and is now considered to be a major pathogenic pathway in age-related and degenerative diseases such as AD, atherosclerosis and cancer[91-95]. In the eye specifically, oxidative stress has been found to

contribute in many common ophthalmic disorders including AMD, cataracts, glaucoma and diabetic retinopathy[54-56,85,86,96,97].

Chemically, oxidation refers to the removal of electrons while reduction describes the gain of electrons[90]. A series of reactions known as the tricarboxylic acid (TCA) cycle is responsible for most of the oxidation of ingested carbohydrates, proteins and lipids. The energy produced is conserved in the form of the reduced electron-accepting coenzymes, NADH and FAD(2H)[98]. The electrons of these coenzymes can be used to reduce oxygen (O_2) to H_2O via the energy transport chain, and this reaction releases energy for the conversion of adenosine diphosphate (ADP) to adenosine triphosphate (ATP) in a process known as oxidative phosphorylation. This occurs in the mitochondria and is catalysed by ATP synthase[99]. The electron transport chain accounts for 90% of our total O_2 consumption, the remainder being utilised by reactions involving oxidases and oxygenases[86]. Reactive oxygen species (ROS) is an umbrella term that describes free radicals (which contain one or more unpaired electrons), hydrogen peroxide (H_2O_2), or singlet oxygen, both of which contain no unpaired electrons but are in an unstable, reactive state[100,101]. In the cell, ROS continually leak from the active sites of enzymes involved in oxidative processes by interacting with O_2 and other compounds[86]. To achieve a stable state or homeostasis, ROS extract electrons from other molecules, which are themselves then rendered unstable, resulting in a cytotoxic oxidative chain reaction[102]. H_2O_2, although containing no unpaired electrons, participates in the Fenton reaction, producing a highly toxic hydroxyl free radical[98]. Carbohydrates, membrane lipids, proteins and nucleic acids are all vulnerable to damage caused by ROS[99,101,103], and this damage is believed to contribute to the pathogenesis of many diseases including diabetes, cancer, Parkinson's disease and AMD[56,91,95,97,99,103,104].

The retina is an ideal environment for the generation of ROS for many reasons. Firstly, oxygen consumption by the retina is much greater than by any other tissue[105,106]. Secondly, the retina is subject to high levels of irradiation. Photochemical retinal injury was first described by Ham et al. when 20 rhesus monkey retinas were exposed to blue light (411nm) for 1000 seconds and showed considerable pathological damage[107]. This pathology resembled changes seen in AMD, including damage to the POS, cellular proliferation, and hypopigmentation of the RPE. These findings have been corroborated many times[108-110]. It has been shown that retinal light damage induces the expression of the anti-oxidative stress protein heme oxygenase-1 (HO-1)[111], highlighting the putative involvement of oxidative stress in retinal light damage. Thirdly, POS are rich in polyunsaturated fatty acids, which are readily oxidised and can initiate a cytotoxic chain-reaction[112-114]. Fourthly, the neurosensory retina and the RPE contain an abundance of photosensitisers or chromophores[115]. Chromophores are molecules that absorb light to produce a chemical

reaction that would not occur in their absence, causing photochemical damage. In the retina, these include rhodopsin, melanin, lipofuscin and mitochondrial respiratory enzymes such as cytochrome c oxidase[115,116]. Finally, the process of POS phagocytosis by the RPE (discussed in chapter 1.9.5) itself causes oxidative stress and results in the generation of ROS, including H_2O_2[117-120].

ROS play an important role in the regulation of many physiological processes involved in intracellular signalling[121], but they can also induce serious damage to molecules; thus, cells have adopted many mechanisms to help protect against the effects of oxygen toxicity. These include cellular compartmentalisation, repair, enzymatic removal of ROS, and 'scavenging' of free radicals by vitamins (including aforementioned micronutrients and trace elements) and antioxidant compounds such as melanin[53,94]. However, stimuli such as irradiation, ageing, inflammation, high-fat diet, and cigarette smoke are known to increase the production of ROS[51,85,122-124]. Increases in ROS render the cell unable to cope with the level of oxidative stress, which is when irreversible damage can occur. Since the RPE monolayer is post mitotic[125], these cells are unable to repair any damage and are therefore particularly vulnerable to oxidative stress-induced pathology. Although the RPE is the main site of early damage in a majority of AMD patients, it is important to note that in some cases primary damage may instead occur in photoreceptors[126] or the choroid[127]. This complexity makes AMD a difficult disease to study. Nonetheless, the RPE layer remains the focus of many studies, including in this thesis.

1.7 The structure of the Retinal Pigment Epithelium

The RPE is a monolayer of hexocuboidal pigmented epithelial cells which form a barrier between the overlying photoreceptors in the neural retina and the underlying choroid[128] [Fig. 2]. The RPE is highly morphologically specialised [Fig. 5] in order to aid its many functions, which are further described in section 1.8. The morphological specialisation of RPE are in part due to its highly polarised nature. As shown in Figure 5, apically RPE cells have long protruding microvilli which extend into and surround the distal tips of the photoreceptors[129] enabling fast and efficient engulfment of shed POS. These microvilli are thought to increase the surface area of the RPE by 30-fold[130]. Microvilli are approximately 5-7µm in length however often the length of the POS cloaked by the microvilli is larger for rods than for cones[131]. On the basal surface of RPE cells, there are highly convoluted invaginations which increase the surface area for metabolite and nutrient exchange between the choroid and the RPE/retina[132] . These can be observed in TEM cross-sections of the mouse outer retina I have prepared and shown in figure 5. Additionally, regional variation in the structure and physiology of the RPE monolayer has been well documented and is likely to reflect the functional demands from the overlying retina as well as the underlying choroid. For instance, in the periphery, RPE cells are short and elongated measuring up to 60µm in diameter. Whereas in the macular region, the RPE cells are narrower and taller, measuring 14µm in diameter[133]. The shape of RPE cells in the macula also become more disorganised and irregular[132]. RPE cells contain many organelles, such as mitochondria and endocytic/membrane-bound vesicles which reflects the high metabolic activity of these cells[134]. Some stratification of intracellular organelles may also be observed in the RPE. For instance, RPE cells have a basally located nucleus, of which some are bi-nucleate[135,136]. Abundant levels of mitochondria are found localised towards the RPE basal surface[125] whereas cigar shaped-melanosomes 2-3µm in length are localised in a vertical orientation towards the apical microvilli[132]. A melanosome is a lysosomal-related compartment which synthesises and stores melanin. The role of melanin is thought to enable RPE cells to cope with high levels of incident light and prevent further diffraction of scattered light[130]. Interestingly, RPE cells in the macular are darker in pigment, which has been attributed to a greater distribution of melanin in this area[137]. However, this peak in melanin density may be due to a denser packing of melanin as the RPE cells in the macular are taller and narrower compared to cells in the peripheral retina. The RPE is the site of primary pathology responsible for a variety of retinopathies including Best, Stargardt's, and, perhaps most commonly, in AMD. Current understanding of the ultrastructure of the RPE comes from conventional 2D imaging techniques such as Transmission Electron Microscopy and Scanning Electron Microscopy, which will be discussed in more details in subsequent chapters.

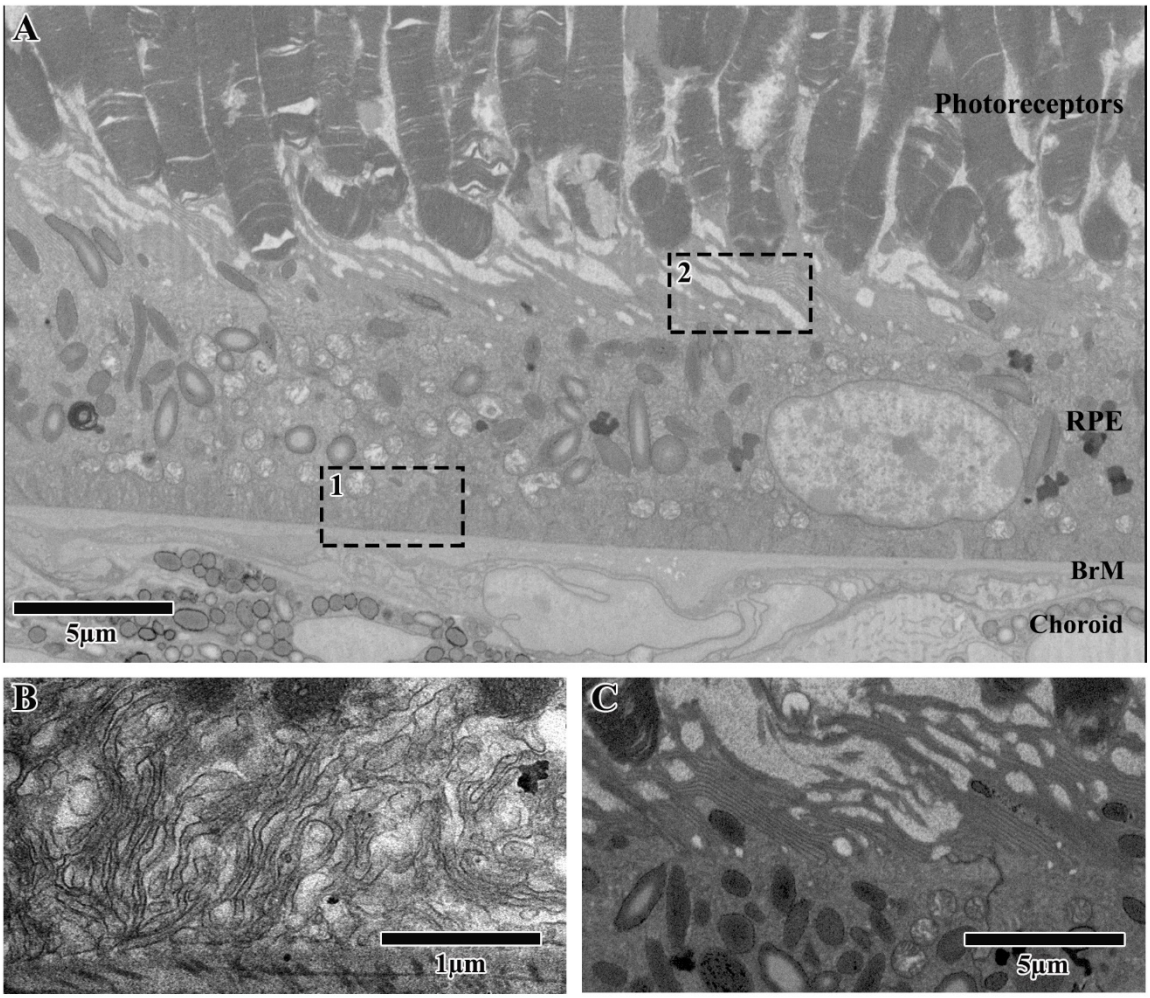

Figure 5: The polarised morphology of the retinal pigment epithelium.
Representative transmission electron micrograph of [A] the mouse outer retina in cross-section showing the polarised nature of the RPE monolayer. [B] Highly invaginated basal infolds in RPE cells can be seen in magnified insert of box 1. [C] Long, thin microvilli that extend from the apical surface of the RPE cell and interdigitate with the overlying photoreceptors can also be seen in magnified insert of box 2, Melanin pigment is typically localised towards the apical portion of the cell, whilst mitochondria are found basally.

1.8 Structural changes to the RPE in ageing and disease

An accumulation of discrete but pronounced changes occur to the RPE in ageing and diseased eyes. These structural changes influence its ability to function optimally. There is overall thickening of the aged retina, primarily due to the loss of neurons from the inner retinal cells, as well as shortening of photoreceptors[138]. Interestingly, BrM is reported to be thickened in aged eyes[139]. Basal deposits on or within BrM accumulate with age, and drusen forms between the basal lamina of the RPE and the inner collagenous layer of BrM[140]. Drusen are lipid-rich extracellular deposits and are considered to be the first clinical hallmark of AMD. Several morphological forms of drusen have been identified, which are characterised according to size and structure. Hard drusen are small (<50µm) and have well defined borders. They are usually found in the peripheral retina and are a part of normal ageing[31]. Soft drusen, however, are larger, often reaching 125µm and have poorly defined edges[31,42]. They reside in the macula, a sign of increased disease susceptibility[141] and often coalesce with one another forming larger deposits. The considerable damage to the RPE and BrM within close proximity to drusen accumulation appears to occur prior to any apparent clinical symptoms[13,14]. More recently, reticular pseudo-drusen has also been described which appears on the apical surface of the RPE, and underneath the photoreceptors[67,142]. They form a lattice-like network and are closely associated with AMD progression. Drusen is known to be composed of over 60 different proteins[143], of which 24 are also common to senile plaques in Alzheimer's brains. This suggests common pathways of disease in AD and AMD.

Other structural changes to tissues in the outer retina with ages includes the loss of defined RPE cell shape, hyperplasia with regions of multi-layered cells, and areas of RPE hyper and hypopigmentation[23]. Interestingly, there are levels of atrophy particularly in areas overlying drusen. It is known that RPE cells are lost with age, with there being a 2.3% decline in a total number of RPE cells lost per decade of life[144]. However, while this is true in the peripheral retina, an age-associated change in RPE cell density is not observed in the fovea[145]. This could be due to an inward migration of peripheral RPE cells to compensate for the loss of foveal RPE[144] as it is reasonable to assume that cell loss will be greater in the macular compared to the periphery due to a higher metabolic demand in the central retina. Consequently, a greater proteolytic stress in macular RPE cells would be anticipated. Ultrastructurally, it has been reported that there is a loss of melanin granules, an increase in the number of residual bodies, and an accumulation of the age pigment lipofuscin[146,147]. RPE microvilli atrophy and thickening and shortening of remaining microvilli have also been reported[130]. Basal infolds are also drastically damaged, with there being a complete absence of, or vastly enlarged, infolds[148]. These age-related changes are

apparent in more marked forms in eyes from AMD patients. These structural changes are known to be associated with oxidative stress and the general decline of RPE function.

1.8.1 Multinucleation of RPE in age and disease

Multi-nucleation and in particular the formation of bi-nucleate RPE cells, has long since been reported in both the rodent and human retina. The number of bi-nucleate RPE cells is much higher in the mouse retina and a subset of these cells are present from birth and is thought to be a developmental mechanism. Despite this, the number of bi-nucleate RPE increase with age in both mouse and human RPE, and this increase is more prevalent in the central retina of mice and the macular in humans. A study by Volland et al., showed that in the mouse central retina 2/3 RPE cells were binucleate whereas this was much lower in the peripheral retina, with only approximately 3% of RPE having 2 or more nuclei[136]. A further study performed by Chen et al., found that there was an age-related increase in the number of bi-nucleate RPE across the retina. In young mice, 33.6% of RPE were found to contain 2 or more nuclei, with this number reaching 80% by 24 months. In the peripheral retina at 3 months, only 1.7% of RPE were multinucleated, and this reached 20.5% by 24 months[149]. In human retinas, the distribution of multinucleate RPE is less well studied and defined. Ts'o and Friedman showing that only 3% of RPE in humans are binucleate and these are found in unspecific regions[150]. There are many theories regarding the presence of bi-nucleate RPE cells in the retina, and how they are formed. One theory is that these binucleate RPE cells are present from birth and is part of a developmental mechanism[151], however, given the increasing number of multinucleate cells across the retina with age, there must be further reasons for their formation. An alternative theory is that the formation of such cells is a pathological condition in a cell under stress, or a healthy cell which has adapted to a changing environment (e.g. with age and/or oxidative stress)[149]. Such theories will be discussed in more detail in chapter 3.

1.9 Function of the RPE

Within its strategic position, the RPE can exert many functions that are essential for maintaining a healthy and functional retina. These include the continuous phagocytosis of shed POS, directional secretion of key proteins towards the neuroretina and choroid, absorption of stray light and transepithelial support of substances between the systemic vasculature (choroid) and the protected retinal environment[125]. The RPE also maintains the immune-privileged state of the retina by forming the BRB with BrM[20].

1.9.1 Blood-retinal barrier

The BRB is the eye's equivalent to the blood brain barrier (BBB), both of which maintain an immune-privileged state of their respective organs by separating the systemic circulation. The BRB is composed of two components which work together to facilitate the specialised retinal environment. The first is formed by the retinal vasculature of the inner retina, while the other is delineated by the RPE and BrM[20]. The lateral surfaces of the RPE are joined by tight-junctions that form a selectively permeable ionic and macromolecular barrier which isolates the retina from the underlying choroid[134,152]. This enables selective transport of nutrients and proteins across the RPE monolayer regulated by the polarised distribution of pumps, receptors, channels, and transporters[134,153]. Tight-junctions are composed of occludins, claudins and zonula occludens (ZO) and the composition of these determines how permeable and selective the BRB is to the diffusion of solutes[20,152,153]. ZO forms early tight-junctions that interact with the actin cytoskeleton as well as the occludin and claudin proteins to create a cellular scaffold[23]. Permeability and selectivity of the barrier are partially determined by which of the 24 claudins are expressed[20,154]. Claudin-19, claudin-3, and claudin-10 have been reported to be present in the tight-junctional complex in human RPE cells[154]. Claudin-19 is the most abundant and mutations within the encoding gene (*CLDN19*) are associated with severe visual impairment[155]. Occludin further regulates tight-junction permability[156]. Adherens junctions are also present between adjunct cells which controls the passage of solutes, while gap junctions allow for metabolic coupling of the RPE[132].

The RPE also regulates the transepithelial transport of ions, fluid and metabolites via specialised transport proteins located within the apical and basal plasma membranes[157,158]. These proteins are maintained in an asymmetric distribution to ensure that the RPE can determine the homeostatic and optimal microenvironment of the photoreceptors. The RPE also regulates the passage of ions such as Cl-, K+, Na+, and HCO_{3-} to and from the retina to allow for the polarisation of cell membranes, fluid transport and maintenance of pH[132]. Impairment to these components are also associated with disease in the retina.

1.9.2 Secretory activity

The RPE secretes numerous growth factors and signalling molecules to allow for communication with its neighbouring tissues, and to maintain the structural integrity of the choroidal vasculature and neural retina[125]. These signalling molecules encompass many molecules implicated in retinal pathologies, such as pigment epithelium-derived growth factor (PEDF)[159] and VEGF[160]. PEDF is secreted apically where it provides neurotrophic support to the photoreceptors layer and helps to maintain an antiangiogenic environment[159]. VEGF is secreted basally and maintains a healthy vasculature[125]. The secretion of both molecules is tightly regulated by the RPE, and perturbations in the levels of VEGF and PEDF secreted leads to proliferative phenotypes, including CNV[161] (see section 1.5.1.3).

1.9.3 Visual cycle

Retinoids are essential in the visual cycle, and the RPE helps maintain levels of key retinoids such as rhodopsin and opsin by storing and transporting them[162]**.** Retinol is delivered from the blood and is then transferred into the cell using a specific binding site located on the basal and basolateral surfaces of the RPE. All-trans-retinol is immediately esterified intracellularly and becomes all-trans-retinyl ester which provides a non-toxic substrate for storage or isomerisation to 11-cis-retinol. All-trans-retinyl ester then binds to retinaldehyde binding protein within the cell and is converted to 11-cis retinal before being transported via interphotoreceptor matrix binding protein to the overlying photoreceptors where it combines with opsin to produce rhodopsin. A complete loop is formed when retinol is transferred back to the RPE as a function of the phagocytosis of POS[132]. Disruption of this cycle is associated with diseases such as AMD.

1.9.4 RPE clearance pathways

The RPE has several clearance mechanisms which function to maintain cellular protein homeostasis (proteostasis) under environmental stress[163]. Three such processes are the endocytosis, phagocytosis and autophagy, all of which are interrelated. A distinct network occurs via the Ubiquitin-Proteasome (UP)[164,165]. Components are directed to a specific clearance pathway; in general, damaged, misfolded or aggregated proteins are targeted to the UP, while membrane-bound or organelle-associated proteins are targeted to lysosomes via endocytic or autophagic pathways[163]. Under normal retinal conditions, POS are endocytosed and targeted to early endosomes, which mature into late endosomes, before fusing with lysosomes to complete degradation. Under conditions of oxidative stress, autophagic vesicles are formed, which causes a subset of POS to be internalised via

phagophores, which form autophagosomes. These vesicles also fuse with lysosomes to complete POS degradation[166].

1.9.5 Phagocytosis and degradation of POS

Due to the post-mitotic nature of the RPE, an efficient lysosomal system is particularly important to remove unwanted or damaged cellular components, as well as being crucial in the daily phagocytosis of POS. The daily ingestion of POS makes the RPE monolayer the most phagocytic cell type in the body, with each cell processing in excess of a billion POS in a 70 year human life span[132,167]. To cope with this high demand, the RPE cells have an extremely active lysosomal system which constitutes a large proportion of the cell's cytoplasmic volume[23]. There are three receptors that are integral for the regulated internalisation of POS; the receptor tyrosine kinase c-mer (MerTK), αvβ5 integrin, and the macrophage phagocytosis receptor CD36. These three receptors operate in a circadian rhythm where αvβ5 integrin is required for mediating POS binding to the RPE[168]. By contrast, CD36 causes the internalisation of POS[125] while MerTK activates RPE phagocytosis[169,170]. Upon ingestion, phagosomes fuse with lysosomes to form a secondary phagosome or phagolysosome. Here, the POS is combined with over 40 lysosomal enzymes, of which cathepsin D is most prominent in the RPE[171]. These enzymes are capable of degrading proteins, polysaccharides, lipids and nucleic acids. The phagocytic load and lysosomal enzyme activity vary greatly with retinal location[172]. The phagocytic load is dependent on the type and density of overlying photoreceptors. Notably, RPE cells in the fovea will phagocytose significantly more cone photoreceptors compared to the RPE in surrounding regions. Also, the mean ratio of photoreceptor cells per RPE cell is higher in the macula compared with other areas[173]. In the central retina, lysosomal enzyme activity also appears to be higher than in the periphery[172]. The end products of POS degradation are either recycled back to the photoreceptors or are removed via the choroid[174]. The endocytic pathway also traffics and sorts cargo originating from the extracellular environment and the plasma membrane, while autophagic vesicles capture cytoplasmic derived cargo, such as large protein inclusions or damaged organelles. Importantly, the endocytic and autophagy pathways share a common termination point at the lysosome [Fig. 6]. In general, POS are internalised through endocytosis into early endosomes, these mature into late endosomes before fusing with lysosomes where the final stages of degradation are completed. Upon nutrient deprivation or levels of phagocytic stress, POS are internalised through phagophore formation, which from autophagosomes which fuse with late endosomes or lysosomes to complete degradation [Fig. 6].

1.9.6 Endo-Lysosomal and autophagy pathways

During endocytosis, cargo internalisation initiates at clathrin-coated pits on the plasma membrane that bud into vesicles. Early endosomes (EE) are found in the peripheral cytoplasm, near the plasma membrane and are relatively small with tubular/vacuolar domains. The size of endosomes appears to range between 200 – 500nm[175]. Individual EEs move along microtubules in a saltatory manner[176]. EEs are considered to be the major sorting point in the endocytic pathway; receiving cargos via the clathrin-mediated pathway as well as other routes including ARF6-dependent and caveolar pathways[177]. Hence, EEs internalise the plasma membrane as well as extracellular materials. The Rab family of small GTPases act as molecular switches that alternate between the activated GTP-bound and the inactivated GDP-bound forms. For instance, EEs contain Rab-4, Rab-5 and Rab-11, which provides a means for further sorting to target destinations[178]. A noteworthy component recruited to the cytosolic surface of EEs is the large, multimeric proton pump termed vacuolar ATPase (vATPase), which functions to allow for the acidification of endosomes as well as lysosomes[179]. The luminal environment within EEs is weakly acidic (pH 5.9-6.8) and contain relatively low Ca^{2+} levels[180,181]. EEs are sites at which intraluminal vesicles (ILV) form, a process that occurs on the luminal side of endosomes involving clathrin and components of the endosomal sorting complex required for transport (ESCRT). ESCRT sorts ubiquitinated membrane proteins into ILVs, leading to the formation of multivesicular bodies (MVBs). MVBs may therefore contain several ILVs[182,183]. These MVBs and a proportion of EEs subsequently mature and become Late Endosomes (LEs).

LEs are derived from vacuolar domains of EEs. Nascent LEs that are positive for Rab-5 associate with Rab-7, resulting in Rab-5/Rab-7 hybrid endosomes. Such hybrid vesicles are short-lived as Rab-5 is rapidly replaced by Rab-7[184]. This process of LE maturation is referred to as 'Rab conversion'[185]. As endosomes mature, their saltatory movement in the cell periphery change to rapid long-range oscillations with net displacement towards the perinuclear zone where lysosomes reside[176,186]. The long-range movement of LEs primarily occurs along microtubules and is dependent on molecular motors such as kinesin and dynein. These molecular engines, along with specific multi-subunit tethering complexes, SNARE proteins, and actin-dependent myosin motors are involved in the fusion of endosomes with each other[187,188]. The formation of LEs is followed by a process of maturation[189,190]. During maturation, tubular extensions of EEs are lost as endosomes become increasingly vesicular shaped. Mature LEs also have a larger diameter (250nm – 1µm) compared to EEs, while increasing acidification results in luminal pH values between 4.9 and 6.0. Decreasing pH levels are important for the activity of luminal hydrolytic enzymes[180]. A similar process of maturation may occur in autophagosomes[191] and phagosomes[192], before fusion with LEs and lysosomes. It is important to note that i*n vivo*

studies of POS impairment in mouse models of retinal degeneration mostly discuss the trafficking of POS cargo in phagosomes rather than endosomes However, Rab markers use to label such compartments do not distinguish between early endosomes and phagosomes, or late endosomes and phagosomes[193]. Indeed, both phagosomes and endosomes mature through similar mechanisms and often fuse together during early maturation[194,195]. Further, both pathways feed into the lysosomes.

Degradative lysosomes result from the merging of cargo-carrying vesicles in the endocytic or autophagic pathways, and vesicles derived from post-Golgi traffic. Intracellular and extracellular macromolecules trafficked via endosomes or autophagosomes are eventually degraded within lysosomes[196]. The limiting outer membrane of lysosomes consists of a single phospholipid bilayer on which lysosome-associated membrane protein 1 (LAMP 1) and LAMP 2 constitute a majority of membrane proteins[197]. LAMP proteins are typically used as markers of these organelles, the diameter of which range between 50nm-1µm[198,199]. Lysosomes form part of a family of communicating, acidic, vesicular compartments where intra-vesicular pH ranges from 3.8 to 5.0[200]. To facilitate degradation, lysosomes contain over 50 lysosomal membrane proteins, including an array of channels/transporters such as vATPase, as well as 60 different types of hydrolytic enzymes[197,201]. This luminal environment provides ideal conditions for the activity of lysosomal enzymes which, according to their preference for substrates, are grouped as lipases, glycosidases, acid phosphatases, proteases, sulfatases and nucleases. Internalised cargos are broken down to generate monosaccharides, amino acids and free fatty acids, amongst other compounds[201,202]. Products of lysosomal digestion are eventually transported to the cytoplasm for use in a variety of biosynthetic activities. Lysosomes are found in the perinuclear region and are transported along microtubules by kinesin and dynein motors[199]. Under normal physiological conditions, the population of lysosomes appears to be largely stable over time, and a single cell may contain up to several hundred lysosomes[203,204].

Autophagy is primarily a non-selective process through which cells degrade intracellular constituents as part of a homeostatic response to nutrient and amino acid starvation. Alternatively, it can function as a selective pathway to degrade misfolded and/or aggregated proteins, and damaged organelles as a quality control mechanism. Therefore, it is a useful mechanism through which the cell copes with stress, low energy stores, and effects associated with ageing. There are three autophagic pathways; (1) microautophagy, (2) chaperone-mediated autophagy, and (3) macroautophagy[205]. Microautophagy is a process through which small quantities of cytoplasm non-selectively enters lysosomes for degradation via membrane invagination. In chaperone-mediated autophagy, cytosolic proteins containing the KFERQ motif, such as the Amyloid Precursor Protein (APP), are preferentially targeted to lysosomes for degradation[206]. This requires the coordinated

function of Lysosomal Membrane Protein 2A (LAMP 2A) and specific molecular chaperones such as Heat Shock Proteins (HSP). Macroautophagy involves the large-scale degradation of cytoplasmic constituents which are engulfed by distinct double membrane-bound organelles referred to as autophagosomes. Autophagosomes fuse with LEs and MVBs to form hybrid amphisomes which eventually mature to lysosomes upon progressive intraluminal acidification[207]. Alternatively, autophagosomes can fuse directly with lysosomes to form autolysosomes, which results in the degradation of cargo and the recycling of cellular components[205]. Recent findings have revealed a further pathway of autophagy; a non-canonical form termed LC3-associated phagocytosis (LAP), through which lapidated LC3 associates with phagosomes[208]. One of the primary regulators of the autophagy pathway is the nutrient sensor mechanistic target of rapamycin complex 1 (mTORC1). In response to nutrient deprivation or amino acid starvation, mTORC1 becomes inhibited as a result of the modulation of various upstream regulators, such as AMP-activated protein kinase (AMPK). This subsequently leads to the activation of the autophagy initiating ULK1 complex, which comprises ULK1-FIP200-Atg13. This complex triggers a cascade of events leading to the activation and recruitment of primary autophagy regulators that facilitate the encapsulation of cargo by a growing autophagosomal membrane. Autophagosomes mature in a similar manner to endosomes and leads to the formation of an autolysosome. Intermediate compartments called amphisomes exist following fusion of autophagosomes with late endosomal compartments, before a subsequent fusion with lysosomes[209]. The major pathways involved in RPE clearance mechanisms can be visualised in Figure 6.

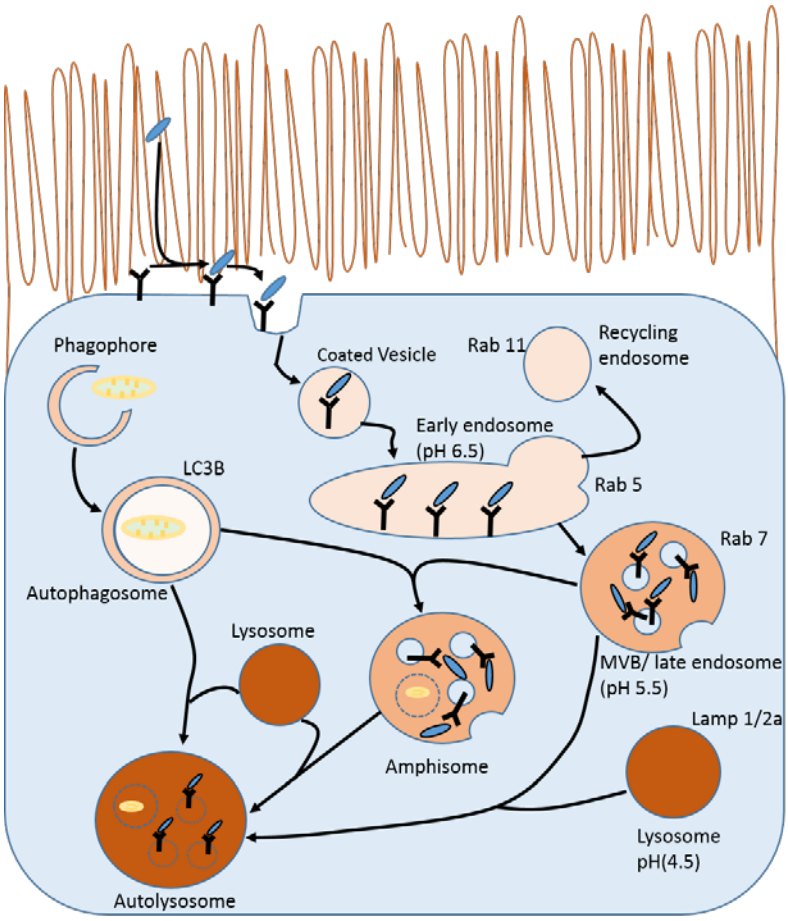

Figure 6: Schematic of the lysosomal system:
Extracellular components are internalised into clathrin-coated pits/ vesicles via binding to receptors. These vesicles then form early endosomes. Some of the internalised cargos are recycled back to the membrane via recycling endosomes while the rest forms MVBs or late endosomes, with a Rab conversion and a decreased in pH. Alongside this, damaged or unwanted organelles such as mitochondria are internalised via phagophores to form autophagosomes. These autophagosomes can fuse with MVBs to form an Amphisome, or with a lysosome to form an autolysosome. Similarly, MVBs can fuse with lysosomes to form autolysosomes where the final stages of degradation are complete.

1.9.7 Impaired cargo clearance in chronic degenerative diseases

Increasing age is thought to correlate with a reduction in cellular ability to effectively clear intracellular proteins. This pathway of damage is common to many cells in a plethora of diseases.

1.9.7.1 Lysosomal storage diseases

Dysfunctional lysosomes accumulate partially processed or undigested material which leads to a group of diseases known as lysosomal storage disorders (LSDs), that have severe consequences for the patient[210]. LSDs are a group of inherited and acquired disorders which affect different cell types, tissues, and organs[198], with two-thirds of LSDs being associated with brain lesions[211]. Many patients with LSDs also have ocular

phenotypes and experience vision loss[212]. Patients with Batten's disease have bull eye's maculopathy characterised by a ring-shaped pattern of damage around the macula. Symptoms including colour blindness, loss of high acuity vision, and night blindness[213]. The majority of LSDs are a result of deficient lysosomal enzyme activity caused by mutations in genes coding for specific lysosomal hydrolases, leading to abnormal storage of macromolecular proteins[214]. However, many also carry mutations in non-enzymatic proteins[197] adding further complexity and clinical heterogeneity to LSDs. Common to all LSDs is an initial accumulation of substrates inside endosomal, lysosomal and autophagic vesicles, leading to the implication of defective lysosomal enzymes as a cause of pathogenesis in LSDs[214,215]. In most LSDs, autophagic flux is reduced[216,217], evident from an elevation of autophagic substrates and autophagosome-associated LC3B[210]. This also leads to the persistence of dysfunctional mitochondria, which is highly pronounced in neurons of patients with Batten's disease[218] and has a major impact on cytoplasmic proteostasis[210]. Reduced autophagic flux also causes a subsequent accumulation of ROS which renders cells more sensitive to apoptotic and inflammatory stimuli[219-222]. Since mitochondria are involved in signalling pathways linked to regulating apoptosis and innate immunity, the decrease in autophagic flux and aberrant mitochondrial function may be responsible for apoptosis and inflammation in the CNS. This is a characteristic of many LSDs[210]. Niemann Pick disease is an LSD, however it shares many intriguing parallels with mechanisms underlying neurodegenerative disorders[223]. In juvenile Niemann Pick type C disease, cholesterol is mistrafficked through the endocytic pathway, resulting in an accumulation in both late endosomes and lysosomes. This is associated with AD-like pathology including neurofibrillary tangles, heightened amyloid genic Aβ precursor protein (APP) processing and characteristic endosomal abnormalities[224,225].

1.9.7.2 Neurodegenerative diseases

Impairment of both the lysosomal-autophagy and UP system leads to aggregation and accumulation of proteins resulting in cellular toxicity[165,226]. This toxicity can contribute to neurodegenerative conditions such as Parkinson's disease (PD), AD, Huntington's disease, and other protein conformation disorders such as amyotrophic lateral sclerosis. PD is one of the most common neurodegenerative diseases in the elderly[227]. A pathological hallmark of the disorder is cytoplasmic inclusions containing aggregated proteins, known as Lewy bodies[228-230]. Despite α-synuclein being the main component of Lewy bodies[210], its role in the pathogenesis of both sporadic and familial PD is poorly understood[231]. Mutations of α-synuclein such as A53T, A30P and E46K have been implicated in the cause of the disease[232-234]. The reduction of proteasome activation and aggregation of abnormal proteins is thought to arise from increased oxidative stress, and the associated depletion in ATP[104]. PD associated mutations in lysosomal ATPase, such as ATP13A2 and parkin, a component

of the ubiquitin-proteasome system, have also been shown to result in impaired protein degradation[227]. Thus, a failure of protein degradation may lead to neuronal cell death in PD and other neurodegenerative diseases such as AD. Oligomerisation of toxic, aggregate-prone, intracytosolic proteins that are unpalatable to the proteasome[235-237] often cause autophagy dysfunction. A lack of autophagy completion leads to the persistence of ubiquitinated and aggregate-prone polypeptides in the cytoplasm, including p62/SQSTM1, α-synuclein, and Huntingtin protein[235,238,239]. α-synuclein contributes to neurodegenerative diseases by reducing the efficiency of autophagosome formation[240]. α-synuclein is usually cleared by autophagy[236], and mutations in the gene, as well as the increase in intracellular concentrations of non-mutant α-synuclein, have been implicated in the pathogenesis of PD[232-234,241]. This supports the hypothesis that impaired autophagic degradation of α-synuclein is an important mechanism of neurodegeneration in PD. In addition, it has been shown that mutant α-synuclein is not translocated into the lysosomes for degradation[242]. This failure to clear mutant α-synucleins may explain their exceptionally high affinity for lysosomal membrane receptors that mediate the autophagic pathway. Their binding is thought to block lysosomal uptake, inhibiting the degradation of mutant α-synucleins as well as other autophagy substrates[210,242]. Accumulations further perturb cellular homeostasis and contribute to neural toxicity. Cathepsin D is a major protease involved in lysosomal clearance of α-synuclein in cellular and animal models of PD. High levels of Cathepsin D have also been shown to reduce α-synuclein aggregation and toxicity[243]. Cathepsin D activity decreases as a result of insufficient endosomal sorting and trafficking of proteases into lysosomes, causing reduced clearance of α-synuclein[244]. Recently, it has also been shown that the endocytic pathway is essential for the autophagic clearance of ubiquitinated proteins, including proteins that accumulate in Huntington's disease. This suggests that degradation through autophagy bodies and the endocytic pathway share regulatory mechanisms and therefore disruption of one of these pathways can influence the function of the other[245]. The activity of the autophagic-lysosomal pathway is also known to decrease with healthy ageing[246], which leaves the senescent brain vulnerable to diseases such as AD and other dementias.

1.9.7.3 Alzheimer's disease

Increasing attention is being paid to the endosomal-lysosomal system, with robust pathology implicating this pathway in AD progression[247-249]. Aβ accumulation in brains of AD patients is an early hallmark of disease[71]. Aβ is a family of misfolded proteins associated with many neurodegenerative diseases[42,69] Aβ is secreted extracellularly from neurons after being sequentially cleaved from the ubiquitously expressed APP[70,71]. Aβ becomes deposited in plaques which also contain many lysosomal enzymes including cathepsin D[245], revealing a broad pattern of lysosomal dysfunction in AD. At least five genetic risk factors

for AD also promote the dysfunction of lysosomes. APP is triplicated in Down syndrome and is believed to drive the early onset of AD in Down syndrome patients[250,251]. In a mouse model of Down syndrome, the triplication of APP is necessary for the development of endocytic pathway dysfunction, the earliest known cellular pathology of AD[252]. ApoE4, the strongest genetic risk factor for AD, exacerbates endosomal pathway dysregulation[253], and increases lysosomal leakage[254]. However, since these endosomal and lysosomal changes are also apparent in the brains of sporadic AD patients[255] in which there is no genetic cause (the most common form of AD), Aβ accumulation must originate from earlier cellular dysfunction. Altered endocytic trafficking and morphology is one of the first known neuropathological changes in AD and can be detected decades before the symptomatic onset of AD[255]. Prior to Aβ deposition, endosomes become enlarged[256,257]. Many of these abnormal endosomes later contain Aβ, which is generated in autophagic vacuoles[258] and endosomes[259,260], amongst others[261-265]. Aβ has been identified at three intra-neuronal sites within the lysosomal system: Rab5 positive endosomes[69], autophagic vacuoles[266,267], and MVBs related to both the endocytic and autophagic pathways[268]. Before Aβ deposition, morphological changes have only been identified in the endosomes[223]. Despite this, the magnitude of autophagic vacuole accumulation within dystrophic neurons is particularly heightened in AD[269] and is a distinguishing factor between this dementia and other late-onset neurodegenerative disorders. Vacuoles accumulate in autophagosomes, autolysosomes and lysosomal dense bodies[270], indicating a gross dysfunction of the autophagic-lysosomal pathway. Accumulation of vacuoles arise from a defect of clearance rather than solely from an increased autophagy induction[245]. An inefficient fusion process is suggested by the presence of both immature autophagic vacuoles and lysosomal dense bodies, while the presence of cathepsin-positive autophagic vacuoles containing LC3 (an Atg protein which is normally degraded rapidly after autolysosome formation) suggests a defect in protein degradation within autolysosomes[271].

1.9.7.4 Impaired cargo clearance in RPE cells as a cause of AMD

The presence of Aβ in extracellular deposits is one of many similarities between AD and AMD[67]. In AMD these deposits are known as drusen and are often used as a diagnostic hallmark for the disease[47,75,140,141,272] (see section 1.8). Alongside drusen, AMD eyes also have lysosomal accumulations of incompletely degraded or removed waste materials, known as lipofuscin. Lipofuscin are often used as a universal index of lysosomal ageing[273], and are auto-fluorescent granules composed of a cocktail of compounds[23,274]. In the RPE lipofuscin accumulation originates primarily from incompletely degraded POS. In a strain of rat which fails to phagocytose shed POS, lipofuscin accumulation is significantly diminished. A2E, a phototoxic derivate of lipofuscin, can irreversibly inhibit lysosomal cathepsin activity upon exposure to light[275], leading to RPE damage. Transgenic mice expressing mutated

and inactive Cathepsin D, and thus have impaired POS degradation, showed increased lipofuscin accumulation. Lipofuscin can first be observed in the basal portion of RPE cells in young eyes but migrates into clumps which fill the entire RPE cytoplasm by the 9th decade of life[23,61]. There is a dense accumulation of lipofuscin within lysosomes in aged RPE cells, accounting for 19% of cytoplasmic volume by the age of 60[147]. This suggests that the accumulation of lipofuscin in aged RPE is connected to a decrease in RPE function due to clogging of the cytoplasm or by increased oxidative damage. This accumulation is further increased by external factors such as poor diet and cigarette smoking[86,276], both of which are risk factors for AMD[13]. Toxic lipofuscin has the ability to disrupt the phagocytic mechanisms of RPE cells[277], impair lysosomal proteases[278]and inhibit the lysosomal ATPase proton pump, hence lysosomes are less acidic. This also causes the leakage of lysosomal contents into the RPE cytosol[277]. Lipofuscin within lysosomes also generates ROS which modifies lipids and forms high molecular weight components that are stable within lysosomes[57,60,109]. Lipofuscin causes lysosomal enzyme activity to decrease by up to 50%[58], and since healthy macular RPE cells have higher levels of lysosomal enzymes than cells in the periphery[172], there is a regional vulnerability of the macula to an AMD phenotype. This underlies the importance of lysosomal damage in AMD. AMD-associated stress conditions such as hypoxia, oxidative stress and inflammation are all enhancers of autophagy[123], reducing the toxic nature of protein aggregates that accumulate in many age-related diseases. However, autophagic activity declines during ageing[246]. For instance, ageing retinas of C57BL/6 mice did not have an increase in autophagy-related compartments[279] suggesting that the defect occurs during autophagosomal formation rather than during degradation. Therefore, if lysosomal functions become impaired, autophagic clearance will also become dysfunctional. This highlights the importance of lysosomes in cell survival.

1.10 Summary: AMD aetiology, an incomplete picture

Despite years of both basic and clinical research, the aetiology of RPE dysfunction and atrophy that precedes advanced AMD remains unclear[280]. The multiple and cumulative alterations to cell structure and function in the macula underpin the molecular basis of disease. This includes age-related alterations to all layers of the outer retina[276]. The RPE has been identified to play a central role in AMD pathology[281] with heterogeneous disease pathways including inflammatory signalling[280], oxidative stress[163], and dysfunctional clearance mechanisms[281]. However, the initial molecular changes that drive these events remain unclear, and to date, no definitive pathways of damage have been identified for the disease. Indeed, it appears that multiple disease pathways converge to trigger and drive disease. Therefore, studying how the structure and function of the RPE and associated tissues changes with age and disease remains critical to elucidating this complex and debilitating disease. Here, we have focused on one particular aspect and risk factor for AMD; the consumption of a high-fat 'western-style' diet and associated oxidative stress mechanisms. Studies have shown that a HFD drastically increases the oxidative stress in the outer retina[282]. Studying how oxidative stress impairs the structure and function of the outer retina, and in particular the RPE, could provide novel insights into fundamental molecular mechanisms that drive retinopathy.

1.11 Study aims and hypothesis

The overall aim of my study was to explore how oxidative stress affects the structure and function of the RPE monolayer, and how this could bring about pathogenesis in the retina. This objective was achieved via three different but complementary approaches within a period of three years.

Study hypothesis:

-Oxidative stress causes structural and functional deficits associated with AMD.

To test my research hypothesis, the following approaches were used:

-I used novel 3D imaging techniques in mouse eyes to obtain novel ultrastructural insights into healthy RPE and photoreceptors.

-I used a HFD mouse model to study effects of unhealthy diet and associated oxidative stress on the ultrastructure of the outer retina.

- I used an *in vitro* cell culture model to investigate effects of HFD, including oxidative stress and impaired lysosomal acidification, and study how early pathology is initiated in RPE cells.

Chapter 2 Materials and Methods

This chapter contains standard methodologies of techniques used throughout the research conducted in this PhD. Specific details of experimental protocols and data analysis can be found in the corresponding methods section of each results chapter.

2.1 ARPE-19 Cell Culture

2.1.1 ARPE-19 Cell line

The non-transformed human cell line, ARPE-19[283] was obtained from the American Tissue Culture Collection (ATCC, USA) and maintained in a 37^{o}C humidified incubator with 5% CO^2 and 95% air. Cells were routinely culture in Dulbecco's Modified Eagle's Medium (DMEM) with 4.5g/l L-D glucose, L-glutamine and pyruvate (Life Technologies, UK), supplemented with 1% heat-inactivated foetal calf serum (FCS; Sigma Aldrich, UK) and 1% penicillin-streptomycin stock solution[284] (10,000 units/ml penicillin, 10mg/ml streptomycin in 0.85% saline; Sigma Aldrich, UK). Cells cultured in a T25 flask were maintained in a 5ml volume of media, with a complete medium change performed every 3-4 days. Post-confluent ARPE-19 cultures between passages 10-20 were maintained for up to 4 months before seeding on 0.4µm pore PET polyester transwell inserts (Sigma Aldrich, UK) pre-coated with 50µg/ml fibronectin (Sigma-Aldrich, UK). ARPE-19 cells were seeded at a density of 1.25x10^4 cells/well on 12mm diameter inserts. Cells were maintained in 0.5ml and 2ml media volume in apical and basal chambers respectively. A complete media change in the apical compartment and a 20% (v) change in the basal compartment was performed every 3-4 days. Cells were cultured for a minimum of 2 months prior to use in experiments.

2.1.2 Cell Passage

Conditioned media was removed by aspiration and cells washed three times in Hank's Balanced Salt Solution (HBSS; Life Technologies, UK). Flasks were incubated for 5 minutes with 1.5ml 0.35% Trypsin/EDTA (Life Technologies, UK) in a 37^{0}C humidified incubator with 5% CO_2 to facilitate cell detachment. 5ml of fresh media was added to inhibit trypsin and the cell suspension centrifuged at 300g for 5 minutes. The resulting cell pellet was resuspended in 2ml fresh media. A small sample was stained with trypan blue (Sigma Aldrich, UK) in a 1:1 dilution. This was transferred to a haemocytometer to allow cell counting prior to seeding on transwells.

2.1.3 Plate coating

Extracellular matrix proteins are used to coat culture vessels to facilitate cellular attachment. Lyophilised fibronectin (Sigma Aldrich, UK) was prepared to a final working concentration of 50µg/ml in double distilled water (ddH_2O) and was applied to the apical surface of the transwell insert. Plates were partially covered and allowed to dry overnight in a laminar flow hood. The following day, the remaining fibronectin was aspirated from the plates and were subsequently washed three times in 1xPBS prior to cell seeding. Reconstituted fibronectin was stored at -20^{o}C and thawed overnight at 4^{o}C prior to plate coating to prevent irreversible precipitation.

2.1.4 Cell Seeding

Following cell passage, P10-20 ARPE-19 cells were seeded on to fibronectin coated culture surfaces at $5x10^4$ cells per well for 24mm transwells, and $1.25x10^4$ for 12mm transwells. Cells were left undisturbed for four days to facilitate adhesion prior to commencing regular media changes described in section 2.1.1.

2.2 Photoreceptor Feeding Assay

Fresh porcine eyes were obtained from Upton's of Basset butchers (Southampton, UK). Retinas were immediately isolated from porcine eyes. An incision was made in proximity to the ora serata, and the anterior eye segment was removed. The retina was then carefully extracted and pooled in KCl buffer (0.3M KCl, 10mM HEPES, 0.5mM $CaCl_2$, 1mM $MgCl_{2;}$ pH 7.0) with 48% (w/v) sucrose solutions. Collected retinas were homogenised by gentle shaking for 2 mins. The solution was then centrifuged at 5000g for 5 mins before the supernatant was passed through a sterile gauze into fresh centrifuge tubes and diluted 1:1 in KCl buffer without sucrose. This preparation was subsequently centrifuged at 4000g for 7 mins, following which the pellet of POS was washed 3 times in PBS through centrifugation at 4000g for 7 mins. POS were resuspended in DMEM with 2.5% sucrose (w/v), Aliquots were stored at -80^{o}C prior to use.

2.2.1 Tagging of POS with FITC

Isolated POS were covalently labelled with the fluorescent dye Fluorescein Isothiocyanate (FITC) to enable visualisation in subsequent experimentation. POS were resuspended 1.5ml FITC stock solution (2mg/ml FITC isomer 1; ThermoFisher, UK; in 0.1M Na_2CP_2 buffer; pH 9.5). The solution was left on a rotating plate (Stuart SB2 Rotator; Camlab Ltd, UK) for 1 hour in the dark to allow for covalent attaching of the FITC conjugate. The POS-FITC solution was subsequently centrifuged at 3000g for 4 mins at 20^{o}C. The solution containing unbound FITC was aspirated, and the FITC-POS pellets were resuspended in DMEM with 2.5% sucrose, aliquoted and stored at -80^{o}C.

2.2.2 BCA protein assay

To quantify the concentration of FITC-POS prepared in section 2.2.1, a BCA protein assay (Pierce, ThermoFisher, UK) was carried out. Standard curves were generated from 2000µg/ml, 1500µg/ml, 1000µg/ml, 750µg/ml, 500µg/ml, 250µg/ml, 125µg/ml, 25µg/ml, and finally 0µg/ml BSA proteins standards, prepared in DMEM with 2.5% sucrose. A 25µl volume of known standards and unknown samples were pipetted into allocated wells of a microplate, along with 200µl of working reagent (50:1 Reagent A: Reagent B). Plates were agitated on an orbital shaker for 30 seconds and were then incubated at 37^{o}C for 30 mins and finally cooled to room temperature. Absorbance was subsequently measured at 562nm using a microtitre plate (spectrophotometer, Infinite F200 Pro, Tecan, Switzerland).

2.2.3 Pulse-chase POS feeding

Mature ARPE-19 monolayers were fed with either 10nM Bafilomycin A1 (Tocris, UK) for 48 hours[285], or 100µM hydrogen peroxide (H_2O_2; Sigma Aldrich, UK) for 24 hours[286], or left untreated as a control. RPE monolayers were fed POS using a pulse-chase method[287] where cells were chilled to 17°C for 30 mins. Cells were then fed with 4µg/cm^2 [288] of POS-FITC and left at 17°C for a further 30 mins to allow for maximal binding and minimal internalisation. Following this, the medium was completely aspirated to remove unbound POS and replaced with fresh pre-warmed medium, and the cells returned to a humidified incubator at 37°C with 5% CO_2 for 2, 4, 6, 12, 24 or 48 hours prior to fixation.

2.3 Immunofluorescence staining and microscopy of ARPE-19 cells

ARPE-19 cultures fed with POS were fixed in 4% formaldehyde for 30 mins at 4°C. Following fixation, cells were washed three times in 1X PBS and permeabilised in 0.1% Triton-X 100 for 30 mins. Cells were subsequently blocked in phosphate-buffered saline (PBS) containing 1% BSA and 0.1% Tween for a further 30 mins. Cells were then incubated with primary antibodies, shown in table 1, diluted in the same solution at 4°C overnight. Following primary antibody incubation, cells were incubated for 1 hour at room temperature with Alexa Fluor-conjugated secondary antibodies shown in table 2 at a dilution of 1:200 in PBS-Tween with BSA and cytopainter phalloidin-iFluor 647 (Abcam, UK; 1:1000). In all cases, 1µg/mL of 4',6'-diamino-2-phenylindole (DAPI; Sigma Aldrich, UK) was used to visualise cell nuclei. Samples were mounted between two glass coverslips using Mowiol (Harlow Chemical Company LTD, UK) with Citifluor antifade (Agar Scientific, UK). Images were acquired using a Leica SP8 (Leica Microsystems, UK) confocal laser scanning microscope. Z-stacks were taken for each field of view using sequential scanning and system optimised settings. For all monoclonal primary antibodies, an isotype control was performed. A secondary antibody control was performed for every secondary antibody used in this thesis. Images for both controls are presented in Appendix C and D.

2.3.1 Analysis of Immunofluorescence images

Quantification of POS-FITC co-localisation with endocytic/phagocytic, lysosomal and autophagy compartments (n≥20 cells/compartment/time point for control data, and n≥ 15 cells/compartment/time point for treatment groups) was performed using Volocity software (Perkin Elmer, UK), which employs the Costes *et al*. automated statistical algorithm[289]. To do this, image stacks were initially opened in FIJI, and the coloured channels were split. The average background pixel intensities were measured for the red and green channels, and this was subtracted from the whole image to minimise any potential false colocalisation results caused by low levels of bleed-through between channels. The red and green channels were then merged and saved as a tif, which was opened in Volocity. Volocity used Costes method of analysing colocalisation between the green channel and the red[289]. A region of interest was drawn around a POS which had been previously identified as being internalised by visual analysis of the Z-stacks. Co-localisation values were plotted for each compartment as a function of time in GraphPad Prism. Individual compartment sizes (15 compartments/ time point/ treatment group) were measured using ImageJ. The middle image from the confocal z-stack was zoomed to 200x, and compartments were chosen at random across the entire image.

2.4 Transmission Electron Microscopy of ARPE-19 cells

2.4.1 Embedding ARPE-19 transwells in resin blocks

After feeding with POS, cultures were fixed with primary fixative comprising 3% glutaraldehyde, 4% formaldehyde in 0.1M piperazine-N, N′-bis (PIPES) buffer (pH 7.2) for a minimum of 1 hour. Posterior poles of murine eyes were fixed in the same way. Specimens were then rinsed in 0.1M PIPES buffer, post-fixed in 1% buffered osmium tetroxide for 1 hour, rinsed in buffer and block stained in 2% aqueous uranyl acetate (20 mins). Samples were then dehydrated in an ethanol gradient (30%, 50%, 70%, 95%) for 10 mins each, followed by absolute ethanol twice for 20 mins. A link reagent acetonitrile was then applied for 10 mins, after which samples were incubated overnight in a 1:1 ratio of acetonitrile to Spurr resin. The following day, samples were submerged in fresh Spurr resin for 6 hour before being embedded and polymerised in Spurr resin at 60^{o}C for 24 hour (Agar Scientific, Stanstead, UK).

2.4.2 Microtomy of ARPE-19 resin blocks

Resin blocks were loaded in a Reichert Ultracut E Microtome (Leica Microsystems, UK). A razor blade was initially used to trim the block into a trapezium around the sample. The block was then loaded into the cutting arm, and a glass knife used to polish the surface before semi-thin sections were taken and stained with toluidine blue. A light microscope was used to identify a smaller area of interest. A trapezium around this area was then cut using a razor blade. 90nm thick silver/gold ultrathin sections were cut, collected on 200 mesh carbon and formvar coated copper/palladium grids, pre-treated with Sodium Hydroxide. Sections were then stained with Reynolds lead stain. Cross sections of samples were viewed on a Hitachi H7700 (Hitachi High Technology, Japan) Transmission Electron Microscope.

2.4.3 Analysis of ARPE-19 TEM images

Images were taken of compartments containing POS across all time points (n≥ 10 images per time point). Identification of compartments was carried out in blinded micrographs. Time points were split into early (2-4 hours), intermediate (6-12 hours) and finally late (24-48 hours) stages. Compartments were identified using a three scale approach where (1) is no degradation observed, (2) shows some level of POS breakdown, and (3) represents POS in discernibly late compartments including lysosomes and/or autophagy bodies. The number of compartments present at each time point stage was quantified by counting. Further, images which included the apical edge were imported in ImageJ. The scale was

set using the microscope generated scale bar, and the distance of the POS- containing compartment from the apical edge of the cell was measured. All data was imported into GraphPad Prism for further analysis.

2.5 In-vivo experimentation

All experimental procedures were approved by a local ethical review committee and conducted in accordance with personal and project licenses under the UK Animals (Scientific Procedures) Act (1986). C57BL/6 mice were bred and maintained at the Biomedical Research Facility at the University of Southampton, UK. All mice were maintained on a 12/12-hour light/dark cycle and provided with food and water ad libitum.

2.5.1 Perfuse fixation

Adult (4-6 month) male and female mice were perfused transcardially with 0.9% saline. Eyes were immediately enucleated and placed in 3% glutaraldehyde in 0.1M cacodylate buffer at pH7.4 for TEM imaging, or 4% PFA for immunofluorescence staining.

2.6 Dissection of posterior poles of murine eyes and cryo-sectioning

Connective tissue and excess optic nerve were removed from the outside of the eye using micro-scissors. A 30G needle was then used to puncture the eye at the edge of the iris. Micro-scissors were inserted into the hole and used to cut along the edge of the iris. The front of the eye was then pulled off with the lens, leaving just the posterior pole for subsequent experiments. The remaining posterior eye cup was post-fixed in 4% PFA for an additional 20 mins, washed 3 times for 5 mins in 1xPBS. Eyes were then cryoprotected by submerging in a sucrose gradient (5%, 10%, 15% and 20%) in PBS for 2 hours in each concentration. Eyes were then left in a 30% sucrose solution overnight. Eyes were subsequently embedded in Tissue-Tek Optimal Cutting Temperature (OCT) compound and frozen on dry ice for 20 mins. All eye samples were stored at -20^{o}C before cryo-sectioning. Eyes were serially sectioned at 16µm using a cryostat at 20^{o}C and were collected consecutively on labelled slides, with approximately 12 sections per slides. Adjacent sections corresponded to a distance of ~192µm. Mounted sections were stored long-term at -20^{o}C.

2.7 Preparation of murine eye flat mounts

Eyes were perfused fixed and dissected as described in sections 2.5.1 and 2.6. Micro-scissors were then used to make 4 or more incisions into the eyecup, allowing the eye to lie flat [Fig. 7]. Flat mounts were placed onto microscope slides and used for immunohistochemistry.

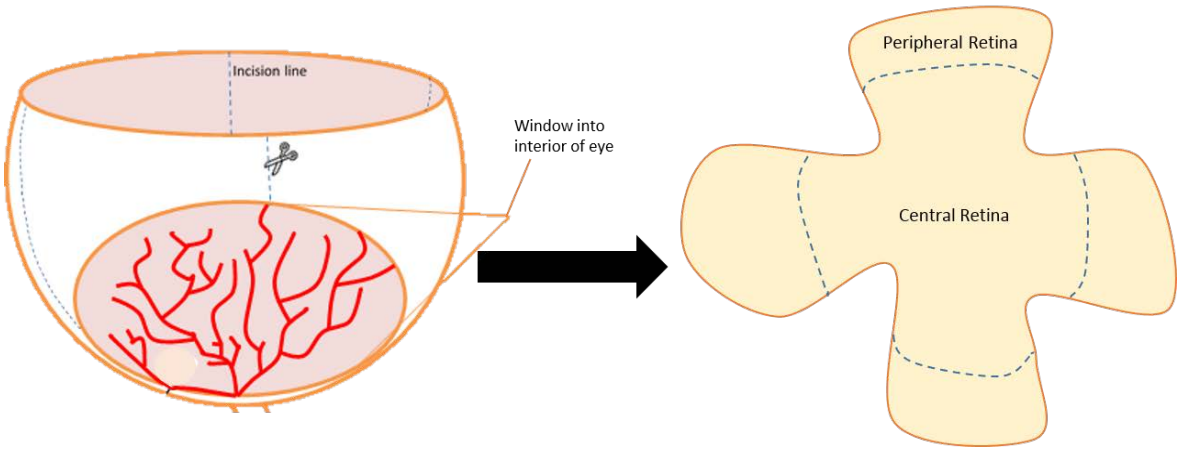

Figure 7: Diagram showing flat mount preparation
First, four incisions are made into the eye cup in order to make it lie flat. Also shown are the central and peripheral borders used when imaging these areas.

2.8 Staining of retinal tissue

Staining of most retinal tissue was immunofluorescence staining, and was performed similarly to that which was outlined for ARPE-19 cell staining (section 2.3). Specific alterations used when staining murine retinas will be described in subsequent results chapters.

2.8.1 Haematoxylin &Eosin (H&E) staining

Slides were dried in an SI60 37^{o}C incubator (Stuart, UK) for 1 hour to remove moisture, and were processed through a series of solutions. Initially, sections were submerged in Haematoxylin (Sigma Aldrich, UK) for 10 mins, before being washed in tap water for 8 mins. 0.03% acid alcohol was then applied to the slide for a further 8 mins before being washed in tap water for 8 mins. Finally, 0.5% Eosin (Sigma Aldrich, UK) was used for 1 min. Slides were then dipped for 30 seconds 5 times in distilled water before the same process was employed to take slides through an alcohol gradient (50% ethanol, 70% ethanol, 90% ethanol and 100% ethanol twice). Finally, slides were submerged in Xylene for 5 mins. Upon completion, slides were mounted with a glass coverslip using DPX mountant (Sigma Aldrich, UK). Imaging of slides was performed using an Olympus dotSlide virtual microscopy system (Olympus, UK) and was visualised using the OlyVIA software suit (Olympus, UK).

2.8.2 Analysis of stained retinal tissue

2.8.2.1 Analysis of immunofluorescence images

Images were opened in ImageJ, and the coloured channels were split. The green channel was converted into a 16-bit image. The image stack was then converted into a Z project to produce an image with maximum intensity from the entire stack. This image was then duplicated. One copy is left untouched. The other was used to create a binary image which was thresholded to remove any background staining. The measurements were set to re-direct to the duplicated, untouched image. The layer (RPE or photoreceptor) was then traced around using the bright field channel. This was pasted onto the binary image and the average intensity measured and recorded in excel. This was repeated for 6 images collected from 3 mices for each stain. The average intensity was measured for both the RPE layer and the photoreceptor layer in control groups and HFD groups. Intensity values were plotted as a function of layer and animal model in GraphPad Prism.

2.8.2.2 Analysis of H&E images

H&E images were opened in FIJI and the scale set using the microscope generated scale bar. 15 measurements of the photoreceptor and RPE/BrM width were taken across each of 6 images from 3 eyes for control and HFD groups.

2.9 Transmission Electron Microscopy of murine eye cups

Embedding and microtomy of murine eye cups follow the same process as described in section 2.4. Specific differences will be outlined in subsequent chapters.

2.9.1 Analysis of retinal TEM images

Images with BrM present were imported into ImageJ. The scale bar was set using the microscope generated scale bar. Ten thickness measurements were taken for each of 10 images across 8 eyes per group.

.

2.10 Serial Block-face Scanning Electron Microscopy

Posterior poles of murine eyes were placed in 3% glutaraldehyde in 0.1M cacodylate buffer at pH 7.4 for 1 hour. 0.1M sodium cacodylate buffer at pH7.4 plus 0.23M sucrose and 2mM calcium chloride were then used as a wash solution twice for 10 mins. Samples were then placed in 3% potassium ferrocyanide in 0.3M cacodylate buffer plus 4mM calcium chloride and 4% osmium tetroxide on ice for 1 hour. The thiocarbohydrazide solution was then made at 60^{o}C, agitated every 10 mins for 1 hour. Once made, it was added to the samples for 20 mins at room temperature. 2% osmium tetroxide was subsequently added for 30 mins, followed by 2% uranyl acetate for 1hr at 4% Walton's lead aspartate solution was added for 30 mins at 60^{o}C. Samples were then put through a 30%-absolute ethanol gradient before acetonitrile was used for 20 mins. Samples were next left in 50:50 acetonitrile:Spurr resin overnight followed by fresh Spurr resin for 6 hours. Blocks were then embedded in capsules with fresh resin and left for 16 hours at 60^{o}C to polymerise.

Initially, the same microtomy technique as described in section 2.8.2 is used. However, after ultrathin sections had been taken and viewed under TEM to check for tissue preservation, a small region of interest was identified. A 500µm block was then cut from the original resin block, and glued onto a roughened aluminium 3-view pin, using silver loaded epoxy glue. This was left to polymerise overnight before the pin was remounted into the ultramicrotome chuck, and further ultra-thin sections taken and viewed on the TEM. The block was then trimmed once more into a small, neat trapezium. Silver dag was applied to the sides of the block, and gold/palladium was used to sputter coat the block for 2 mins to aid dissipation. Glue was then applied to the wide, bottom edge of the trapezium and loaded into the 3-view microscope.

The diamond knife was brought into contact with the block, and the electron chamber evacuated to create a vacuum. The vacuum prevented air from interacting with bombarding electrons required to produce an image. The area of interest was imaged at a magnification of 4512x, an energy beam of 3.0kC, and a slice thickness of 50nm. A total of 1353 images were acquired on the initial imaging session. Since then 2 more stacks of a similar size have been created. Each image took an average of 3mins to take and were 8192x8192 pixels (pixel size =0.0041µm).

2.10.1 Post-image processing of SBSEM and segmentation of images

Since eyes have an inherent curvature, the RPE layer slowly moves out of view whilst being imaged. The block must therefore be manually shifted back to keep the RPE layer in view. In such cases images are misaligned. In order to realign the images, the entire stack was

opened in FIJI and the plugin “register virtual stack slices” was used. This plugin realigns a sequence of images with an enlarged canvas according to a user chosen reference image. In this case, the first image of the stack was used. It must be noted that the plugin does not work with faulty or blurry images. In such cases, the damaged images were replaced by the succeeding image before realignment. This was completed by duplicating the subsequent image and renaming the duplicated file with the same file name as the fault image so the sequence can still be read as a stack. Images were further modified to allow easier edge detection and improve portability of image files, while preserving detail. First, a Gaussian Blur with a 1.00 radius was applied to all images to reduce noise by creating an average pixel within the set radius. This improved edge detection. Since the raw images from the microscope are large, they are converted from a colour depth of 16-bit to 8-bit grayscale images using FIJI. Image size was then reduced in half, from a width and height of 8192 x 8192 to 4096 x 4096 pixels. The stack of images was visually checked for any entire RPE cells (our area of interest), which were isolated into a separate, smaller stack of images. This smaller stack was then opened into TrakEM2, a FIJI plugin[290]. Area lists were assigned for each section to be segmented. In this case; the RPE membrane, nucleus, apical microvilli, basal infolds and lumen. Colours were then assigned to each area lists before each section is drawn around by hand and filled in with its assigned colour [Fig. 8]. Once a section was finished, the area list was exported as an Amira file which could be opened into an Amira project to render in 3D [Fig. 9]. Area lists could be combined with the original image files to visualise the layers in 3D. Following segmentation volumetric and surface area data for each area could be extracted using the FIJI ‘measure’ function. Amira allowed for semi-automatic segmentation of photoreceptors due to their darker appearance on the image. This was performed using the magic wand tool, in which any contact areas within a user defined intensity range are automatically segmented. Any photoreceptors not catered for by the RPE cell of interest would then have to be manually erased. A macro was also written (see appendix 1) to obtain information about the surface area of two edges in contact.

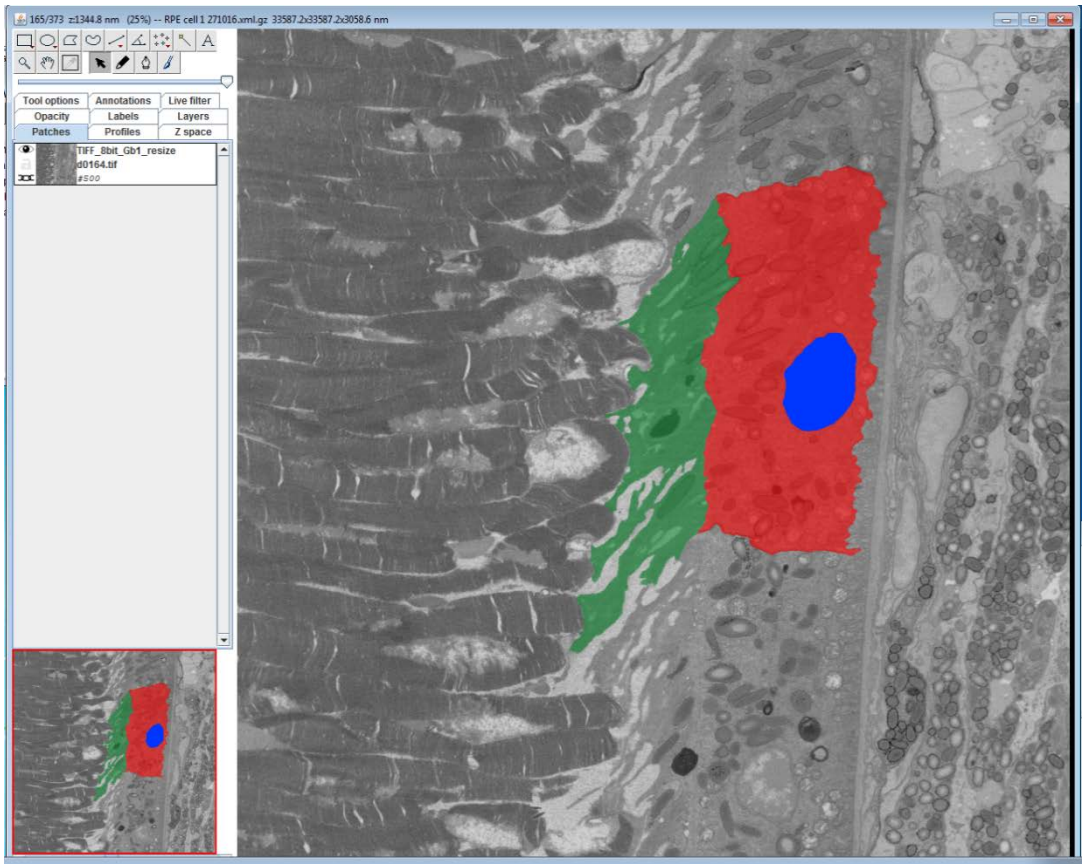

Figure 8: An example image of segmentation using TrakEM2.
Each area of interest of the RPE cell has been assigned a colour and manually traced around for every slice in the stack of images. (Blue= nucleus, red = cytoplasm, green = microvilli).

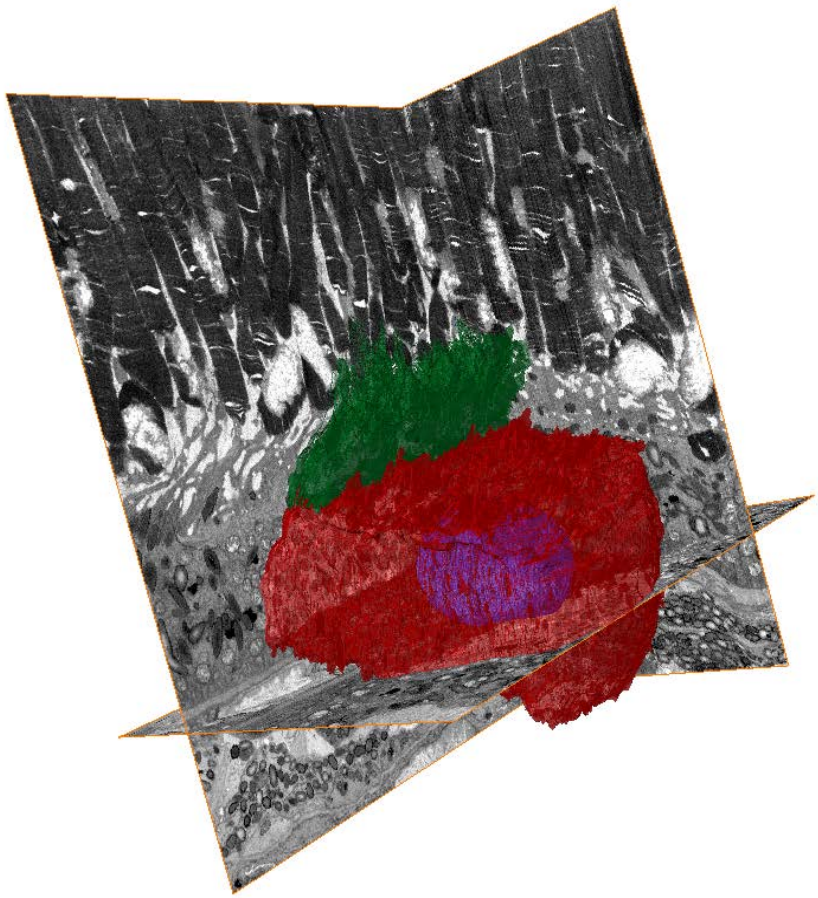

Figure 9: An example image of 3D reconstruction of a bi-nucleate RPE cell in Amira.
Once segmented, each area-list can be imported into Amira and reconstructed in 3D. Orthogonal sections in x, y and z planes are shown. Red = Cytoplasm, Green = Microvilli, Blue = Nucleus.

2.11 Statistical Analysis

All statistical tests were performed using GraphPad Prism Software (GraphPad, CA, USA). Distribution of data was initially assessed using a D'Agostino Pearson omnibus normality test. The statistical significances of normally distributed data was determined by an unpaired t-test or a one-way ANOVA followed by a Turkey's multiple comparison tests. When data were not normally distributed, a Kruskal-Wallis test was performed, followed by Dunn's multiple comparison tests. Data are expressed as means ± standard deviation (SD) with statistical significance denoted as * for $p \leq 0.05$, ** for $p \leq 0.01$ and finally *** for $p \leq 0.001$.

Table 1: Primary Antibodies used during immunofluorescence studies

Details of the primary antibodies used for laser scanning confocal microscopy. In all cases, antibodies were diluted in 1% BSA in 0.1% PBS-Tween in the ratios specified on the right-hand column.

Product Name	Company	Catalogue Number	Clone/Isotype	Species	Dilution
Rab-5	Abcam	Ab18211	IgG, pAb	Rabbit	1:1000
Rab-7	Abcam	Ab137029	IgG, mAb	Rabbit	1:200
Lamp-1	Abcam	Ab24170	IgG, pAb	Rabbit	1:1000
Lamp-2A	Abcam	Ab18528	IgG, pAb	Rabbit	1:200
LC3B	Abcam	Ab48394	IgG, pAb	Rabbit	1:1000
ZO1	Invitrogen	40-2200	IgG, pAb	Rabbit	1:100
MerTK	Abcam	Ab95925	IgG, mAb	Rabbit	1:100
αvβ5 Integrin	Abcam	Ab24694	IgG1, mAb	Mouse	1:100
TIMP3	Abcam	Ab85926	IgG, pAb	Rabbit	1:200
βIII-tubulin	Abcam	Ab18207	IgG, pAb	Rabbit	1:200

Coll IV	Abcam	Ab6586	IgG, pAB	Rabbit	1:800
Clusterin	Abcam	Ab69644	IgG, pAB	Rabbit	1:100

Table 2: Secondary Antibodies used during immunofluorescence studies.

Details of the secondary antibodies used for laser scanning confocal microscopy. Antibodies were diluted in 1% BSA in PBS-Tween to the ratios specified in the right-hand column.

Product Name	Company	Catalogue Number	Species	Reactivity	Dilution
Alexa Fluor 546	Life Technologies	A11071	Goat	Rabbit	1:200
Alexa Fluor 594	Life Technologies	A11072	Goat	Rabbit	1:200
Alexa Fluor 594	Life Technologies	A11020	Goat	Mouse	1:100

Table 3: Staining reagents used in immunofluorescence studies.

Details of the staining reagents used during laser scanning confocal microscopy experiments. DAPI: 4', 6'-diamino-2-phenylindole

Product Name	Company	Catalogue Number	Dilution
FITC-488	Life Technologies	F1906	N/A
Cytopainter Phalloidin-iFlour 647	Abcam	Ab176759	1:1000
DAPI	Sigma-Aldrich	D9542	1:1000
Oil Red O	Sigma-Aldrich	O0625	N/A

Chapter 3 Visualising the 3-dimensional ultrastructure of the RPE monolayer and associated retinal layers

3.1 Introduction

As described previously, the RPE monolayer is highly morphologically specialised to carry out its functions (see section 1.7). However, thus far the RPE structure has only been studied using conventional 2D imaging techniques such as Transmission Electron Microscopy (TEM) and Scanning Electron Microscopy (SEM). TEM, providing a resolution greater than light microscopes, was first developed in 1931[8]. This allowed tissues to be viewed in greater detail than ever before and gave way to a fresh understanding of structures. For instance, a detailed analysis of intracellular organelles could be completed. However, since these images were in 2D, many assumptions were made about volumetric and structural properties based on extrapolation of 2D images, which may prove inaccurate upon 3D examination. TEM uses an electromagnetic lens which focuses a beam of electrons through an ultrathin (<100µm) section of fixed, stained, dehydrated and resin-embedded tissue. Some electrons pass through the section whilst others are scattered, depending on the section density. This creates a high-resolution image of the cell ultrastructure. However, in order for samples to be able to withstand low pressure / high vacuum, and bombardment of accelerated electrons, tissues must be processed using chemicals and heat which could introduce artefacts and potential shrinkage. The inherently 2D nature of TEM has previously been overcome by serial section TEM, and TEM tomography. Serial section TEM however is technically difficult, as each subsequent section needs serially collected, imaged, and reconstructed accurately. Nonetheless, this has provided high-resolution 3D results[291]. TEM tomography involves imaging a section repeatedly whilst it is tilted incrementally around its axis. The series of images are subsequently used to reconstruct a 3D image of the sample. However, this does cause a 'missing wedge', due to a limited tilt range of ~60^{O}[292]. SEM uses a beam of electrons which are raster-scanned over a fixed, dehydrated, dried and conductive (by coating with a metal) tissue. The beam interacts with the sample producing secondary electrons, backscattered electrons and x-rays which are collected to form an image. SEM resolutions range from 20µm to 0.4nm depending on the accelerating voltage, spot size, scanning speed and vacuum level[292]. Although SEM conveys 3D impressions of structures by focussing over a range of distances giving a large depth of field, the technique is essentially 2D as depth

perception is limited and no information about the interior of the surface can be gained, only surface topography.

As far back as the 1970s, 2D imaging approaches were used to study the ultrastructure of the RPE monolayer alongside adjacent tissues in the outer retina. For instance, Hogan *et al.* used conventional TEM to illustrate the apical specialisation of RPE cells to great effect. These micrographs showed long apical microvilli which protrude to surround the distal tips of overlying photoreceptors[125]. RPE cells also have highly invaginated basal infolds that increase the basolateral footprint of cells[129]. TEM studies have shown the stratified and polarised distribution of organelles within the RPE cells. For instance, melanin pigment granules are found on the apical side closest to the light-sensitive photoreceptor layer, which is unsurprising due to their role in absorbing stray light. In contrast, mitochondria and nuclei are located more basally[125,132]. Until recently 3D imaging of cellular ultrastructure was not possible and therefore 2D data have been extrapolated to make assumptions about the 3D structure of RPE cells, which has formed the basis of their morphology since then. For example, based on the cobblestone appearance of RPE cells, the monolayer is thought to be composed of many hexo-cuboidal shaped cells[13]. The inherently 2D imaging approaches have meant that we are still unaware of any volumetric information pertaining to RPE structure. Such lack of knowledge also extends to the intracellular volumes of specific organelles such as lysosomes and mitochondria that are known to be damaged and play an important role in retinopathy[286,293-296]. Fortunately, such important gaps in knowledge can now be addressed by exploiting new imaging techniques such as Serial Block-face Scanning Electron Microscopy (SBSEM). SBSEM uses an internal microtome to shave off slices of pre-defined thickness (in this case 50nm thick serial sections) from the top of the sample immediately after imaging with an electron beam [Fig. 10]. In this way, a sequential stack of images can be collected from the entire sample. This provides detailed volumetric as well as structural information. The image stack can be used to segment (outline and assign colours) and identify distinct areas of the tissue/sample [Fig. 13B]. This information is then modelled and reconstructed via software such as Amira, to render the pre-selected regions of the tissue in 3D. SBSEM has already proved to be an invaluable technique in other areas of neuroscience and biology. For example, for the first time it has been possible to reconstruct almost complete invertebrate and sizable fractions of vertebrate nervous systems[297]. When combined with light microscopy, SBSEM has been used to provide a platform where cellular events can be selected and imaged at high resolution. For instance, this approach has been utilised to study mitotic spindle architecture at high resolution in 3D[298]. SBSEM reconstructions have also been used to reconstruct the keratocytes and collagen fibrils of the developing chick corneal stroma. Such 3D data revealed that there was a much larger volume of corneal matrix compared to extracellular components, which had not been previously realised using conventional 2D imaging[9].

As this novel technique has not been utilised to fully investigate the delicate soft tissues of the outer retina, we used wildtype mouse eyes for our studies. Mouse eyes are an excellent representation of the mammalian eye and are similar in many respects to the human equivalent despite the lack of anatomical macula [Fig. 11]. Murine eyes are also readily available and, of critical importance to our study, can be perfuse-fixed while the animal is still alive, which allows for the best possible structural preservation of these delicate tissues. By contrast, it is not possible to retrieve such high-quality tissues from human donors, which are typically available in the UK only after 48 hours post mortem (and often even longer) by which time their structure is irrevocably altered.

In order to study the native 3D structure of the mammalian RPE, we, therefore, used perfused-fixed wildtype mouse eyes and prepared tissue samples from the central mouse retina from SBSEM. We adjusted the microscope to acquire images of the outer retina at an optimal magnification such that the entire RPE monolayer was captured at high resolution alongside adjacent photoreceptors on the apical interface as well as the BrM choriocapillaris on the basal side. Of three separate mouse eyes imaged via the 3View microscope, we selected a single patch of RPE cells from a single eye to further segment and reconstruct in 3D. The presence of bi-nucleate and multi-nucleate RPE cells is often reported[136], however little is known about the structural and functional implications of their presence. We, therefore, decided to segment and reconstruct a path of RPE which included both a mono-nucleate and bi-nucleate RPE cell to compare any structural differences between the two.

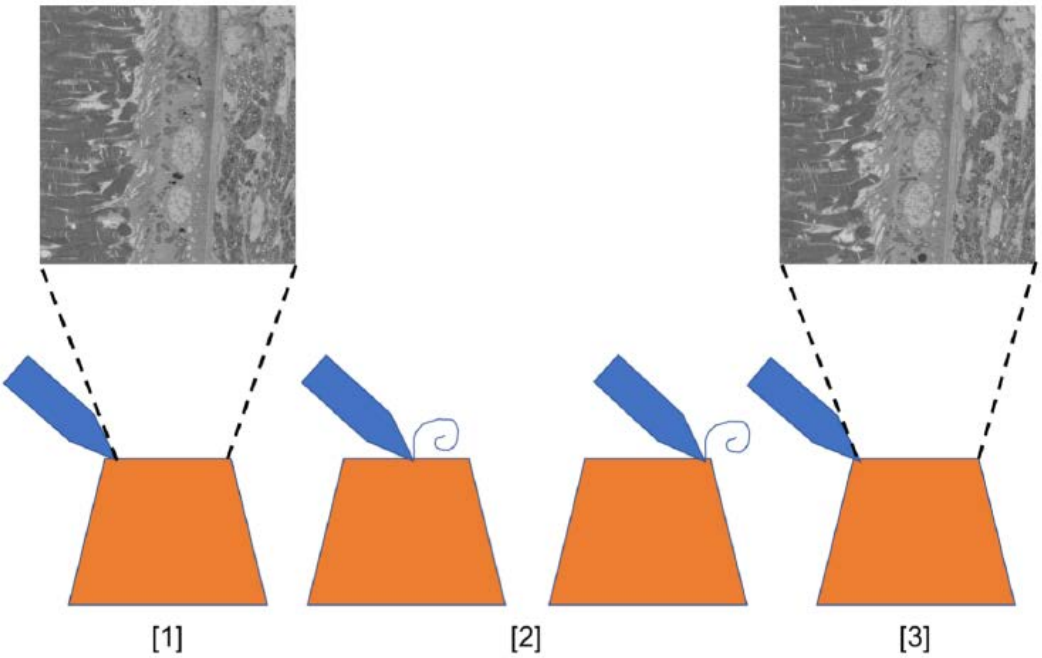

Figure 10: The principle of SBSEM.
[1] An SEM image is taken of the area of interest in the resin block (orange) using an electron beam. [2] A diamond knife (blue) which is internal to the microscope shaves off and discards an ultrathin (50nm thick) section of the resin block. [3] When the knife is retracted, the next SBSEM image is taken of the subsequent layer.

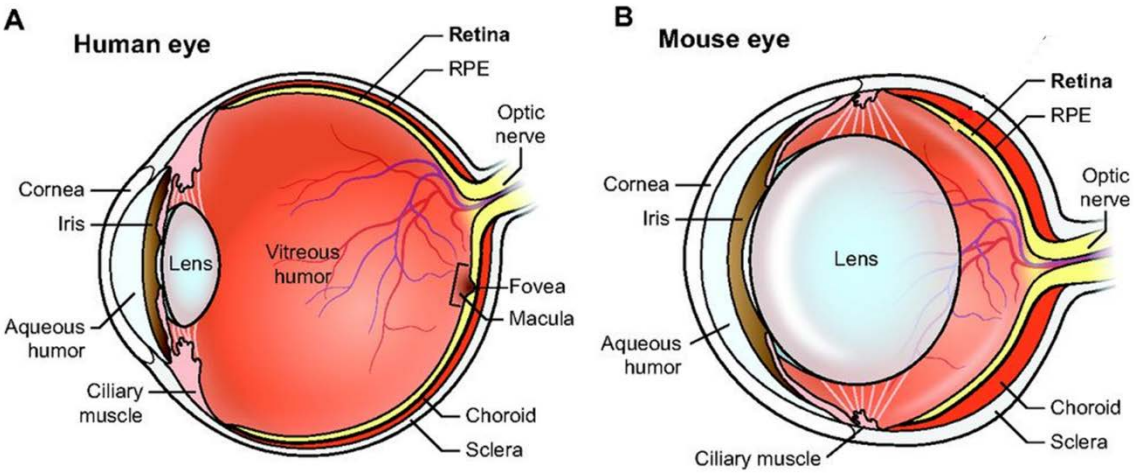

Figure 11: Schematic comparing human and mouse eyes.
[A] Human eye cross section. [B] Murine eye cross section. Note the lack of macula and fovea in the mouse eye. Structurally, however, there are remarkable similarities between tissues of the outer retina in humans and mice. Figure adapted from Veleri et al., 2015[299].

Hypothesis: Novel ultrastructural imaging techniques will provide altogether new information on the structure of the RPE and associated tissues of the outer retina, including volumetric information. This will reveal a more realistic and accurate picture of RPE cells and help understand how this critical monolayer alters with age and disease.

Aims: Use Serial block-face Scanning Electron Microscopy (SBSEM) to study the ultrastructure of the murine RPE monolayer and associated tissues.

3.2 Methods

4 month old wildtype C57BL/6 mouse eyes were enucleated, and the posterior pole fixed and stained with heavy metals before being embedded in resin capsules according to an adapted Ellisman protocol[300], as outlined in chapter 2. Semi-thin and ultra-thin sections were imaged using a Hitachi H7700 TEM to check for sample preservation and identify a region of interest (ROI) in the central retina. Subsequently, a 500µm cube which contained the central retina ROI was then cut out of the resin block, glued onto an aluminium 3-view pin using silver loaded epoxy glue and sputter coated with gold and palladium. This was loaded into an FEI Quanta 250 FEG SEM fitted with a Gatan 3-view 2XP system (Gatan, Roper Technologies, USA). The area of interest was imaged at a magnification of 4512x, beam energy of 3.0kV and images were collected from serial 50nm thick sections for the entire sample depth. The dimension of each microscopic image was 8192 x 8192 pixels, where the pixel size was 4.2nm x 4.2nm. Each image was a total of 33.78µm in size.

Once imaged, a Gaussian Blur with a 1.00 radius was applied to all images in the stack. This reduces the image noise by creating an averaged pixel within the set radius, which facilitates the detection of edges. Images were also transformed from a colour depth of 16-bitmap to 8-bitmap. This modifies the images from 256 colour states to 64 colour states, which softens and reduces image definitions, creating a more manageable image stack for segmentation. Images were also resized from a width and height of 8192x 8192 pixels to 4096 x 4096 pixels. This lowers the resolution by a quarter of the original images, and an averaged pixel is generated from 4 pixels, which facilitates image segmentation. This also creates a smaller and more portable image file. As the eye sample has a slight curvature, the RPE cell layer often moves out of view during imaging. In this case, the sample is manually adjusted back into its original position. However, this causes the ROI to move from one side of the image to the centre, creating a staggered reconstruction, if segmentation is carried out before the stack is aligned. Therefore, before segmentation occurs, the images are realigned using the FIJI plugin, Register Virtual Stack Slices. This realigns the sequence of images with an enlarged canvas, according to a reference image (see section 2.10.1). Once realignment had occurred, TrakEM2, a FIJI plugin, was then used to segment images by manually tracing around the structures of interest in different colours. Colour coded ROIs can be reconstructed in 3D using Amira software. Detailed methodologies can be found in Chapter 2. 2D measurements of the BrM thickness, microvilli length and angle from the start of each cell and every subsequent 50 slices (until the last image in the cell stack) were measured (n=10 per image). A macro was written to measure the touching edge surface area of 2 adjacent volumes (see Appendix A for macro details).

In a separate experiment, posterior poles from eyes of three adult mice (12 weeks) and 3 aged mice (52 weeks) were dissected to produce RPE flat-mounts. Cell nuclei and margins were labelled with DAPI and ZO-1 labelling and imaged as a stack by confocal microscopy. Three images of the posterior and central retina were taken per eye [Fig. 7].

All statistical tests were performed using GraphPad Prism. Data were first tested for normal distribution. Those that were significantly distributed were analysed using an unpaired student's t-test of a one-way ANOVA followed by Turkey's multiple comparison tests. Data that were not normally distributed were analysed using a Kruskal-Wallis test followed by Dunn's multiple comparison tests. All stats were reported as * representing $p \leq 0.05$, ** showing $p \leq 0.01$, *** indicating $p \leq 0.001$ and **** is $p \leq 0.0001$.

3.3 Results

3.3.1 Bi-nucleate RPE cells in the mouse outer retina

Given recent findings which indicate that bi-nucleate RPE cells may initiate retinopathy[136,149,301] we first compared mono-nucleate vs bi-nucleate RPE cells in the mouse retina. Murine RPE flat-mounts from two different age groups (2-3 months and 12 months) were stained with ZO1 and DAPI [Fig. 12A, B, C and D]. We then used FIJI software to count the number of mono-nucleate and bi-nucleate/multi-nucleate RPE cells in each image in an unbiased manner. We found there to be 11% bi-nucleate RPE cells in the young peripheral retina which increased to 28% with age [Fig, 12 A, C and E]. In the central retina of younger animals, there was a significant increase in the number of bi-nucleate cells compared to the peripheral retina (60% compared to 11%), which increased further to 72% bi-nucleate RPE cells in aged mice [Fig. 12B, D and E]. This revealed that the highest number of bi-nucleate RPE were in the central retinas of older mice.

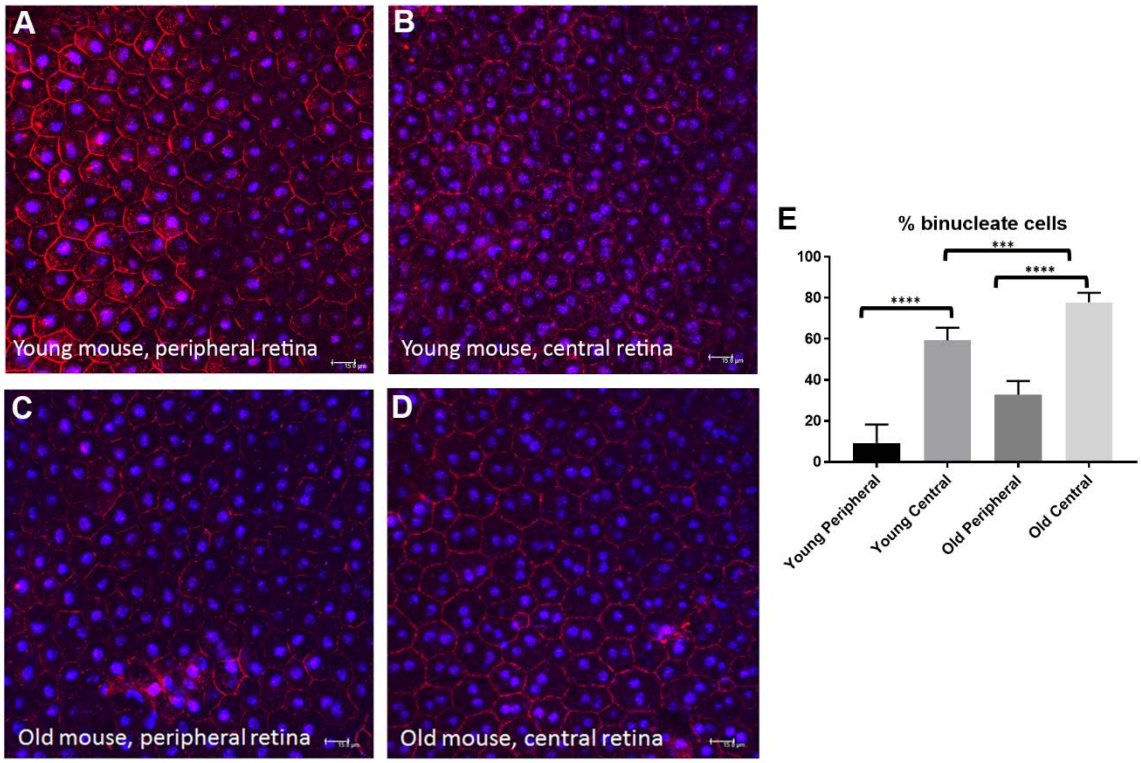

Figure 12: Confocal images of a whole mount retina.
[A] Representative image of the peripheral retinal of a young mouse. The tight junctions (ZO1) between cells are shown in red while the nuclei have been stained with DAPI and are blue. Note that almost all the cells are mono-nucleate with very few instances of bi-nucleate cells. [B] Representaitve confocal image of the central retina of a young mouse eye. Note the increase in bi-nucleation compared to the peripheral retina. [C] Representative image of the peripheral retina of an aged mouse. Note that most cells are mono-nucleate with few bi-nucleate or multi-nucleate cells. D] A representative image of the central retina from an aged mouse. Note the increase in the numbers of bi-nucleate cells compared to image C. Scale bars in A and B represent 15µm. E] The number of mono-nucleate and bi-nucleate RPE cells in the peripheral and central retinas of young and aged mice, shown as a percentage of total cells. Error bars represent the standard deviation (SD). N= 9 per group (from 3 different eyes of three animals) where significance was assessed using one-way ANOVA followed by Turkey's multiple comparison test. *** denotes a significance of $p \leq 0.001$ and **** indicates a significance of $p \leq 0.0001$.

3.3.2 Segmentation and comparison of a mono-nucleate and a bi-nucleate RPE cell.

To study the ultrastructure of healthy RPE cells, eyes from 3 different mice were embedded in resin capsules and imaged via SBSEM [Fig. 14A]. In this instance, images from the central retina of a single eye were used for 3D reconstruction. An intact and whole RPE cell from the larger serial image series was identified and isolated into a smaller image stack (henceforth referred to as cell 1). The apical microvilli, basal infolds, lumen, nuclei, and cytoplasmic space were segmented in distinct colours using the FIJI plugin, TrakEM2 [Fig. 13B] and reconstructed using Amira [Fig. 14]. The use of different colours allowed individual measurements/ analysis of distinct parts of the cell as well as the collective analysis of the RPE cell as a whole. Surrounding RPE cells were also segmented similarly and rendered in 3D. This 'RPE monolayer patch' consisted of an entire bi-nucleate RPE (cell 2), as well as 2 incomplete bi-nucleate cells (referred to as cells 3 and cell 4, respectively) [Fig 14 A-D, Fig. 17]. In this way, we started assembling data to reconstruct a 'patch' of RPE in 3D for the first time. See supplementary figures included in the attached USB drive; the files are explained in detail in Appendix B, but briefly, there is an interactive pdf document which has preselected images of the monolayer in 3D. These can be moved around using the document pan and the scroll functions. Different structures can be made transparent or invisible in each plane using the colour chart buttons at the bottom.

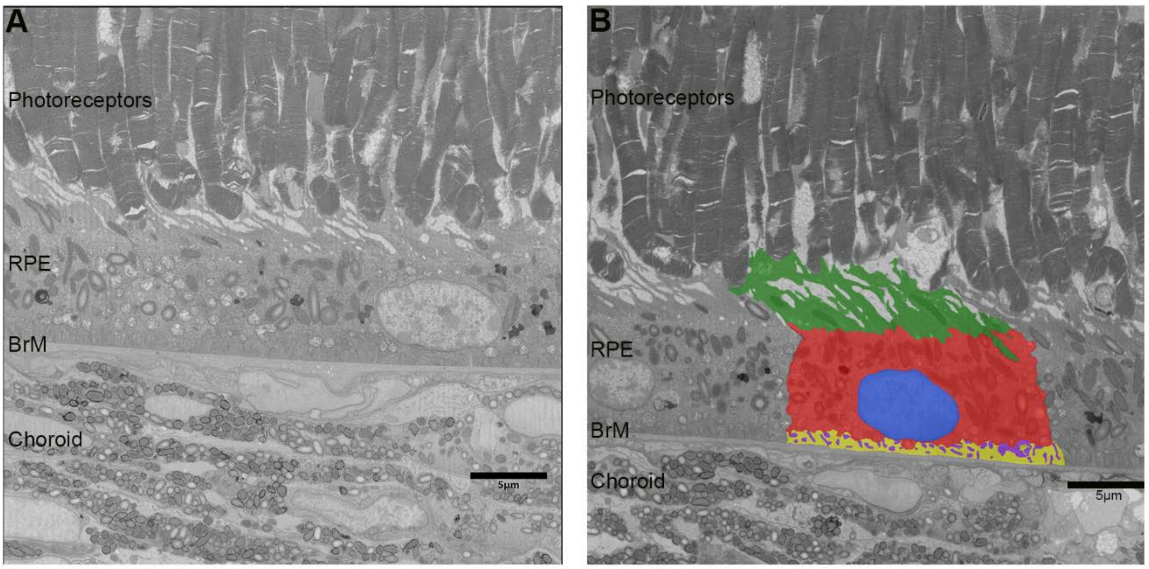

Figure 13: Representative images from the 3view microscope.
[A] An image was taken from a stack of 3-view images and rotated by 90º. Adjacent tissues and components of the RPE are labelled. [B] Individual areas segmented in distinct colours (colour-coded) where blue = nucleus, red = cytoplasm, green = microvilli, purple = lumen and yellow= basal infolds. Scale bars represent 5µm.

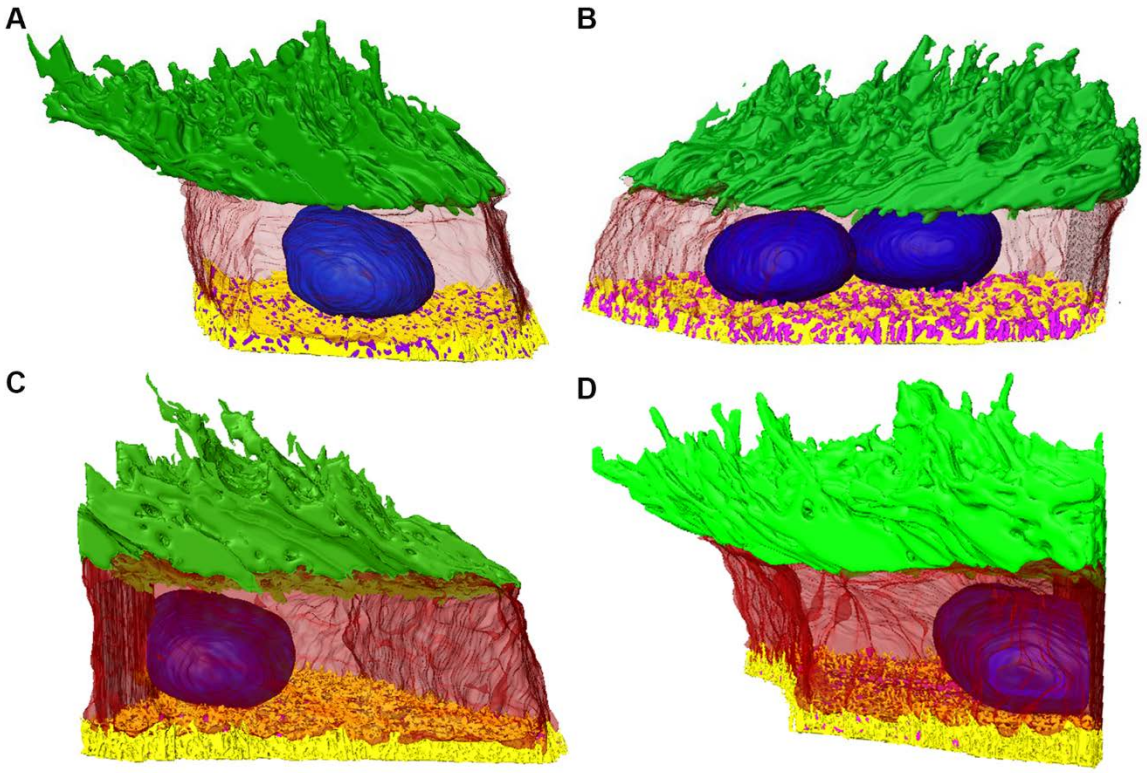

Figure 14: RPE cells after segmentation and reconstruction in 3D.
[A] A mono-nucleate RPE cell that has been fully imaged (the whole cell captured). [B] A complete bi-nucleate cell. [C and D] Two separate incompletely imaged bi-nucleate RPE cells. The microvilli are shown in green, the nuclei in blue and the cell body are in red, with basal infolds and lumen coloured in yellow and purple respectively.

3.3.2.1 Differences in the shapes of bi-nucleate and mono-nucleate RPE cells

It has been reported that RPE cells have a distinct hexo-cuboidal shape[132,276]. However, our findings show that only subset cells exhibit this characteristic shape, whereas other RPE cells appear to be more cuboidal in arrangement [Fig. 16, 17A, B]. These observations are based on visual analysis of RPE cells throughout the generated stacks. Our data also reveal that RPE cells are slightly tilted, with one side closing at the basal infolds and the other at the apical microvilli thus forming a rhombus shape as shown in Figure 15. This assessment is based on an analysis of segmented images as well as unsegmented or unprocessed raw SBSEM data. This tilt in the cell surface would have the effect of increasing the surface area of the cell: cell contacts.

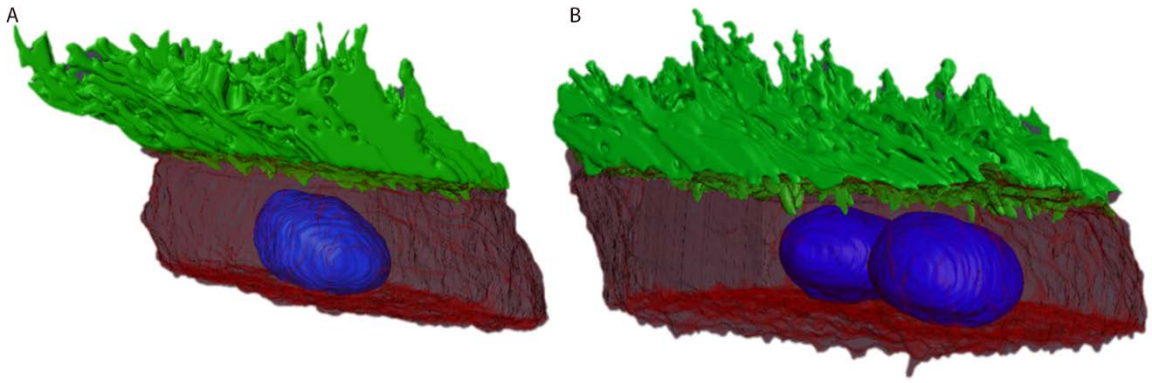

Figure 15: Images of reconstructed cells to show the rhombus shape.
Cross-sectional views of cell 1 [A] and cell 2 [B]. The basal infolds and lumen have been hidden in order to highlight the cross-sectional rhomboid shape of the cell body. Note the microvilli lie in the same direction as the rhombus shape. (red = cytoplasm, blue = nuclei, green = microvilli).

3.3.2.2 The surface area of the adjacent cell: cell contacts

Using a specially written ImageJ macro (appendix 1) we were able to garner insights into the surface area of the cell: cell contacts, thus allowing us to evaluate the extent of interactions between adjacent RPE cells in the monolayer. We found that there were varying amounts of contact across the RPE patch, with the smallest interaction being between cells 3 and 4 (25869nm^2), and the largest between cells 1 and 3 (51188nm^2) [Fig. 16]. At no point were there any borders or a shared interface between cells 1 and 2. There were also interactions between cell 2 and 3 (39829nm^2) and cell 2 and 4 (45774nm^2).

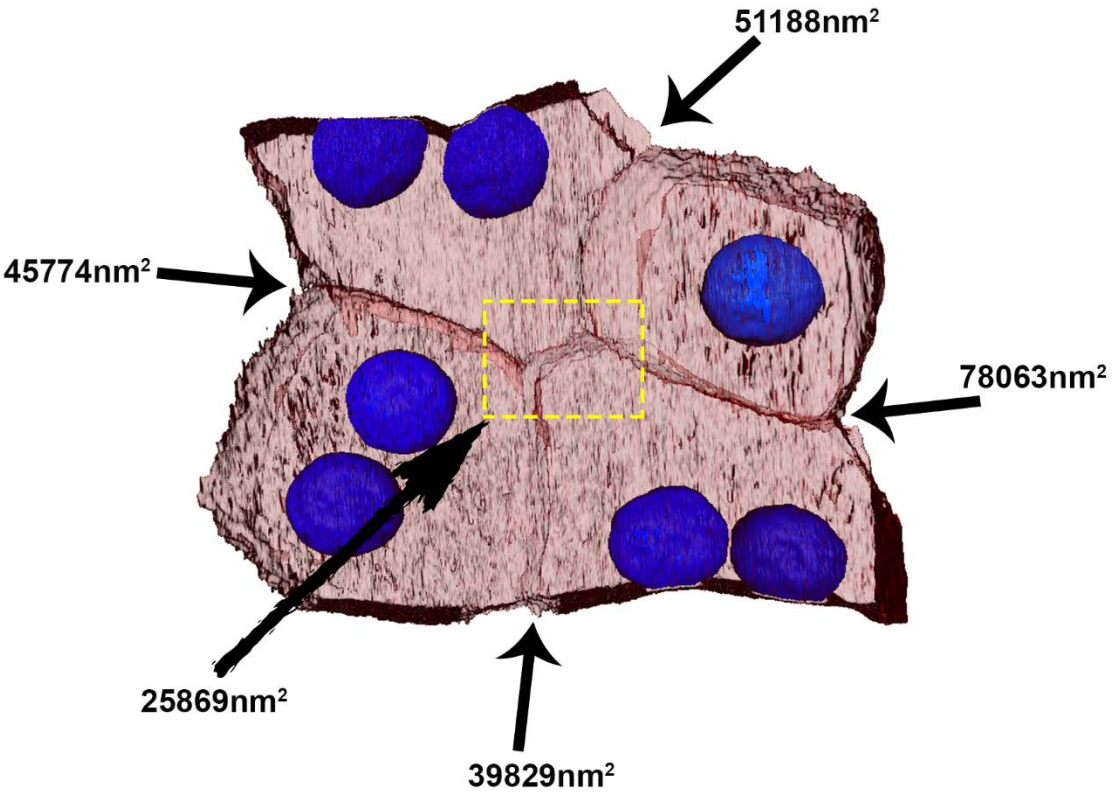

Figure 16: A top-down view of the reconstructed cytoplasm and nuclei of the patch of RPE. The arrows indicate the border at which two interfaces from the adjacent cells interact. The surface area of these contacts is shown in nm^2. Cell 1 is top right; cell 2 is bottom left, cell 3 bottom right and cell 4 top left. Red = Cytoplasm, Blue = Nuclei.

3.3.2.3 Differences in mono-nucleate and bi-nucleate RPE nuclei and cytoplasm

Our data shown in Figure 17 revealed that cell nuclei exhibit an ellipsoid-like shape, and have comparable volumes regardless of the number of nuclei in each RPE cell (Cell 1 = 141μm^3, Cell 2 = 156.8μm^3, 144μm^3, Cell 3 = 139.5μm^3, 126.5μm^3, Cell 4 = 128.2μm^3 and 138.1μm^3). The somewhat smaller nuclei volumes of Cells 3 and 4 are due to the incomplete imaging of these cells (part of their nuclei were not included in the 3D reconstructions and lay outside the sample). The surface area of each nuclei were also largely similar (Cell 1 = 172.1μm^2, Cell 2 = 197.3μm^2 and 186.5μm^2, Cell 3 = 171.5μm^2 and 158.2μm^2, Cell 4 = 164.2μm^2 and 169.2μm^2). Measurements of the RPE cell cytoplasm (without nuclei) show that whilst the surface area of the bi-nucleate cell is almost 50% larger than that the mono-nucleate RPE cell (1564μm^2 and 2104μm^2), the cytoplasmic volume of both cells remains broadly similar (the cytoplasmic volume of cell 1 and cell 2 were 2068μm^3 and 2110μm^3 respectively). Since cell 3 and cell 4 were incompletely imaged, their cytoplasmic volumes and surface areas are excluded from comparisons.

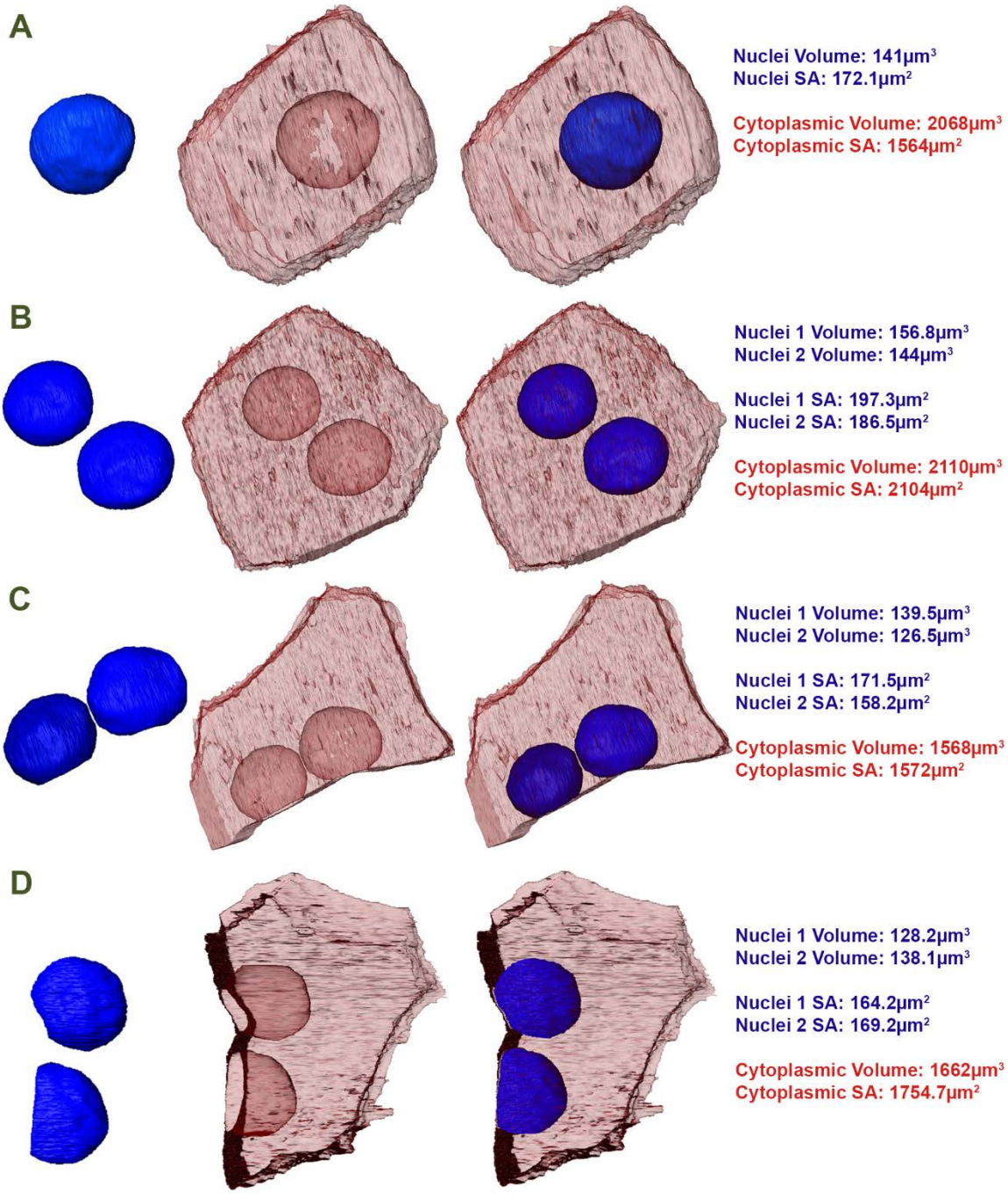

Figure 17: Segmented and 3D reconstructed nuclei and cytoplasm
Cell 1 [A] Nucleus and cytoplasm of Cell 1. [B] Nuclei and cytoplasm of cell 2 [C] Nuclei and cytoplasm of cell 3 and [D] nuclei and cytoplasm of cell 4. In all cases, nuclei and cytoplasm have also been combined. Volumetric and surface area (SA) data are shown for each reconstructed area. Note the differences in shapes between cells, particularly cells 1 and cell 2.Red = cytoplasm blue = nuclei.

3.3.2.4 Comparison of basal infolds in mono-nucleate and bi-nucleate RPE cells.

Since the image resolution in our stacks was somewhat sub-optimal to accurately segment/capture each membrane in all the basal infolds per se, we instead segmented lighter areas between membranes which represented luminal space between the basal infolds. Here, the darker regions of magnified images represented the basal infolds themselves. This enabled us to approximately evaluate the space between basal infolds and thus record any differences in these structures between mono-nucleate and bi-nucleate RPE cells. We found that the mono-nucleate cell 1 had a basal infold volume of 152.2μm^3 with a surface area of 976.4μm^2. Cell 1 also had a lumen volume of 40.9μm^3 and surface area of 537.9μm^2 [Fig. 18A]. This resulted in a ratio of basal infold volume: lumen volume of 3.72. For cell 2 (the complete bi-nucleate cells), the volume of basal infolds was 250μm^3, while the surface area was 2220.8μm^2. The volume of the lumen was recorded as 164.1μm^3 with the surface area at 1637.1μm^2, resulting in a ratio of 1.53 [Fig. 18B]. Cell 3 (an incomplete bi-nucleate cell) had a basal infold volume of 165μm^3 and surface area of 2017.9μm^2, while the luminal volume was 92.4μm^3 and the surface area 1682.2μm^2. Its basal infold volume: lumen volume ratio was 1.79 [Fig. 18C]. For cell 4, also an incomplete bi-nucleate RPE cell, the basal infold volume was 141μm^3 with a surface area of 1882.3μm^2 and lumen volume of 116.7μm^3. Its surface area was 1884.3μm^2, resulting in a final ratio of 1.21 [Fig. 18D]. Our findings reveal that there is a lot more 'empty' lumen space underneath bi-nucleate cells compared to the mono-nucleate RPE cells. This is evident in the middle and right panels in Figure 18, which clearly shows increased luminal space in panels B, C and D and A.

In order to better understand the arrangement of basal infolds in each cell, we also ran the contact macro for the basal infold and lumen of each cell. We found that the surface area of the contacting edge (of basal infolds and lumen) is 0.365μm^2 for cell 1, 1.23μm^2 for cell 2, 1.15μm^2 for cell 3, and 1.28μm^2 for cell 4, respectively [Fig.19B]. This data reveals that the total surface area of the basal infolds is much less for the mono-nucleate cell compared to the bi-nucleate RPE cells. Alongside the total surface area of contacting edges, the macro also enabled us to gather data on the Surface Area (SA) of the contacting edge per slice (thus compare between mono and bi-nucleate RPE) in order to test for any significant differences between cells [Fig. 19A]. This revealed that there is a marked decrease in the SA of basal infolds per slice in cell 1 (mono-nucleate) compared to all 3 other bi-nucleate RPE cells.

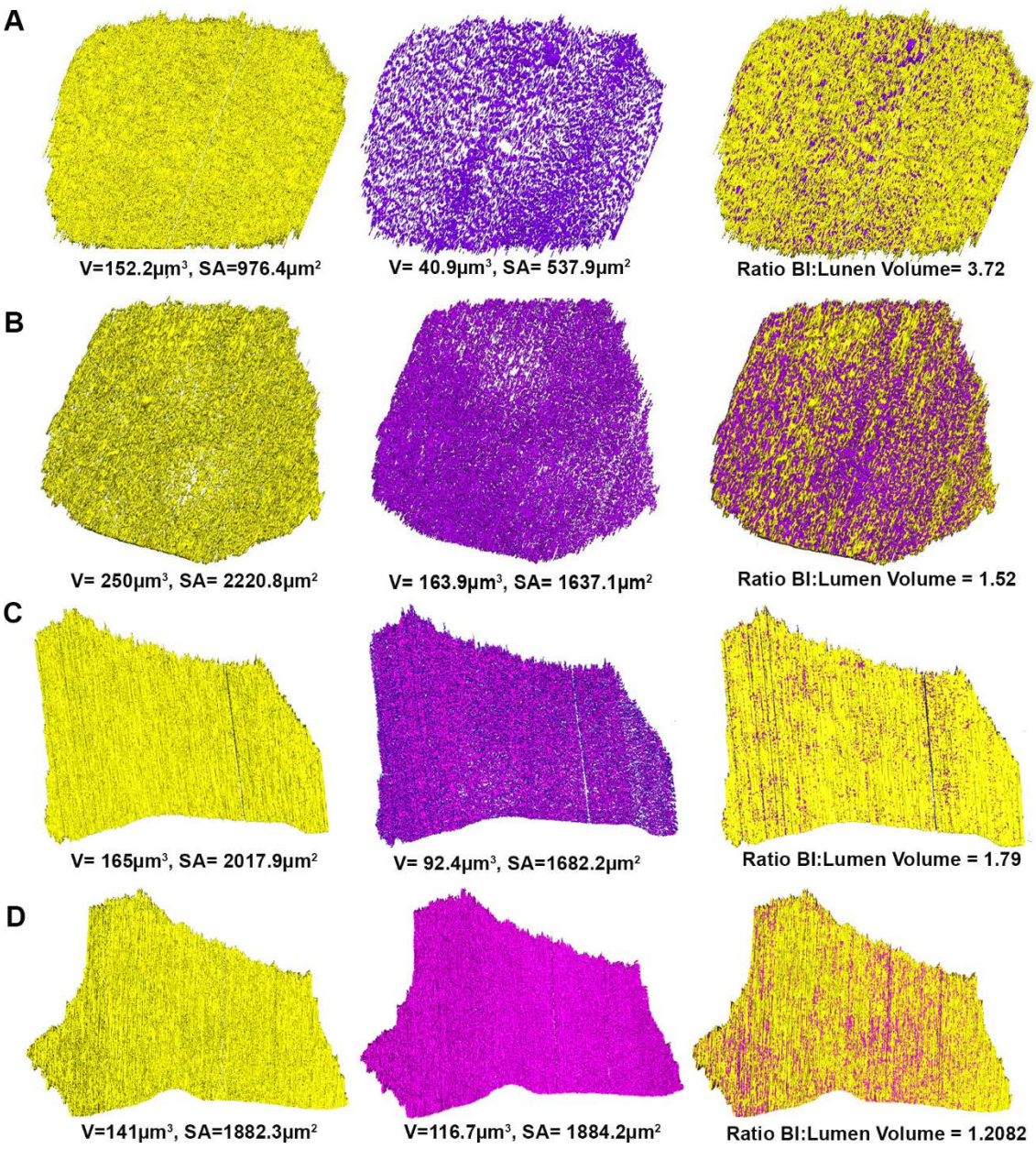

Figure 18: Segmented and 3D reconstructed basal infolds and lumen data
Cell 1 [A], Cell 2 [B], Cell 3 [C] and Cell 4 [D]. In all cases the left hand column in basal infolds, the middle column in the lumen and the right column is the two volumes combined. Volumetric and Surface area information is shown underneath each reconstructed area, and a ratio of basal infold: lumen space is highlighted for each cell. V= volume, SA= surface area. Yellow = basal infolds, purple = lumen.

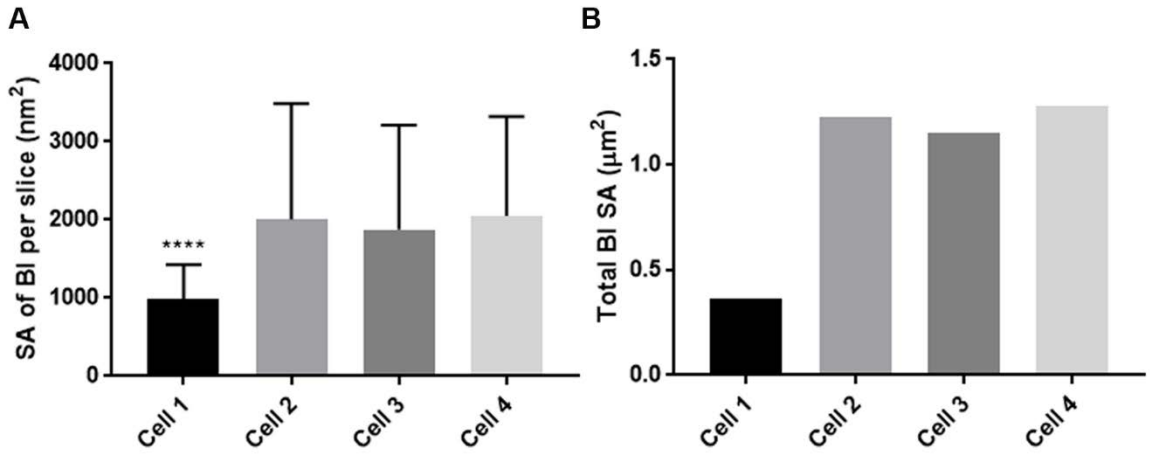

Figure 19: Surface area of the contacting edge of basal infolds and lumen in each RPE cell. A] Shows the surface area of each slice (n≥373). Error bars are shown for standard deviation and **** represents a significance of p≤ 0.0001 compared to all other cells individually. Statistical significance was measured by a one-way ANOVA followed by Turkey's multiple comparison tests. B] The total surface area of the contacting edge between basal infolds and lumen for each cell. Note: As this is a single measurement for each 3D reconstructed cell, no statistics could be performed and no error bars are shown.

3.3.2.5 Comparison of microvilli in mono-nucleate and bi-nucleate RPE cells.

Reconstruction of RPE cells in Amira revealed that the microvilli of the monolayer were found to point uni-directionally. Furthermore, there were multiple indentations at the top of RPE microvilli; points at which overlying POS associated with these structures. These indents, therefore, represent 'footprints' of overlying photoreceptors [Fig. 20]. The length of apical microvilli in RPE cells have not been measured in 3D reconstructed samples. Our 2D measurements across the entire image stack revealed that the average apical microvilli length was comparable across all RPE cells, with the average length for cell 1 measuring 5255.5nm ±800.1. Average microvilli in Cell 2 measured 5295.8nm ±972.9 in length, whilst the average length of microvilli in cell 3 was 5336.6nm ±1177.6. The microvilli of cell 4 measured 5682.6nm ±935.6 which were significantly longer than the microvilli associated with all other cells (p= 0.0226, p= 0.0225 and p= 0.0413 for cell 1, 2, and 3 respectively) [Fig. 21A]. We also measured the angle of microvilli for each cell and found that all cells had comparable angles of microvilli. However, cell 2 had more angled microvilli than cell 1 and cell 4 (p = 0.0051 and p= 0.0010 respectively). The average values of microvilli angle in cell 1 was 142.2^{o} (SD=6.88) whilst the microvilli in cell 2 were at an angle of 146.3^{o} (SD=6.91. The incompletely imaged cells had microvilli angles of 144.3^{o} ±6.5 for cell 3 and 142.1^{o} ±7.8 in cell 4 [Fig 21B].

Volumetric analysis of the microvilli revealed that the bi-nucleate cell 2 had a slightly larger microvilli volume compared to the mono-nucleate RPE cell 1 (877µm^3 and 538.5µm^3 respectively) [Fig. 20A, B]. Since cell 3 and cell 4 were incompletely imaged we carried out

a ratio of microvilli volume: cytoplasmic volume in order to make all 4 cells comparable. Cell 1 had a volume ratio of 0.26, Cell 2 0.42, Cell 3 0.39 and Cell 4 0.67 [Fig. 20A-D]. This decrease in microvilli volume for cell 3 compared to the 2 other bi-nucleate cells was unsurprising given that many of its microvilli were not included in the 3D-reconstructed image as they were cut off and outside the sample area [Fig. 20C]. However, it is interesting that there are fewer microvilli per cytoplasmic area (μm^3) in cell 1 compared to those in any of the bi-nucleate cells.

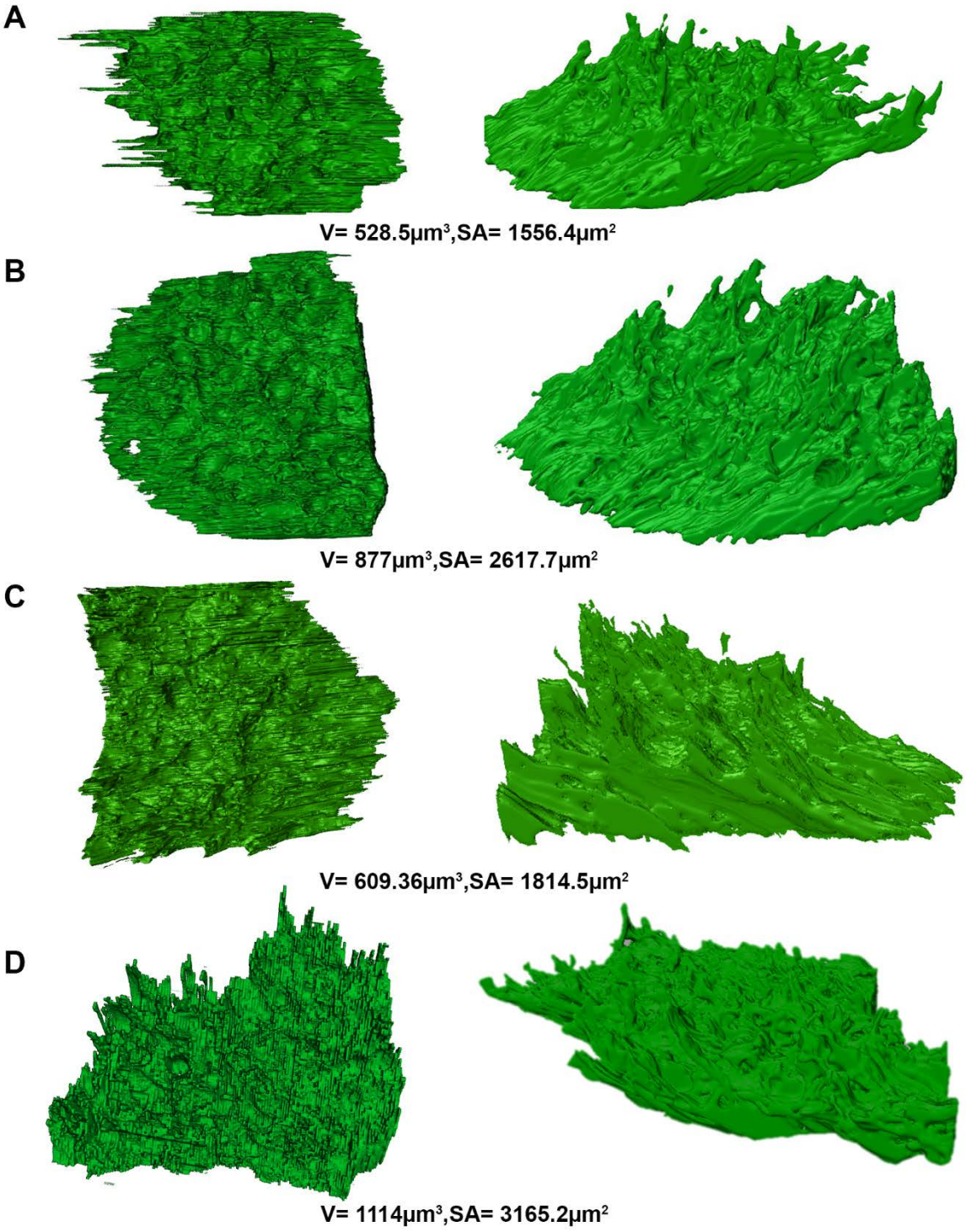

Figure 20: Segmented and reconstructed microvilli
cell 1 [A], cell 2 [B], cell 3 [C] and cell 4 [D]. The left hand panel of each cell shows the top down view of the microvilli, whilst the right hand panel is a side view. Note the indents seen in the microvilli layer, where they wrap around overlying photoreceptors. V= volume, SA= Surface Area.

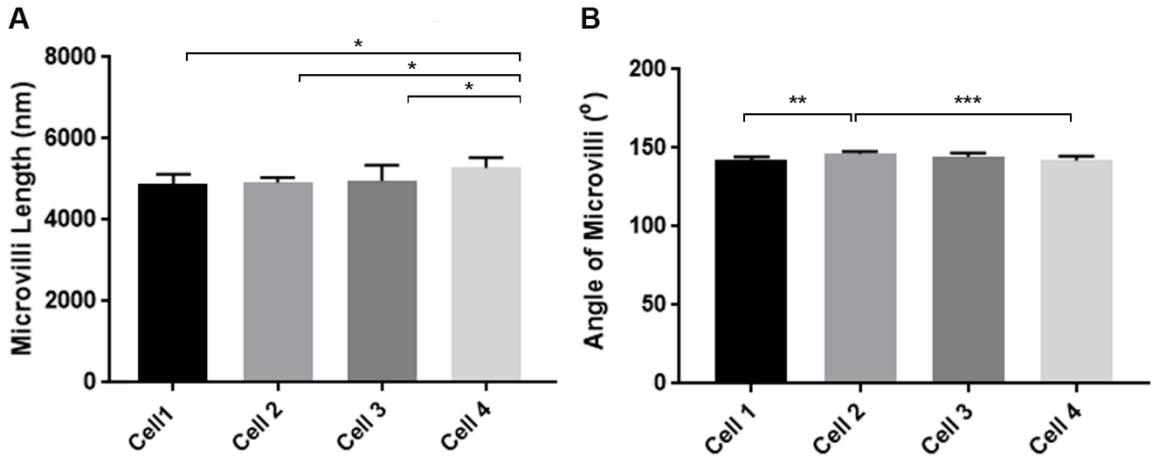

Figure 21: Microvilli measurements across each cell
A] Microvilli length for each cell. Error bars show standard deviation. Statistical significance was measured by a one-way ANOVA followed by a Turkey's multiple comparison tests where * shows the significance of p≤0.05. B] Microvilli angle for each cell. Error bars represent standard deviation. Statistical significance was measured by a Kruskal-Wallis test followed by Dunn's multiple comparison tests. ** denotes p≤0.01 and *** shows p≤0.001. n≥7 per cell.

3.3.2.6 Comparison of photoreceptors associated with mono-nucleate and bi-nucleate RPE cells

To understand the relationship between healthy RPE cells and the overlying photoreceptors, we reconstructed the latter in 3D for the first time. We used the higher contrast level in photoreceptors to reconstruct these cells via a semi-automatic method of segmentation in Amira [Fig. 22A-D]. Two independent assessors counted the number of photoreceptors overlying each RPE cell. Where differences were found, photoreceptors were recounted, or an average recorded when differences were ≤2 photoreceptors. We found that cell 1 was positioned under 90 photoreceptors, cell 2 catered for 132.5 photoreceptors, whilst cell 3 and cell 4 were associated with 102 and 216.5 photoreceptors respectively [Fig. 23]. Once reconstructed in Amira, the microvilli, which makes intimate connections with photoreceptors by wrapping around their outer segments, can be visualised in an unprecedented manner [Fig. 22E]. To study this relationship further, we used a macro to quantify the surface area of RPE microvilli in contact with the photoreceptors. We found that there was a larger area of RPE-photoreceptor contact in cell 2 (90000nm^2) compared to cell 1 (51462nm^2). This increase was not seen in cell 3 or cell 4 (48732nm^2 and 73118nm^2 respectively) but since they are incomplete this is perhaps unsurprising. We further found that the binucleate cells had significantly more contact with the photoreceptors than the mono-nucleate RPE cell [Fig. 24A]. Another useful output would have been the volume of photoreceptor outer segments. However, it was not possible to obtain this data as our imaging parameters did not capture these wholly. Instead we were able to measure the ratio of photoreceptors per microvilli volume (µm^3), which provided an

analysis of RPE-photoreceptor interactions at the RPE microvilli scale. For cell 1 and 2 this ratio was 0.1703 and 0.151 respectively. Cell 3 had 0.167 photoreceptors per μm^3 of microvilli whilst the ratio for cell 4 was 0.194 [Fig. 25A]. Since these values are comparable across all cells, we can conclude that the microvilli volume is directly correlated to the number of photoreceptors catered by RPE cells. Interestingly, when we calculated the ratio of photoreceptors per μm^3 of RPE cell cytoplasm, cell 1 had a ratio of 0.044, whilst cell 2 and cell 3 had 0.063 and 0.065 respectively with a value of 0.130 for cell 4 [Fig. 25B].

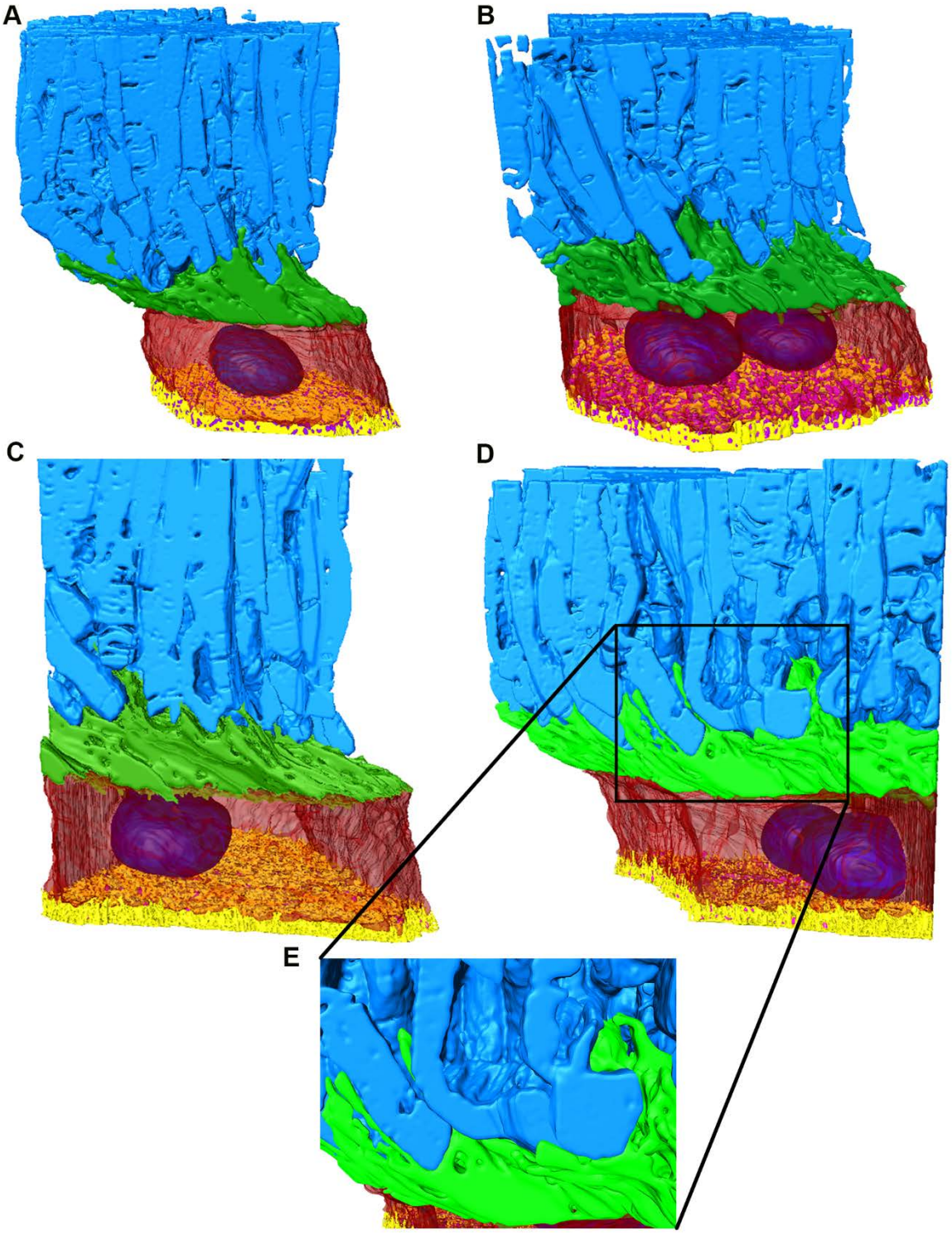

Figure 22: Amira 3D reconstructions of cells and photoreceptors
[A-D] The relationship between overlying POS and the underlying RPE cells were studied for each of cells 1-4 respectively. [E] A magnified cross-section showing RPE microvilli-POS interactions in unprecedented detail. Pale blue = photoreceptors, green = microvilli, red = cytoplasm, dark blue = nuclei, yellow = basal infolds, and purple = lumen.

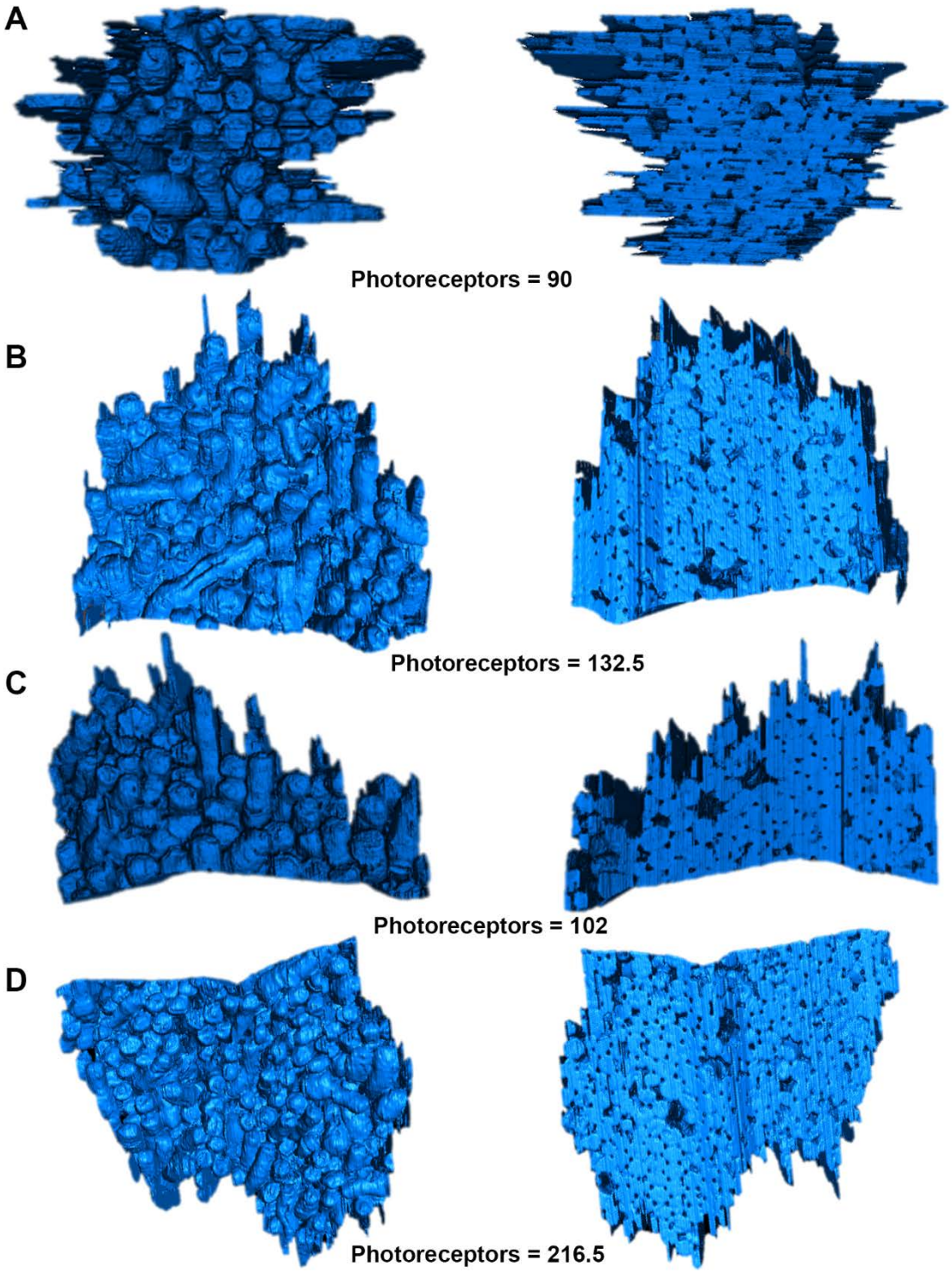

Figure 23: Segmented and 3D reconstructed photoreceptors
Cell 1 [A], cell 2 [B], cell 3 [C] and cell 4 [D]. The number of photoreceptors counted for each cell is indicated. For each cell, the bottom up view is shown on the left hand panel, which illustrates the basal side of the photoreceptors that interact with the microvilli. The right hand panel shows a top down view of the photoreceptors.

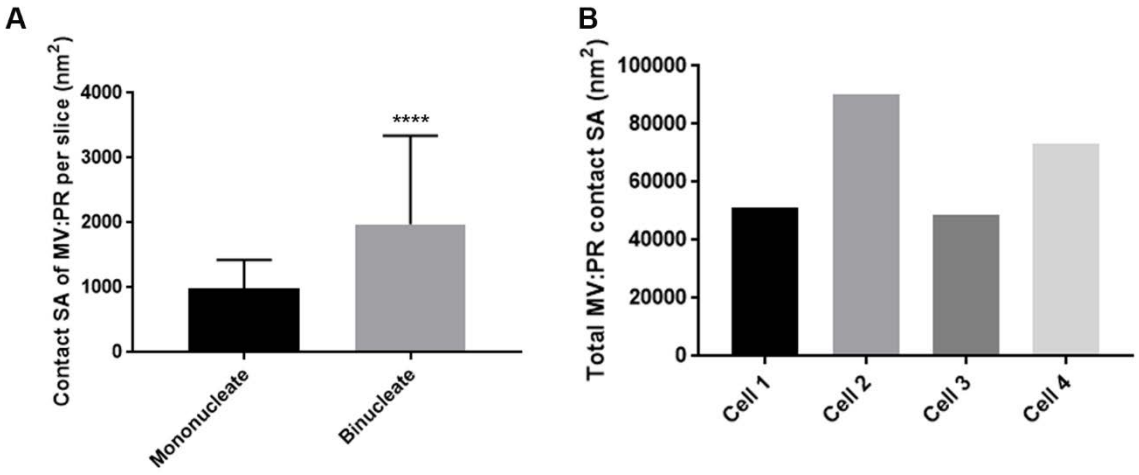

Figure 24: Surface area of RPE microvilli in contact with photoreceptor outer segments for each cell.
[A] The average surface area of microvilli per slice for mononucleate and binucleate RPE (n≥ 373). Error bars show standard deviation. When compared, **** represents a significance of p≤ 0.0001 measured by an unpaired student's t-test [B] The total surface area of the contacting edge between photoreceptors and microvilli for each cell. Since this is a single measurement, no statistics could be performed, and no error bars are present.

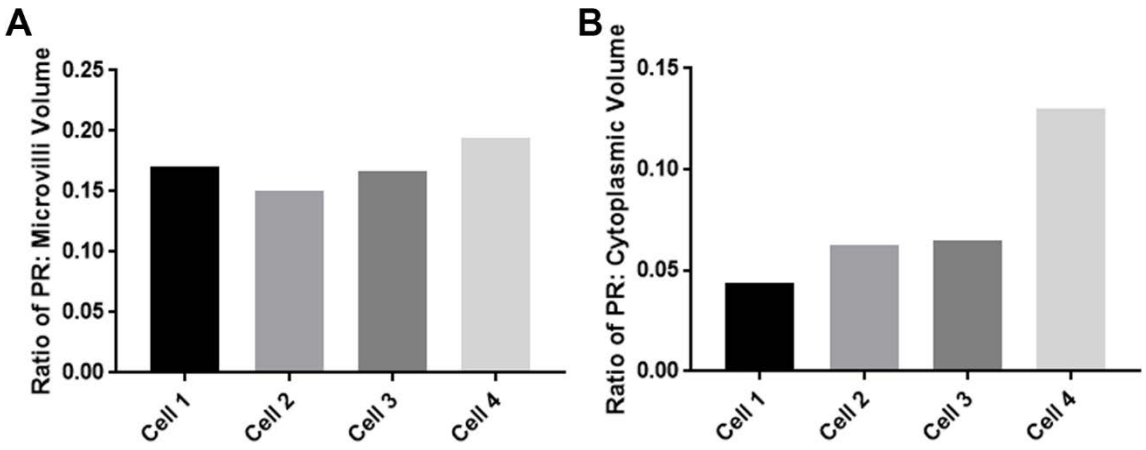

Figure 25: The ratio of POS to RPE microvilli volume and cytoplasmic volume
[A] The ratio of photoreceptors per μm^3 of RPE microvilli volume for each cell [B] The ratio of photoreceptors per μm^3 of RPE cytoplasmic volume for each cell. No errors bars are shown as these are representative of an entire RPE cell, not per slice.

3.3.2.7 Comparison of Bruch's membrane associated with mono-nucleate and bi-nucleate RPE cells

Next, we studied the interaction between RPE cells and the underlying/supportive BrM. To quantify this relationship at an ultrastructural level, we measured the BrM thickness at 10 separate locations in images every 50 slices apart for each RPE cell [Fig. 26]. The BrM associated with Cell 1 was significantly thinner than all other cells ($p = 0.0477$ for cell 2, $p= 0.0062$ for cell 3 and $p= 0.0012$ for cell 4). For cell 1, the lowest measurement for BrM thickness measured 221.4nm while the thickest measured 762.6nm. The average BrM thickness for the entire RPE cell was calculated to be 423.9nm. For cell 2, BrM had a minimum thickness of 246nm and reached a maximum of 1461.58nm. The average thickness of BrM underlying cell 2 was 440.1nm. Cell 3 had a minimum BrM thickness of 270.6nm and maximum of 1058.1. The average BrM thickness for cell 3 was 496.9nm. Cell 4 BrM had a minimum thickness of 271.7nm and maximum of 1116.3nm, with an average value of 507.4nm.

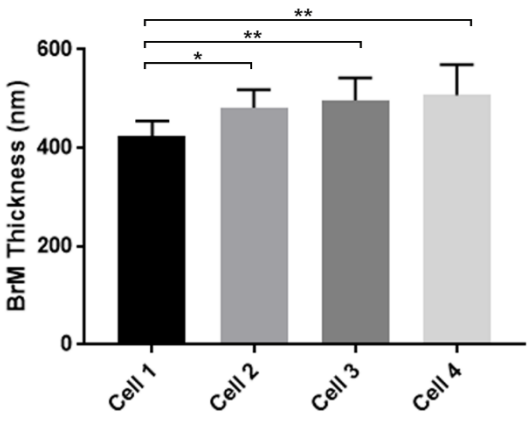

Figure 26: BrM thickness as measured under each RPE cell.
The thickness of BrM under each cell was measured. The BrM under cell 1 was significantly thinner than under any of the bi-nucleate cells. No significant difference was recorded between any of the 3 bi-nucleate RPE cells (cell 2, 3 and 4). Error bars show standard deviation. Statistical significance was measured by a one-way ANOVA, followed by Turkey's multiple comparison tests. * shows significance of $p\leq 0.05$, ** represents $p\leq 0.01$ whilst *** is $p\leq 0.001$. $n \geq 9$ images per cell.

3.4 Discussion

All knowledge of the RPE monolayer is based on conventional 2D imaging techniques. However recent advances in 3D imaging technology have allowed researchers to delve further into the morphology of different cell types. For example, this technology has been used to reconstruct capillary vessels in the inner nuclear layer and the retinal ganglion layer of the inner retina. This revealed the accumulation of vacuoles in the basement membrane at the glia interface with increasing age, a phenotype that is usually considered to be pathological[302]. 3D reconstructions of RPE cells have revealed some surprising morphological features, including the rhomboid cross-sectional shape of each cell with one side opening at the basal infolds and the other closing at the microvilli. This increases the surface area of cell contacts. This might help aid the barrier properties of the monolayer. We measured the surface area of the cell: cell contact to garner an idea of the level at which each cell interacts with another. We found that there was no point at which all the cells interacted, and instead the contacts were slightly staggered to one another. However, given that all data discussed in this chapter is from four cells with only one being mono-nucleate, these findings might not be truly representative of the latter cell type, and therefore it would be useful to study more mono-nucleate cells to substantiate any conclusions drawn.

3.4.1 Quantification of bi-nucleate cells across the murine retina

2D imaging techniques have been utilised in numerous studies on murine retinas, many of which have identified the presence of bi-nucleate RPE cells. It has been shown that 67% of the central mouse retina consist of bi-nucleate RPE cells compared to just 3% in the periphery. This equates to approximately 35% of all RPE cells in the murine retina being bi-nucleate[136]. The number of RPE cells are known to decline with increasing age[145]. However, in healthy aged eyes, the RPE monolayer is maintained, which suggests a compensatory mechanism in old age. It must be noted that a subset of binucleate cells in murine eyes are attained shortly after birth and therefore multinucleation is often reported to be, in part, a developmental process[151]. Studies have shown that RPE cells not only increase in size, but a parallel process of multi-nucleation also occurs with age in both murine and human eyes[135]. Our studies quantified this in the eyes of young and aged mice and found that there were significantly more bi-nucleate RPE cells in the central retina compared to the peripheral retina. Furthermore, there was an age-related increase in bi-nucleate RPE cells across the whole retina, regardless of the location. Chen et al., also reported that RPE displays an age-dependent increase in bi-nucleate cells. For instance, 24-month old mice have nearly 80% bi-nucleate or multi-nucleate cells in the central retina, whereas levels in the peripheral retina were only ~20%[149]. Bi-nucleate RPE have also been reported in the

human eye and represents approximately 3% of the RPE monolayer. Bi-nucleation of RPE is also reported to increase as humans age[135]. The formation of bi-nucleate RPE cells may, therefore, represent a pathological process under conditions of chronic stress, or an adaption by healthy RPE to ageing in an attempt to maintain an intact/functional monolayer. If these bi-nucleate RPE cells are fully functional or whether they are particularly susceptible to disease is not yet fully understood.

3.4.2 Structural comparisons between bi-nucleate and mono-nucleate RPE cells

Although bi-nucleate RPE cells have often been reported previously [135,303,304], very little is in fact known about the differences between mono-nucleate and bi-nucleate RPE cells. For the first time, we have been able to draw direct comparisons between their overall 3D morphology as well as volume and surface areas of distinct components of the cells. This can also be seen in the supplementary information on the provided USB stick. It has previously been reported that RPE cells cater for up to 45 photoreceptors per RPE cell[132,305]. However we have found that it was, in fact, double this number in mono-nucleate RPE, whilst bi-nucleate cells cater for up 216 photoreceptors in an incompletely imaged cell. This may be somewhat unsurprising as macular RPE is thought to cater for higher POS load/sq. area compared to peripheral RPE[173], although it has never been reported to this extent before.

Interestingly, we also found that microvilli volume increases with the number of photoreceptors the cell caters for, showing an inherent link between the two structures. The same was not true, however, for the cytoplasmic volume of each cell, suggesting that bi-nucleate cells may not be able to cope with this increased burden. Due to this increased phagocytic and proteolytic burden, bi-nucleate RPE is likely to have a higher metabolic demand and therefore susceptible to damage with increasing age[296]. Interestingly, we also found that bi-nucleate RPE microvilli make more contact with photoreceptors than the mono-nucleate RPE, suggesting an adaptive mechanism to cope with this increased burden. Photoreceptor outer segments and modification to these form the largest source of oxidative stress and damage to RPE cells[119,120,174,295,306]. Our 3D data provides support to this pathway of damage from an altogether novel and structural perspective.

The increased basolateral surface area and disrupted basal infolds of bi-nucleate RPE cells also suggest that they may be more susceptible to age-related damage[23,86,132]. The accumulation of macular drusen under the RPE is a key feature of early AMD[141,307]. Basal linear deposits accumulate between the RPE plasma membrane and the RPE basal lamina[308], whilst basal laminar deposits build up between the RPE basal lamina and the inner collagenous layer of BrM[309]. The latter is more associated with AMD progression and

are likely to affect cells with a larger basolateral footprint and thus more contacts with BrM[48,141,310], both of which are evident in the 3D reconstructed bi-nucleate cells. Interestingly, a study by Glen Jeffery showed that bi-nucleate cells appeared in increased numbers in close proximity to drusen, a pathological hallmark of AMD[311].

Our data support reported BrM thickness measurements of 400-500nm in the mouse central retina[136]. However, our analysis also revealed that bi-nucleate RPE cells overlie areas of considerable BrM thickening; a structural change often observed in patients with AMD[64,312,313]. This level of BrM thickening was not apparent under mono-nucleate RPE cells, suggesting a vulnerability of bi-nucleate cells to BrM-related pathologies.

3.4.3 Insights into the formation of bi-nucleate RPE

Formation of multi-nucleated cells has been previously reported in osteoclasts by cell fusion[314,315]. However, these cells can also form by mechanisms such as phagocytosis of live cells, or failure of cytokinesis in dividing cells[316]. In the study by Chen et al., primary mouse RPE cells were fed either POS or oxidised POS (oxPOS); both of which causes a dose-dependent increase in multi-nucleation and suppression of RPE cell proliferation. Interestingly, exposure to latex beads did not cause these effects, suggesting a process driven specifically by photoreceptor-derived material. In their experiments, under standard culture conditions (DMEM with 10% FCS) and in the absence of any POS, 3% of primary mouse RPE cells in culture were reported to be bi-nucleate. However, the number of bi-nucleate RPE increased to 15% and 20% following POS and oxPOS treatment respectively. This phenomenon was also observed when similar experiments were carried out using the widely-utilised ARPE-19 cell-line[149]. These data suggest that exposure to, and phagocytosis of, POS cargos induces RPE cell multi-nucleation. This is interesting in light of our findings, which showed that bi-nucleate RPE microvilli have a higher level of contact with photoreceptors compared to mono-nucleate RPE, and therefore may cater to higher POS numbers. Perhaps this increase occurs as a result of bi-nucleate cell formation and is at a level sufficient to restrict cytokinesis. Given the increase in microvilli surface area and volume in bi-nucleate RPE cells compared to mono-nucleate cells, it is perhaps unsurprising that they cater for more photoreceptors than mono-nucleate cells. However, given that there is no extra cytoplasmic volume, their ability to cope with this extra burden may be limited. This idea is corroborated by studies that showed bi-nucleate RPE cells phagocytose significantly higher levels of E.Coli BioParticles compared to mono-nucleate counterparts[149]. This begins to reveal the reasons that bi-nucleate cells are more susceptible to damage in diseases such as AMD. It is not currently known whether multi-nucleation is induced by POS as the result of phagocytosis of neighbouring cells or due to failed cytokinesis. Delving further into the intracellular structure of 3D-reconstructed cells,

our studies show that RPE has similarly sized nuclei regardless of the number of nuclei in each cell. There is an increase in surface area but not the cytoplasmic volume of the bi-nucleate cells. Therefore, if these RPE cells were to split, the volume of the daughter cells would be half that of the parent's cells, while the surface area of the cell and total nuclei volume would be similar to that of the mono-nucleate cell, as would be expected[317]. This suggests that the formation of bi-nucleate cells are due to a failure in cytokinesis. It can, therefore, be hypothesised that atrophy of RPE cells during ageing and disease causes a POS-induced formation of multinucleate cells by cytokinesis inhibition and prevention of RPE proliferation. Loss of contact between the photoreceptors and RPE appears to cause RPE migration, proliferation and epithelial-mesenchymal transition, with cells eventually adopting fibroblastic characteristics[318]; a phenomenon observed in proliferative vitreoretinopathy[319]. Consequently, a major function of RPE-POS interaction may be to maintain homeostatic integrity and the 'post-mitotic' phenotype of the RPE monolayer. However, with age, many factors including oxidative stress may compromise this arrangement as patches of RPE begin to atrophy. To overcome this degenerative process, RPE cells may enlarge in an attempt to repair defective areas of the monolayer. POS continues to exert a suppressive effect on RPE proliferation, causing enlarged cells to undergo mitosis but where full cell cytokinesis and division is prevented. As a result, the aged RPE monolayer will eventually consist of heterogeneously shaped cells with multiple nuclei, but whose function is nonetheless preserved[149]. This possibility is supported by our findings which show that not all 3D-reconstructed cells exhibit a characteristic hexo-cuboidal shape that is widely reported in the literature. Indeed, some RPE cells appear more cuboidal in shape, perhaps to increase tessellation and thus maintain the integrity of this important monolayer. However, the potential for increases in cell size (hypertrophy) even with the formation of multiple nuclei is limited, as shown by muscle cells, and such cells are often weakened[320]. Consequently, bi-nucleate RPE cells may be more prone to apoptotic death[321]. Interestingly, apoptotic death is known to occur in nvAMD[144]. Such events could also cause patches of RPE to die, which could initiate early stages of GA AMD[67].

3.5 Summary

3D analysis of RPE cells have therefore provided new information and insights into how AMD may initiate and develop in the outer retina, and why some RPE cells may be more susceptible to damage compared to others; an issue which has long puzzled the research community investigating the aetiology of retinal diseases such as AMD. We have shown that bi-nucleate RPE cells are likely to process higher numbers of POS on a daily basis. Since proteolytic processing of POS is the largest contributor to oxidative stress and damage in the RPE monolayer[53,54], our findings shed new light from an altogether novel structural perspective. Furthermore, we have shown that bi-nucleate cells have a larger basal footprint; a key point where drusen-like basal laminar deposits accumulate, which is the earliest hallmark of AMD [140]. The finding that the nuclei and cytoplasm in all RPE have comparable volumes, regardless of the number of nuclei in each cell, while the surface area of the cell increases in bi-nucleate cells begin to shed light onto the formation of these cells. Under normal circumstances, following the completion of the cell cycle, any daughter cells produced would have comparable nuclei to that of the mother cell but would have a smaller cytoplasmic volume. Therefore, our findings suggest that bi-nucleate cell formation exists as a failure of cytokinesis. This is in parallel with previous findings that have shown that exposure to, and phagocytosis of POS cargos induces RPE cell multi-nucleation, and without this contact, RPE cells can complete division and form 2 daughter mono-nucleate cells[149]. However, the relatively small number of cells used in this study limits the conclusions that can be drawn and further imaging and analysis needs to be performed to validate the resuls that have been found. Nonetheless, insights from this work invite further questions into structural changes associated with oxidative stress and damage in the senescent retina.

Chapter 4 The effect of a high-fat diet on the ultrastructure of the RPE and associated retinal layers

4.1 Introduction

Given that bi-nucleate RPE cells appear to be more vulnerable to oxidative stress-related damage than mono-nucleate RPE cells, we wanted to better understand the effects of oxidative stress on the structure of the RPE monolayer. Oxidative stress results from disturbances in the pro-oxidative/ anti-oxidative cellular balance due to elevated levels of ROS produced from oxidation reactions. Although the generation of ROS has long been considered to have harmful effects on the RPE monolayer, they also have a physiological role which is essential for the normal cellular function. ROS signals a wide range of cellular feedback including regulation after excessive metabolism[322], in response to hypoxia via HIF-1α[323], regulation of autophagy through ATF4[324], and regulation of the inflammatory response[221,222,325]. The macula is positioned within a high oxidative environment, partly caused by unique sources of ROS and oxidative stress. The RPE has a large metabolic demand which produces a high level of ROS for signal transduction. Given this high metabolic demand, the macula receives some of the highest blood flow in the body. This causes the RPE to be exposed to high ambient oxygen partial pressures, in the region of 70-90mmHg[326]. Substantial levels of ROS are produced from cellular metabolism required to meet the functional demands of the RPE. The metabolic demand of the RPE causes an enrichment of mitochondria, which creates a further major source of ROS in the RPE[327,328]. Compared with young cells, mitochondria in ageing cells generate more ROS. Consequently ageing cells become progressively more susceptible to mitochondria-derived ROS[85]. Another unique source of oxidative stress in the RPE derives from the daily ingestion and phagocytosis of shed POS[329]. Photo-oxidative stress from processing light for vision is perhaps the msot unique source of oxidative stress. Since the work of Ham *et al*. in 1978, photo-oxidative stress has been linked to damage in the neuroretina, RPE and choroid[86,107]. This data is correlated with epidemiological studies which show a link between sunlight exposure and AMD risk[330,331].

The RPE cells have developed several mechanisms to protect themselves from potentially damaging effects of oxidative stress yet still allow for vital signalling through physiological ROS. Some of these mechanisms include oxidant-producing enzymes being located adjacent to their intended targets[85] and oxidants having a regulated entry into and out of

organelles. For instance, H_2O_2 has been shown to move through aquaporin channels[332]. ROS also have a short-half life and are transiently produced which spatially limits ROS to certain locations where they can be neutralised if necessary. Cellular antioxidant response can be induced in response to oxidative stress, which has been linked to the activation of autophagy through the Keap1/Nrf2 pathway[333-335]. Nf2 is often reduced in ageing, impairing the signalling pathway. Nrf2 signalling protects against dysregulated innate immune response[336]. Abundant oxidative stress can magnify the innate immune response, converting it from a protective to a pathological response. Therefore deficient Nrf2 signalling predisposes to prolonged inflammatory response and the development of chronic inflammation[337], a susceptibility factor for AMD[13]. In the brain of elderly mice, Nrf2 deficiency increases oxidative damage and complement C3 deposition[338]. A consequence of inadequately neutralised oxidative stress is degradative non-enzymatic reactions, such as the peroxidation of polyunsaturated fatty acids, which generate high reactive oxidised lipids[336]. Lipid peroxidation gives rise to products such as advanced glycation end-products (AGEs) that have the ability to modify proteins, lipids and DNA on cellular and extracellular components[339]. These modifications result in altered structures that can themselves activate the innate immune response and have oxidative specific epitopes (OSEs). OSEs are long-lived and serve as a chronic inducer of oxidative stress and the innate immune response if they are not neutralised or removed[339]. OSEs have been identified in a wide range of diseases including diabetes, AD and AMD[339]. The macula has unique sources of OSEs. In the retina, docosahexaenoic acid (DHA) is the most abundant fatty acid in photoreceptor tips, and is the most oxidisable fatty acid in the body due to its unsaturated structure[336]. In the high oxidative stress environment of the macula, DHA is uniquely oxidiatively modified to carboxyethylpyrrole (CEP)[340]. CEP is found in at higher levels in the outer retina of AMD patients compared to age matched controls. CEP is also found in drusen of AMD patients[341]. This has been modelled in mice and led to patches of RPE atrophy, as well as damaged photoreceptors and basal laminar deposits[342]. Taken together, it is clear there is a delicate balance between physiological oxidative stress and the onset of pathological oxidative stress which is lost in AMD, resulting in considerable damage to tissues of the outer retina.

The oxidative burden on the RPE is exacerbated by a western lifestyle, disrupting the precarious balance of the cells protecting themselves from damaging effects of oxidative stress whilst still enabling the vital roles that ROS contribute to. Cigarette smoking adds to the oxidative stress since it contains over 4700 chemical components, many of which are strong oxidants themselves[343,344]. These chemical oxidants deplete tissues of ascorbic acid and protein sulfhydryl groups. This causes the oxidation of DNA, lipids and proteins[345-347]. Many of these changes, such as malondialdehyde (MDA), 4-hydroxynonenal (4-HNE) and AGE compounds, have been identified in AMD, and indicate that oxidative damage is an important factor in the mechanism of disease pathology[85]. Another life-style habit that

contributes to AMD is the intake of a high-fat diet (HFD), which also induces oxidative stress[44,45,78,80,348]. The intake of a 'Western-style' diet rich in saturated fat, trans-fatty acids, red meat, sodium, fructose and sucrose but low in fibre, plant-derived proteins and mono/polyunsaturated fats are associated with major diseases including diabetes, metabolic disorder and obesity. Typically, these foods are also highly refined and processed. Their consumption is further linked with impaired long-term potentiation and metabolic changes in the brain and degenerative conditions such as AMD[78,349]. Dietary intake of such foods is associated with activation of major pathogenic mechanisms including oxidative stress, the intracellular accumulation and extracellular deposition of lipids and cholesterol as well as dysfunctional clearance pathways and chronic inflammation[84,85]. An unhealthy diet contributes to the risk of developing AMD in the same way that a healthier 'Mediterranean' diet or an increased intake of fish and nuts appear to confer protection[45,78,350,351]. A HFD leads to damage of the retina by increasing the number of lipids in circulation. Many of these lipids become deposited in the retina and as sub-RPE deposits such as Drusen[352]. Having excess lipids in circulation causes an increase in lipid peroxidation leading to oxidative stress and damage[88]. This also occurs by a HFD increasing plasma triglycerides, total cholesterol, and non-esterified fatty acid levels, increasing blood oxidative stress parameters[88]. Nonetheless, many aspects of this diet-disease axis remain to be elucidated. For instance, how the lack of micronutrients and unhealthy foods trigger disease at the molecular level is still poorly understood[83]. The mechanisms underlying the elevation of oxidative stress upon HFD consumption are also not fully understood, but are thought to be a result of mitochondrial dysfunction[353], augmented NADPH oxidase activity[354], and increased fatty acid oxidation[355]. The full effects of a HFD on the structure and function of the retina has not yet been elucidated. In this chapter, we focus on studying how high oxidative stress associated with an unhealthy HFD alters the ultrastructure of the RPE monolayer and associated tissues of the outer retina. In order to do this, we have utilised a HFD mouse model in which mice are fed a 45% fat diet (Appendix F), which is relevant to a typical American or European diet that contains approximately 40-50% fat. The composition of the diet has an omega 3: omega 6 ratio of 1:14.7 which further mimics the human diet[356].

Hypothesis: Consumption of a HFD drives structural and functional deficits associated with AMD.

Aims:

-Use conventional TEM imaging to study how the ultrastructure of the retina changes in mice fed a HFD.

- Use confocal immunofluorescence microscopy to study how some protein expression levels are altered in mice fed a HFD.

4.2 Methods

At 5 weeks of age, C57BL/6 mice were fed with either a normal chow-based diet containing 7% kcal fat (RM1 diet; Special Diet Service (SDS) Ltd, UK) or a HFD containing 45% kcal fat (SDS Ltd, UK). The full components of each diet are listed in Appendix F. Mice were maintained up to 52 weeks of age when they were perfused transcardially with 4% PFA in 0.9% Saline. 8 eyes (from different mice) were cut and embedded for TEM as described in section 2.4.1. 3 eyes were retained for histological analysis and were cryo-embedded, sectioned and stained for H&E, Oil Red O or immunohistochemistry. Whilst cutting, slides were made up that were representative of the entire eye and were randomly assigned to each of the 3 groups.

For H&E staining, three slides were selected, and the frozen sections were dried at 37^{o}C for 1 hour. The slides were then soaked in Mayer's Haematoxylin for 5 mins and left in running tap water over the sink for 5 mins. Slides were then stained in eosin for 5 mins and rinsed briefly in ddH_2O followed by an ethanol dehydration gradient. Slides were mounted in Pertex and covered with coverslips. Finally, slides were scanned at 2x magnification on a conventional Olympus microscope with a dotSlide system built in. This created an overview image of the whole slide. Areas with retinal layers attached (at least 2 sections per slide) were then identified and further imaged at a higher magnification (x40). All solutions were prepared and supplied by the Histochemistry Research Unit, Southampton. H&E images were opened in FIJI, and 15 width measurements were taken for the photoreceptors and RPE/BrM across each of 6 images from 3 eyes for control and HFD groups.

For Oil Red O staining, 1mg/ml of Oil Red O (Sigma Aldrich, UK) stock solution was made up in 60% isopropyl alcohol. The solution was warmed in a 56^{o}C water bath for 1 hour. Six parts of the stock solution were mixed with 4 parts ddH_2O and left for 10 mins. The solution was passed through fine filter paper to remove sediments, leaving the Oil Red O working solution. 3 slides were selected, and the frozen sections were dried for 1 hour. Slides were rinsed in 60% isopropyl alcohol for 30 seconds and stained in Oil Red O working solution for 10mins. Slides were then washed briefly in 60% isopropyl and soaked in running water for 1 minute. Slides were then counterstained with Mayer's Hematoxylin for 1 minute and then blued in running tap water for 5 mins. Each slide was mounted with Pertex and incubated at 80^{o}C for 20 mins. Slides were imaged as described for H&E staining. Oil Red O images were opened in FIJI. The pink 'droplets' were counted for each of 6 images from 3 eyes for control and HFD groups. Measurements were of the width of the RPE and the photoreceptor layers. Values were recorded in Excel and then imported into GraphPad Prism for statistical analysis using a Student's T-test.

For immunohistochemistry, slides were selected for both control and HFD groups, with a further wildtype slide being retained for secondary antibody control. The frozen sections were dried at 37^{o}C for 1 hour before being washed three times in 1xPBS. 1% BSA (Sigma Aldrich, UK) in 0.3% PBS-Tween was then added for 1 hour. Slides were then washed in 1xPBS and incubated overnight at 4^{o}C in primary antibody. In this case primary antibodies used were specific for clusterin, collagen IV or TIMP3. The secondary only control was incubated in blocking buffer. All slides were kept in a light-protected moist chamber. Slides were washed a further three times in 1xPBS before the secondary antibody solution was added for 1 hour. Samples were then incubated for 10 mins in DAPI (Sigma Aldrich, UK) and mounted with a glass coverslip using Mowiol mounting media. Slides were then imaged using a confocal microscope. Images of areas where all layers of the retina were attached were taken at 90^{o} vertically or horizontal. Images were acquired at x40 magnification using a Leica SP8 laser-scanning confocal microscope (Leica Microsystems, UK). Z-stacks were taken of pre-selected areas using system optimised settings for each field of view. Confocal images were opened in FIJI, and the coloured channels were split. The green channel was converted into a 16-bit image. The image stack was then converted into a Z project to produce an image with maximum intensity from the entire stack. This image was then duplicated. One copy is left untouched. The other was used to create a binary image with the same threshold used for all images of the stain. The measurements were set to re-direct to the duplicated, untouched image. The layer (RPE or photoreceptor) was then traced around using the bright field channel. This was pasted onto the binary image and the average intensity measured and recorded in excel. This was repeated for 6 images for each stain. The average intensity was measured for both the RPE layer and the photoreceptor layer in control groups and HFD groups. Values were then imported into GraphPad Prism and statistical analysis was performed using an unpaired student's t-test.

TEM blocks were cut and imaged as described in section 2.6.2. Images were analysed using FIJI. The scale was set using the scale bar acquired on the TEM. 10 thickness measurements were taken for each of 10 images across 8 different eyes for control and HFD groups. Values were imported into GraphPad Prism for statistical analysis.

4.3 Results

Mice were fed either a normal chow-based diet (7% kcal fat) or transferred onto a high-fat Western-style diet at 5 weeks. This high-fat diet contains 45% kcal fat, 20% kcal protein, 35% kcal carbohydrate (SDS, UK). The mice were aged to 52 weeks, by which time they had become obese [Fig. 27] and weighed approximately 48g, compared to the average weight of 31g of normal aged mice.

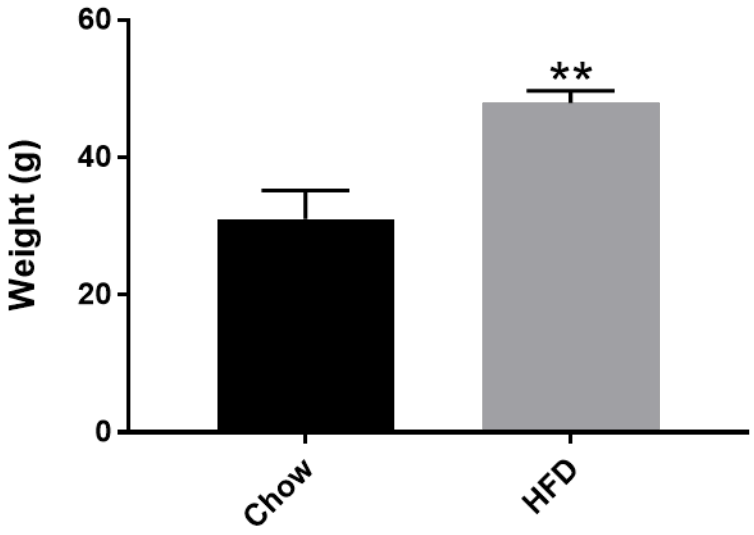

Figure 27: Weights of chow-fed control mice and HFD mice at 52 weeks.
Mice were weighed immediately before culling and mice fed an HFD were significantly heavier than mice fed a chow-based diet. Statistical analysis was performed using an unpaired student's t-test. ** represents a p-value of ≤0.01 and error bars show Standard Deviation. N= 15 mice per group.

4.3.1 Diet-induced oxidative stress caused an increase in retinal layer thickness

After creating this model of environmentally (HFD) induced oxidative stress, we wanted to observe the differences a HFD had on the outer retina compared to age matched normal chow-fed mice. Using H&E imaging, we were able to distinctly identify the layers of the retina [Fig. 28A]. These images were used to measure the thickness of each retinal layer, and it was revealed that both the photoreceptor layer and the RPE/BrM were significantly increased in the HFD model [Fig. 28B, C, D]. In healthy aged eyes, the RPE/BrM layers measured 7.125µm ± 2.135, whilst in HFD eyes this had significantly increased to 8.833µm ± 2.1119 ($p \leq 0.0001$). The thickness of the photoreceptor layer in control eyes was 53.69nm ± 7.667 whilst in HFD eyes this had increased significantly to 62nm ± 15.93 ($p = 0.0016$). There also appeared to be disruption to retinal layers, with evidence of apparent fragmentation, particularly in the photoreceptors and inner and outer nuclear layers. Since

it is not possible to distinguish BrM from the RPE in the H&E images, we used TEM images to measure the thickness of BrM [Fig. 29A, B]. This revealed that BrM had almost doubled in thickness [Fig. 29C] from 649.4nm ± 138.1nm to 1077nm ± 360.4nm (p≤0.0001). BrM is known for its pentalaminar structure[14] [Fig. 29A]. However images have shown that BrM in HFD eyes appears to have lost several of these distinct layers [Fig. 29B].

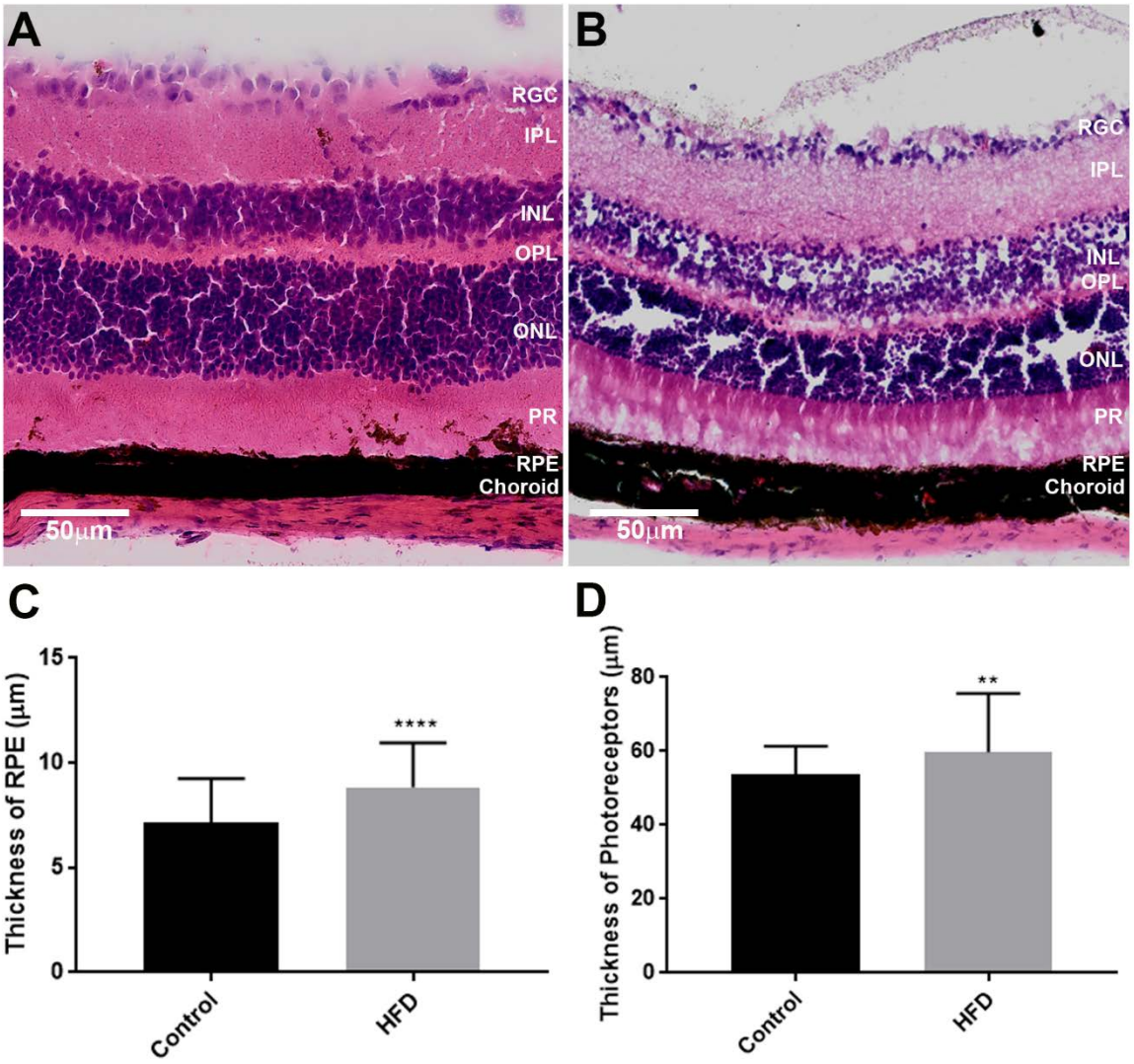

Figure 28: H&E images of murine retinas.
[A] Aged C57BL/6 wildtype mouse eye and [B] aged C57BL/6 HFD mouse eye. Scale bar represents 50µm. Layers of the retina are labelled. White arrows indicate the thickened RPE and retina in the HFD eye. [C] Thickness measurements of the RPE (n=6). **** shows a statistical significance of p≤ 0.0001 when measured by a student's T-test. Error bars show standard deviation. [D] Thickness measurements of the photoreceptor layer (n= 6), ** represents a statistical significance of p≤ 0.01 as measured by a student's T-test. Error bars show standard deviation. (RGC, retinal ganglion cells; IPL, inner plexiform layer; INL, inner nuclear layer; OPL, outer plexiform layer; ONL, outer nuclear layer; PR, photoreceptors; RPE, retinal pigment epithelium).

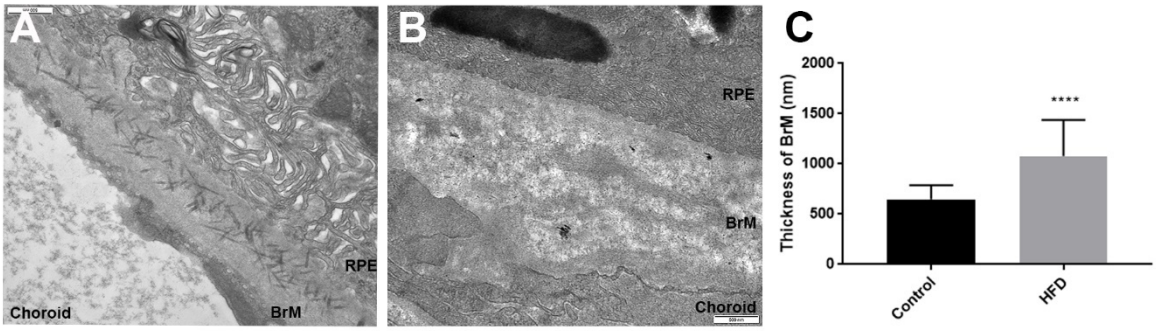

Figure 29: Images and analysis of BrM thickness in control and HFD mice.
[A] BrM in a 52-week old C57BL/6 mouse fed a normal chow diet. Note the penta-laminar structure that is characteristic of BrM. Scale bar representative of 500nm [B] Thickened BrM in an HFD mouse at 52 weeks. Note the thickening of BrM and the absence of several layers. Scale bar representative of 50nm. [C] The measurements of BrM (n=10 mice). Statistical significance was measured using an unpaired student's t-test, and **** represents p≤ 0.0001. Error bars show standard deviation.

4.3.2 Consumption of a high-fat diet causes structural changes to the layers of the outer retina

TEM image analysis also revealed some structural changes that begin to shed light onto why the consumption of an HFD has such a major impact on the function of the outer retina. In control group eyes, the photoreceptors remained in intimate contact with the RPE microvilli, and no areas of significant photoreceptor atrophy were observed [Fig. 30A]. However, in the images taken of the HFD eyes, there are multiple, large areas of photoreceptor atrophy observed [Fig. 30A vs 30B]. There are also vacuoles forming in the microvilli layer and between photoreceptors [Fig. 30E vs30F] and evidence of incompletely digested or internalised POS accumulation in the HFD retina [Fig 30C vs 30D]. These both appear to push the photoreceptors up and away from the RPE apical microvilli, disrupting their intimate contact.

As previously mentioned, the RPE monolayer has invaginated basal infolds and, in healthy aged eyes, the RPE monolayer retains these highly convoluted infolds that are characteristic of RPE cells [Fig. 31A]. However, in a HFD disease model, these infolds are found to be disrupted, with some areas of increased invaginations and others with a complete loss of infolds [Fig. 31B]. HFD eyes also show regions of drusen-like deposits, or basal laminar accumulations, building up between the RPE monolayer and BrM [Fig. 31C vs 31D]. Drusen is often used as a diagnostic hallmark of AMD and is highly correlated with disease progression. In addition, BrM in HFD eyes have areas of increased thickness, as well as some breakages in the pentalaminar structure [31C,E vs 31D,F] There also appears to be a decrease in the number of melanin granules in eyes from mice fed an HFD compared to control eyes [Fig. 31E vs 31F].

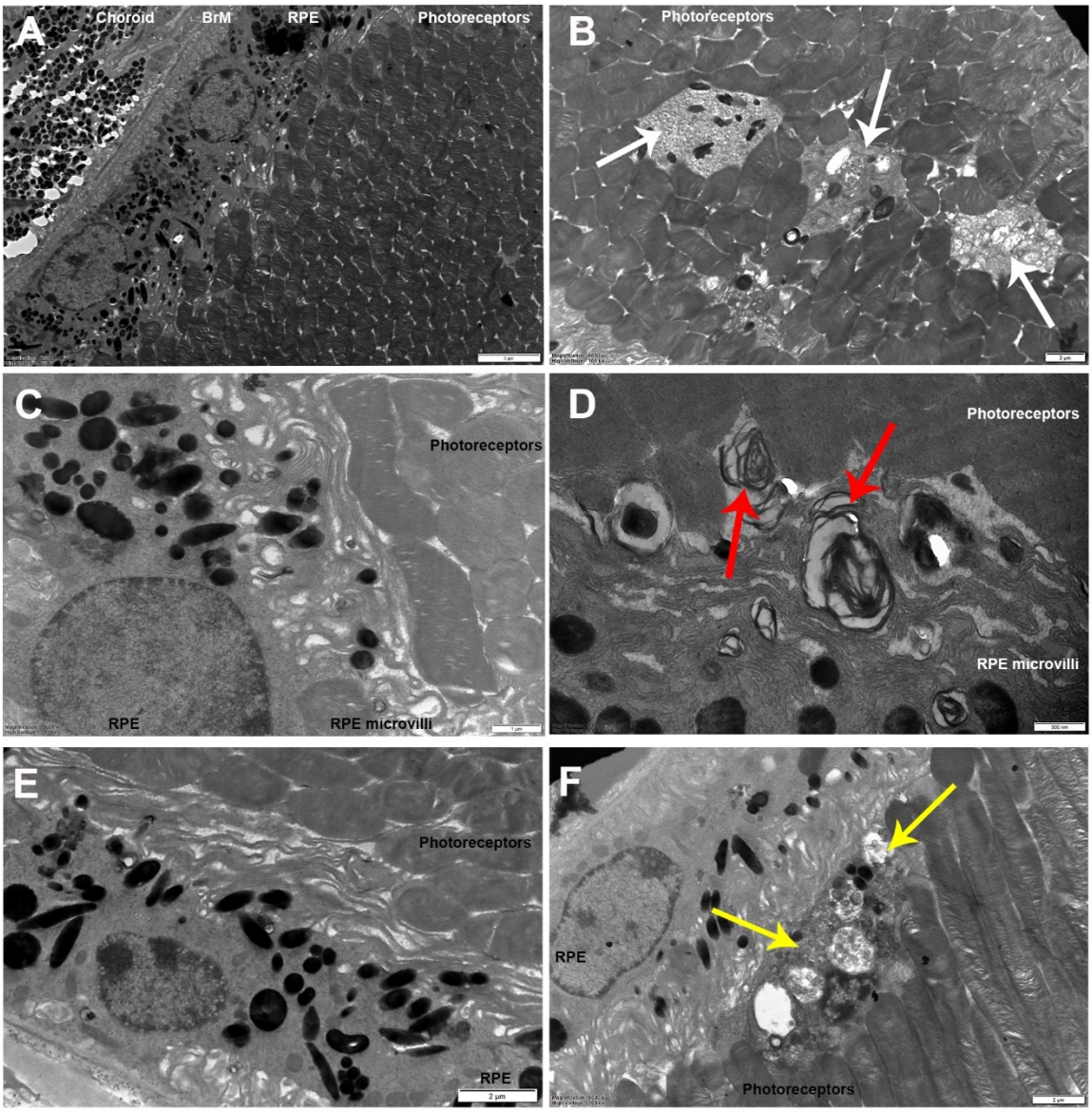

Figure 30: Structural changes to the photoreceptor layer and RPE caused by a high-fat diet. [A] The structure of control aged mouse eyes fed with a chow based diet. Scale bar shows 5µm [B] Mice fed HFD show areas of photoreceptor atrophy which were not present in the control group. In total 6 of 8 mice showed these areas of damage (white arrows). These are filled with lipid dense vesicles. Scale bar represents 2µm. [C] Structure of control aged eyes with no incompletely digested POS accumulation. [D] Incompletely internalised and digested POS accumulate at the interface of the RPE microvilli and photoreceptors in the HFD groups, as shown by the red arrows. Scale bar represents 500nm. [E] Control aged eyes with no vacuoles between the photoreceptor and microvilli interface, and all the microvilli remain in contact with photoreceptors. [F] Vacuoles also form at the photoreceptor and microvilli interface. These appear to push the photoreceptors up and out of contact with the underlying RPE microvilli, interrupting their intimate contact (yellow arrows). Scale bar shows 2µm.

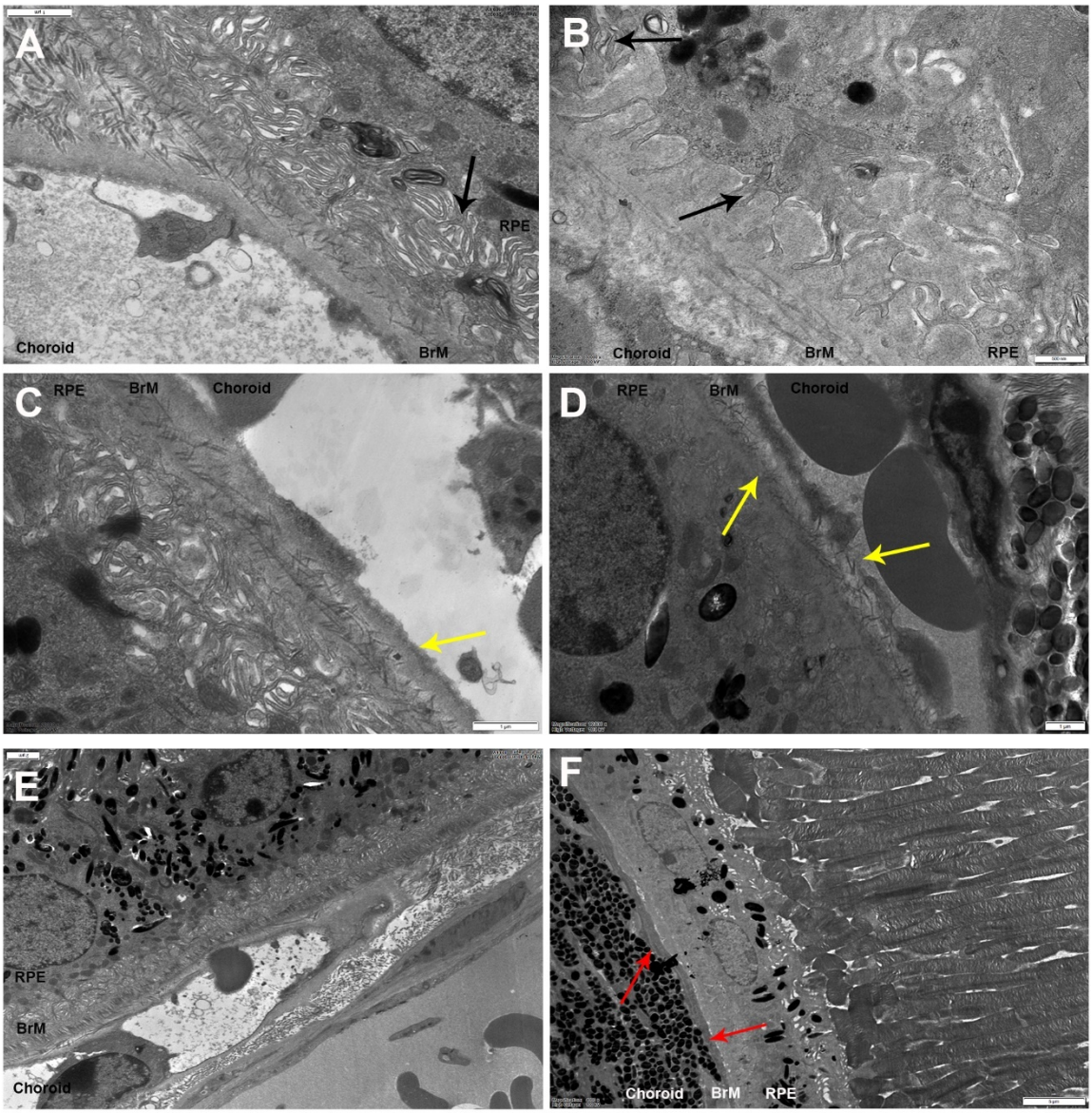

Figure 31: Structural changes to the basal infolds and BrM following diet-induced oxidative stress.
[A] Basal infolds and BrM from the control group. Note the highly convoluted and invaginated basal infolds (black arrow) and the pentalaminar structure of BrM. Scale bar represents 1µm. [B] Disrupted and misfolded Basal infolds that appear in the HFD eyes. Note areas of extra convolutions (white arrow) and areas lacking invaginations (black arrow). Scale bar represents 500nm. [C] Control eyes have a clearly defined pentalaminar structure of BrM (yellow arrow) with no deposition below the RPE. [D] Basal deposits accumulating in HFD retinas (red arrows), appearing to resemble basal laminar deposits, which are equivalent to drusen and are highly associated with disease progression. Scale bar represents 5µm. [E] Control eyes show consistent thickness BrM across the retina. [F] Areas of BrM breakages in the HFD group (yellow arrows). These are often found following areas of BrM thickening. Scale bar shows 1µm.

4.3.3 Increased neutral lipid deposits are found in the outer retina of eyes from mice fed a high-fat diet.

After observing the numerous structural changes following consumption of a high-fat diet, we wanted to study the effects of diet-induced changes to several key proteins known to be affected in retinopathies including AMD. Oil Red O is a neutral lipid stain that is used for detecting hydrophobic lipid droplets containing esterified cholesterol, triglycerides and free fatty acids[357]. It is known that such lipids accumulate in murine livers following ingestion of a HFD[282]. We wanted to study whether a HFD also caused lipid accumulation in the retina. Images taken by a dotSlide scanner revealed increased Oil Red O droplets in HFD eyes [Fig. 32B] compared to healthy aged eyes [Fig. 32A]. This number was quantified in the photoreceptors [Fig. 32C] where healthy aged controls had an average of 6.667 ± 3.226 lipid droplets per image whilst 51 ± 7.659 lipid droplets were counted for high-fat diet eyes ($p = 0.0016$).

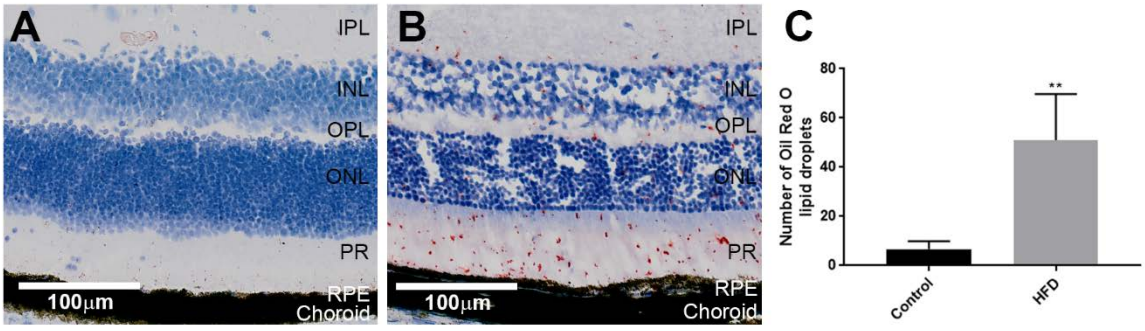

Figure 32: DotSlide images of Oil Red O stained neutral lipids in control and HFD retinas. [A] DotSlide image of Oil Red O stain in control eyes. A few droplets are seen, but these are small and scarce. [B] Oil Red O droplets are seen in a much higher density in HFD eyes, particularly in the photoreceptor layer. For both images, the scale bar represents 100μm. [C] Quantification of neutral lipid droplets in both the control and HFD images revealed a significant increase in the HFD group compared to the controls (n= 6). Statistical analysis was performed using an unpaired student's t-test. ** denotes statistical significance where p≤ 0.01. Error bars show standard deviation. (IPL, inner plexiform layer; INL, inner nuclear layer; OPL, outer plexiform layer; ONL, outer nuclear layer; PR, photoreceptors; RPE, retinal pigment epithelium).

4.3.4 Clusterin is increased in the RPE following diet-induced oxidative stress.

Since we observed the accumulation of basal linear deposits, we wanted to assess the effect of consumption of a HFD on components of drusen. Once such protein is clusterin, or Apolipoprotein J, which is one of the major proteins that accumulate in drusen[341,358]. Clusterin is involved in the clearance of cellular debris and apoptosis. Clusterin has been implicated in many degenerative diseases, including in AD where it has been shown to contribute to early-stage pathogenesis[359]. In order to study the effect of diet-induced oxidative stress on clusterin levels we stained sections using an antibody specific to clusterin. Analysis of stain intensity revealed that there was a significant increase in the amount of clusterin in the RPE layer following consumption of a HFD (48.05au (arbitrary units) ± 3.568) as compared to a normal chow based diet (27.87au ± 8.74) ($p= 0.0226$) [Fig. 33A-E]. An increase was also seen in the photoreceptor layer of HFD eyes (156.8au ± 26.52 compared to 107.6 ± 50.82) however this difference was not significant ($p= 0.0622$) [Fig. 33F].

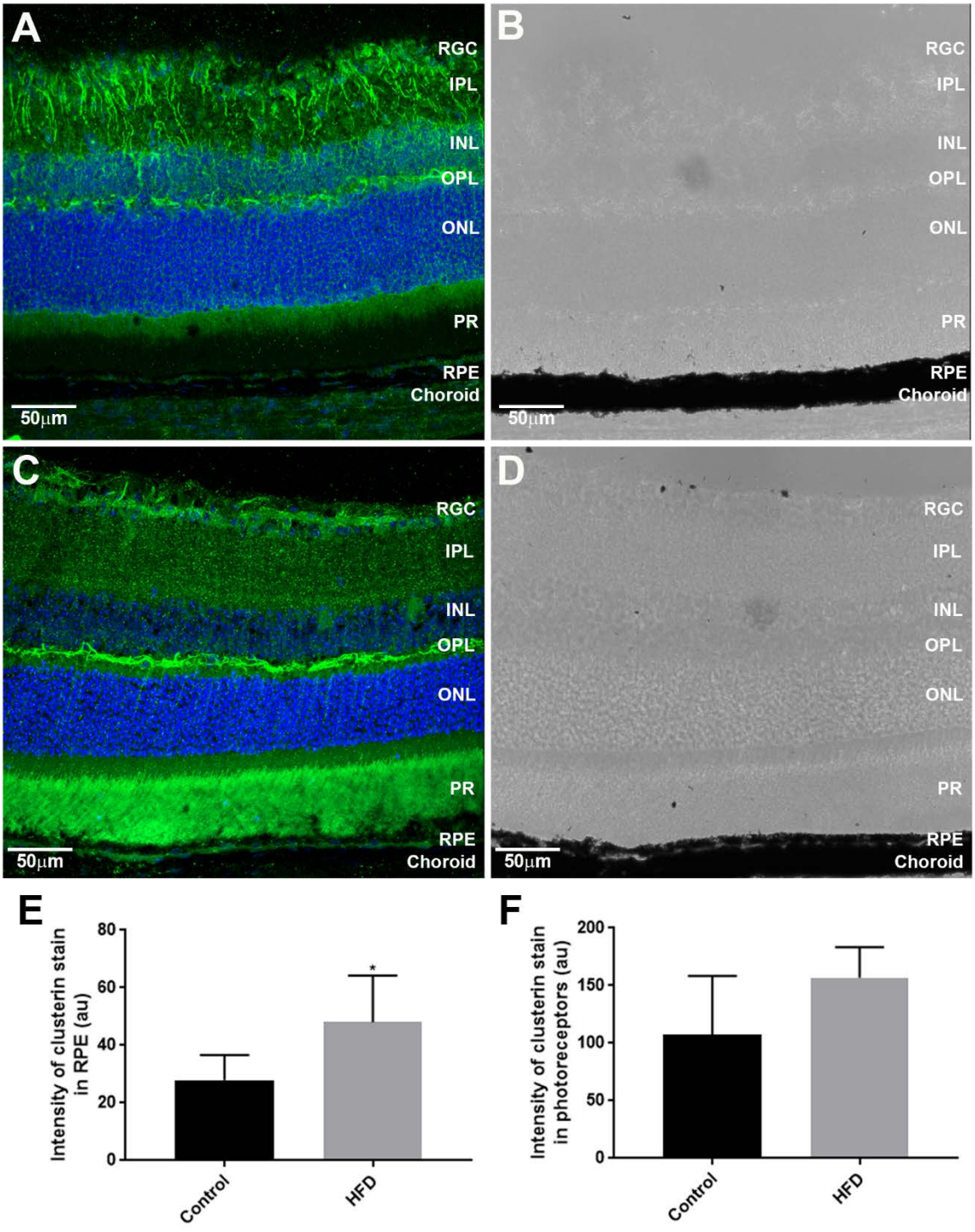

Figure 33: Confocal images of clusterin stain in the retina of control and HFD eyes.
[A] Clusterin (green) and DAPI (blue) stain in a control group eye [B] Bright field image showing the retinal layers which were used to trace the area of interest to complete the analysis. [C] Clusterin and DAPI stains merged in the HFD group. [D] Bright field image showing the retinal layers of an HFD image. Scale bars represent 50μm. [E] Analysis of average clusterin intensity across the RPE monolayer in control and HFD groups (n=6). Statistical analysis was performed using an unpaired student's t-test. * represents significance where $p \leq 0.05$. Error bars show standard deviation. [F] Analysis of average clusterin intensity across the photoreceptor layer in control and HFD groups. Statistical significance was measured using an unpaired student's t-test however no significance was found. Error bars show standard deviation. (RGC, retinal ganglion cells; IPL, inner plexiform layer; INL, inner nuclear layer; OPL, outer plexiform layer; ONL, outer nuclear layer; PR, photoreceptors; RPE, retinal pigment epithelium).

4.3.5 Collagen IV is decreased in the RPE following consumption of a high-fat diet.

Collagen IV is a major constituent of basement membranes and is essential in maintaining their stability. Collagen IV is synthesised by the RPE and is present in both BrM and the choroid. Here, we used Collagen IV as a marker of endothelial cell changes, which often become proliferative in nvAMD[360]. In eyes from mice fed a HFD, we observed only a very slight decrease in the RPE-BrM layers (3.82au ± 2.657 in control eyes vs 2.738au ± 2.832; p= 0.5105) [Fig. 34A, C, E] and a significant decrease in the photoreceptor layer from a staining intensity of 17.23au ± 7.301 in health aged eyes to just 8.252au ± 0.8772 in eyes fed an HFD (p= 0.0136) [Fig. 34A, C, F]. In healthy aged eyes, collagen IV appears to accumulate on the basal surface of photoreceptors [Fig. 34A], where they interact with the RPE. This staining appears to be completely absent in the HFD eyes [Fig. 34C].

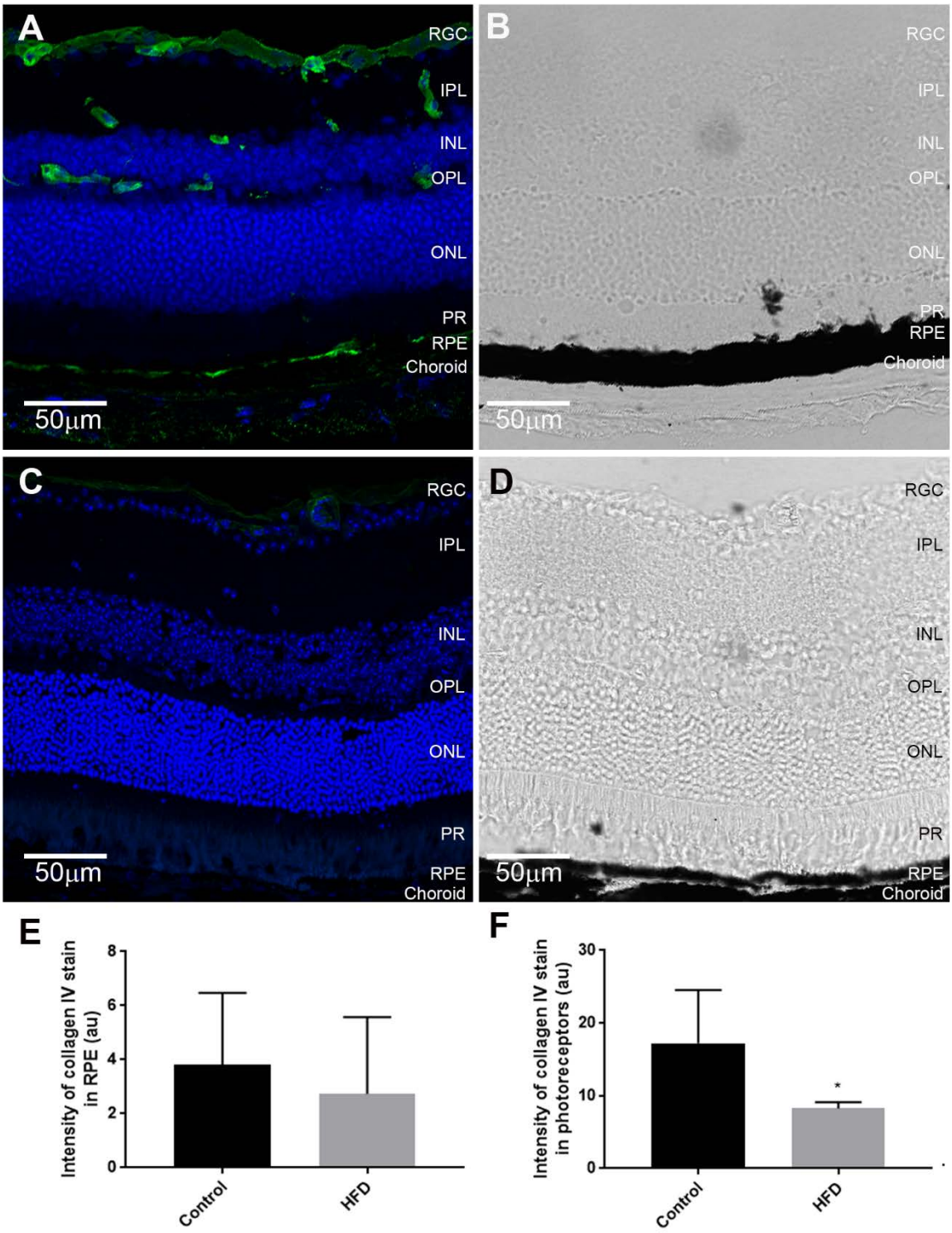

Figure 34: Confocal images of collagen IV stain in the retina of control and HFD eyes.
[A] Collagen IV (green) and DAPI (blue) stain in a control eye. [B] Bright field image showing the retinal layers which were used to trace the area of interest to complete the analysis.[C] Collagen IV and DAPI stains merged in the HFD group (n=6). [D] Bright field image showing the retinal layers of an HFD image. Scale bars represent 50µm. [E] Analysis of average collagen intensity across the RPE monolayer in control and HFD groups. Statistical analysis was performed using an unpaired student's t-test, but no significance was found. Error bars show standard deviation. [F] Analysis of average collagen IV intensity across the photoreceptor layer in control and HFD groups (n=6 images from 3 eyes per group). Statistical significance was measured using an unpaired Student's t-test, * represents significance where $p \leq 0.05$. Error bars show standard deviation. (RGC, retinal ganglion cells; IPL, inner plexiform layer; INL, inner nuclear layer; OPL, outer plexiform layer; ONL, outer nuclear layer; PR, photoreceptors; RPE, retinal pigment epithelium).

4.3.6 Diet-induced oxidative stress causes an increase in TIMP3 levels in the RPE

Tissue inhibitor of metalloproteinase-3, or TIMP3, is involved in the degradation of the extracellular matrix and mediates extracellular barrier function[361]. TIMP3 is a normal component of BrM and is also present in drusen and other deposits associated with retinal diseases, including those found in Sorsby's Fundus Dystrophy. Confocal images of TIMP3 staining shows decreased levels throughout the retina [Fig. 35A, C] which was quantified in the photoreceptor layer with control eyes showing a staining intensity of 70.43au ± 14.29 compared to an intensity if 59.84au ± 9.43 in experimental eyes. However, this was not significant ($p= 0.1609$) [Fig. 35F]. In the RPE layer, though, levels of TIMP3 were significantly increased from 9.58au ± 2.228 in control eyes to 20.98au ± 3.31 in HFD eyes ($p\leq0.0001$) [Fig. 35E].

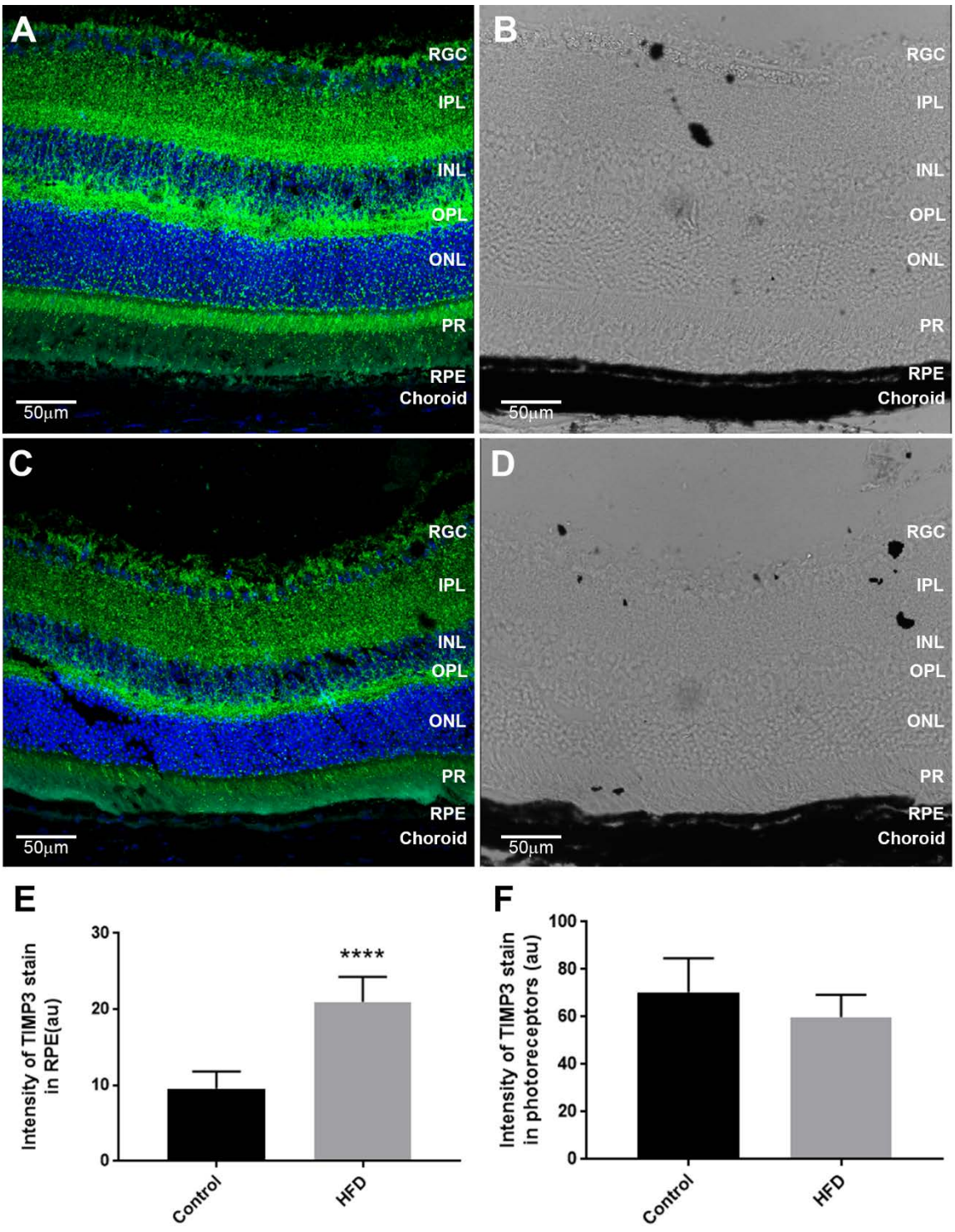

Figure 35: Confocal images of TIMP3 stain in the retina of control and HFD eyes.
[A] TIMP3 (green) and DAPI (blue) stain in a control group eye [B] the bright field image showing the retinal layers which were used to trace the area of interest to complete the analysis.[C] TIMP3 and DAPI stains merged in the HFD group. [D] Bright field image showing the retinal layers of an HFD image. Scale bars represent 50µm. [E] Analysis of average TIMP3 intensity across the RPE monolayer in control and HFD groups (n=6). Statistical analysis was performed using an unpaired student's t-test. **** represents statistical significance where p≤ 0.0001. Error bars show standard deviation. F] Analysis of average TIMP3 intensity across the photoreceptor layer in control and HFD groups. Statistical significance was measured using an unpaired student's t-test, but no significance was found. Error bars show standard deviation. (RGC, retinal ganglion cells; IPL, inner plexiform layer; INL, inner nuclear layer; OPL, outer plexiform layer; ONL, outer nuclear layer; PR, photoreceptors; RPE, retinal pigment epithelium).

4.4 Discussion

In this study, the consequences of diet-induced oxidative stress on the structure, and protein expression of the outer retina was examined in HFD mouse eyes. TEM analysis was performed instead of SBSEM as used in chapter 3, due to the considerable time constraints involved with fully imaging and reconstructing each RPE cell. Instead, 8 eyes from each group were embedded and imaged using conventional TEM to obtain a broader picture of the structural defects associated with consumption of a HFD. A further 3 eyes were retained for histological studies, including H&E imaging and immunofluorescence microscopy. In this study, we revealed considerable structural damage to all layers of the outer retina. However, it is important to note that in this chapter the effects of high-fat diet have been examined, a process by with oxidative stress can increase in cells and tissues. It would therefore be useful to demonstrate that cells were exhibiting oxidative stress markers in response to HFD by performing a lipid peroxidation assay.

4.4.1 Changes to the photoreceptor layer following a high-fat diet

In the photoreceptors, there were large areas of atrophy with the appearance of lipid dense vesicles. This is often reported as a secondary effect of AMD following RPE dysfunction[362]. However, some studies have shown the implicit role of photoreceptors in early disease stages[17,363]. There was also evidence of vacuoles appearing between the microvilli of the RPE cells and the photoreceptors, thus disrupting their intimate contact which is usually characteristic of these tissues. This loss of contact would disrupt POS phagocytosis[174]. This is further evident due to the appearance of undigested or internalised POS accumulating above the RPE monolayer, which is not apparent in control eyes. The RPE monolayer and the photoreceptors were both thickened in HFD eyes. In a study on patients with AMD compared to elderly control subjects without eye diseases, the photoreceptor layer thickness was measured using OCT imaging. This revealed that regions neighbouring drusen had increased photoreceptor thickness[364] whereas photoreceptors overlying drusen were reduced[365]. One hypothesis for the widespread thickening of photoreceptors, except directly above drusen, is the possibility that oxidative stress drives hypertrophy of cells, such as Müller cell processes, that extend into the photoreceptor layer causing a thickening before overt atrophy ensues[366-368]. One of the earliest disease features that appear before visual degeneration is Müller cell hypertrophy, which is particularly marked in retinas with high levels of oxidative stress[369].

Ingestion of a HFD has been shown to cause lipid accumulation in multiple organs, including livers and kidneys. Since the retina is notable for its high lipid content[370], we wanted to study how lipid deposition in the eye is affected by a HFD. The neutral lipid stain oil red O was

used, which showed a significant increase in the number of lipids deposited in the photoreceptor layer. The disruption or abnormal metabolic processes associated with lipid metabolism plays a key role in AMD pathogenesis. Oxidative stress from smoking or intake of an unhealthy western style diet causes lipid dysregulation via the activation of the complement pathway, which leads to lipid accumulation and secretion[124]. It was therefore unsurprising to observe the increase in lipid deposits within the outer retina of HFD eyes.

4.4.2 Changes to the RPE and BrM following consumption of a high-fat diet

In our study, the RPE monolayer was significantly thickened in mice fed a HFD. An increase in the density of residual bodies, the accumulation of lipofuscin and basal deposits, as well as the formation of drusen and basal laminar deposits, all lead to a thickening of the RPE in age and disease when measured by OCT[371-373]. This has been associated with disease progression to AMD[49,374]. Contradictorily, it has been shown that the RPE overlying drusen are reduced in thickness[364,375,376], which is correlated with a localised loss of vision[138,377]. However, more recently, it has been reported that the RPE is thicker at drusen sites prior to its deposition, than compared to adjacent drusen-free areas. This thickening of the RPE directly correlated with the drusen severity (based on the height of drusen deposits)[50]. Therefore, this indicates that RPE thickening may predict sites of drusen formation, suggesting that the mice fed an HFD would be more susceptible to drusen and basal laminar deposits than mice fed a normal chow diet.

Following consumption of a HFD, the basal infolds appeared to be misfolded and disorganised when compared to normal chow fed mouse eyes. Disrupted basal infolding have previously been reported as a sign of oxidative damage and is therefore an unsurprising finding. Basal infolds are essential in increasing the surface area of the RPE to allow for efficient passing of nutrients from the underlying choroid. A loss of basal infolds would disrupt this process leading to RPE and photoreceptor damage. Areas in which there are misfolded basal infolds also create potential ‘space’ for the basal linear and basal laminar deposits to accumulate[309]. These deposits, which we observed in HFD mouse eyes, are similar to drusen which is a clinical hallmark of AMD, suggesting that HFD eyes have undergone some disease-related changes. Clusterin is a key component of drusen, and we have shown that its levels were significantly increased in the RPE/BrM of HFD eyes. This is unsurprising given the finding of the basal laminar deposits, and instead adds further weight to the argument that such deposits in mouse eyes share key components with drusen in humans. Another component of drusen is TIMP3 which was also found to be elevated in the RPE/BrM of HFD eyes. TIMP3 is expressed by the RPE and secreted into BrM where it binds to components of the ECM. Since it is not easily possible to delineate between the RPE and BrM at the light microscopy level, it is possible that this increase is

largely due to TIMP3 changes in the BrM rather than the RPE *per se*. TIMP3 regulates the rate of BrM turnover and limits choroidal neovascularisation[361]. Sorsby's fundus dystrophy (SFD) is an early onset inherited form of macular degeneration and is characterised by thickening of BrM and submacular neovascularisation[361], both of which are also features of AMD. Mutations in the TIMP3 gene have been found in families with SFD[378]. Studies of donor eyes from patient's with SFD show extensive accumulation of TIMP3 in the thickened BrM[379]. This led to similar studies being performed in AMD donor eyes[380,381]. Studies of this kind revealed significantly elevated levels of TIMP3 in the macula of AMD eyes compared to healthy control eyes. TIMP3 accumulation within the ECM could prevent normal matrix remodelling, resulting in the increased thickening of BrM associated with AMD[382].

We have revealed a vast thickening of BrM in eyes of the HFD mice. A diffuse thickening of BrM is often reported with age, and has been shown to increase by 135% in 10 decades of life[383,384]. The thickening appears to occur predominantly in the Inner Collagenous Layer (ICL) followed by the Outer Collagenous Layer (OCL)[139]. Disease risk is associated with the increase in the thickness of BrM[383,384]. In general, the thickening is thought to be associated with increased deposition and cross-linking of less soluble collagen fibres, and increased deposition of oxidised waste products of RPE metabolism[139]. The thickening of BrM eventually leads to functional changes, including changes to elasticity and permeability, affecting its ability to act as an effective barrier[14]. Thickening also causes altered nutrition to, and consequent abnormal function of the RPE and photoreceptors[385-387]. The pentalaminar structure that is characteristic of BrM also appeared to be disrupted in diseased eyes. Although this has not been previously reported *per se*, the Elastin Layer (EL) thickens at a slower rate than other layers of BrM, and in fact, decreases relative to overall thickening of BrM[388,389]. A similar pattern is seen in collagen III and IV[390] which regulate the attachment of BrM to RPE[391]. Long-lived proteins such as collagen IV are modified in vivo by non-enzymatic reactions as well as by free radical reactions that yield AGEs. Such reactions also cause the formation of lipid-derived reactive carbonyl species known as lipoperoxidation end products (ALEs), such as 4-hyproxyhexenal and linoleate hydroperoxide[390]. Accumulation of AGEs and ALEs are characteristic of a high-fat, western style diet[392,393]. It is therefore unsurprising that the levels of Collagen IV decreased in HFD eyes. However, this was mainly localised to the photoreceptors, which is surprising due to the functional role of collagen IV in the BrM. There are only a few reports discussing the presence of collagen IV in the basement membrane of photoreceptors.

Oxidative stress is known to reduce melanosomes, as we have shown in the RPE of our HFD eyes. The pigment melanin is believed to play a protective role against oxidative stress and damage by acting as a cellular antioxidant. There is an age and disease-related decline in the number of these pigment granules in RPE cells[394]. One possible explanation for this

is the chemical degradation of melanin due to oxidative stress and blue-light damage[52,146]. This highlights a negative loop during which oxidative stress impairs the cell, making it more susceptible to further oxidative damage from environmental factors such as a HFD.

4.5 Conclusions

To summarise, the study of HFD mouse eyes have revealed important structural defects associated with AMD. There is a marked increase in photoreceptor atrophy in HFD eyes. A thickening of all layers of the retina was also observed, which has previously been reported to predict the severity of drusen accumulation in AMD. We also presented data that showed the accumulation of drusen related proteins including TIMP3 and clusterin in HFD eyes. The accumulation of such proteins would further thicken and impede BrM, decreasing its elasticity and potentially altering the nutrition of the overlying RPE and photoreceptors. We have argued how HFD associated oxidative stress can damage the RPE layer in such a way that this critical monolayer becomes more vulnerable to further oxidative damage. This may occur due to diminished melanin granules in RPE cells. Oxidative stress also causes lipid deposition which is known to be a key driver in AMD pathogenesis. These findings go some way towards revealing how the intake of high-fat foods lead to increased disease susceptibility.

.

Chapter 5 The effect of oxidative stress and impaired vesicle acidification on cargo trafficking and proteolytic clearance mechanisms in the RPE.

5.1 Introduction

After visualising the effects of a HFD and oxidative stress on the ultrastructure of RPE cells and other tissues of the outer retina, we next assessed potential functional effects on RPE physiology. A key function of the RPE monolayer is the daily ingestion and degradation of spent POS in the phagosome and autophagy-lysosomal pathways, and its dysfunction is linked with retinopathies including AMD, Stargardt disease and choroideremia[171,395-400], as described in sections 1.9.5 to 1.9.7.4. Photoreceptors shed ~10% of their distal tips on a daily basis which is engulfed by the underlying RPE[401]. Studies in non-human primates reveal that a single RPE cell in the parafovea is exposed to 2000 discs daily, whilst exposure in the perifovea and periphery approximate to 3500 disks and 4000 discs respectively, with each RPE processing up to a billion photoreceptor disks over a 70 year period[167]. However, these statistics are based on each RPE catering for 45 photoreceptors, and our results in chapter 3 show that actual figures might be more than double this. This makes the RPE one of the most proteolytically stressed tissues in the body. POS cargos have been shown to bind to RPE within 1-2 hours, be engulfed between 4-6 hours and digested within a period of 16-20 hours following initial POS challenge[274,402]. Impaired acidification of lysosomes is thought to result in an inefficient fusion between lysosomes and autophagosomes which leads to dysregulated autophagy[403,404]. There is ample evidence to support disrupted acidification of RPE lysosomes in retinopathies[405-407]. Whether by an increase in acidity or by alkalinisation of lysosomes, fusion with autophagosomes is disrupted, since this is dependent on specific intra-lysosomal conditions[166]. Unsurprisingly, analysis of donor tissues from AMD patients shows evidence of dysregulated autophagy[335,408]. Upon disruption of the lysosomes, partially degraded POS accumulate as lipofuscin and its photo-oxidative derivatives in the senescent RPE; a key feature of diseases including AMD and retinopathies such as Stargardt disease[395-397]. These lipid/protein aggregates accumulate within the RPE lysosomes and related organelles, with approximately 20% of the cell cytosol consisting of such material by the 8th decade of life[409]. These events which lead to oxidative stress may be exacerbated under a chronic hypoxic environment, with elevated metabolic activity and cumulative ultraviolet/blue light-induced damage in the retina[85,86,410]. Risk of

disease is exacerbated by the accumulation of lipid/cholesterol aggregates within late endosomes and lysosomes of RPE cells[85,402]. Autophagy represents a strand of the lysosome-directed degradation pathway and a process by which damaged organelles, misfolded proteins and pathogens are eliminated by the cell[273,411,412]. This pathway is also harnessed to recycle cellular constituents in times of starvation. A HFD is known to negatively influence this pathway by decreasing lysosomal acidity and reducing fusion between autophagosomes and lysosomes[403,404].

In this chapter, we sought to investigate the consequences of high oxidative stress and dysregulated intracellular trafficking on POS internalisation and processing which contributes to several forms of retinopathy. Studying the physiology and pathophysiology of AMD in the RPE *in vivo* has proven difficult. This is largely because access to the posterior eye is limited and imaging techniques that can accurately resolve the RPE in its native state are scarce. As a result, some of the earliest structural and pathophysiological changes in tissues of the outer retina associated with early disease still remains to be fully understood. Use of *ex vivo* cell-based models and *in vitro* cultures present an opportunity to investigate alterations in RPE function and fill this knowledge gap. These cultures can also be used to study cellular pathways activated in response to various factors implicated in disease. One such *ex vivo*/*in vitro* model utilises RPE cells grown in a transwell system, which uses a porous support to mimic the native BrM, enabling RPE to form a mature, confluent cuboidal monolayer, comparable to native tissues[413] [Fig. 36]. This has previously been unachievable using standard cell culture plastic dishes. Several groups have optimised this technique using porcine RPE[414], human foetal RPE[128,413,415,416], human adult RPE[417], and the ARPE-19 human cell line[284,416]. In all cases, a desirable RPE phenotype has been achieved, which includes pigmentation, the formation of BRB components, apical and basal polarisation, and polarised secretion of molecules. This model can also recapitulate features of early AMD, including the formation of drusen[418]. Thus, this cell culture model represents a highly useful tool to study RPE pathophysiology associated with AMD phenotypes. Here, we used the widely utilised ARPE-19 cell line[283]. ARPE-19 cells have been extensively used in the literature and provide an invaluable tool for determining RPE physiology and function. The culture of ARPE-19 was recently improved by altering the cell culture media to facilitate pigmentation, which is characteristic of native RPE[284,416]. We have adopted this protocol, and hence our ARPE-19 cultures are also pigmented. We maintain cultures for long periods, typically 2-4 months prior to experimentation to allow for structural and functional specialisation of the RPE monolayers[419]. This highly manipulatable and versatile cell culture system will enable us to address how oxidative stress and impaired lysosomal processing affects the ability of the RPE to traffic POS cargos. Conditions of elevated oxidative stress were recapitulated in culture by using H_2O_2[286], whilst impaired lysosomal acidification was modelled using bafilomycin A1[420,421]. Bafilomycin is known to selectively inhibit vacuolar

type ATPase (vATPase) on the lysosomal membrane, increasing the lysosomal pH[422]. Concentrations used in this study have previously been shown to be non-toxic to ARPE-19 cells, with no off-target effects[285]. Similarly, a non-toxic dose of hydrogen peroxide has also been used[286,423]. Both Bafilomycin and H_2O_2 have frequently been used in ARPE-19 cells at similar concentrations in order to disrupt lysosomal processing/ autophagy[424] and increase ROS levels[425] respectively. H_2O_2 levels used in this study are similar to those reported in human vitreous[426].

Fixing ARPE-19 cells grown in a transwell system allows detailed studies of different intracellular organelles of interest. Staining for specific compartments using primary antibodies and a fluorescently probed secondary antibody combined with laser scanning confocal microscopy can be used to visualise organelles such as those of the phagosome, endosomes, lysosome, and autophagy pathways where we have carried out this study. In this form of microscopy, a laser light excites tissue which has been stained with fluorescent dyes specific for individual cell components (e.g. actin filaments stained with phalloidin and ZO1 staining of tight junctions). The tissue is then imaged at different focal planes using a pinhole detector to exclude any out of focus light. A stack of 2D sections can be acquired which enables a 3D representation of internal cellular structures. Growing cells in this manner allows for good image resolution without interference from thick plastic dishes.

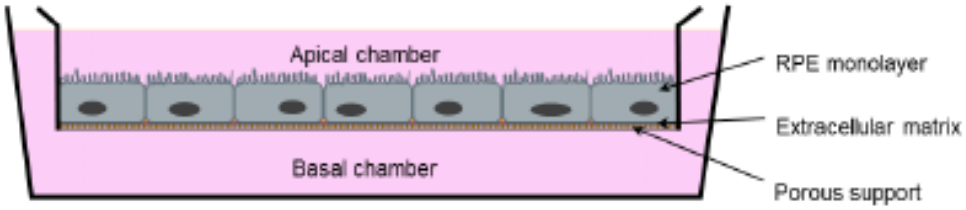

Figure 36: Schematic of ex-vivo cell culture model.
A diagram to represent RPE cells grown on a porous support in a transwell system. Together the RPE/porous support complex forms the blood-retinal barrier, mimicking the native RPE/BrM complex. RPE cells are seeded onto the porous support pre-treated with an appropriate extracellular matrix component, such as fibronectin. Cell cultures maintained for a minimum of two months differentiate into a confluent monolayer of cuboidal RPE cells which are comparable in morphology and function to native RPE cells. Image source: Ratnayaka JA, An ex-vivo platform for manipulation and study of Retinal Pigment Epithelial (RPE) cells in long-term culture. IOVS; 2015.

Hypothesis: Oxidative stress and impaired vesicle acidification will disrupt cargo trafficking and processing in RPE cells.

Aims:

1. Study the internalisation and trafficking of POS cargos through the endo-lysosomal pathway in healthy RPE cells.
2. Determine how oxidative stress and dysregulated intracellular trafficking affects POS trafficking in RPE cells.

5.2 Methods

ARPE-19 cells were seeded on pre-coated transwell membranes and maintained in culture (as described in chapters 2.1) for 2-4 months to ensure that desirable structural and functional specialisation of monolayers were achieved before experiments. POS from porcine eyes were isolated as described in chapter 2.2 and fed to cultures using a pulse-chase method. Cells were fixed in 4% PFA, stained using Rab5, Rab7, Lamp1, Lamp2 and LC3B as described in section 2.2. Cultures were imaged using a confocal laser scanning microscope (chapter 2.3) to determine the internalisation pathway and timeframe of POS cargo trafficking through the endo-lysosomal and autophagy pathways. Using pharmacological agents (H_2O_2 and Bafilomycin A1) prior to POS feeding, we recapitulated oxidative stress and impaired lysosomal acidification respectively. Immunofluorescence images were quantified in an unbiased manner using Volocity software (chapter 2.3.1). A full description of all methodological approaches used in this chapter is detailed in chapter 2.

Transwell membranes across every time point were also embedded in resin capsules to be sectioned and imaged by TEM. In this case, cultures were fixed with 3% glutaraldehyde, 4% formaldehyde in 0.1M PIPES buffer, and immersed in a series of solutions, as outlined in section 2.4.1. Following imaging, collected micrographs were blinded and analysed according to a three-scale approach where (1) is no degradation observed, (2) shows some level of POS breakdown, and (3) represents POS in discernibly late compartments including lysosomes and/or autophagy bodies. To do this, images were split into early (2-4 hours), intermediate (6-12hours) and finally late (24-48 hours) stages. The number of compartments present in each time point stage was quantified by counting ($n > 20$ compartments/ time point, from $n \geq 5$ images across 3 independent experiments). Images which included the apical edge were then imported in ImageJ. The scale was set using the microscope generated scale bar, and the distance of the POS- containing compartment from the apical edge of the cell was measured ($n \geq 10$ measurements/ degradation state, from $n > 3$ images from 3 independent experiments). Further details can be found in section 2.4.

5.3 Results

Initially we wanted to determine the exact pathway and timeframe of POS degradation in our cell culture system. To do this, 2-4 month old ARPE-19 monolayers were fed POS using a pulse chase method[287] in which cells were kept at a lower temperature immediately after POS feeding to allow for synchronisation of internalisation and trafficking. To test whether this lower temperature would disrupt the RPE monolayer, cultures were stained for the epithelial early integral tight junction protein ZO1 after the procedure. Transwells were therefore left either in the incubator at 37ºC as a control or incubated at 17ºC for 30 minutes, before evaluating their junctional integrity.

Our findings in Figure 37 shows that a decrease in temperature did not adversely affect the RPE monolayer; as ZO1 tight junctions remained intact and undisturbed. However, some nuclear ZO1 staining was also apparent, particularly in the culture following a reduced temperature. DAPI staining highlighted the relative positioning of cells in the monolayer which also appeared unaffected. Having confirmed that cooling RPE cells for the pulse assay did not adversely affect its integrity, we confidently proceeded with planned experiments.

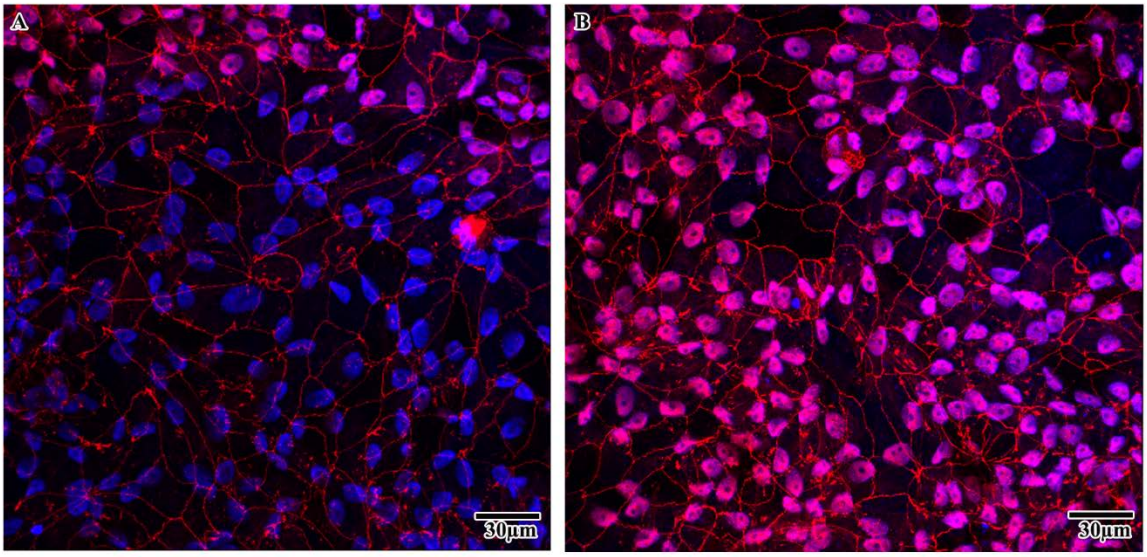

Figure 37: Confocal images of ZO1 and DAPI stains with and without incubation at 17ºC
[A] ZO1 and DAPI stain of cells not left at 17ºC and [B] ZO1 and DAPI stain of cells incubated at 17ºC for 30 minutes. ZO1 shows that tight junctions are unaffected by this lower temperature. Scale bars correspond to 30µm. ZO1= red, DAPI = blue.

5.3.1 Receptor mediated binding and pulse-chase methodology

It is known that POS bind to αvβ5 and MerTK receptors expressed on the apical surface of RPE cells in order for internalisation of these cargos to occur[168,169]. We wanted to assess whether the same was true for POS cargos fed to our RPE culture model. Co-labelling with antibodies showed that POS binding was mediated via MerTK and αvβ5 receptors [Fig. 38A]. Furthermore, all bound POS were associated with receptor complexes, although those that had not bound to any cargo (typically isolated receptors) were also visible. In order to assess whether the pulse-chase method of feeding POS was successful, transwells were fixed immediately after removal from 17°C. Figure 38B shows that POS were bound to the RPE monolayer at this time point, but with no evidence of internalisation. Thus, the pulse-chase methodology appeared to be successful for feeding POS and ensuring maximal synchronous internalisation of cargos.

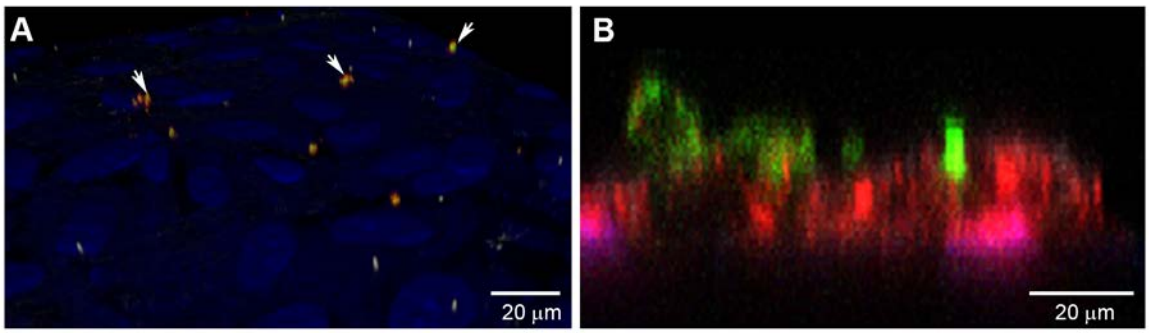

Figure 38: Representative confocal image of cultured RPE cells after POS feeding and rendered in 3D.
[A] Bound POS molecules (green) on the RPE cell surface which co-localise with receptor MerTK (red) and αvβ5 integrin (grey) indicated by arrows. A wash step ensures the removal of any unbound cargos so that only receptor-bound POS is subsequently internalised. Some αvβ5 receptors that have not bound to POS are visible in grey. Scale bar corresponds to 20μm. [B] Cells fixed immediately after removal from 17°C show POS bound to the monolayer with no evidence of internalisation. Red = Rab 5, Green = POS, Nuclei = Blue.

5.3.2 The trafficking of POS cargos in healthy RPE cells

Fluorescently tagged POS molecules were used to track degradation through the endosomal/ lysosomal and autophagic pathways [Fig. 39A]. Four hours after commencing the feeding assay, POS was observed localised to Rab5 labelled early compartments [Fig. 39B]. Six hours after the assay had begun, cargos were found in Rab7 positive vesicles, corresponding to late phagosomes/endosomes [Fig. 39C]. Although representative images are shown for each compartment, during initial stages of trafficking cargos are likely to move through a mixture of Rab5 and Rab7 vesicles at any given time point. 24 hours after the initiation of the feeding assay, most cargos were localised to LAMP1-positive early

lysosomes [Fig. 39D] or LAMP2-labelled mature lysosomes [Fig. 39E]. POS in lysosomes had a predominantly perinuclear arrangement, consistent with findings that cargos intended for degradation are trafficked to compartments deeper in the cell and in proximity to the nucleus[166]. By 48 hours, most POS molecules had co-localised to LC3b labelled compartments, which also had a largely perinuclear distribution [Fig. 39F].

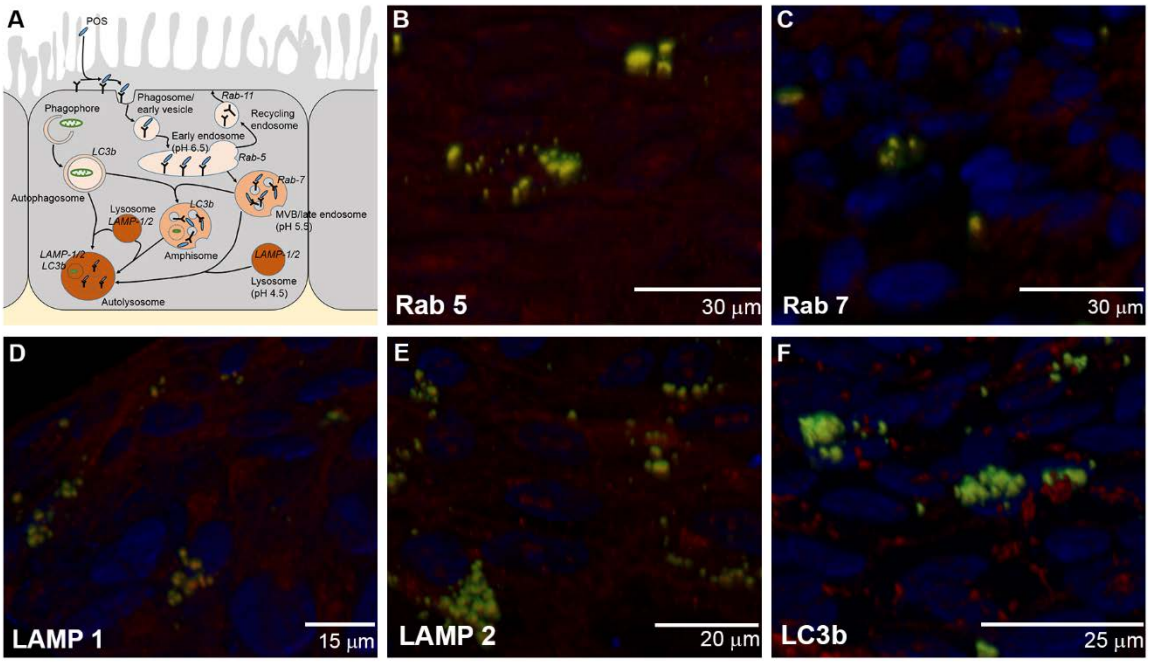

Figure 39: Tracking cargo trafficking in healthy RPE
A] Schematic diagram illustrating the pathway through which photoreceptor outer segment (POS) cargos bind to receptors on RPE cells and are processed via the phagosome/endosome and lysosomal-autophagy pathways. Early compartments are labelled with Rab5 whilst late compartments are stained with Rab7. Lysosomes are indicated by LAMP1 and LAMP2 markers, whilst autophagy bodies are labelled with LC3b. Isolated POS are fluorescently labelled and can be used to study the effects of disease conditions on cargo trafficking in cultured RPE. [B] Representative confocal image taken at 4 hours after starting the feeding assay showing early trafficking of POS cargos (green) in Rab5 (red) compartments. Co-localised vesicles appear yellow. Scale bar corresponds to 30μm. [C] Representative confocal image was taken 6 hours after the feeding assay showing trafficking of POS cargo (green) in Rab7 (red) vesicles. Co-localised compartments appear yellow. Scale bar corresponds to 30μm. Representative confocal images collected at 24 hours after the feeding assay showed POS cargo (green) predominantly co-localised to [D] LAMP1 (red) and [E] LAMP2 (red) labelled compartments. Lysosomes containing POS molecules appear yellow. Note the perinuclear arrangement of lysosomes trafficking POS cargos. Scale bars in panels D and E correspond to 15μm and 20μm respectively. [F] Representative confocal image taken at 48 hours after feeding assay showed that by this stage most POS cargos (green) had been trafficked to LC3b positive (red) compartments. Co-localisation is indicated in yellow. Scale bar corresponds to 25μm. Nuclei in panels B-F are labelled with DAPI and appear blue. Panels B-F show three-dimensional RPE monolayers with intracellular cargo which were captured using a confocal microscope and reconstructed using Amira software.

In order to quantify trafficking of POS cargos through distinct intracellular vesicles, we used an automated statistical method described by Costes *et al.* [289]. This approach allows for an unbiased assessment of the number of POS molecules co-localising with each intracellular marker. The extent of POS in each compartment is shown as a decimal where a value of 1.0 represents 100% co-localisation. During the first 2-4 hours after POS feeding, a large proportion of cargos were observed co-localised with Rab5 early compartments. Subsequently, the extent of co-localisation dropped significantly, and from 12 hours onwards only a small proportion of cargos remained in Rab5 vesicles [Fig.40A]. Assessment of trafficking using the Rab7 marker indicated that the greatest extent of co-localisation was at 6 hours. POS levels within Rab7 compartments then dropped significantly. Surprisingly, a substantial proportion of cargos remained within Rab7 vesicles as late as 24 hours after POS feeding (~50% co-localisation) [Fig. 40B and Appendix C, Table 1]. Although Rab7 labelling can distinguish between late phagosomes/endosomes vs lysosomes, there is evidence to suggest that some lysosomes are also positive for Rab7[166,427,428]. In order to assess whether this occurs in the RPE, living cells were transfected with a genetic lysosomal marker and subsequently stained with a Rab7 specific antibody. Although a majority of late vesicles were labelled for either Rab7 or lysosomes, on occasion we observed the co-localisation of these two respective markers to a single compartment [Fig. 40F]. Quantification of POS trafficked to LAMP1 positive early lysosomes showed a gradual increase, with the greatest extent of co-localisation 24 hours after the pulse-chase [Fig. 40C]. In contrast, only low levels of POS co-localised with LAMP2 compartments during initial stages (up to 6 hours) after which ~90% of cargos had trafficked to mature lysosomes by 24 hours [Fig 40D and Appendix C, Table 1]. Levels of POS in LC3b labelled membranes were also initially observed to be at low levels but increased significantly from 12 hours onwards to reach a maximal extent of co-localisation of ~90% by 48 hours [Fig 40E and Appendix C, Table 1].

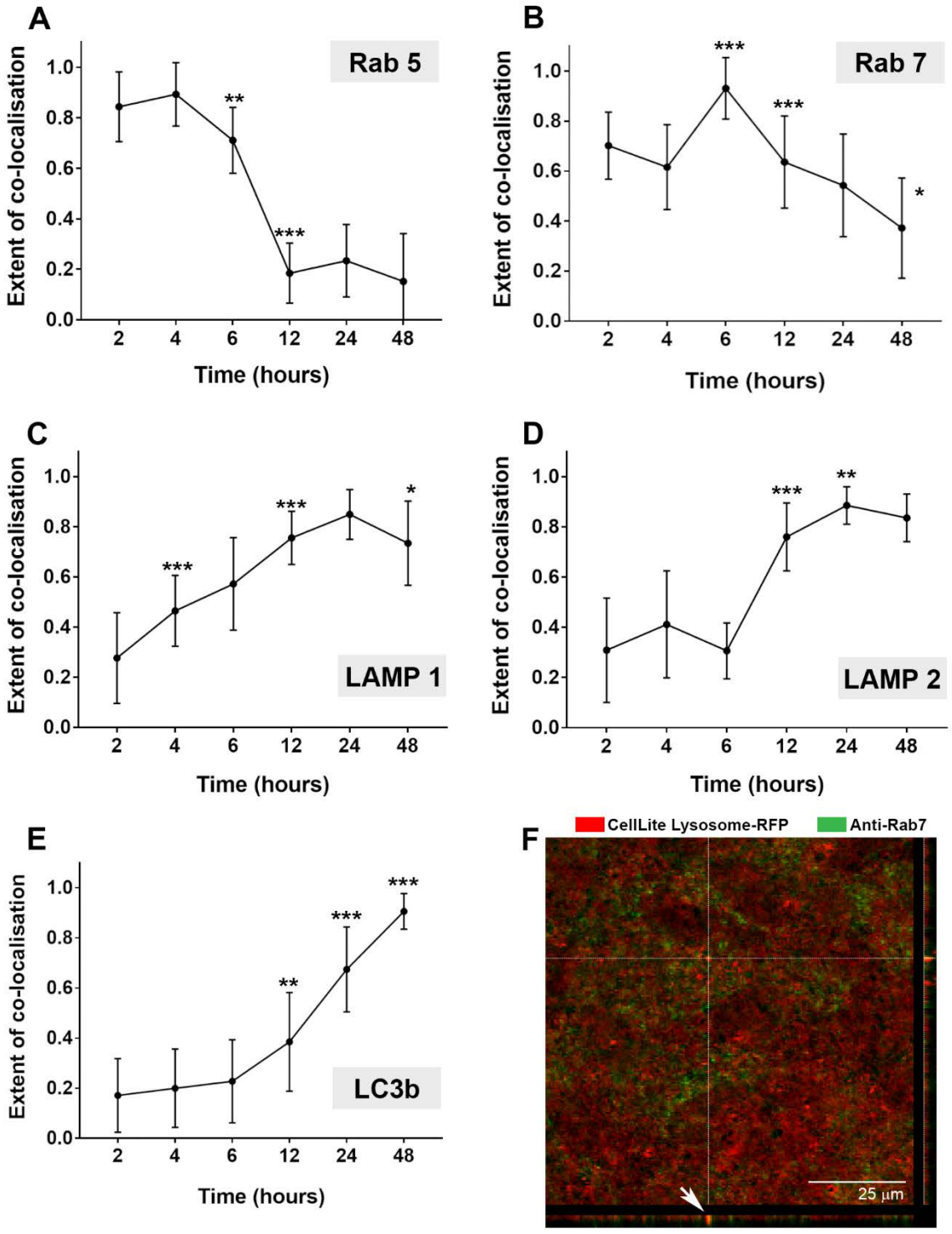

Figure 40: The trafficking of POS cargos in healthy RPE cells.
The trafficking of internalised POS molecules in phagosomes/endosomes and in the lysosomal-autophagy pathway was studied using an automated, unbiased quantification method described by Costes *et al*. The extent of co-localisation in distinct compartments at each time point is shown as mean values (1.0 represents 100% co-localisation). [A] The trafficking of POS cargos in Rab5 labelled vesicles peaked between 2-6 hours following the feeding assay with the maximum extent of co-localisation at 4 hours after which values returned to significantly lower levels by 12 hours. [B] Although some cargos had entered Rab7 labelled vesicles as early as 2-4 hours, the highest extent of co-localisation was recorded at 6 hours after which they declined in successive time points. [C] From early on, a small proportion of POS cargos appeared to be trafficked to LAMP1 positive lysosomes, which increased gradually with each time point. However, peak levels of trafficking was observed between 12-48 hours with the maximal extent of co-localisation recorded at 24 hours. [D]

In contrast, the small proportion of POS cargos trafficked to LAMP2 positive vesicles at early time points (2-6 hours) remained constant. However, the extent of co-localisation increased significantly thereafter at 12 hours and followed a similar pattern observed in early (LAMP1) lysosomes. [E] A small number of POS cargos appeared to co-localise with LC3b labelled membranes between 2-6 hours after the feeding assay. The extent of trafficking to LC3b positive compartments increased significantly thereafter at 12 hours and continued to increase at each time point to record the maximal extent of co-localisation at 48 hours. Error bars represent the standard deviation. Data from four independent experiments with a minimum of n=20 cells/time point. Statistical comparisons using ANOVA where a significance of $p \leq 0.05$ (*), $p \leq 0.01$ (**) and $p \leq 0.001$ (***) was recorded with the previous time point in the assay. [F] Lysosomes of living RPE were labelled with CellLite Lysosomes-RFP (red) after which cultures were probed with an antibody against Rab7 (green). This revealed distinct populations of lysosomes and Rab7 labelled late compartments. However, we detected lysosomes that were also positive for Rab7 (co-localisation indicated by yellow). Representative image from a single plane of a confocal z-stack where crossbar indicate co-localisation (orthogonal view shows co-labelling marked by a white arrow). Scale bar corresponds to 25µm.

5.3.3 Assessment of POS trafficking by transmission electron microscopy

Next, we assessed the passage of POS through different intracellular compartments by TEM. The trafficking of cargos at each time point was captured in a series of micrographs. Compartments were identified by a blinded assessor, which revealed that most POS were localised to early compartments at 2 hours. Internalised POS cargos remained largely intact within these vesicles with little evidence of significant degradation [Fig. 41A]. Between 6 and 12 hours, however, most cargos were observed in late compartments with evidence of some POS breakdown [Fig. 41B, C]. By 24 hours, cargos almost exclusively appeared in late compartments/lysosomes containing a mixture of POS and associated electron-dense material showing further signs of degradation [Fig. 41D, E]. The appearance of double membrane structures at the 24 hour time point indicated the formation of autophagosomes associated with terminal stages of the proteolytic pathway [Fig. 41E]. In order to quantify how POS cargos are degraded over time, electron micrographs taken at early (2-4 hours), intermediate (6-12 hours) and late (24-48 hours) time points were assessed for the extent of cargo breakdown [Fig. 42]. Assessment of POS proteolysis was based on (1) no evidence of degradation, (2) some level of breakdown or (3) POS in discernibly late compartments including lysosomes and/or autophagy bodies. Between early and late time points, the number of compartments with no POS degradation decreased ($p \leq 0.0001$), whilst vesicles with some POS breakdown increased ($p \leq 0.03$). Between intermediate and late time points, the number of vesicles with some level of POS degradation decreased ($p \leq 0.005$) whilst POS in late compartments increased ($p \leq 0.004$) [Fig. 41]. Hence, the extent of POS proteolysis at the ultrastructural level correlated with reported timelines of cargo breakdown by confocal-immunofluorescence studies.

TEM images were also assessed to determine how POS cargos are broken down within intracellular compartments based on their distance from the apical RPE surface. Quantification was again based on counting POS positive vesicles with (1) no degradation, (2) some evidence of degradation or (3) late compartments consisting of lysosomes and/or autophagy bodies. No sign of degradation was observed in proximity to the apical RPE surface [Fig. 43A]. However, significant levels of some cargo breakdown was evident as POS were trafficked further into the cell ($p \leq 0.0001$) [Fig. 43C]. More POS appeared in late compartments located basolaterally and in proximity to the nucleus, although these were not significantly different in number ($p \leq 0.085$) [Fig. 43B, C].

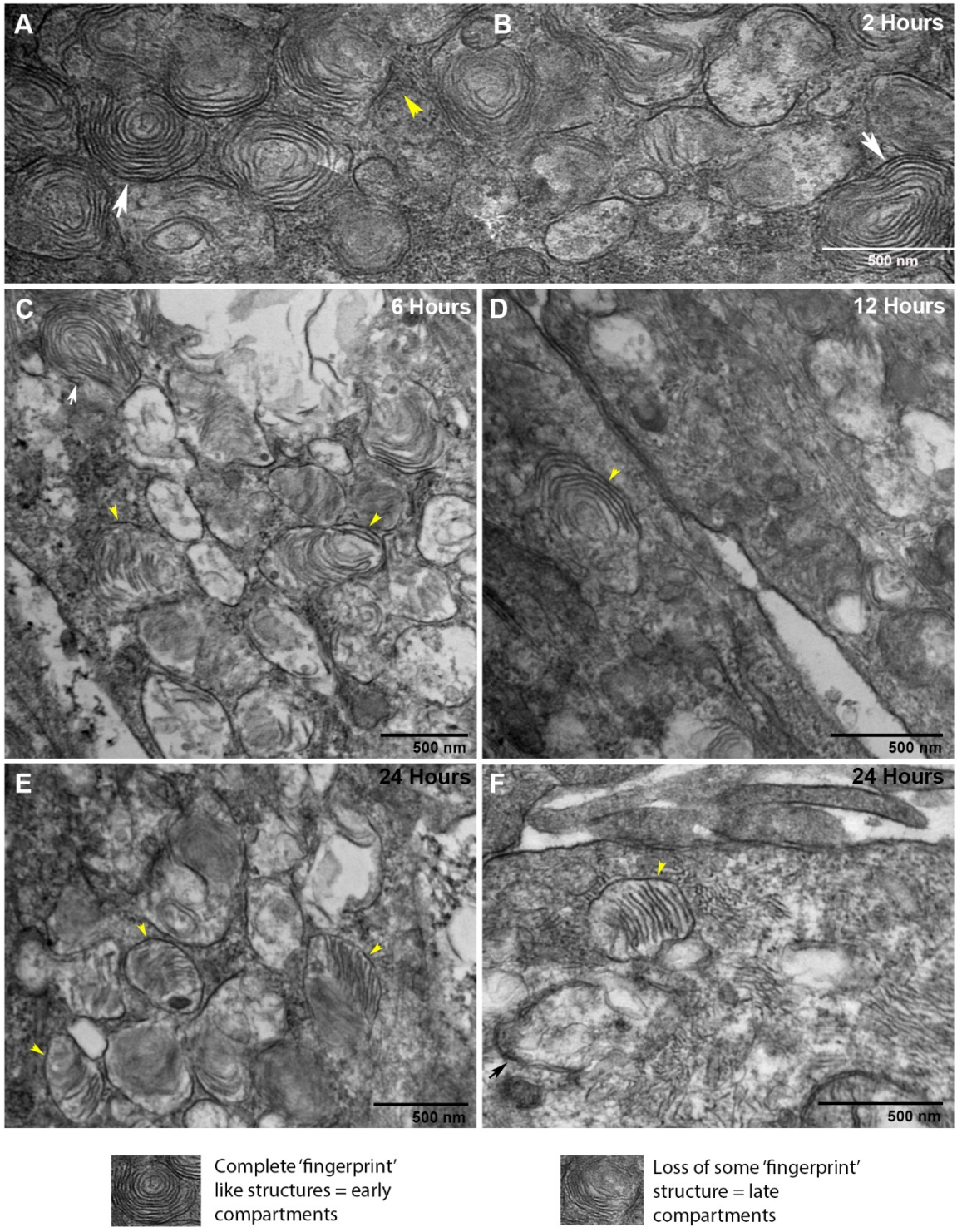

Figure 41: Vesicle dynamics in the trafficking pathway and evidence of POS trafficking at an ultrastructural resolution in RPE cells.
[A] Evidence for cargo trafficking was assessed by transmission electron microscopy in healthy RPE after POS feeding. Representative electron micrograph at the 2 hour time point following feeding showing numerous POS-containing early compartments (white arrows). There is evidence that some cargos had been trafficked to late compartments (yellow arrowhead) at this early stage. [B] Electron micrograph was taken 6 hours after the feeding assay shows that most cargos had already been trafficked to late compartments (yellow arrowheads), although there was still some evidence of POS in early vesicles (white arrow). [C] Representative micrograph from 12 hours following the feeding assay showing POS cargos in late compartments (yellow arrowhead). There were no obvious indication of any cargos in early compartments by this stage. [D-E] 24 hours after the feeding assay

cargos were observed localised to late compartments/lysosomes containing a mixture of partially degraded POS and electron dense material (yellow arrowheads). We found no evidence of any early compartments with POS at this late time point. [E] The presence of double membrane phagophores (black arrow) at the 24 hour time point indicate likely trafficking to autophagosomes. Scale bars in panels correspond to 500nm.

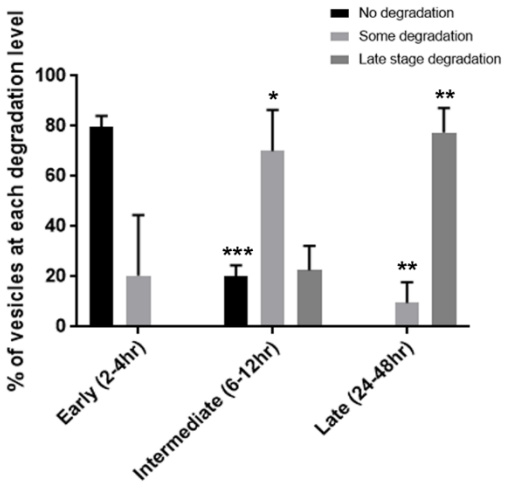

Figure 42: POS degradation in healthy RPE as a function of time.
Electron micrographs were taken at early (2-4 hours), intermediate (6-12 hours) and late (24-48 hours) time points. Images were assessed for the extent of cargo breakdown within compartments based on (1) no evidence of degradation, (2) some level of breakdown and (3) POS in discernibly late compartments, including lysosomes and/or autophagy bodies. The extent of POS proteolysis at the ultrastructural level correlated with reported timelines of cargo breakdown by confocal-immunofluorescence studies. Error bars represent the standard deviation. Data from 3 independent experiments with n=20 compartments/ time point. Statistical comparison using a one-way ANOVA followed by Turkey's multiple comparison tests. * denotes $p \leq 0.05$, ** indicates $p \leq 0.01$, whilst *** shows $p \leq 0.001$.

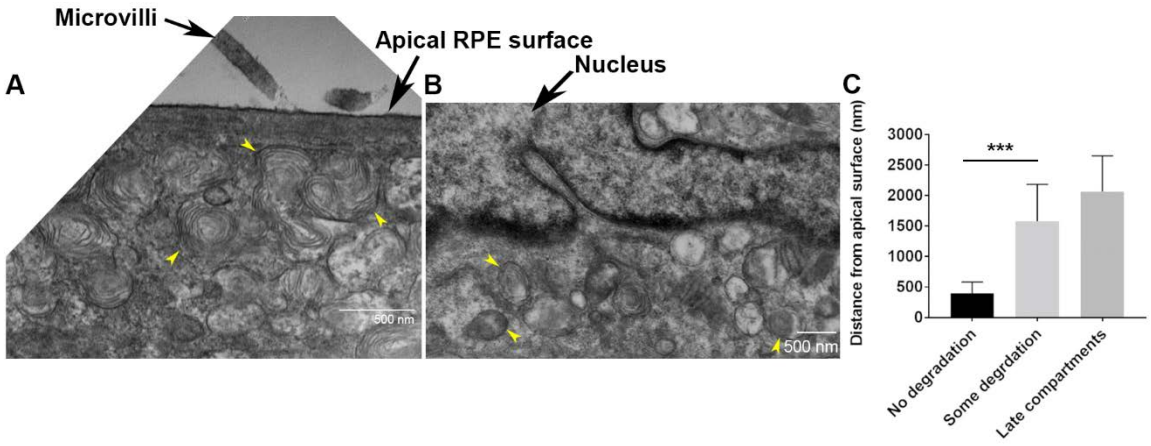

Figure 43: Analysis of the location of vesicles during degradation of POS along the apical-basal axis.
[A] Representative electron micrograph showing vesicles with largely undigested POS cargos in proximity to the apical RPE surface, likely to be early compartments (arrowheads). [B] Representative image showing vesicles containing partially degraded POS alongside electron-dense material (arrowheads), some of which morphologically resemble lysosomes. [C] Vesicles with no discernible POS degradation remained close to the apical surface, whereas vesicles containing some degradation, and later compartments with high levels of degradation were found further along the apical-basal axis, in the perinuclear region. Statistical analysis was performed using a one-way ANOVA followed by Turkeys multiple comparisons test. *** denotes the significance of $p \leq 0.001$. Scale bars correspond to 500nm.

5.3.4 Oxidative stress causes the rapid and premature trafficking of POS to late compartments

We studied the potential effects of high oxidative stress on POS trafficking by exposing cultured RPE to 100µM H_2O_2. We observed a marked decrease of cargos in Rab5 early compartments in cells treated with H_2O_2 compared to untreated control cultures (on average only 38% of cargos were trafficked in Rab5 vesicles throughout the experiment under conditions of oxidative stress compared to 50% in healthy cells). However, the extent of co-localisation in Rab5 vesicles increased at 24 and 48 hours in H_2O_2 treated cells compared to controls [Fig. 44A]. A similar pattern of low-level POS co-localisation was observed in Rab7 compartments compared to untreated cultures (on average only 35% of cargos were trafficked in Rab7 vesicles throughout the experiment under conditions of oxidative stress vs 63% in heathy controls) [Fig. 44B and Appendix C, Table 1]. By contrast, approximately 80% of POS had co-localised to LAMP1 compartments after just 2 hours in RPE exposed to high levels of oxidative stress (compared to only 28% in untreated cultures at the same time point). Moreover, the extent of co-localisation in early lysosomes remained consistently high thereafter with a maximal value of 96% recorded 24 hours after POS pulse [Fig. 44C]. We also observed high levels of POS co-localisation in LAMP2 positive compartments (89% compared to only 31% in controls at the 2 hour time point). Elevated levels of POS continued to localise to these mature lysosomes at subsequent time points to reach a maximal value of 94% by 48 hours after POS feeding [Fig.44D and Appendix C, Table 1]. Under conditions of elevated oxidative stress, cargos also localised prematurely to LC3b labelled compartments compared to untreated cultures (66% compared to only 17% in controls at the 2 hour time point). High levels of cargos remained associated with LC3b labelled membranes thereafter, and increased significantly at each subsequent time point, to reach a maximal value of ~90% at 48hours, at which cargos in LC3b compartments in control cultures had also reached similar levels [Fig.44E and Appendix C, Table 1].

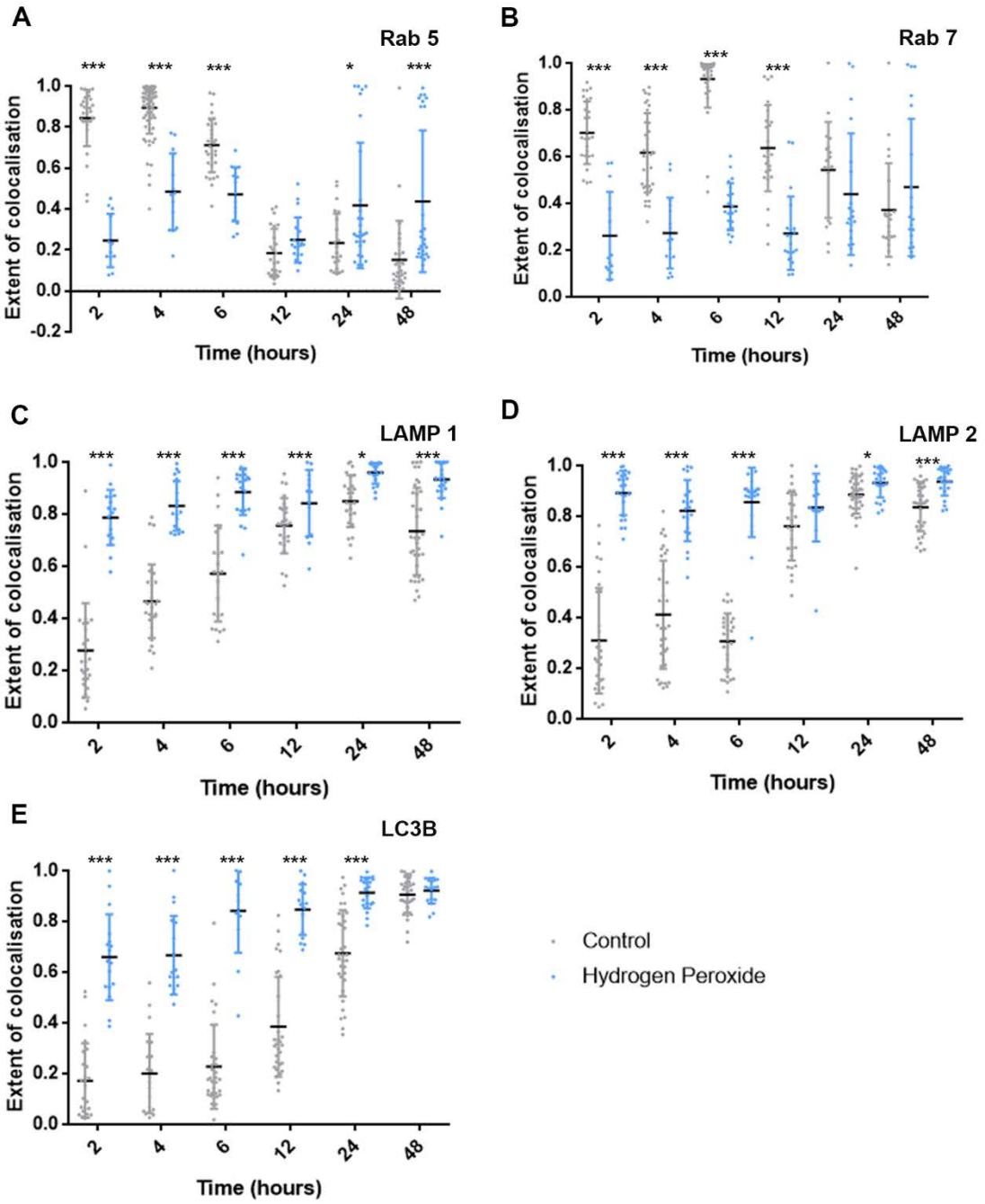

Figure 44: High levels of oxidative stress in RPE cells causes premature trafficking of POS cargos to late compartments.
The extent of co-localisation between internalised POS cargos and components of the proteolytic pathway was evaluated using an automated, unbiased quantification method described by Costes *et al*. Data shown as mean values (1.0 represents 100% co-localisation). [A] The co-localisation of POS cargos to Rab5 labelled vesicles in cells treated with 100µM H_2O_2 show a significant reduction during early time points (2-6 hours) compared to controls. This low level of Rab5 co-localisation remained constant throughout the experiment, although this meant that a proportion of cargos remained in these early compartments even at late time points. [B] Trafficking of cargos to Rab7 vesicles show a similar pattern where only a small proportion localised within these late compartments throughout the time course compared to controls. [C] Treatment with100µM H_2O_2 however significantly increased the proportion of POS cargos that were co-localised to LAMP1 and [D] LAMP2 lysosomes compared to controls. [E] A substantial proportion of POS cargos also co-localised with LC3b labelled vesicles at early time points, which continued to increase further at each time point compared to untreated control cultures. Error bars represent the standard deviation. Data from three independent experiments with a minimum of n=15 cells/time point. Statistical comparisons using a two-tailed

unpaired Student's t-test comparing differences between conditions for each time point. * denotes a significance of $p \leq 0.05$ whilst *** indicated a significance $p \leq 0.001$.

5.3.5 Dysregulated intracellular trafficking leads to POS being sequestered in early compartments

Impairment of intracellular trafficking was induced by exposing cells to bafilomycin A1, which disrupts acidification of intracellular compartments thus hindering fusion events along the phagosome/endosomal and autophagy pathways. Cultured RPE were treated with 10nM bafilomycin after which the extent of POS trafficking in each compartment was quantified as before. Cargos were initially observed to localise with Rab5 labelled vesicles at equivalent levels recorded in untreated cultures. However, in bafilomycin treated cells, cargos continued to be associated with Rab5 vesicles at subsequent time points long after they had been trafficked to downstream compartments in untreated/healthy RPE. We recorded a maximal extent (95%) of POS co-localised with these early compartments at 24 hours in bafilomycin treated cells compared to only 23% in control RPE at the same time point [Fig. 45A and Appendix C, Table 1]. A similar pattern was observed in Rab7 labelled vesicles, where on average 87% of cargos had been trafficked throughout the experiment in bafilomycin treated cells compared to only 63% in healthy RPE. Cargos continued to be sequestered in Rab7 compartments at late time points with the greatest extent of co-localisation recorded at 48 hours (93%) compared to only 37% in control cells at the same time point [Fig. 45B and Appendix C, Table 1]. Assessment of LAMP1 labelled compartments revealed diminished levels of POS compared to healthy RPE. When vesicle maturation was disrupted, on average only 39% of cargos were trafficked to early lysosomes throughout the experiment compared to 61% in healthy RPE. This discrepancy was particularly evident 12 hours after initial POS feeding when most cargos had been trafficked to lysosomes under normal circumstances [Fig. 45C]. In cultures treated with bafilomycin, a similar pattern was observed in LAMP2 labelled compartments which contained only low levels of POS compared to untreated cells. This was evident 12 hours after the POS pulse chase had commenced when healthy RPE had trafficked a large proportion of cargos to mature lysosomes. Consequently, on average only 29% of cargos co-localised to LAMP1 vesicles throughout the experiment compared to 58% in untreated/control cells [Fig. 45D and Appendix C, Table 1]. Quantification of POS in LC3b labelled compartments, however, revealed higher levels of co-localisation to autophagosomes from early time points in cells treated with bafilomycin compared to healthy RPE. Association with LC3b labelled membranes remained significantly high at subsequent time points compared to untreated cells. However, 48 hours after the POS pulse had commenced, the extent of cargos in LC3b compartments was similar in both treated and control cultures [Fig. 45E].

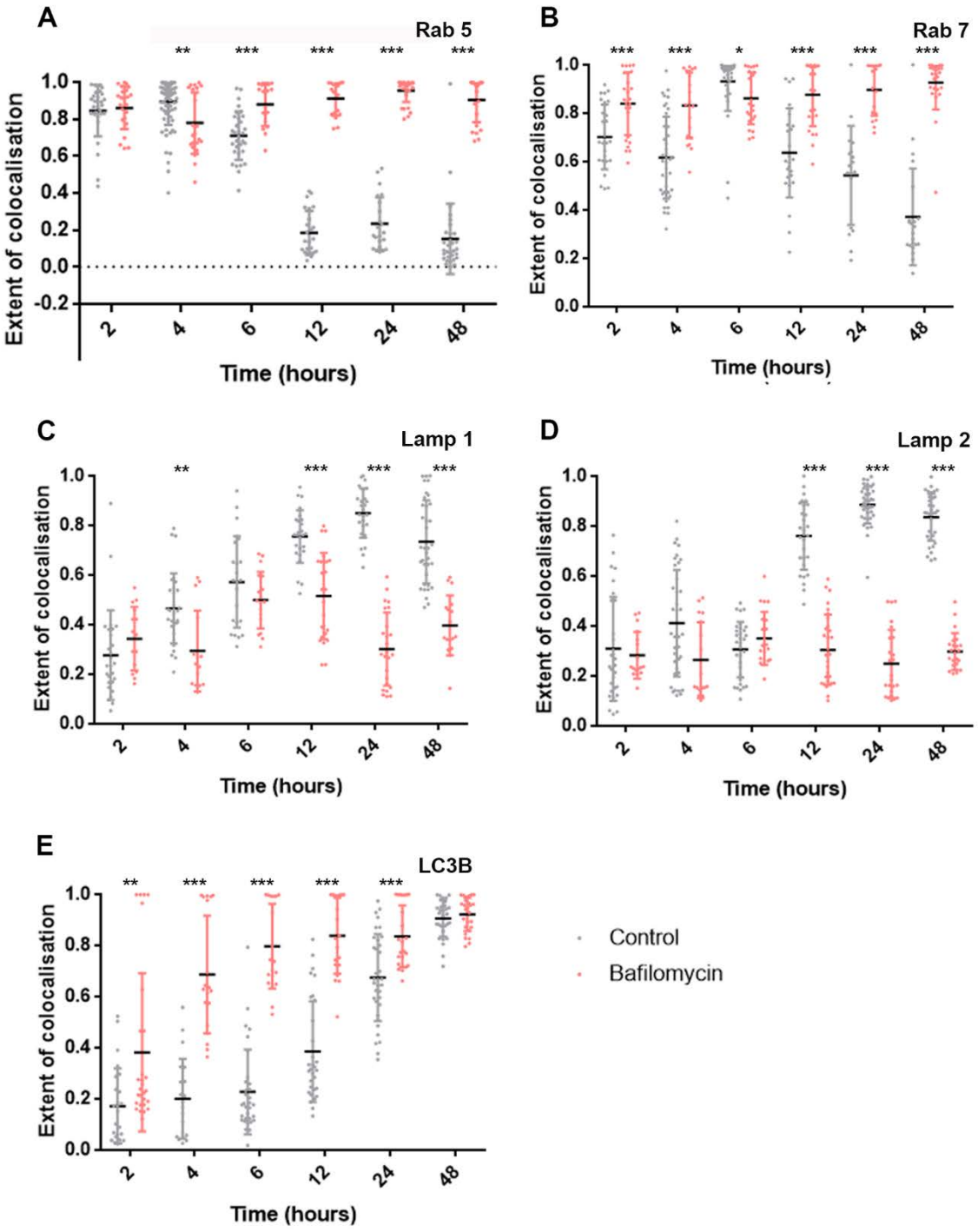

Figure 45: Dysregulated intracellular trafficking in the RPE leads to POS cargos being sequestered in early vesicles whilst a proportion of cargos are prematurely trafficked to LC3b positive compartments.
The extent of co-localisation between POS and intracellular compartments was evaluated using an automated, unbiased quantification method described by Costes *et al.* and shown as mean values (1.0 represents 100% co-localisation). [A] Exposure of cultured RPE cells to 10nM bafilomycin results in a large proportion of POS cargos being retained in Rab5 and [B] Rab7 labelled vesicles compared to untreated controls. [C] POS cargos remain sequestered in early compartments and fail to be trafficked to lysosomes. Consequently, only a small proportion of cargos co-localise with LAMP1 and [D] LAMP2 lysosomes compared to controls. This effect appeared exaggerated in LAMP2 compartments, which remain at a constantly low level throughout all time points. [E] A significant proportion of POS cargos appear to co-localise with LC3b labelled compartments at early time points (4-12 hours) compared to untreated cells. The level of co-localisation with this autophagy marker increased thereafter at each time point until they had reached a similar level to healthy RPE by 48

hours after the feeding assay. Error bars represent the standard deviation. Data from three independent experiments with a minimum of n=15 cells/time point. Statistical comparisons using a two-tailed unpaired Student's t-test comparing differences between conditions for each time point. * denotes a significance of $p \leq 0.05$, ** indicates $p \leq 0.01$ whilst *** shows a significance of $p \leq 0.001$.

5.3.6 Oxidative stress and dysregulated membrane trafficking affects the size of intracellular compartments in the POS trafficking pathway

As abnormalities in endosomes and lysosomes are reported to be indicators of incipient pathology, we studied whether elevated oxidative stress and impaired intracellular trafficking could alter the size of compartments in the POS trafficking pathway. Exposure to 100µM H_2O_2 resulted in significantly larger Rab5 labelled vesicles at 6 and 24 hours compared to untreated cells [Fig. 46A and Appendix C, Table 2]. In earlier studies, elevated levels of POS co-localised with Rab5 at the 24 and 48 hour time points [Fig. 44A]. We noticed that larger Rab5 vesicles correlated with this increase at 24 hours but there were no appreciable differences in vesicle size by 48 hours. Analysis of Rab7 vesicles showed that exposure to H_2O_2 had produced no appreciable effects on the size of these compartments bar at 48 hours when significantly larger Rab7 vesicles were recorded [Fig.46B]. However, measurement of LAMP1 positive lysosomes containing POS revealed a significant increase in size following exposure to H_2O_2. This was evident from the first time point at 2 hours when lysosomes were 1.02µm ± 0.15 compared to 0.84µm ± 0.14 in healthy RPE. At time points at which significant differences were recorded, the average size of these early lysosomes measured 1.28µm ± 0.21 compared to 0.92µm ± 0.16 in untreated cells [Fig. 46C, Appendix C, Table 2]. Swollen LAMP1 vesicles also correlated with abnormally high POS from an early time point [Fig. 44C]. We observed a similar pattern of enlarged LAMP2 vesicles in cells exposed to H_2O_2. However, this was evident only at later time points. Where significant differences were recorded, the average size of mature lysosomes measured 1.36µm ± 0.17 compared 1.03µm ± 0.12 in untreated cells with the most difference at 48 hours (1.39µm ± 0.18 compared to 0.76µm ± 0.15 in healthy RPE) [Fig. 46D and Appendix C, Table 2]. This may reflect the rapid/premature POS trafficking to LAMP2 compartments under conditions of oxidative stress [Fig.44D]. Quantification of LC3b labelled autophagosomes revealed significant increases in their size between 4 and 12 hours, and at 48 hours under oxidative stress with average sizes of 1.23µm ± 0.19 vs 0.84µm ± 0.12 in healthy RPE at these time points. The most significant size difference in autophagosomes between H_2O_2 and untreated cultures was recorded at 6 hours (1.15µm ± 0.14 vs 0.63µm ± 0.05, respectively) when most cargos had not yet reached these compartments under normal circumstances [Fig. 46E and Appendix C, Table 2]. The increased size of LC3b labelled vesicles broadly correlated with premature POS localisation to these compartments [Fig. 44E]. Where significant differences in the size of compartments were recorded between H_2O_2 exposed and control cultures, we also measured the size of

fluorescent vesicles without any POS cargo [Appendix C, Table 3]. We were surprised to find that the size of respective compartments in treated cultures remained unaffected and similar to the size of their counterparts in untreated/healthy RPE.

Next, we studied whether exposure to bafilomycin affected the size of intracellular compartments in the POS trafficking pathway. Measurement of POS containing Rab5 vesicles, at time points where significant differences in co-localisation were recorded, showed a marked increase in size after 6 hours with an average value of 0.83µm ± 0.13 compared to 0.48µm ± 0.1 in healthy RPE [Fig. 46F and Appendix C, Table 2]. We noticed that enlarged Rab5 vesicles correlated with time points at which elevated POS was also trafficked to these early compartments [Fig. 45A]. Analysis of Rab7 compartments showed initially smaller vesicles (at the 2 hour time point) becoming larger from 4 hours onwards compared to controls. At time points in which significant increases were recorded in co-localisation, the average size of enlarged Rab7 vesicles measured 1.04µm ± 0.15 compared to 0.62µm ± 0.13 in healthy RPE [Fig. 46F, 47A, B and Appendix C, Table 2]. Enlarged Rab7 vesicles broadly correlated with elevated POS trafficking to these compartments particularly at later time points [Fig. 45B]. In contrast to enlarged Rab5 and Rab7 compartments, we observed a marked reduction in the size of LAMP1 vesicles with POS. Although there were no differences at the initial 2 hour time point, the size of early lysosomes were substantially smaller between 4 and 24 hours. At time points where significant differences were recorded in co-localisation, their average size measured only 0.65µm ± 0.08 compared to 1.05µm ± 0.15 in healthy RPE. The abnormal size of small lysosomes had returned to normal levels by 48 hours [Fig. 46H and Appendix C, Table 2]. Fluctuations in the size of LAMP1 compartments corresponded with time points at which diminished POS levels co-localised to these organelles [Fig. 45C]. A broadly similar pattern was observed in LAMP2 compartments which were significantly smaller between 2-24 hours compared to those in control RPE cells. Measurement of mature lysosomes at these time points showed an average size of 0.61µm ± 0.08 compared to 1.06µm ± 0.11 in RPE where autophagy was normal. The size of LAMP2 compartments had returned to normal levels by 48 hours [Fig. 46I and Appendix C, Table 2]. Variations in the size of mature lysosomes broadly corresponded with diminished POS trafficking to these compartments, particularly at late time points [Fig. 45D]. Measurement of LC3b membranes with POS showed smaller sized autophagosomes at 4, 12, 24 and 48 hours compared to controls. Their average size at these time points corresponded to 0.61µm ± 0.09 compared to 0.97µm ± 0.15 in healthy RPE cells [Fig. 46J and Appendix C, Table 2]. In marked contrast to the broad correlation between vesicle size and the extent of co-localisation in Rab5, Rab7 and LAMP1/2 lysosomes, we found that smaller LC3b compartments generally appeared to have a significantly higher incidence of POS labelling [Fig. 45E]. Where significant size differences were recorded between bafilomycin treated and untreated cultures, we also

measured the size of compartments without any POS cargos, which revealed normally sized vesicles in treated cells [Appendix C, Table 3].

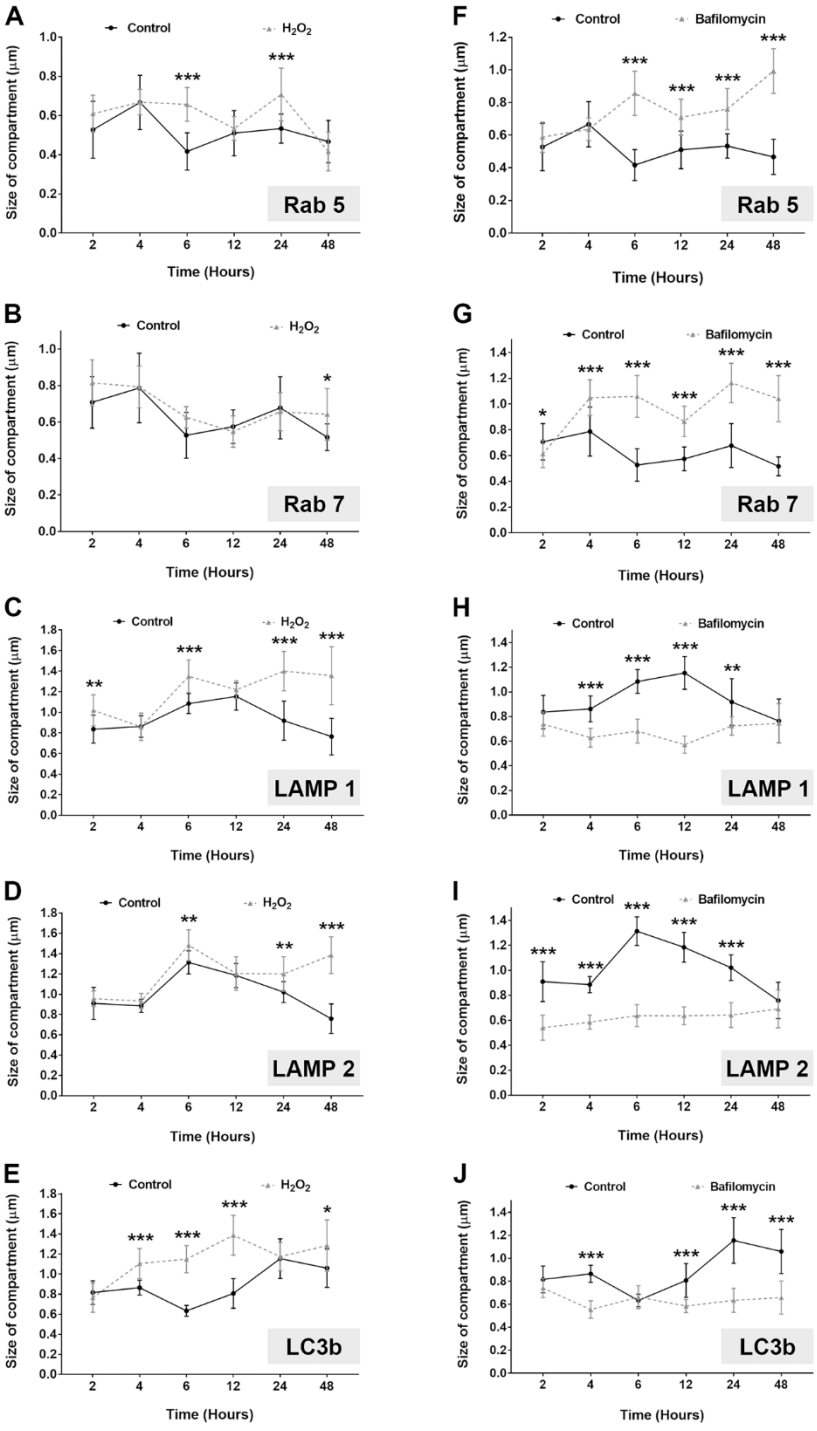

Figure 46: Effects of high oxidative stress and dysregulated autophagy on the size of intracellular compartments in the POS trafficking pathway.
Potential effects of H_2O_2 or bafilomycin treatment were assessed by quantifying the size of POS-trafficking intracellular compartments in RPE cells. [A] Effects of H_2O_2 on the Rab5 early compartment show enlarged vesicles at 6 and 24 hours compared to untreated cells. [B] Exposure to H_2O_2 had no appreciable effects on the size of Rab7 vesicles until 48 hours. [C] By contrast, treatment with H_2O_2 led to a significant increase in the size of early and [D] late lysosomes. Enlarged early lysosomes were observed from the first time point of 2 hours after POS feeding. However, differences with normal lysosomes were most obvious at later time points. [E] An increase in the sizes of autophagy bodies over those present in healthy cells were also detected as a consequence of H_2O_2 treatment. [F] Effects of bafilomycin treatment on Rab5 labelled vesicles show a significant increase in the size of compartments over those in control cells from 6 hours onwards. [G] A similar effect was observed

in Rab7 vesicles but from the first time point of 2 hours. [H] In contrast, treatment with bafilomycin significantly reduced the size of early and [I] late lysosomes. This effect was obvious in late lysosomes from the first time point of 2 hours. However, swollen lysosomes returned to normal levels by 48 hours. [J] Exposure to bafilomycin also resulted in a significant decrease in the size of LC3b labelled autophagy compartments over those in untreated cells. Error bars represent the standard deviation. Images collected from three independent experiments. n=15 separate measurements for each marker per time point. Statistical analysis was performed using an unpaired student's t-test where * denotes a significance of $p \leq 0.05$, ** indicates $p \leq 0.01$ whilst *** shows a significance of ≤ $p \leq 0.001$.

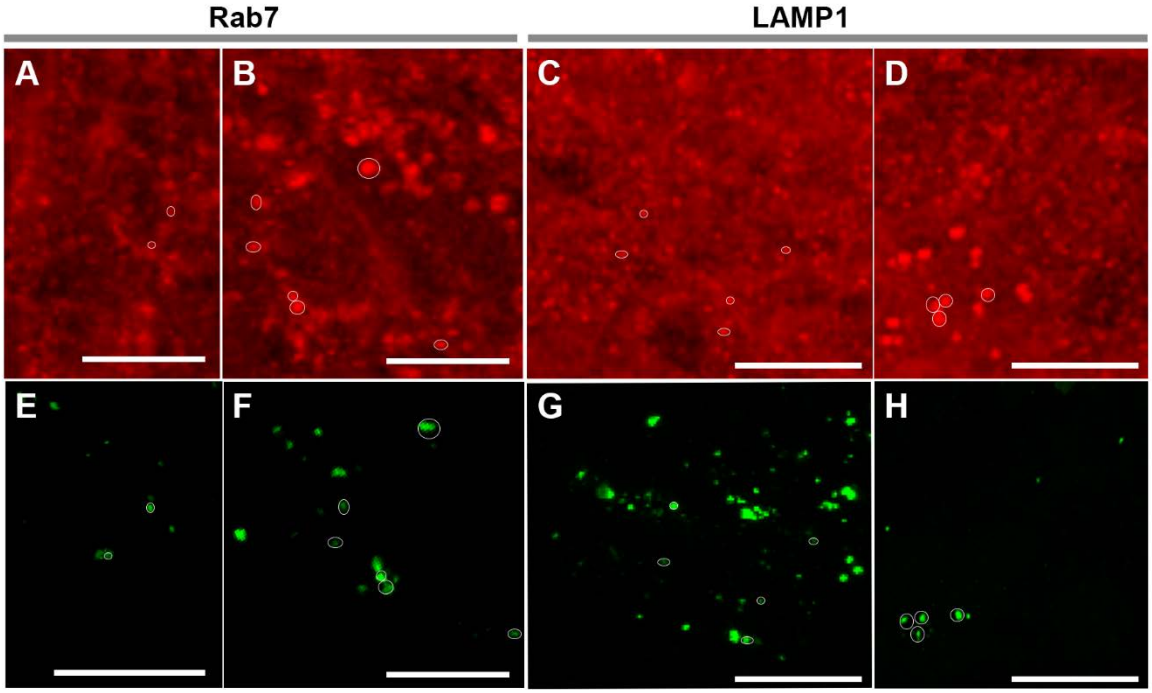

Figure 47: Bafilomycin and H_2O_2 treatment impair intracellular vesicles in the RPE.
Representative confocal immunofluorescence images are showing [A] size of normal POS- carrying Rab7 compartments at 24 hours and [B] enlarged Rab7 with POS following exposure to bafilomycin. Cultures probed with LAMP1 after 48 hours showing [C] size of normal lysosomes with POS and [D] swollen lysosomes with POS following treatment with H_2O_2. Several Rab7 and LAMP1 labelled compartments have been circled in white. The green channel (POS) has been switched off to facilitate ease of comparisons in vesicle size between treated and untreated cultures, however has been turned back on in [E] Rab 7 compartments at 24 hours, [F] Rab 7 compartments at 24 hours following exposure to Bafilomycin, [G] Lamp 1 compartments at 24hours and [H] Lamp 1 compartments at 24hours following H_2O_2 exposure. The scale bars correspond to 10mm.

5.4 Discussion

Understanding the molecular mechanisms through which oxidative damage, from an unhealthy diet for example, results in pathogenic alternations at the cellular level has become an area of increasing importance, especially in age-related degenerative diseases such as AMD. Here, we explored how this diet-disease axis could cause retinal damage by studying pathogenic processes associated with an unhealthy Western-style diet in the RPE.

5.4.1 A pulse-chase method of tracking POS degradation

As POS binding to αvβ5 integrin stimulates focal adhesion kinase to activate MerTK[429], we first confirmed that POS internalisation in our assay was mediated via these receptors. We used POS feeding coupled to a pulse-chase assay to maximise the extent of cargo binding whilst minimising its premature internalisation, thus synchronising POS trafficking in order to track temporal changes[287]. We next wanted to confirm that the lower temperature required in the pulse chase assay did not harm the monolayer. To test this, we used a ZO1 stain to assess the tight junctions of the monolayer and confirmed it was still intact. However, in addition to the typical peripheral staining pattern expected, there was also a degree of ZO1 staining in the cytoplasm and nucleus. This has previously been reported and is likely to be attributed to the proposed function of ZO1 in growth and proliferation. This observation reflects the limited barrier function of ARPE-19 cells, which exhibit relatively leaky tight-junctions in comparison to nature RPE[430]. Nonetheless, ZO1 is often used as a tight junction stain in APRE-19 cells. We also fixed cells immediately after removal from 17^{o}C to check our pulse assay was effective, and POS were bound to the monolayer, but no internalisation had occurred. We then labelled the major early, intermediate and late compartments in the trafficking pathway to obtain a dynamic and nuanced picture of POS degradation in healthy RPE cells.

For the first time, we can visualise the sequential trafficking of POS cargos by 3D-rendered confocal immunofluorescence microscopy. We utilised an algorithm widely employed in studies of this kind to automatically quantify the extent of POS co-localisation in each compartment[289], which revealed temporal dynamics of this process. Early trafficking to Rab5 vesicles reached a peak at 4 hours, after which cargos peaked in Rab7 compartments by 6 hours. Surprisingly, POS positive Rab7 vesicles were evident even at late time points (24 - 48 hours) when cargos are expected to have been trafficked through mature phagosomes and endosomes. However, co-labelling studies using a Rab7 specific antibody as well as a lysosomal probe indicated that some lysosomes were also positive for Rab7, similar to what has previously been reported[166,427,428], which may account for this observation. The internalisation of POS in early compartments was also assessed by electron microscopy,

which initially showed little or no evidence of degradation. However, there were some signs of POS breakdown by 6-12 hours by which time immunofluorescence studies revealed most cargos to be in Rab7 late phagosomes/endosomes. POS started to appear incrementally in early lysosomes, and significantly at later time points in mature lysosomes. POS reached a peak in both LAMP1/2 lysosomes by 24 hours. This was consistent with ultrastructural data which showed the appearance of degraded POS associated with electron-dense material indicating further processing in the proteolytic pathway. Quantification of cargo processing in electron micrographs was based on the extent of POS breakdown, as well as the reported morphology of lysosomes[431]. Moreover, POS proteolysis appeared to occur along the apical-basal axis of RPE cells, with the highest level of degradation within compartments in proximity to the basolateral membrane. Collectively, these findings show progressive signs of POS degradation correlated with increasing distance from the apical RPE surface, where cargos were initially phagocytosed.

Cargos finally co-localised with LC3b labelled compartments, initially at low levels during early time points (2-6 hours) but increased significantly after 12 hours to reach a peak by 48 hours. Electron micrographs taken at 24 hours captured double-membrane autophagosomes that typically associate with LC3b in conventional autophagy[432], further demonstrating the transfer of POS to terminal stages of the proteolytic pathway. However, since we observed few examples of double-membrane autophagosomes, this could suggest that POS in LC3 compartments are part of the non-canonical pathway[433,434]. This could be further verified using immunogold labelling of compartments. Our detailed breakdown of POS trafficking in healthy RPE was in-line with broad timeframes in which these cargos are reportedly engulfed and degraded[274,306,402]. Our studies also show the dynamic nature of POS trafficking and insights into how some intracellular compartments can have multiple identities or markers, perhaps indicating transition states or multiple functions. This would be consistent with recent discoveries that reveal new roles for lysosomes and the different ways in which intracellular compartments communicate with each other[166,427,428,435,436]. Importantly, our findings revealed that although a majority of POS cargos are tightly shuttled via Rab5, Rab7 and LAMP1, 2 and LC3b compartments in healthy RPE, there is also a considerable degree of flexibility and variation in this process. Such insights contribute to the current understanding of how cargos are trafficked and processed in the RPE. Although we and others have utilised well-characterised approaches to ensure a tight pulse chase[166,287,306,419,437], the possibility of some premature POS internalisation due to leakage cannot be fully excluded.

5.4.2 The effect of oxidative stress on POS degradation

POS trafficking was significantly altered when RPE were subjected to oxidative stress utilising a well-established method[164,408]. The amount of H_2O_2 used was also similar to their concentration in the human vitreous[426]. We observed markedly diminished levels of POS in Rab5 and Rab7 vesicles compared to healthy RPE. We attributed this to the rapid trafficking of cargos to early and mature lysosomes as well as LC3b labelled compartments. POS cargos could bypass early and intermediate compartments under oxidative stress to prematurely co-localise with apical lysosomes. Such apically distributed lysosomes have been reported in proximity to RPE microvilli in a rat model of inherited retinopathy[438]. Although the Costes method[289] provides a direct readout of the incidence/extent of co-localisation, it cannot measure the amount of POS in each compartment. Consequently, we were unable to determine whether prematurely targeted POS remained sequestered in lysosomes and autophagosomes from early time points. However, rapid trafficking of POS that had bypassed upstream processing events may contribute to the likelihood of proteolytically indigestible material accumulating within RPE lysosomes, and a potential mechanism for lipofuscin biogenesis as, once formed, lipofuscin is considered to be resistant to degradation and cannot be transported outside the cell by exocytosis[439]. Indeed, the accumulation of high molecular weight aggregates within lysosomes, and related organelles is a major feature of degenerative conditions such as AD and AMD[395,409,440,441]. We measured the size of compartments in oxidatively stressed and healthy RPE, which revealed a significant increase in the size of LAMP1 and LAMP2 labelled vesicles as well as autophagosomes carrying POS from early time points. This is consistent with enlarged and swollen lysosomes reported in neurons of Alzheimer's patients, which is one of the earliest neuropathological features that appear decades before symptoms[69]. Of note, the size of lysosomes without POS cargos in oxidatively stressed RPE remained normal, suggesting a mechanism in which only those vesicles carrying POS are affected.

5.4.3 The effect of impaired intracellular trafficking on POS degradation

We treated cultured RPE with bafilomycin A1 to disrupt lysosomal acidification, preventing fusion with autophagosomes and disrupting maturation along the endocytic pathway. We observed significantly high levels of POS in Rab5 and Rab7 vesicles at late time points (12-48 hours), which was in sharp contrast to cargos being trafficked away from these compartments in healthy RPE. POS, therefore, appeared to be sequestered in early and late phagosomes/endosomes, which was supported by our observation that cargos failed to be subsequently trafficked to LAMP1/2 lysosomes. Although we cannot directly comment on whether POS were sequestered in Rab5 and Rab7 compartments *per se*, we recorded a significant increase in the size of POS positive phagosomes/endosomes whilst the size

of lysosomes was markedly smaller compared to healthy RPE. In contrast, the size of Rab5, Rab7 and lysosomes devoid of POS in bafilomycin treated cells were broadly similar to their counterparts in untreated/healthy RPE, indicating a cargo-specific effect. Enlarged endosomes is a known feature of early stages of neuropathological conditions such as AD and Down syndrome where misfolded proteins principally localise to Rab5 vesicles[442]. Swollen endosomes are also reported in RPE of aged human donors and Abca4$^{-/-}$ mouse model of Stargardt disease[443]. The failure of POS cargos to reach terminal stages of the proteolytic pathway could lead to their accumulation in RPE cells. The importance of lytic compartments to retinal function was demonstrated by findings showing high levels of lysosomal cathepsin D and acid phosphatase in macular RPE cells relative to RPE in the nasal/mid-zone and peripheral retina. Lysosomal enzyme activity also decreased by ~50% when exposed to lipofuscin, suggesting vulnerability of macular RPE to intracellular protein aggregation[58,172]. Although a large proportion of POS failed to be trafficked to lysosomes, we noticed a significant increase in LC3b labelled compartments from early time points. Our results indicate that a proportion of POS cargos had bypassed the conventional trafficking pathway, suggesting a compensatory mechanism as a consequence of lysosomal dysfunction. Recent findings have revealed a non-canonical form of autophagy termed LC3-associated phagocytosis (LAP)[208] through which lipidated LC3 associates with phagosomes in an Atg5 and Beclin1-dependent manner, but independently of the autophagy pre-initiation Ulk1/Atg13/Fip200 complex. The importance of this pathway was demonstrated in mice lacking Atg5 where phagosomes containing undigested POS were unable to penetrate the RPE. Phagocytosed POS also failed to associate with LAMP1/2 and cathepsin D, suggesting a role for Atg5 in POS trafficking to lysosomes. Furthermore, Atg5 deficient mice showed defective retinal function although there was no obvious damage to photoreceptors suggesting these effects are subtle but impact vision nonetheless[444]. Increased autophagy triggered by cyclical shedding of POS with at least part of the autophagy machinery directly involved in phagosome maturation may explain our observations in culture, although further studies are required to confirm this. The presence of significantly smaller sized LC3b compartments despite increased POS co-localisation in bafilomycin treated RPE may indicate cargos associating with simpler membranes and evidence for non-canonical autophagy. Impaired autophagy in the RPE also leads to inflammasome activation and angiogenesis[395,445], linking dysfunction of cargo trafficking and clearance mechanisms with other well-recognised features of retinal degeneration.

5.5 Summary

In summary, this detailed study shows how POS cargos are tightly regulated and trafficked through the phagosome and autophagy-lysosomal pathways. Although a majority of cargos are transported in this manner, there appears to be some variability, perhaps indicating a degree of flexibility which could help RPE to cope with stressful conditions. The importance of correct cargo trafficking and timely proteolytic degradation is demonstrated by evidence from diverse neurodegenerative and storage diseases which reveal an impairment of these mechanisms in early stages of pathology[69,166,443,446]. Our studies also reveal divergent outcomes for POS trafficking under conditions of oxidative stress, impaired lysosomal function and disrupted autophagy all of which can occur simultaneously in the senescent RPE[447]. Some of these mechanisms may play a prominent role in retinas of certain patients whilst not in others, or indeed feature in different stages of the disease. This illustrates some of the challenges in treating complex conditions such as AMD. Intriguingly, pathology appeared to be confined to vesicles containing POS, whilst the size of Rab5, Rab7, LAMP1/2 and LC3b compartments without cargos were broadly within normal parameters, suggesting a population of healthy compartments even in stressed or diseased RPE. These could be harnessed to rejuvenate RPE as an alternative approach for lysosomal rescue which has already been explored[405]. Insights from this work also invite further questions to the manner in which endocytic compartments communicate with one another, and the origins and lifespan/turnover of lysosomes. Such questions are highly pertinent given recent findings demonstrating new functions for lysosomes in nutrient-sensing and metabolic homeostasis[435,436], and the central role played by misfolded proteins and impaired clearance mechanisms in diseases such as AD and AMD.

Chapter 6 Final discussion and future work

6.1 Final Discussion

The studies presented in my thesis explores the relationship between HFD induced oxidative stress and structural and functional alterations associated with retinal degeneration. We have reported novel findings on how the consumption of an unhealthy diet, such as food rich in high fat and cholesterol, causes pathogenic changes in the outer retina, and began to explore the functional effects this might have on the RPE monolayer. A summary of these changes can be seen in Figure 48.

The investigations presented in chapter 3 provide novel insights into the 3-dimensional ultrastructure of the RPE monolayer and associated photoreceptors. Our discoveries reveal why some RPE cells appear to be more susceptible to age-related damage than others. Our studies also provided new information on the arrangements and shape of healthy RPE cells. For instance, despite what has previously been reported not all RPE cells have a typical hexocuboidal shape as our findings indicate this is only the case for a subset of cells. It appears some RPE cells are infact more cuboidal in shape. I hypothesise that the cuboidal arrangement increases tessellation allowing for a tighter control of nutrients and molecules through the BRB. Similarly, we also observed the rhomboidal cross-sectional shape of RPE cells. This shape will increase cell: cell contacts, and perhaps also help to increase barrier efficacy. By segmenting the photoreceptors, we were able to accurately count the number of photoreceptors associated with each RPE cell for the first time. Interestingly this ranged between 90 and 216 photoreceptors, which is in stark contrast to the previously reported 45 photoreceptors per RPE cell. Our novel findings therefore highlight the true magnitude of the daily proteolytic burden placed upon RPE cells.

Although bi-nucleate RPE cells are often reported, few studies have been undertaken to elucidate the differences between bi-nucleate and mono-nucleate RPE. The data presented here demonstrate novel and fundamental structural differences between mono-nucleate and bi-nucleate RPE cells. Using immunofluorescence staining of murine flat mounts, we observed an increase in bi-nucleate and multi-nucleate cells in the central retina compared to the peripheral retina. We also observed an increase in the presence of bi-nucleate and multi-nucleate cells throughout the retina with age. This is corroborated by previous studies[136]. Given that the overall number of RPE cells is known to decline with increasing age[145] yet, in healthy aged eyes, the RPE monolayer remains intact, the formation of bi-nucleate RPE cells could occur as a compensatory mechanism to overcome cellular apoptosis. Our 3D reconstructed cells offer novel information about the structural

differences between the two cell types, offer support for theories of the way in which bi-nucleate cells are formed, and begin to unveil ways in which bi-nucleate cells are more susceptible to disease pathology. Our data show and increased number of photoreceptors overlying each bi-nucleate RPE compared to mono-nucleate cells. It remains to be elucidated whether this increase in POS number is as a result of larger multi-nucleate cells forming to compensate for apoptosis, or whether the increase in POS number causes the threshold of cytokinesis inhibition to be reached, resulting in bi-nucleate cell formation. Nonetheless, these findings reinforce current thinking and evidence that bi-nucleate RPE are indeed points at which early pathology could develop in the senescent retina. My studies revealed the bi-nucleate RPE cells are in proximity to abnormally thickened BrM. This suggests that multi-nucleate RPE has consequence beyond the RPE monolayer with pathogenic changes occurring, presumable subsequently, in the underlying BrM.

Given the importance of oxidative stress to the formation of bi-nucleate RPE, we next studied the in-vivo effects of oxidative stress in living eyes. In chapter 4 I describe my novel findings in a HFD mouse model. Pathogenic changes in HFD mice include depositions/ inclusions in the photoreceptor layer, which appear to be lipid dense. These depositions have destroyed the close associated of photoreceptors with the RPE microvilli. RPE also showed evidence of disease pathology such as disrupted basal infolds. BrM was thickened, as is often reported in disease phenotypes. Drusen-like basal laminar deposits high in levels of clusterin were found between the RPE and BrM. The importance of such focal deposits and local pathology is consistent with ideas of how incipient pathology develops in the ageing retina, leading to conditions such as AMD. Many of these changes were common to structural alterations seen in bi-nucleate RPE, suggesting a potential predisposition of bi-nucleate cells to oxidative stress/damage.

In chapter 5, I delved further into oxidative stress mechanisms at the level of RPE cells, and studied how its effects could influence intracellular cell physiology. We used an in vitro RPE model in which POS were synchronously fed to mimic cargo trafficking and processing activities that follow light onset. By labelling distinct intracellular compartments, I studied how POS are trafficked and degraded in endosomes and the autophagy-lysosomal pathways of RPE cells. My findings revealed novel information showing details of how POS cargos are trafficked and processed by healthy RPE. Mimicking conditions of oxidative stress caused POS cargos to bypass early compartments and rapidly shuttle to lysosomes and autophagy vesicles. However, impairment of vesicles acidification caused sequestering of POS in early and late endosomes with an apparently failure of trafficking to the lysosomes. This revealed divergent outcomes for POS trafficking under conditions of oxidative stress, impaired lysosomal function and disrupted autophagy. These findings align with how deficits in POS trafficking/ processing lead to the build-up of lipofuscin within RPE

cells, a hallmark of early retinopathy. Such insoluble lipid/protein aggregates impede cell function and are thought to contribute to the formation of nascent pathogenic deposits in the RPE-BrM interface. Interestingly, our results suggest the cellular pathology is confined to vesicles containing POS, whilst compartments without any POS cargos appear to be unaffected. These data suggest that a population of healthy lysosomes are maintained even in stressed or diseased RPE cells, which could be harnessed to rejuvenate these cells as a potential therapeutic intervention.

Healthy Ageing

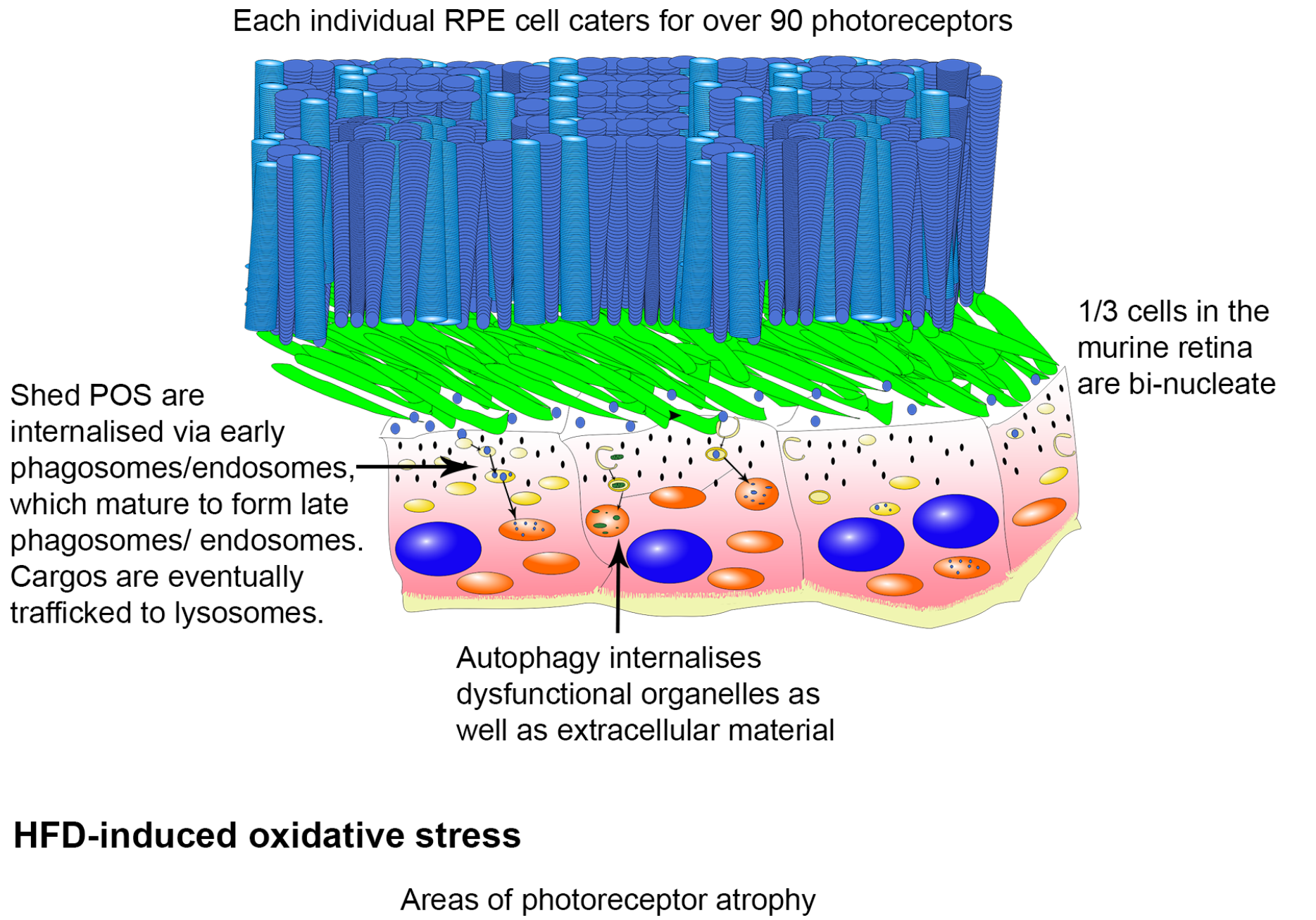

HFD-induced oxidative stress

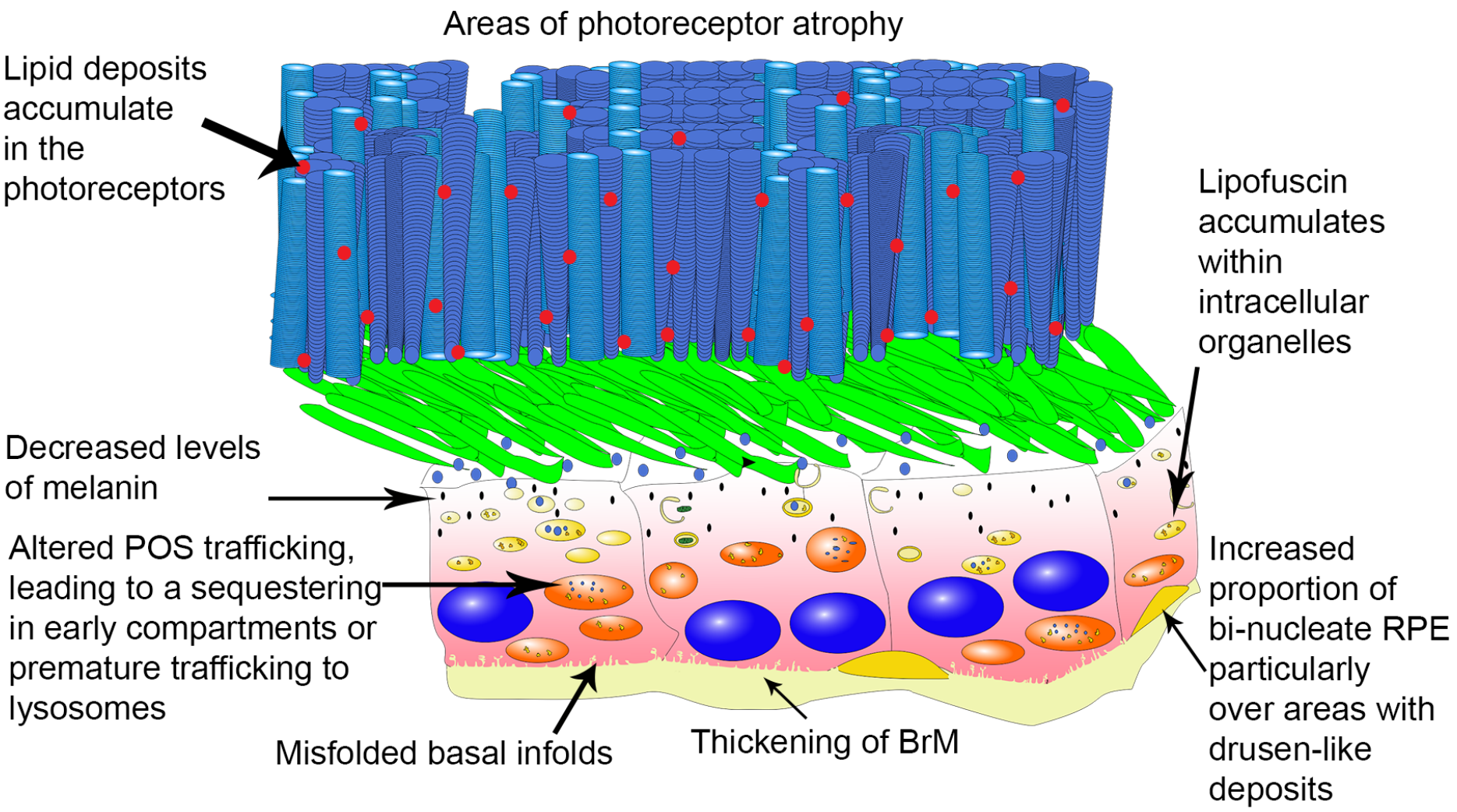

Figure 48: Summary diagram of work presented in thesis

The top panel shows a healthy aged RPE cell. 1/3 of RPE cells are bi-nucleate with similar sized ellipsoid nuclei. Abundant apical melanin is found in all cells (black ovals). Each RPE cell caters for over 90 rod and cone photoreceptors, which are composed of POS (blue discs). POS are shed daily, and are internalised and broken down by the underlying RPE cells. Endosomes, lysosomes and autophagy bodies all contribute to the degradation of POS in healthy cells. The bottom panel shows RPE following HFD-induced oxidative stress. There are areas of photoreceptor atrophy, and decreased levels of apical melanin. In addition, there is the formation of lipid deposits within the photoreceptor layer (red ovals). Further, there is an increased proportion of bi-nucleate RPE cells, which often occur over levels of drusen-like basal laminar deposits (yellow mounds), which contain clusterin. BrM is vastly thickened, whilst the basal infolds are disrupted and misfolded. There are also increased levels of TIMP3 within the BrM, altering its morphology. We have also shown altered POS trafficking following HFD effects of oxidative stress and impaired lysosomal acidification. This causes the accumulation of incompletely degraded POS and lipofuscin (yellow shapes) within intracellular organelles, further impeding their function.

6.2 Implications for AMD research, pathology and treatments

The novel findings presented in this thesis add to a growing body of literature that suggests a role for HFD and oxidative stress along with impairment of RPE clearance mechanisms in the initial stages of AMD. We have uncovered mechanisms underpinning impairment of the RPE endo-lysosomal system and autophagy pathways that occur in early AMD. We have revealed divergent outcomes of POS trafficked under conditions of oxidative stress, impaired lysosomal functional and disrupted autophagy, all of which occur simultaneously in the senescent RPE and are a feature of AMD. Insights from our 3D studies have revealed how bi-nucleate RPE may be structurally prone to disease. Further studies into RPE ultrastructural changes could help guide functional work. For example, our findings showing the RPE cells in fact 'cater' for many more photoreceptors than initially thought provide insights into actual levels of proteolytic stresses under which RPE exist, and reveals the importance of the lysosomal pathway in maintaining a healthy and functioning retina.

6.3 Future directions

The novel data presented in this body of work have opened several research avenues in regards to investigating oxidative stress as a key molecular pathway that underpins retinal disease. The following sections describe some work that could be undertaken to further exploit these new discoveries.

6.3.1 Reconstruction of human RPE

As mentioned in chapter 3, it is incredibly difficult to acquire well preserved human eyes given the lack of donation centres around the UK. However, Southampton is in the process of setting up an Eye Biobank as a repository for such tissues. Having the on-site biobank will reduce post-mortem times before the eyes can be fixed, which will increase the likelihood of obtaining high quality, well-preserved donor eyes for future 3D ultrastructural studies. Once this eye biobank is in place it would be insightful to compare the structure of other outer retina of AMD eyes with age matched controls. Donations will also be linked with patient's genetics and lifestyle, allowing comparisons across different AMD stages as well as with healthy control eyes. Machine learning could also be harnessed. Since we have fully reconstructed 4 eyes, and indeed a further RPE cell from a different eye is currently being segmented, we have enough data to begin to teach a computer how to accurately segment the different cellular components. This would dramatically speed up reconstruction and make further investigations more viable.

6.3.2 Further investigations into HFD eyes

Findings presented in chapter 4 are obtained from aged mice. It would, therefore, be interesting to repeat the study on neonates and young mice as well as in aged HFD eyes. This would allow us to map the timelines of HFD induced changes in the outer retina. Furthermore, if HFD driven structural effects occur in young mice, it would be interesting to determine whether these are reversible upon switching to a normal diet. Studies could also include the use of SBSEM approaches to provide novel insights into HFD induced changes in 3D ultrastructure. This would include the volume of each cellular component, as well as the surface area of interacting edges between cells, amongst other parameters, which can be compared to normal chow fed mouse eyes. Given the theory that bi-nucleate RPE cells are more prone to oxidative stress, it would also be interesting to compare the number of bi-nucleate RPE in the retina of an HFD mouse with normal chow-fed animals. If the number of multi-nucleate RPE cells increased, it could suggest that these cells are already damaged before becoming bi-nucleate. However, if this number did not increase, it would reveal that bi-nucleate RPE is instead more prone to oxidative stress. Therefore, ways to inhibit the

multi-nucleation process and instead encourage RPE to complete cytokinesis and form a more homologous monolayer could be investigated as a new prevention therapy for AMD.

6.3.3 Boosting lysosomal function to rescue AMD-like pathology

Recent discoveries have identified a network of promoters referred to as Co-ordinated Lysosomal Expression and Regulation (CLEAR) elements which are activated by a DNA-binding protein called transcription factor EB (TFEB). Studies in RPE have shown that over-expression of TFEB can rescue cells from serum starvation and lysosomal stress. It is also thought that the over-expression of TFEB may be a mechanism by which neurons try to counteract the accumulation of lysosomal debris in AD. We could exploit these discoveries by expressing TFEB in ARPE-19 cells grown in the system used in Chapter 5. This will boost the number of RPE lysosomes. Cells could then be fed UV-irradiated POS which mimic protein aggregation in the aged retina. This would test the ability of the RPE with boosted lysosomes to clear cargoes that are normally resistant to degradation. I would hypothesize that the new populations of lysosomes will boost the ability of the RPE to clear such debris. If this is correct, TFEB could be packaged into an adenoviral or lentiviral vector to be injected into a suitable mouse model to show that RPE lysosomes can also be boosted *in vivo*. This strategy, therefore, opens a novel pathway to boost RPE lysosomes in living eyes so that an altogether new method of treating conditions such as AMD may be devised. Such a strategy has been used successfully to treat a cell model of Pompe disease; an LSD that normally results in childhood death.

6.4 Final thoughts

Understanding the impact of oxidative stress and damage to the outer retina and the role this has in AMD is fundamental to discovering new pathways for therapeutic interventions. The novel findings presented in my thesis demonstrates that oxidative stress has major structural and functional consequences not only on the RPE monolayer but also in adjacent tissues of the outer retina. My findings link oxidative stress mechanism associated with a HFD to structural and functional changes at single cell level. It also reveals the extent of the proteolytic burden placed upon these cells, something that is often drastically underestimated, helping to explain why the lysosomal pathway often fails in age and disease. Key questions remain unanswered about how the 3D ultrastructure of RPE cells are affected following oxidative stress as well as details of functional consequences on other layers of the outer retina. Nonetheless, novel insights from the data presented here paves the way for designing new interventions to target the oxidative stress pathway, and planning new ways to rejuvenate or even rescue damaged RPE cells in AMD patients.

.

Appendix A

```
object1 = "Untitled";
object2 = "Untitled";
Dialog.create("Measuring shared area between");
Dialog.addString("Object1:", object1);
Dialog.addString("Object2:", object2);
Dialog.show();
object1 = Dialog.getString();
object2 = Dialog.getString();

path = File.directory();
title_orig = getTitle();
getVoxelSize(width, height, depth, unit);
pixelWidth = width;
pixelDepth = depth;
pixelUnit = unit;


junctionArea_total = 0;
junctionArea_array = newArray(0);
imageNbr = nSlices();



for(i=1; i<imageNbr; i++){


	selectWindow(title_orig);
	setSlice(i);


	run("Duplicate...", "title=Object1.tif");
	setAutoThreshold("Default");
	//run("Threshold...");
	setAutoThreshold("Default dark");
	setThreshold(1, 1);
	setOption("BlackBackground", false);
	run("Convert to Mask");
	rename("Object1_binary.tif");
	run("Dilate");

	selectWindow(title_orig);
	run("Duplicate...", "title=Object2.tif");
	setAutoThreshold("Default");
	//run("Threshold...");
	setAutoThreshold("Default dark");
	setThreshold(2, 2);
	setOption("BlackBackground", false);
	run("Convert to Mask");
	rename("Object2_binary.tif");
	//run("Dilate");
	//run("Fill Holes");
```

```
	imageCalculator("AND create", "Object1_binary.tif","Object2_binary.tif");


	selectWindow("Object1_binary.tif");
	close();
	selectWindow("Object2_binary.tif");
	close();


	selectWindow("Result of Object1_binary.tif");
	setAutoThreshold("Default dark");
	//run("Threshold...");
	setAutoThreshold("Default");
	run("Create Selection");


	getSelectionBounds(xRect0, yRect0, xWidth, yHeight);
	selectionArray = newArray(xWidth*yHeight);
	a = 0;
	for(y=yRect0; y < yRect0+yHeight; y++){
		for(x=xRect0; x < xRect0+xWidth; x++){
			selectionArray[a++] = getPixel(x,y);
		}
	}


	selectionArray2 = newArray(0);
	for(c = 0; c < selectionArray.length; c++){
		if (selectionArray[c] > 254){
			selectionArray2 = Array.concat(selectionArray2, selectionArray[c]);
		}
	}
	nbrPixel = selectionArray2.length;
	junctionLength = nbrPixel * pixelWidth;
	junctionArea = junctionLength * pixelDepth;
	junctionArea_array = Array.concat(junctionArea_array, junctionArea);
	junctionArea_total = junctionArea_total + junctionArea;


	selectWindow("Result of Object1_binary.tif");
	close();
}


if (nResults>=0) {
	run("Clear Results");
}
i = nResults;


for (n=0; n < junctionArea_array.length; n++){
	setResult("Slice", i, n);
	setResult("Pixel_Unit", 0, pixelUnit);
	setResult("Surf.Area_stack", 0,  junctionArea_total);
	setResult("Surf.Area_slices", i, junctionArea_array[n]);
	i = nResults;
}

updateResults;
```

```
saveAs("Results", path + "SharedSA_"+object1+"_"+object2+".csv");
run("Close");
selectWindow(title_orig);
close();


exit("ANALYSIS FINISHED");
```

Appendix B

Figures presented in appendix 2 are specific to those cross-referenced in chapter 3. Please see electronic appendix 2 for an interactive 3D PDF of the reconstructed patch or RPE cells.

In order to enable 3D rendering in Adobe, go to Edit -> Preferences-> 3D & Multimedia -> select enable playing 3D content.

Appendix C

Table 4: The extent of colocalisation between vesicles and POS
Stained transwells were imaged using a confocal microscope and analysed using Costes automatic colocalisation analysis. Mean levels of colocalisation along with standard deviation (SD) is shown for each compartment across 6 time points for control cultures, as well as those fed Hydrogen Peroxide (H_2O_2) or Bafilomycin A1. Values are reported as a decimal where a recorded value of 1.0 shows 100% colocalisation. n≥20 cells for control measurements, and n≥15 cells for treatment groups.

Supplementary Table 1

	Extent of co-localisation																																	
	2 Hours						4 Hours						6 Hours						12 Hours						24 Hours						48 Hours					
	Control		H_2O_2		Bafilomycin		Control		H_2O_2		Bafilomycin		Control		H_2O_2		Bafilomycin		Control		H_2O_2		Bafilomycin		Control		H_2O_2		Bafilomycin		Control		H_2O_2		Bafilomycin	
	Mean	SD	Mean	SD	Mean	SD	Mean	SD	Mean	SD	Mean	SD	Mean	SD	Mean	SD	Mean	SD	Mean	SD	Mean	SD	Mean	SD	Mean	SD	Mean	SD	Mean	SD	Mean	SD	Mean	SD	Mean	SD
Rab5	0.84	0.14	0.25	0.13	0.86	0.11	0.89	0.13	0.48	0.19	0.78	0.17	0.71	0.13	0.47	0.13	0.88	0.12	0.18	0.12	0.25	0.11	0.91	0.09	0.23	0.14	0.42	0.31	0.95	0.06	0.15	0.19	0.44	0.35	0.9	0.12
Rab7	0.7	0.13	0.26	0.19	0.84	0.13	0.62	0.17	0.27	0.15	0.83	0.14	0.93	0.12	0.39	0.1	0.86	0.11	0.64	0.18	0.27	0.16	0.88	0.13	0.54	0.21	0.44	0.26	0.9	0.11	0.37	0.2	0.47	0.29	0.93	0.11
LAMP1	0.28	0.18	0.79	0.11	0.34	0.13	0.47	0.14	0.83	0.1	0.29	0.16	0.57	0.18	0.88	0.09	0.5	0.11	0.76	0.11	0.84	0.13	0.52	0.17	0.85	0.1	0.96	0.04	0.3	0.15	0.73	0.17	0.93	0.07	0.4	0.12
LAMP2	0.31	0.21	0.89	0.09	0.28	0.09	0.41	0.21	0.82	0.12	0.26	0.15	0.31	0.11	0.86	0.14	0.35	0.11	0.76	0.13	0.83	0.13	0.3	0.14	0.89	0.07	0.93	0.06	0.25	0.14	0.84	0.09	0.94	0.05	0.3	0.07
LC3b	0.17	0.15	0.66	0.17	0.38	0.31	0.2	0.16	0.67	0.15	0.69	0.23	0.23	0.17	0.84	0.17	0.8	0.17	0.39	0.2	0.85	0.1	0.84	0.15	0.67	0.17	0.91	0.06	0.84	0.12	0.91	0.07	0.92	0.05	0.92	0.07

Table 5: The size of vesicles containing POS
Images of ARPE-19 cells fed with POS were taken using a confocal microscope. Images were then imported into FIJI where vesicles containing POS were measured at their widest point. Size measurements are reported for each compartment across 6 time points for control cultures, as well as H_2O_2 and Bafilomycin treatment groups. Values shown are in µm. Mean values are reported alongside standard deviation (SD) for n=15 measurements/group/time point.

Supplementary Table 2

	Size of compartment (µm) in vesicles with POS																																	
	2 Hours						4 Hours						6 Hours						12 Hours						24 Hours						48 Hours					
	Control		H_2O_2		Bafilomycin		Control		H_2O_2		Bafilomycin		Control		H_2O_2		Bafilomycin		Control		H_2O_2		Bafilomycin		Control		H_2O_2		Bafilomycin		Control		H_2O_2		Bafilomycin	
	Mean	SD	Mean	SD	Mean	SD	Mean	SD	Mean	SD	Mean	SD	Mean	SD	Mean	SD	Mean	SD	Mean	SD	Mean	SD	Mean	SD	Mean	SD	Mean	SD	Mean	SD	Mean	SD	Mean	SD	Mean	SD
Rab5	0.53	0.15	0.61	0.09	0.59	0.09	0.67	0.14	0.67	0.06	0.64	0.07	0.42	0.09	0.66	0.09	0.86	0.14	0.51	0.12	0.53	0.06	0.71	0.11	0.53	0.07	0.55	0.13	0.76	0.13	0.47	0.11	0.42	0.1	0.99	0.14
Rab7	0.71	0.14	0.82	0.13	0.61	0.11	0.79	0.19	0.79	0.11	1.05	0.14	0.53	0.13	0.63	0.06	1.06	0.16	0.57	0.09	0.55	0.09	0.87	0.12	0.68	0.17	0.66	0.1	1.16	0.15	0.52	0.07	0.64	0.14	1.04	0.18
LAMP1	0.84	0.14	1.02	0.15	0.74	0.10	0.86	0.1	0.86	0.13	0.63	0.08	1.14	0.14	1.34	0.2	0.68	0.10	1.27	0.18	1.05	0.15	0.57	0.07	0.92	0.19	1.40	0.19	0.72	0.07	0.76	0.18	1.36	0.28	0.75	0.16
LAMP2	0.91	0.16	0.96	0.08	0.54	0.10	0.89	0.06	0.93	0.07	0.59	0.06	1.31	0.11	1.48	0.15	0.64	0.09	1.18	0.12	1.21	0.17	0.64	0.07	1.02	0.1	1.20	0.17	0.64	0.10	0.76	0.15	1.39	0.18	0.69	0.15
LC3b	0.82	0.12	0.77	0.15	0.74	0.08	0.86	0.07	1.10	0.15	0.55	0.08	0.63	0.05	1.15	0.14	0.66	0.10	0.81	0.15	1.39	0.2	0.59	0.06	1.15	0.2	1.17	0.14	0.63	0.10	1.06	0.19	1.28	0.26	0.66	0.14

Table 6: The size of vesicles not containing POS

Images where there was a difference in size of compartments between treated and control cultures were also analysed to measure the size of vesicles not containing POS. This was to see if the change in size effected all compartments or just those containing POS. Values are reported as µm. Mean values are noted alongside standard deviation (SD). P-values of differences between control groups and treatment groups are noted. N=15 measurement/ compartment/time point.

Supplementary Table 3

	Size of vesicle without POS																																	
	2 Hours						4 Hours						6 Hours						12 Hours						24 Hours						48 Hours					
	H_2O_2			Bafilomycin			H_2O_2			Bafilomycin			H_2O_2			Bafilomycin			H_2O_2			Bafilomycin			H_2O_2			Bafilomycin			H_2O_2			Bafilomycin		
	Mean	SD	P-value	Mean	SD	P-value	Mean	SD	P-value	Mean	SD	P-value	Mean	SD	P-value	Mean	SD	P-value	Mean	SD	P-value	Mean	SD	P-value	Mean	SD	P-value	Mean	SD	P-value	Mean	SD	P-value	Mean	SD	P-value
Rab5	N/A			N/A			N/A			N/A			0.39	0.1	0.64	0.39	0.13	0.92	N/A			0.5	0.1	0.96	0.06	0.11	0.64	0.51	0.07	0.90	N/A			0.47	0.1	0.98
Rab7	N/A			0.76	0.13	0.79	N/A			0.76	0.12	0.96	N/A			0.6	0.07	0.31	N/A			0.56	0.1	0.96	N/A			0.62	0.08	0.70	0.52	0.1	0.87	0.51	0.13	0.96
LAMP1	0.86	0.1	0.98	N/A			N/A			0.85	0.11	0.96	1.09	0.22	0.98	1.13	0.22	0.81	N/A			1.23	0.15	0.46	0.93	0.12	0.98	0.92	0.07	0.96	0.74	0.19	0.98	N/A		
LAMP2	N/A			0.91	0.17	1.00	N/A			0.82	0.15	0.53	1.26	0.23	0.78	1.32	0.14	0.98	N/A			1.12	0.19	0.73	1.04	0.13	0.92	1.04	0.1	0.92	0.76	0.11	0.96	N/A		
LC3b	N/A			N/A			0.86	0.11	0.98	0.82	0.12	0.67	0.61	0.11	0.95	N/A			0.8	0.1	0.98	0.81	0.08	0.91	N/A			1.07	0.17	0.67	1.04	0.15	0.98	1.04	0.11	0.91

Note: Comparisons where significant differences were recorded in the size of compartments in treated vs. control cultures.
SD: Standard deviation

Appendix D

Figures presented in Appendix D are represented images of controls for each secondary antibody used throughout this thesis.

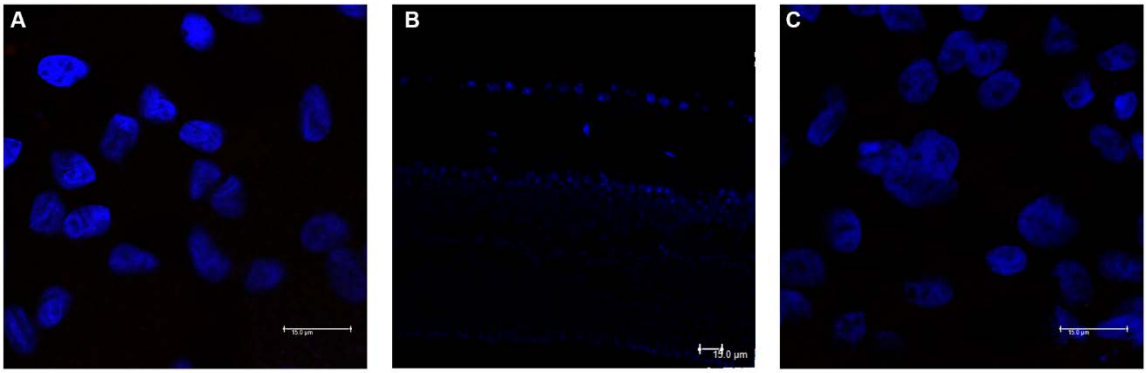

Figure 49: Secondary antibody control confocal images
Representative confocal-immunofluorescence images showing absence of signals after only probing with [A] Alexa Fluor 594 goat anti-rabbit. [B] Alexa Fluor 546 Goat anti-rabbit. [C] Alexa Fluor 594 Goat anti-Mouse secondary antibodies. Nuclei are labelled with DAPI (blue). The scale bars correspond to 15µm

Appendix E

Figures presented in Appendix E are representative images of isotype controls for each monoclonal antibody used throughout this thesis

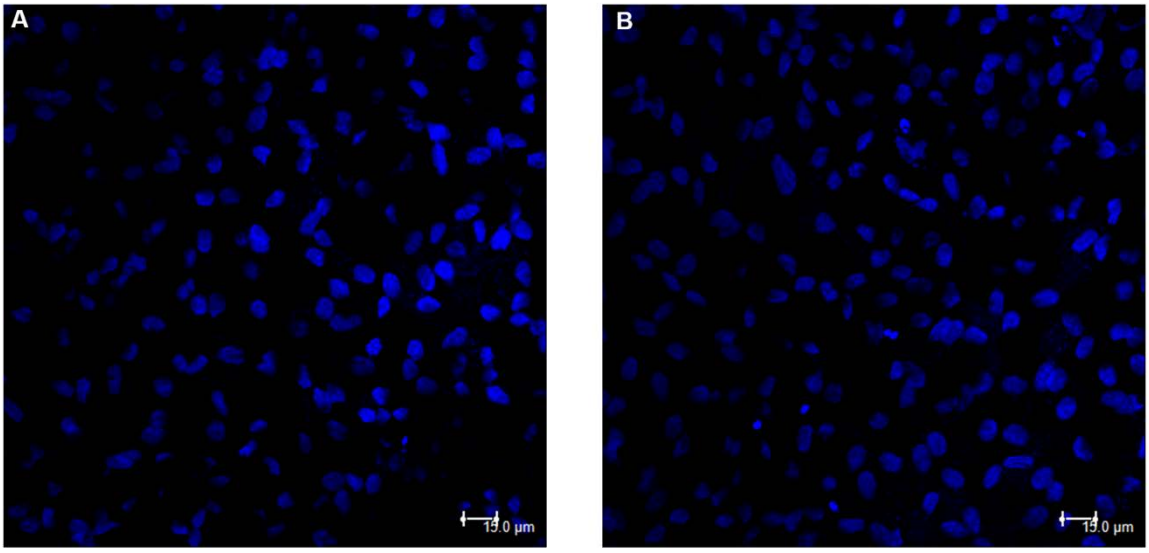

Figure 50: Isotype control confocal images
Representative confocal-immunofluorescence images showing absence of signals after probing with [A] mouse IgG1 isotype or [B] Rabbit IgG isotype. Nuclei are labelled with DAPI (blue). Scale bars represent 15µm

Appendix F

A. Normal diet

Special Diets Services

Rat and Mouse No.1 Maintenance

Pelleted, Expanded and Expanded Ground

SUITABLE SPECIES AND APPLICATIONS

Rats and mice for long and short term maintenance.

BENEFITS

- High quality human food grade soya bean concentrate provides a less variable source of protein.
- Low protein level promotes longer life expectancy, reducing obesity and associated problems in the aged animal.
- Low nutrient levels reduce the risk of undesirable side-effects in toxicity trials being masked.

FEEDING GUIDE

Ad-lib feeding is recommended.

AVAILABLE AS

Diet	Form	Product Code
Standard		
RM1 (P)	*9.5mm Pelleted*	*801151*
RM1 (E)	*Expanded*	*801002*
SQC		
RM1 (E) SQC	*Expanded*	*811002*
RM1 (E) FG SQC	*Expanded Ground*	*811004*

- All diets are available irradiated and are available in a range of packaging.
- All Standard diets are available with full analysis on request.

INGREDIENTS

Wheat, Barley, Wheatfeed, De-hulled Extracted Toasted Soya, Soya Protein Concentrate, Macro Minerals, Soya Oil, Whey Powder, Amino Acids, Vitamins, Micro Minerals.

Email: info@sdsdiets.com

Catalogue revision 4 0103

Calculated Analysis

NUTRIENTS		Total	Supp (9)
Proximate Analysis			
Moisture (1)	%	10.00	
Crude Oil	%	2.71	
Crude Protein	%	14.38	
Crude Fibre	%	4.65	
Ash	%	6.00	
Nitrogen Free Extract	%	61.73	
Digestibility Co-Efficients (7)			
Digestible Crude Oil	%	2.47	
Digestible Crude Protein	%	12.92	
Carbohydrates, Fibre and Non Starch Polysaccharides (NSP)			
Total Dietary Fibre	%	17.05	
Pectin	%	1.52	
Hemicellulose	%	10.17	
Cellulose	%	4.32	
Lignin	%	1.68	
Starch	%	44.97	
Sugar	%	4.05	
Energy (5)			
Gross Energy	MJ/kg	14.74	
Digestible Energy (15)	MJ/kg	11.90	
Metabolisable Energy (15)	MJ/kg	10.74	
Atwater Fuel Energy (AFE)(8)	MJ/kg	13.75	
AFE from Oil	%	7.42	
AFE from Protein	%	17.49	
AFE from Carbohydrate	%	75.09	
Fatty Acids			
Saturated Fatty Acids			
C12:0 Lauric	%	0.02	
C14:0 Myristic	%	0.14	
C16:0 Palmitic	%	0.31	
C18:0 Stearic	%	0.04	
Monounsaturated Fatty Acids			
C14:1 Myristoleic	%	0.02	
C16:1 Palmitoleic	%	0.09	
C18:1 Oleic	%	0.77	
Polyunsaturated Fatty Acids			
C18:2(ω6) Linoleic	%	0.69	
C18:3(ω3) Linolenic	%	0.06	
C20:4(ω6) Arachidonic	%	0.13	
C22:5(ω3) Clupanodonic	%		
Amino Acids			
Arginine	%	0.91	
Lysine (6)	%	0.66	0.07
Methionine	%	0.22	0.04
Cystine	%	0.24	
Tryptophan	%	0.18	
Histidine	%	0.35	
Threonine	%	0.49	
Isoleucine	%	0.54	
Leucine	%	0.98	
Phenylalanine	%	0.66	
Valine	%	0.69	
Tyrosine	%	0.49	
Taurine	%		
Glycine	%	1.11	
Aspartic Acid	%	0.67	

NUTRIENTS		Total	Supp (9)
Glutamic Acid	%	3.17	
Proline	%	1.20	
Serine	%	0.56	
Hydroxyproline	%		
Hydroxylysine	%		
Alanine	%	0.16	
Macro Minerals			
Calcium	%	0.73	0.63
Total Phosphorus	%	0.52	0.04
Phytate Phosphorus	%	0.24	
Available Phosphorus	%	0.28	0.04
Sodium	%	0.25	0.19
Chloride	%	0.38	0.32
Potassium	%	0.67	
Magnesium	%	0.23	
Micro Minerals			
Iron	mg/kg	159.30	82.50
Copper	mg/kg	11.50	1.94
Manganese	mg/kg	72.44	19.22
Zinc	mg/kg	35.75	
Cobalt	µg/kg	634.10	550.00
Iodine	µg/kg	1202.69	1085.00
Selenium	µg/kg	298.99	100.00
Fluorine	mg/kg	10.49	
Vitamins			
β-Carotene (2)	mg/kg	0.16	
Retinol (2)	µg/kg	2566.38	2400.00
Vitamin A (2)	iu/kg	8554.27	8000.00
Cholecalciferol (3)	µg/kg	15.54	15.00
Vitamin D (3)	iu/kg	621.70	600.00
α-Tocopherol (4)	mg/kg	76.45	56.82
Vitamin E (4)	iu/kg	84.10	62.50
Vitamin B_1 (Thiamine)	mg/kg	8.58	1.96
Vitamin B_2 (Riboflavin)	mg/kg	4.33	2.94
Vitamin B_6 (Pyridoxine)	mg/kg	4.81	0.98
Vitamin B_{12} (Cyanocobalamine)	µg/kg	7.49	6.00
Vitamin C (Ascorbic Acid)	mg/kg	2.59	
Vitamin K (Menadione)	mg/kg	10.17	9.36
Folic Acid (Vitamin B_9)	mg/kg	0.79	
Nicotinic Acid (Vitamin PP) (6)	mg/kg	61.32	2.45
Pantothenic Acid (Vitamin B_{35})	mg/kg	20.17	5.80
Choline (Vitamin B_{97})	mg/kg	1080.14	366.60
Inositol	mg/kg	2369.59	
Biotin (Vitamin H) (6)	µg/kg	277.13	

Notes

1. All values are calculated using a moisture basis of 10%.
   Typical moisture levels will range between 9.5 - 11.5%.
2. a. Vitamin A includes Retinol and the Retinol equivalents of β-carotene
   b. Retinol includes the Retinol equivalents of β-Carotene.
   c. 0.48 µg Retinol = 1 µg β-carotene = 1.6 iu Vitamin A activity
   d. 1 µg Retinol = 3.33* iu Vitamin A activity
   e. 1 iu Vitamin A = 0.3 µg Retinol = 0.6 µg β-carotene
   f. The standard analysis for Vitamin A does not detect β-carotene
3. 1 µg Cholecalciferol (D_3) = 40.0 iu Vitamin D
4. 1 mg all-*rac*-α-tocopherol = 1.1 iu Vitamin E activity
   1 mg all-*rac*-α-tocopherol acetate = 1.0 iu Vitamin E activity
5. 1 MJ = 239.23 Kcalories = 239.23 Calories = 239,230 calories
6. These nutrients coming from natural raw materials such as cereals may have low availabilities due to the interactions with other compounds.
7. Based on in-vitro digestibility analysis.
8. AF Energy = Atwater Fuel Energy = (((CO%/100)*9000)+(((CP%/100)*4000)+(((NFE%/100)*4000)/239.23
9. Supplemented nutrients from manufactured and mined sources.
15. Calculated.

B- HFD

Special Diets Services

DIET FORMULATION AND SPECIFICATION DATA

BASIC DIET INFORMATIO

Code:	824053
Name:	RM AFE45%FAT 20%CP 35%CHO(P)
Date:	23/03/2017

CALCULATED ANALYSIS:

		FRESH	10% H2O
PROXIMATES			
CRUDE OIL	%	22.56	21.26
CRUDE PROTEIN	%	23.04	21.72
CRUDE FIBRE	%	4.60	4.34
ASH	%	4.45	4.19
NFE	%	39.65	37.37
ENERGY			
AF ENERGY	kcal/kg	4537.43	4276.56
AF ENERGY	MJ/kg	18.97	17.88
FATTY ACIDS			
C14 1 MYRISTOLEIC	%	0.02	0.02
C16 1 PALMITOLEIC	%	0.03	0.03
C18 1 W9 OLEIC	%	6.43	6.06
C18 2 W6 LINOLEIC	%	3.75	3.53
C18 3 W3 LINOLENIC	%	0.39	0.37
C20 4 W6 ARICHIDONIC	%	0.01	0.01
C22 5 W3 CLUPANODONIC	%	0.00	0.00
C12:0 LAURIC	%	0.03	0.03
C14:0 MYRISTIC	%	0.31	0.29
C16:0 PALMITIC	%	4.28	4.03
C18:0 STEARIC	%	1.91	1.80
AMINO ACIDS			
ARGININE	%	0.73	0.69
LYSINE	%	1.46	1.38
S LYS	%	0.00	0.00
METHIONINE	%	0.57	0.54
S METH	%	0.00	0.00
CYSTINE	%	0.45	0.42
S CYST	%	0.39	0.37
TRYPTOPHAN	%	0.20	0.19
S TRYPT	%	0.00	0.00
HISTIDINE	%	0.53	0.50
THREONINE	%	0.80	0.75

		FRESH	10% H2O
MINERALS CONT'D			
CL	%	0.28	0.26
S CL	%	0.19	0.18
K	%	0.45	0.42
S K	%	0.44	0.41
MG	%	0.08	0.08
S MG	%	0.06	0.06
FE	mg/kg	59.90	56.46
S FE	mg/kg	52.97	49.92
CU	mg/kg	8.76	8.26
S CU	mg/kg	7.44	7.01
MN	mg/kg	13.84	13.04
S MN	mg/kg	12.52	11.80
ZN	mg/kg	68.97	65.00
S ZN	mg/kg	37.13	35.00
CO	µg/kg	0.00	0.00
S CO	µg/kg	0.00	0.00
I	µg/kg	254.84	240.19
S I	µg/kg	254.84	240.19
SE	µg/kg	197.40	186.05
S SE	µg/kg	197.40	186.05
F	mg/kg	1.24	1.17
VITAMINS			
VIT A	iu/kg	4936.44	4652.63
S VIT A	iu/kg	4936.44	4652.63
VIT D3	iu/kg	1416.63	1335.18
S VIT D3	iu/kg	1234.11	1163.16
VIT E	iu/kg	100.72	94.93
S VIT E	iu/kg	92.56	87.24
VIT B1 THI	mg/kg	6.10	5.75
S VIT B1	mg/kg	6.00	5.66
VIT B2 RIB	mg/kg	6.37	6.00
S VIT B2	mg/kg	5.92	5.58
VIT B6 PYR	mg/kg	7.15	6.74
S VIT B6	mg/kg	7.04	6.64
VIT B12 CY	µg/kg	30.85	29.08
S VIT B12	µg/kg	30.85	29.08

This information is intended as a guide only. For actual data we recommend that analysis work is carried out to confirm the nutrient parameters precisely

S THREO	%	0.00	0.00
ISOLEUCINE	%	1.16	1.09
LEUCINE	%	1.76	1.66
PHENYLALAN	%	0.96	0.90
VALINE	%	1.39	1.31
TYROSINE	%	0.96	0.90
TAURINE	%	0.00	0.00
GLYCINE	%	0.91	0.86
ASPARTIC A	%	1.30	1.23
GLUTAMIC A	%	3.77	3.55
PROLINE	%	1.58	1.49
SERINE	%	0.87	0.82
HYD PROLIN	%	0.00	0.00
HYD LYSINE	%	0.00	0.00
ALANINE	%	0.74	0.70
MINERALS			
CA	%	0.63	0.59
S CA	%	0.62	0.58
TOTAL P	%	0.37	0.35
S PHOS	%	0.29	0.27
PHYTATE P	%	0.00	0.00
AVAIL P	%	0.37	0.35
NA	%	0.16	0.15
S NA	%	0.12	0.11

VIT C ASCO	mg/kg	0.00	0.00
S VIT C	mg/kg	0.00	0.00
VIT K MENE	mg/kg	0.95	0.90
S VIT K	mg/kg	0.95	0.90
FOLIC ACID	mg/kg	2.38	2.24
S FOLIC	mg/kg	2.34	2.21
NICOTINIC	mg/kg	36.65	34.54
S NICOTIN	mg/kg	36.28	34.19
PANTOTHENII	mg/kg	18.48	17.42
S PANTOTH	mg/kg	17.71	16.69
CHOLINE	mg/kg	1392.58	1312.52
S CHOLINE	mg/kg	1217.33	1147.34
INOSITOL	mg/kg	0.00	0.00
S INOSITOL	mg/kg	0.00	0.00
BIOTIN	µg/kg	246.82	232.63
S BIOTIN	µg/kg	246.82	232.63

INGREDIENTS:

NAME	% INCLUSION
RICE STARCH	28.34
CASEIN	26.53
LARD	17.89
SUCROSE	10.49
CELLULOSE	6.17
SOYA OIL	4.32
MINERAL MIX	4.32
VITAMIN MIX	1.23
L-CYSTINE	0.40
CHOLINE BITARTRATE	0.30

Reference list

1. Land MF, Nilsson D-E. *Animal eyes*: Oxford University Press; 2012.

2. Nilsson D-E. The evolution of eyes and visually guided behaviour. *Philosophical Transactions of the Royal Society of London B: Biological Sciences* 2009;364(1531):2833-47.

3. Duncan RD, Jenkins SH. Use of visual cues in foraging by a diurnal herbivore, Belding's ground squirrel. *Canadian Journal of Zoology* 1998;76(9):1766-70.

4. Ruggeri M, Major JC, McKeown C, et al. Retinal structure of birds of prey revealed by ultra-high resolution spectral-domain optical coherence tomography. *Investigative ophthalmology & visual science* 2010;51(11):5789-95.

5. Vasicek CA, Oosthuizen MK, Cooper HM, et al. Circadian rhythms of locomotor activity in the subterranean Mashona mole rat, Cryptomys darlingi. *Physiology & behavior* 2005;84(2):181-91.

6. Fritsche LG, Fariss RN, Stambolian D, et al. Age-related macular degeneration: genetics and biology coming together. *Annual review of genomics and human genetics* 2014;15:151.

7. Owen CG, Jarrar Z, Wormald R, et al. The estimated prevalence and incidence of late stage age related macular degeneration in the UK. *British Journal of Ophthalmology* 2012:bjophthalmol-2011-301109.

8. Ruska E. The development of the electron microscope and of electron microscopy (Nobel lecture). *Angewandte Chemie International Edition in English* 1987;26(7):595-605.

9. Young RD, Knupp C, Pinali C, et al. Three-dimensional aspects of matrix assembly by cells in the developing cornea. *Proceedings of the National Academy of Sciences* 2014;111(2):687-92.

10. Kolb H. *Webvision: The Organization of the Retina and Visual System*. http://onlinebooks.library.upenn.edu/webbin/book/lookupid?key=olbp60030.

11. Purves D, Augustine GJ, Fitzpatrick D, et al. Neuroscience, 2008. *De Boeck, Sinauer, Sunderland, Mass* 2014.

12. Yanoff M, Duker J. Text Book of Ophthalmology: China: Mosby Elsevier Health Sciences, 2009.

13. Khandhadia S, Cherry J, Lotery AJ. Age-related macular degeneration *Neurodegenerative Diseases*: Springer; 2012 p15-36.

14. Bhutto I, Lutty G. Understanding age-related macular degeneration (AMD): Relationships between the photoreceptor/retinal pigment epithelium/Bruch's membrane/choriocapillaris complex. *Molecular aspects of medicine* 2012;33(4):295-317.

15. Lamb TD. Why rods and cones? *Eye (Lond)* 2016;30(2):179-85.

16. Curcio CA, Sloan KR, Kalina RE, et al. Human photoreceptor topography. *Journal of comparative neurology* 1990;292(4):497-523.

17. Curcio CA. Photoreceptor topography in ageing and age-related maculopathy. *Eye* 2001;15(3):376.

18. Bowmaker JK, Dartnall H. Visual pigments of rods and cones in a human retina. *The Journal of physiology* 1980;298(1):501-11.

19. Zinn K, Benjamin-Henkind J. Anatomy of the Human Pigment Epithelial Cell: Cambridge, MA: Harvard Univ. Press, 1979.

20. Rizzolo LJ. Barrier properties of cultured retinal pigment epithelium. *Experimental eye research* 2014;126:16-26.

21. Tso M, La FP. The human fovea after sungazing. *Transactions. Section on Ophthalmology. American Academy of Ophthalmology and Otolaryngology* 1975;79(6):OP788-95.

22. Wikler KC, Rakic P. Distribution of photoreceptor subtypes in the retina of diurnal and nocturnal primates. *Journal of Neuroscience* 1990;10(10):3390-401.

23. Bonilha VL. Age and disease-related structural changes in the retinal pigment epithelium. *Clin Ophthalmol* 2008;2(2):413-24.

24. Gordois A, Cutler H, Pezzullo L, et al. An estimation of the worldwide economic and health burden of visual impairment. *Global public health* 2012;7(5):465-81.

25. Lotery A, Trump D. Progress in defining the molecular biology of age related macular degeneration. *Human genetics* 2007;122(3-4):219-36.

26. Stuck AE, Walthert JM, Nikolaus T, et al. Risk factors for functional status decline in community-living elderly people: a systematic literature review. *Social science & medicine* 1999;48(4):445-69.

27. Owen C, Fletcher A, Donoghue M, et al. How big is the burden of visual loss caused by age related macular degeneration in the United Kingdom? *British Journal of Ophthalmology* 2003;87(3):312-17.

28. Rovner BW, Zisselman PM, Shmuely-Dulitzki Y. Depression and disability in older people with impaired vision: a follow-up study. *Journal of the American Geriatrics Society* 1996;44(2):181-84.

29. Gehrs KM, Anderson DH, Johnson LV, et al. Age-related macular degeneration—emerging pathogenetic and therapeutic concepts. *Annals of medicine* 2006;38(7):450-71.

30. Ho L, van Leeuwen R, de Jong P, et al. Epidemiology of AMD *Age-related Macular Degeneration*: Springer; 2013 p3-32.

31. Lim LS, Mitchell P, Seddon JM, et al. Age-related macular degeneration. *The Lancet*;379(9827):1728-38.

32. Group A-REDSR. The Age-Related Eye Disease Study severity scale for age-related macular degeneration: AREDS report no. 17. *Archives of ophthalmology* 2005;123(11):1484.

33. Cheung CM, Wong TY. Is age-related macular degeneration a manifestation of systemic disease? New prospects for early intervention and treatment. *J Intern Med* 2014;276(2):140-53.

34. Sarks J, Sarks S, Killingsworth M. Evolution of geographic atrophy of the retinal pigment epithelium. *Eye* 1988;2(Pt 5):552-77.

35. De Jong PT. Age-related macular degeneration. *New England Journal of Medicine* 2006;355(14):1474-85.

36. Amoaku W, Chakravarthy U, Gale R, et al. Defining response to anti-VEGF therapies in neovascular AMD. *Eye* 2015;29(6):721-31.

37. Amadio M, Govoni S, Pascale A. Targeting VEGF in eye neovascularization: what's new?: a comprehensive review on current therapies and oligonucleotide-based interventions under development. *Pharmacological research* 2016;103:253-69.

38. Rosenfeld PJ, Moshfeghi AA, Puliafito CA. Optical coherence tomography findings after an intravitreal injection of bevacizumab (Avastin®) for neovascular age-related macular degeneration. *Ophthalmic Surgery, Lasers and Imaging Retina* 2005;36(4):331-35.

39. Falavarjani KG, Nguyen QD. Adverse events and complications associated with intravitreal injection of anti-VEGF agents: a review of literature. *Eye* 2013;27(7):787-94.

40. Grunwald JE, Pistilli M, Ying G-s, et al. Growth of geographic atrophy in the comparison of age-related macular degeneration treatments trials. *Ophthalmology* 2015;122(4):809-16.

41. Lois N, Mcbain V, Abdelkader E, et al. RETINAL PIGMENT EPITHELIAL ATROPHY IN PATIENTS WITH EXUDATIVE AGE-RELATED MACULAR DEGENERATION UNDERGOING ANTI–VASCULAR ENDOTHELIAL GROWTH FACTOR THERAPY. *Retina* 2013;33(1):13-22.

42. Ratnayaka J, Serpell L, Lotery A. Dementia of the eye: the role of amyloid beta in retinal degeneration. *Eye* 2015;29(8):1013-26.

43. Seddon JM, Willett WC, Speizer FE, et al. A prospective study of cigarette smoking and age-related macular degeneration in women. *Jama* 1996;276(14):1141-46.

44. Seddon JM, Rosner B, Sperduto RD, et al. Dietary fat and risk for advanced age-related macular degeneration. *Archives of ophthalmology* 2001;119(8):1191-99.

45. Seddon JM, Cote J, Rosner B. Progression of age-related macular degeneration: association with dietary fat, transunsaturated fat, nuts, and fish intake. *Archives of ophthalmology* 2003;121(12):1728-37.

46. Cho E, Hung S, Willett WC, et al. Prospective study of dietary fat and the risk of age-related macular degeneration–. *The American journal of clinical nutrition* 2001;73(2):209-18.

47. Pauleikhoff D, Barondes M, Minassian D, et al. Drusen as risk factors in age-related macular disease. *American journal of ophthalmology* 1990;109(1):38-43.

48. Mullins RF, Russell SR, Anderson DH, et al. Drusen associated with aging and age-related macular degeneration contain proteins common to extracellular deposits associated with atherosclerosis, elastosis, amyloidosis, and dense deposit disease. *The FASEB Journal* 2000;14(7):835-46.

49. Bressler SB, Maguire MG, Bressler NM, et al. Relationship of drusen and abnormalities of the retinal pigment epithelium to the prognosis of neovascular macular degeneration. *Archives of ophthalmology* 1990;108(10):1442-47.

50. Nivison-Smith L, Wang H, Assaad N, et al. Retinal thickness changes throughout the natural history of drusen in age-related macular degeneration. *Optometry and Vision Science* 2018;95(8):648-55.

51. Algvere PV, Marshall J, Seregard S. Age-related maculopathy and the impact of blue light hazard. *Acta Ophthalmol Scand* 2006;84(1):4-15.

52. Jarrett SG, Boulton ME. Consequences of oxidative stress in age-related macular degeneration. *Molecular aspects of medicine* 2012;33(4):399-417.

53. Cai J, Nelson KC, Wu M, et al. Oxidative damage and protection of the RPE. *Progress in retinal and eye research* 2000;19(2):205-21.

54. Qin S. Oxidative damage of retinal pigment epithelial cells and age-related macular degeneration. *Drug development research* 2007;68(5):213-25.

55. Blasiak J, Petrovski G, Veréb Z, et al. Oxidative stress, hypoxia, and autophagy in the neovascular processes of age-related macular degeneration. *BioMed research international* 2014;2014.

56. Yildirim Z, Ucgun NI, Yildirim F. The role of oxidative stress and antioxidants in the pathogenesis of age-related macular degeneration. *Clinics* 2011;66(5):743-46.

57. Brunk U, Wihlmark U, Wrigstad A, et al. Accumulation of lipofuscin within retinal pigment epithelial cells results in enhanced sensitivity to photo-oxidation. *Gerontology* 1995;41(Suppl. 2):201-12.

58. Shamsi FA, Boulton ME. Inhibition of RPE lysosomal and antioxidant activity by the age pigment lipofuscin. *Investigative Ophthalmology and Visual Science* 2001;42(12):3041-46.

59. Kennedy CJ, Rakoczy PE, Constable IJ. Lipofuscin of the retinal pigment epithelium: a review. *Eye* 1995;9(6):763-71.

60. Brunk UT, Terman A. Lipofuscin: mechanisms of age-related accumulation and influence on cell function. *Free Radical Biology and Medicine* 2002;33(5):611-19.

61. Wing GL, Blanchard GC, Weiter JJ. The topography and age relationship of lipofuscin concentration in the retinal pigment epithelium. *Invest Ophthalmol Vis Sci* 1978;17(7):601-07.

62. Fritsche LG, Igl W, Bailey JNC, et al. A large genome-wide association study of age-related macular degeneration highlights contributions of rare and common variants. *Nature genetics* 2016;48(2):134-43.

63. Consortium AG. Seven new loci associated with age-related macular degeneration. *Nature genetics* 2013;45(4):433-39.

64. Edwards AO, Malek G. Molecular genetics of AMD and current animal models. *Angiogenesis* 2007;10(2):119-32.

65. Ratnapriya R, Zhan X, Fariss RN, et al. Rare and common variants in extracellular matrix gene Fibrillin 2 (FBN2) are associated with macular degeneration. *Human molecular genetics* 2014;23(21):5827-37.

66. Goverdhan SV, Howell MW, Mullins RF, et al. Association of HLA class I and class II polymorphisms with age-related macular degeneration. *Investigative ophthalmology & visual science* 2005;46(5):1726-34.

67. Lynn SA, Keeling E, Munday R, et al. The complexities underlying age-related macular degeneration: could amyloid beta play an important role? *Neural Regeneration Research* 2017;12(4):538.

68. Taylor-Walker G, Lynn SA, Keeling E, et al. The Alzheimer's-related amyloid beta peptide is internalised by R28 neuroretinal cells and disrupts the microtubule associated protein 2 (MAP-2). *Experimental eye research* 2016;153:110-21.

69. Cataldo AM, Petanceska S, Terio NB, et al. Abeta localization in abnormal endosomes: association with earliest Abeta elevations in AD and Down syndrome. *Neurobiol Aging* 2004;25.

70. Jarrett JT, Berger EP, Lansbury Jr PT. The carboxy terminus of the. beta. amyloid protein is critical for the seeding of amyloid formation: Implications for the pathogenesis of Alzheimer's disease. *Biochemistry* 1993;32(18):4693-97.

71. Hardy J, Selkoe DJ. The amyloid hypothesis of Alzheimer's disease: progress and problems on the road to therapeutics. *science* 2002;297(5580):353-56.

72. Ohno-Matsui K. Parallel findings in age-related macular degeneration and Alzheimer's disease. *Progress in retinal and eye research* 2011;30(4):217-38.

73. Wang J, Ohno-Matsui K, Morita I. Elevated amyloid β production in senescent retinal pigment epithelium, a possible mechanism of subretinal deposition of amyloid β in age-related macular degeneration. *Biochemical and biophysical research communications* 2012;423(1):73-78.

74. Johnson LV, Leitner WP, Rivest AJ, et al. The Alzheimer's Aβ-peptide is deposited at sites of complement activation in pathologic deposits associated with aging and age-related macular degeneration. *Proceedings of the National Academy of Sciences* 2002;99(18):11830-35.

75. Anderson DH, Talaga KC, Rivest AJ, et al. Characterization of β amyloid assemblies in drusen: the deposits associated with aging and age-related macular degeneration. *Experimental eye research* 2004;78(2):243-56.

76. Kam JH, Lenassi E, Jeffery G. Viewing ageing eyes: diverse sites of amyloid Beta accumulation in the ageing mouse retina and the up-regulation of macrophages. *PloS one* 2010;5(10):e13127.

77. Who J, Consultation FE. Diet, nutrition and the prevention of chronic diseases. *World Health Organ Tech Rep Ser* 2003;916(i-viii).

78. Chiu C-J, Chang M-L, Zhang FF, et al. The relationship of major American dietary patterns to age-related macular degeneration. *American journal of ophthalmology* 2014;158(1):118-27. e1.

79. Seddon JM, Rosner B, Sperduto RD, et al. Dietary fat and risk for advanced age-related macular degeneration. *Archives of Ophthalmology* 2001;119(8):1191-99.

80. Mares-Perlman JA, Brady WE, Klein R, et al. Dietary fat and age-related maculopathy. *Archives of ophthalmology* 1995;113(6):743-48.

81. Weikel KA, Chiu CJ, Taylor A. Nutritional modulation of age-related macular degeneration. *Molecular aspects of medicine* 2012;33(4):318-75.

82. Gorusupudi A, Nelson K, Bernstein PS. The Age-Related Eye Disease 2 Study: Micronutrients in the Treatment of Macular Degeneration–. *Advances in Nutrition* 2017;8(1):40-53.

83. Rowan S, Taylor A. Gene-Diet Interactions in Age-Related Macular Degeneration *Retinal Degenerative Diseases*: Springer; 2016 p95-101.

84. Pikuleva IA, Curcio CA. Cholesterol in the retina: the best is yet to come. *Progress in retinal and eye research* 2014;41:64-89.

85. Datta S, Cano M, Ebrahimi K, et al. The impact of oxidative stress and inflammation on RPE degeneration in non-neovascular AMD. *Progress in retinal and eye research* 2017;60:201-18.

86. Beatty S, Koh H-H, Phil M, et al. The role of oxidative stress in the pathogenesis of age-related macular degeneration. *Survey of ophthalmology* 2000;45(2):115-34.

87. Du Z, Yang Y, Hu Y, et al. A long-term high-fat diet increases oxidative stress, mitochondrial damage and apoptosis in the inner ear of D-galactose-induced aging rats. *Hearing Research* 2012;287(1-2):15-24.

88. Tan BL, Norhaizan ME, Liew W-P-P. Nutrients and oxidative stress: friend or foe? *Oxidative medicine and cellular longevity* 2018;2018.

89. Sies H, Cadenas E. Oxidative stress: damage to intact cells and organs. *Phil. Trans. R. Soc. Lond. B* 1985;311(1152):617-31.

90. Cadenas E, Sies H. Oxidative stress: excited oxygen species and enzyme activity. *Advances in enzyme regulation* 1985;23:217-37.

91. Aruoma OI. Free radicals, oxidative stress, and antioxidants in human health and disease. *Journal of the American oil chemists' society* 1998;75(2):199-212.

92. Finkel T, Holbrook NJ. Oxidants, oxidative stress and the biology of ageing. *Nature* 2000;408(6809):239.

93. Markesbery WR. Oxidative stress hypothesis in Alzheimer's disease. *Free radical Biology and medicine* 1997;23(1):134-47.

94. Sies H. Oxidative stress: from basic research to clinical application. *The American journal of medicine* 1991;91(3):S31-S38.

95. Berlett BS, Stadtman ER. Protein oxidation in aging, disease, and oxidative stress. *Journal of Biological Chemistry* 1997;272(33):20313-16.

96. Kurtz JC, Jones DP, Sternberg P, et al. Antioxidant functions of glutathione in human retinal pigment epithelium in relation to age-related macular degeneration. In: Coscas G, Piccolino FC (eds.) *Retinal Pigment Epithelium and Macular Diseases*. Dordrecht: Springer Netherlands; 1998 p47-57.

97. Nunomura A, Perry G, Aliev G, et al. Oxidative damage is the earliest event in Alzheimer disease. *Journal of Neuropathology & Experimental Neurology* 2001;60(8):759-67.

98. Sies H, Berndt C, Jones DP. Oxidative stress. *Annual review of biochemistry* 2017;86:715-48.

99. Halliwell B, Gutteridge JM. *Free radicals in biology and medicine*: Oxford University Press, USA; 2015.

100. . *Mayo Clinic Proceedings*: Elsevier.

101. Halliwell B. Reactive oxygen species in living systems: source, biochemistry, and role in human disease. *The American journal of medicine* 1991;91(3):S14-S22.

102. Girotti AW. Photosensitized oxidation of membrane lipids: reaction pathways, cytotoxic effects, and cytoprotective mechanisms. *Journal of Photochemistry and Photobiology B: Biology* 2001;63(1-3):103-13.

103. Davies KJ. *Oxidative damage & repair: Chemical, biological and medical aspects*: Elsevier; 2013.

104. Norris EH, Giasson BI. Role of oxidative damage in protein aggregation associated with Parkinson's disease and related disorders. *Antioxidants & redox signaling* 2005;7(5-6):672-84.

105. Braun RD, Linsenmeier RA, Goldstick TK. Oxygen consumption in the inner and outer retina of the cat. *Investigative ophthalmology & visual science* 1995;36(3):542-54.

106. Stefánsson E, Wolbarsht ML, Landers III MB. In vivo O2 consumption in rhesus monkeys in light and dark. *Experimental eye research* 1983;37(3):251-56.

107. Ham W, Ruffolo J, Mueller H, et al. Histologic analysis of photochemical lesions produced in rhesus retina by short-wave-length light. *Investigative ophthalmology & visual science* 1978;17(10):1029-35.

108. Algvere PV, Marshall J, Seregard S. Age-related maculopathy and the impact of blue light hazard. *Acta Ophthalmologica Scandinavica* 2006;84(1):4-15.

109. Godley BF, Shamsi FA, Liang FQ, et al. Blue light induces mitochondrial DNA damage and free radical production in epithelial cells. *J Biol Chem* 2005;280(22):21061-6.

110. Dorey CK, Delori FC, Akeo K. Growth of cultured RPE and endothelial cells is inhibited by blue light but not green or red light. *Current eye research* 1990;9(6):549-59.

111. Organisciak DT, Darrow RM, Barsalou L, et al. Light history and age-related changes in retinal light damage. *Investigative ophthalmology & visual science* 1998;39(7):1107-16.

112. Anderson RE, Benolken R, Dudley PA, et al. Polyunsaturated fatty acids of photoreceptor membranes. *Experimental eye research* 1974;18(3):205-13.

113. Uauy R, Hoffman DR, Peirano P, et al. Essential fatty acids in visual and brain development. *Lipids* 2001;36(9):885-95.

114. Pham-Huy LA, He H, Pham-Huy C. Free radicals, antioxidants in disease and health. *International journal of biomedical science: IJBS* 2008;4(2):89.

115. Boulton M, Różanowska M, Różanowski B. Retinal photodamage. *Journal of Photochemistry and Photobiology B: Biology* 2001;64(2-3):144-61.

116. Wu J, Seregard S, Algvere PV. Photochemical damage of the retina. *Survey of ophthalmology* 2006;51(5):461-81.

117. Tate D, Miceli MV, Newsome DA. Phagocytosis and H2O2 induce catalase and metallothionein gene expression in human retinal pigment epithelial cells. *Investigative ophthalmology & visual science* 1995;36(7):1271-79.

118. Mustafi D, Kevany BM, Genoud C, et al. Defective photoreceptor phagocytosis in a mouse model of enhanced S-cone syndrome causes progressive retinal degeneration. *The FASEB Journal* 2011;25(9):3157-76.

119. Kaemmerer E, Schutt F, Krohne TU, et al. Effects of Lipid Peroxidation-Related Protein Modifications on RPE Lysosomal Functions and POS Phagocytosis. *Investigative ophthalmology & visual science* 2007;48(3):1342-47.

120. Miceli MV, Liles MR, Newsome DA. Evaluation of oxidative processes in human pigment epithelial cells associated with retinal outer segment phagocytosis. *Experimental cell research* 1994;214(1):242-49.

121. Finkel T. Signal transduction by reactive oxygen species. *The Journal of cell biology* 2011;194(1):7-15.

122. Cano M, Thimmalappula R, Fujihara M, et al. Cigarette smoking, oxidative stress, the anti-oxidant response through Nrf2 signaling, and age-related macular degeneration. *Vision research* 2010;50(7):652-64.

123. Khandhadia S, Lotery A. Oxidation and age-related macular degeneration: insights from molecular biology. *Expert reviews in molecular medicine* 2010;12:e34.

124. Kunchithapautham K, Atkinson C, Rohrer B. Smoke-exposure causes endoplasmic reticulum stress and lipid accumulation in retinal pigment epithelium through oxidative stress and complement activation. *Journal of Biological Chemistry* 2014:jbc. M114. 564674.

125. Strauss O. The retinal pigment epithelium in visual function. *Physiological reviews* 2005;85(3):845-81.

126. Bird AC, Phillips RL, Hageman GS. Geographic atrophy: a histopathological assessment. *JAMA ophthalmology* 2014;132(3):338-45.

127. Spaide RF. Age-related choroidal atrophy. *American journal of ophthalmology* 2009;147(5):801-10.

128. Sonoda S, Spee C, Barron E, et al. A protocol for the culture and differentiation of highly polarized human retinal pigment epithelial cells. *Nat Protoc* 2009;4(5):662-73.

129. Bok D. The retinal pigment epithelium: a versatile partner in vision. *J Cell Sci* 1993;1993(Supplement 17):189-95.

130. R Sparrrow J, Hicks D, P Hamel C. The retinal pigment epithelium in health and disease. *Current molecular medicine* 2010;10(9):802-23.

131. Anderson DH, Fisher SK. The relationship of primate foveal cones to the pigment epithelium. *Journal of ultrastructure research* 1979;67(1):23-32.

132. Boulton M, Dayhaw-Barker P. The role of the retinal pigment epithelium: topographical variation and ageing changes. *Eye* 2001;15(3):384-89.

133. Cavallotti CA, Schveoller M. Aging of the retinal pigmented epithelium *Age-Related Changes of the Human Eye*: Springer; 2008 p203-15.

134. Strauss O. The retinal pigment epithelium by Olaf Strauss.

135. Ts'o M, Friedman E. The retinal pigment epithelium. 3. Growth and development. *Archives of ophthalmology* 1968;80(2):214-16.

136. Volland S, Esteve-Rudd J, Hoo J, et al. A comparison of some organizational characteristics of the mouse central retina and the human macula. *PloS one* 2015;10(4):e0125631.

137. Boulton M. The role of melanin in the RPE. *The retinal pigment epithelium. Oxford University Press, Oxford* 1998:68-85.

138. Pappuru RR, Ouyang Y, Nittala MG, et al. Relationship between outer retinal thickness substructures and visual acuity in eyes with dry age-related macular degeneration. *Investigative ophthalmology & visual science* 2011;52(9):6743-48.

139. Guymer R, Luthert P, Bird A. Changes in Bruch's membrane and related structures with age. *Progress in retinal and eye research* 1999;18(1):59-90.

140. Spaide RF, Curcio CA, Zweifel SA. Drusen, an old but new frontier. *Retina (Philadelphia, Pa.)* 2010;30(8):1163.

141. Sarks S, Arnold J, Killingsworth M, et al. Early drusen formation in the normal and aging eye and their relation to age related maculopathy: a clinicopathological study. *British Journal of Ophthalmology* 1999;83(3):358-68.

142. Klein R, Meuer SM, Knudtson MD, et al. The epidemiology of retinal reticular drusen. *American journal of ophthalmology* 2008;145(2):317-26. e1.

143. Umeda S, Suzuki MT, Okamoto H, et al. Molecular composition of drusen and possible involvement of anti-retinal autoimmunity in two different forms of macular degeneration in cynomolgus monkey (Macaca fascicularis). *The FASEB journal* 2005;19(12):1683-85.

144. Del Priore LV, Kuo Y-H, Tezel TH. Age-related changes in human RPE cell density and apoptosis proportion in situ. *Investigative ophthalmology & visual science* 2002;43(10):3312-18.

145. Gao H, Hollyfield J. Aging of the human retina. Differential loss of neurons and retinal pigment epithelial cells. *Investigative ophthalmology & visual science* 1992;33(1):1-17.

146. Sarna T, Burke JM, Korytowski W, et al. Loss of melanin from human RPE with aging: possible role of melanin photooxidation. *Experimental eye research* 2003;76(1):89-98.

147. Boulton ME. Studying melanin and lipofuscin in RPE cell culture models. *Experimental eye research* 2014;126:61-67.

148. Katz ML, Robison Jr WG. Age-related changes in the retinal pigment epithelium of pigmented rats. *Experimental eye research* 1984;38(2):137-51.

149. Chen M, Rajapakse D, Fraczek M, et al. Retinal pigment epithelial cell multinucleation in the aging eye–a mechanism to repair damage and maintain homoeostasis. *Aging cell* 2016;15(3):436-45.

150. Ts'o MO, Friedman E. The retinal pigment epithelium: I. Comparative histology. *Archives of ophthalmology* 1967;78(5):641-49.

151. Bodenstein L, Sidman RL. Growth and development of the mouse retinal pigment epithelium: I. Cell and tissue morphometrics and topography of mitotic activity. *Developmental biology* 1987;121(1):192-204.

152. Peng S, Gan G, Qiu C, et al. Engineering a Blood-Retinal Barrier With Human Embryonic Stem Cell-Derived Retinal Pigment Epithelium: Transcriptome and Functional Analysis. *Stem cells translational medicine* 2013;2(7):534-44.

153. Rizzolo LJ, Peng S, Luo Y, et al. Integration of tight junctions and claudins with the barrier functions of the retinal pigment epithelium. *Progress in retinal and eye research* 2011;30(5):296-323.

154. Peng S, Rao VS, Adelman RA, et al. Claudin-19 and the barrier properties of the human retinal pigment epithelium. *Investigative ophthalmology & visual science* 2011;52(3):1392-403.

155. Konrad M, Schaller A, Seelow D, et al. Mutations in the tight-junction gene claudin 19 (CLDN19) are associated with renal magnesium wasting, renal failure, and severe ocular involvement. *The American Journal of Human Genetics* 2006;79(5):949-57.

156. Chiba H, Osanai M, Murata M, et al. Transmembrane proteins of tight junctions. *Biochimica et Biophysica Acta (BBA)-Biomembranes* 2008;1778(3):588-600.

157. Hughes B, Gallemore R, Miller S. Transport mechanisms in the retinal pigment epithelium. *The retinal pigment epithelium* 1998:103-34.

158. Rizzolo L. Polarity and the development of the outer blood-retinal barrier. *Histology and histopathology* 1997;12(4):1057-67.

159. Jablonski MM, Tombran-Tink J, Mrazek DA, et al. Pigment epithelium-derived factor supports normal development of photoreceptor neurons and opsin expression after retinal pigment epithelium removal. *Journal of Neuroscience* 2000;20(19):7149-57.

160. Marneros AG, Fan J, Yokoyama Y, et al. Vascular endothelial growth factor expression in the retinal pigment epithelium is essential for choriocapillaris development and visual function. *The American journal of pathology* 2005;167(5):1451-59.

161. Bhutto IA, McLeod DS, Hasegawa T, et al. Pigment epithelium-derived factor (PEDF) and vascular endothelial growth factor (VEGF) in aged human choroid and eyes with age-related macular degeneration. *Experimental eye research* 2006;82(1):99-110.

162. Chader G, Pepperberg D, Crouch R, et al. Retinoids and the retinal pigment epithelium. *The retinal pigment epithelium: Function and disease* 1998:135-51.

163. Kinnunen K, Petrovski G, Moe MC, et al. Molecular mechanisms of retinal pigment epithelium damage and development of age-related macular degeneration. *Acta ophthalmologica* 2012;90(4):299-309.

164. Ryhanen T, Hyttinen JM, Kopitz J, et al. Crosstalk between Hsp70 molecular chaperone, lysosomes and proteasomes in autophagy-mediated proteolysis in human retinal pigment epithelial cells. *J Cell Mol Med* 2009;13(9B):3616-31.

165. Ciechanover A. Proteolysis: from the lysosome to ubiquitin and the proteasome. *Nature reviews Molecular cell biology* 2005;6(1):79.

166. Keeling E, Lotery AJ, Tumbarello DA, et al. Impaired Cargo Clearance in the Retinal Pigment Epithelium (RPE) Underlies Irreversible Blinding Diseases. *Cells* 2018;7(2):16.

167. Young RW. The renewal of rod and cone outer segments in the rhesus monkey. *The Journal of cell biology* 1971;49(2):303-18.

168. Finnemann SC, Bonilha VL, Marmorstein AD, et al. Phagocytosis of rod outer segments by retinal pigment epithelial cells requires alpha(v)beta5 integrin for binding but not for internalization. *Proc Natl Acad Sci U S A* 1997;94(24):12932-7.

169. Feng W, Yasumura D, Matthes MT, et al. Mertk triggers uptake of photoreceptor outer segments during phagocytosis by cultured retinal pigment epithelial cells. *Journal of Biological Chemistry* 2002;277(19):17016-22.

170. D'Cruz PM, Yasumura D, Weir J, et al. Mutation of the receptor tyrosine kinase gene Mertk in the retinal dystrophic RCS rat. *Hum Mol Genet* 2000;9(4):645-51.

171. RAKOCZY PE, SARKS SH, DAW N, et al. Distribution of cathepsin D in human eyes with or without age-related maculopathy. *Experimental eye research* 1999;69(4):367-74.

172. Boulton M, Moriarty P, Jarvis-Evans J, et al. Regional variation and age-related changes of lysosomal enzymes in the human retinal pigment epithelium. *British Journal of Ophthalmology* 1994;78(2):125-29.

173. Dorey CK, Wu G, Ebenstein D, et al. Cell loss in the aging retina. Relationship to lipofuscin accumulation and macular degeneration. *Investigative ophthalmology & visual science* 1989;30(8):1691-99.

174. Kevany BM, Palczewski K. Phagocytosis of retinal rod and cone photoreceptors. *Physiology* 2010;25(1):8-15.

175. Roberts R, Barbieri M, Pryse K, et al. Endosome fusion in living cells overexpressing GFP-rab5. *J Cell Sci* 1999;112(21):3667-75.

176. Nielsen E, Severin F, Backer JM, et al. Rab5 regulates motility of early endosomes on microtubules. *Nature cell biology* 1999;1(6):376.

177. Mayor S, Pagano RE. Pathways of clathrin-independent endocytosis. *Nature reviews Molecular cell biology* 2007;8(8):603.

178. Bonifacino JS, Rojas R. Retrograde transport from endosomes to the trans-Golgi network. *Nature reviews Molecular cell biology* 2006;7(8):568.

179. Maxson ME, Grinstein S. The vacuolar-type H(+)-ATPase at a glance - more than a proton pump. *J Cell Sci* 2014;127.

180. Maxfield FR, Yamashiro DJ. Endosome acidification and the pathways of receptor-mediated endocytosis *Immunobiology of Proteins and Peptides IV*: Springer; 1987 p189-98.

181. Gerasimenko JV, Tepikin AV, Petersen OH, et al. Calcium uptake via endocytosis with rapid release from acidifying endosomes. *Current Biology* 1998;8(24):1335-38.

182. Sachse M, Urbé S, Oorschot V, et al. Bilayered clathrin coats on endosomal vacuoles are involved in protein sorting toward lysosomes. *Molecular biology of the cell* 2002;13(4):1313-28.

183. Raiborg C, Stenmark H. The ESCRT machinery in endosomal sorting of ubiquitylated membrane proteins. *Nature* 2009;458.

184. Rink J, Ghigo E, Kalaidzidis Y, et al. Rab conversion as a mechanism of progression from early to late endosomes. *Cell* 2005;122(5):735-49.

185. Poteryaev D, Datta S, Ackema K, et al. Identification of the switch in early-to-late endosome transition. *Cell* 2010;141.

186. Collinet C, Stöter M, Bradshaw CR, et al. Systems survey of endocytosis by multiparametric image analysis. *Nature* 2010;464(7286):243.

187. Bayer N, Schober D, Prchla E, et al. Effect of bafilomycin A1 and nocodazole on endocytic transport in HeLa cells: implications for viral uncoating and infection. *Journal of virology* 1998;72(12):9645-55.

188. Driskell OJ, Mironov A, Allan VJ, et al. Dynein is required for receptor sorting and the morphogenesis of early endosomes. *Nature cell biology* 2007;9(1):113.

189. Huotari J, Helenius A. Endosome maturation. *EMBO J* 2011;30.

190. Hu Y-B, Dammer BE, Ren R-J, et al. The endosomal-lysosomal system: from acidification and cargo sorting to neurodegeneration. *Translational Neurodegeneration* 2015;4(1):1-10.

191. Eskelinen E-L. New insights into the mechanisms of macroautophagy in mammalian cells. *International review of cell and molecular biology* 2008;266:207-47.

192. Kinchen JM, Ravichandran KS. Phagosome maturation: going through the acid test. *Nature reviews Molecular cell biology* 2008;9(10):781.

193. Seabra MC, Mules EH, Hume AN. Rab GTPases, intracellular traffic and disease. *Trends in molecular medicine* 2002;8(1):23-30.

194. Fairn GD, Grinstein S. How nascent phagosomes mature to become phagolysosomes. *Trends in immunology* 2012;33(8):397-405.

195. Duclos S, Diez R, Garin J, et al. Rab5 regulates the kiss and run fusion between phagosomes and endosomes and the acquisition of phagosome leishmanicidal properties in RAW 264.7 macrophages. *Journal of cell science* 2000;113(19):3531-41.

196. Luzio JP, Pryor PR, Bright NA. Lysosomes: fusion and function. *Nature reviews Molecular cell biology* 2007;8(8):622-32.

197. Saftig P, Klumperman J. Lysosome biogenesis and lysosomal membrane proteins: trafficking meets function. *Nature reviews Molecular cell biology* 2009;10(9):623-35.

198. Alroy J, Lyons JA. Lysosomal storage diseases. *Journal of Inborn Errors of Metabolism and Screening* 2014;2:2326409813517663.

199. Bandyopadhyay D, Cyphersmith A, Zapata JA, et al. Lysosome transport as a function of lysosome diameter. *PloS one* 2014;9(1):e86847.

200. Klettner A, Kauppinen A, Blasiak J, et al. Cellular and molecular mechanisms of age-related macular degeneration: from impaired autophagy to neovascularization. *The international journal of biochemistry & cell biology* 2013;45(7):1457-67.

201. Xu H, Ren D. Lysosomal physiology. *Annual review of physiology* 2015;77:57-80.

202. Perera RM, Zoncu R. The lysosome as a regulatory hub. *Annual review of cell and developmental biology* 2016;32:223-53.

203. Maejima I, Takahashi A, Omori H, et al. Autophagy sequesters damaged lysosomes to control lysosomal biogenesis and kidney injury. *The EMBO journal* 2013;32(17):2336-47.

204. Yu L, McPhee CK, Zheng L, et al. Termination of autophagy and reformation of lysosomes regulated by mTOR. *Nature* 2010;465(7300):942.

205. Galluzzi L, Baehrecke EH, Ballabio A, et al. Molecular definitions of autophagy and related processes. *The EMBO journal* 2017;36(13):1811-36.

206. Cuervo AM, Wong E. Chaperone-mediated autophagy: roles in disease and aging. *Cell research* 2014;24(1):92.

207. Berg TO, Fengsrud M, Strømhaug PE, et al. Isolation and Characterization of Rat Liver Amphisomes EVIDENCE FOR FUSION OF AUTOPHAGOSOMES WITH BOTH EARLY AND LATE ENDOSOMES. *Journal of Biological Chemistry* 1998;273(34):21883-92.

208. Heckmann BL, Boada-Romero E, Cunha LD, et al. LC3-associated phagocytosis and inflammation. *Journal of molecular biology* 2017;429(23):3561-76.

209. Dunn W. Studies on the mechanisms of autophagy: formation of the autophagic vacuole. *The Journal of cell biology* 1990;110(6):1923-33.

210. Platt FM, Boland B, van der Spoel AC. Lysosomal storage disorders: the cellular impact of lysosomal dysfunction. *J Cell Biol* 2012;199(5):723-34.

211. Von Figura K. Metachromatic leukodystrophy. *The metabolic and molecular bases of inherited disease* 2001:3695-724.

212. Biswas J, Nandi K, Sridharan S, et al. Ocular manifestation of storage diseases. *Current opinion in ophthalmology* 2008;19(6):507-11.

213. Spalton D, Taylor D, Sanders M. Juvenile Batten's disease: an ophthalmological assessment of 26 patients. *British Journal of Ophthalmology* 1980;64(10):726-32.

214. Winchester BG. Primary defects in lysosomal enzymes: Oxford University Press; 2004.

215. Hers H. α-Glucosidase deficiency in generalized glycogen-storage disease (Pompe's disease). *Biochemical Journal* 1963;86(1):11.

216. Ballabio A. Disease pathogenesis explained by basic science: lysosomal storage diseases as autophagocytic disorders. *International journal of clinical pharmacology and therapeutics* 2009;47:S34-8.

217. Raben N, Shea L, Hill V, et al. Monitoring autophagy in lysosomal storage disorders. *Methods in enzymology* 2009;453:417-49.

218. Ezaki J, Wolfe LS, Kominami E. Specific delay in the degradation of mitochondrial ATP synthase subunit c in late infantile neuronal ceroid lipofuscinosis is derived from cellular proteolytic dysfunction rather than structural alteration of subunit c. *Journal of neurochemistry* 1996;67(4):1677-87.

219. Terman A, Kurz T, Navratil M, et al. Mitochondrial turnover and aging of long-lived postmitotic cells: the mitochondrial–lysosomal axis theory of aging. *Antioxidants & redox signaling* 2010;12(4):503-35.

220. Green DR, Galluzzi L, Kroemer G. Mitochondria and the autophagy–inflammation–cell death axis in organismal aging. *Science* 2011;333(6046):1109-12.

221. Nakahira K, Haspel JA, Rathinam VA, et al. Autophagy proteins regulate innate immune responses by inhibiting the release of mitochondrial DNA mediated by the NALP3 inflammasome. *Nature immunology* 2011;12(3):222-30.

222. Zhou R, Yazdi AS, Menu P, et al. A role for mitochondria in NLRP3 inflammasome activation. *Nature* 2011;469(7329):221-25.

223. Nixon RA, Cataldo AM. Lysosomal system pathways: genes to neurodegeneration in Alzheimer's disease. *Journal of Alzheimer's Disease* 2006;9(s3):277-89.

224. Jin L-W, Maezawa I, Vincent I, et al. Intracellular accumulation of amyloidogenic fragments of amyloid-β precursor protein in neurons with Niemann-Pick type C defects is associated with endosomal abnormalities. *The American journal of pathology* 2004;164(3):975-85.

225. Nixon RA. Niemann-Pick Type C disease and Alzheimer's disease: the APP-endosome connection fattens up. *The American journal of pathology* 2004;164(3):757-61.

226. Rubinsztein DC. The roles of intracellular protein-degradation pathways in neurodegeneration. *Nature* 2006;443(7113):780.

227. Pan T, Kondo S, Le W, et al. The role of autophagy-lysosome pathway in neurodegeneration associated with Parkinson's disease. *Brain* 2008;131(8):1969-78.

228. Taylor JP, Hardy J, Fischbeck KH. Toxic proteins in neurodegenerative disease. *Science* 2002;296(5575):1991-95.

229. Braak H, Del Tredici K, Rüb U, et al. Staging of brain pathology related to sporadic Parkinson's disease. *Neurobiology of aging* 2003;24(2):197-211.

230. McNaught KSP, Olanow CW. Protein aggregation in the pathogenesis of familial and sporadic Parkinson's disease. *Neurobiology of aging* 2006;27(4):530-45.

231. Lin Chua CE, Tang BL. α-synuclein and Parkinson's disease: the first roadblock. *Journal of cellular and molecular medicine* 2006;10(4):828-37.

232. Polymeropoulos MH, Lavedan C, Leroy E, et al. Mutation in the α-synuclein gene identified in families with Parkinson's disease. *Science* 1997;276(5321):2045-47.

233. Krüger R, Kuhn W, Müller T, et al. AlaSOPro mutation in the gene encoding α-synuclein in Parkinson's disease. *Nature genetics* 1998;18(2):106-08.

234. Zarranz JJ, Alegre J, Gómez-Esteban JC, et al. The new mutation, E46K, of α-synuclein causes parkinson and Lewy body dementia. *Annals of Neurology: Official Journal of the American Neurological Association and the Child Neurology Society* 2004;55(2):164-73.

235. Ravikumar B, Duden R, Rubinsztein DC. Aggregate-prone proteins with polyglutamine and polyalanine expansions are degraded by autophagy. *Human molecular genetics* 2002;11(9):1107-17.

236. Webb JL, Ravikumar B, Atkins J, et al. α-Synuclein is degraded by both autophagy and the proteasome. *Journal of Biological Chemistry* 2003;278(27):25009-13.

237. Ravikumar B, Vacher C, Berger Z, et al. Inhibition of mTOR induces autophagy and reduces toxicity of polyglutamine expansions in fly and mouse models of Huntington disease. *Nature genetics* 2004;36(6):585.

238. Suzuki K, Iseki E, Togo T, et al. Neuronal and glial accumulation of α-and β-synucleins in human lipidoses. *Acta neuropathologica* 2007;114(5):481-89.

239. Settembre C, Fraldi A, Jahreiss L, et al. A block of autophagy in lysosomal storage disorders. *Human molecular genetics* 2007;17(1):119-29.

240. Winslow AR, Chen C-W, Corrochano S, et al. α-Synuclein impairs macroautophagy: implications for Parkinson's disease. *The Journal of cell biology* 2010;190(6):1023-37.

241. Singleton A, Farrer M, Johnson J, et al. α-Synuclein locus triplication causes Parkinson's disease. *Science* 2003;302(5646):841-41.

242. Cuervo AM, Stefanis L, Fredenburg R, et al. Impaired degradation of mutant α-synuclein by chaperone-mediated autophagy. *Science* 2004;305(5688):1292-95.

243. Stoka V, Turk V, Turk B. Lysosomal cathepsins and their regulation in aging and neurodegeneration. *Ageing research reviews* 2016;32:22-37.

244. Aufschnaiter A, Kohler V, Büttner S. Taking out the garbage: cathepsin D and calcineurin in neurodegeneration. *Neural regeneration research* 2017;12(11):1776.

245. Nixon RA, Yang DS, Lee JH. Neurodegenerative lysosomal disorders: a continuum from development to late age. *Autophagy* 2008;4(5):590-9.

246. Cuervo AM, Dice JF. Age-related decline in chaperone-mediated autophagy. *Journal of Biological Chemistry* 2000;275(40):31505-13.

247. Tan J, Evin G. Beta-site APP-cleaving enzyme 1 trafficking and Alzheimer's disease pathogenesis. *J Neurochem* 2012;120.

248. Wu J, Petralia RS, Kurushima H, et al. Arc/Arg3.1 regulates an endosomal pathway essential for activity-dependent beta-amyloid generation. *Cell* 2011;147.

249. Neefjes J, Kant R. Stuck in traffic: an emerging theme in diseases of the nervous system. *Trends Neurosci* 2014;37.

250. Margallo-Lana M, Morris C, Gibson A, et al. Influence of the amyloid precursor protein locus on dementia in Down syndrome. *Neurology* 2004;62(11):1996-98.

251. Prasher V, Farrer MJ, Kessling AM, et al. Molecular mapping of Alzheimer-type dementia in Down's syndrome. *Annals of neurology* 1998;43(3):380-83.

252. Cataldo AM, Petanceska S, Peterhoff CM, et al. App gene dosage modulates endosomal abnormalities of Alzheimer's disease in a segmental trisomy 16 mouse model of down syndrome. *Journal of Neuroscience* 2003;23(17):6788-92.

253. Cataldo AM, Barnett JL, Pieroni C, et al. Increased neuronal endocytosis and protease delivery to early endosomes in sporadic Alzheimer's disease: neuropathologic evidence for a mechanism of increased beta-amyloidogenesis. *J Neurosci* 1997;17.

254. Ji Z-S, Miranda RD, Newhouse YM, et al. Apolipoprotein E4 potentiates amyloid β peptide-induced lysosomal leakage and apoptosis in neuronal cells. *Journal of Biological Chemistry* 2002;277(24):21821-28.

255. Nixon RA, Cataldo AM, Mathews PM. The endosomal-lysosomal system of neurons in Alzheimer's disease pathogenesis: a review. *Neurochemical research* 2000;25(9-10):1161-72.

256. Cataldo AM, Barnett JL, Pieroni C, et al. Increased neuronal endocytosis and protease delivery to early endosomes in sporadic Alzheimer’s disease: neuropathologic evidence for a mechanism of increased β-amyloidogenesis. *Journal of Neuroscience* 1997;17(16):6142-51.

257. Cataldo AM, Peterhoff CM, Troncoso JC, et al. Endocytic pathway abnormalities precede amyloid β deposition in sporadic Alzheimer’s disease and Down syndrome: differential effects of APOE genotype and presenilin mutations. *The American journal of pathology* 2000;157(1):277-86.

258. Li N, Ragheb K, Lawler G, et al. Mitochondrial complex I inhibitor rotenone induces apoptosis through enhancing mitochondrial reactive oxygen species production. *Journal of Biological Chemistry* 2003;278(10):8516-25.

259. Haass C, Schlossmacher MG, Hung AY, et al. Amyloid β-peptide is produced by cultured cells during normal metabolism. *Nature* 1992;359(6393):322-25.

260. Koo EH, Squazzo SL. Evidence that production and release of amyloid beta-protein involves the endocytic pathway. *Journal of Biological Chemistry* 1994;269(26):17386-89.

261. Chyung AS, Greenberg BD, Cook DG, et al. Novel β-secretase cleavage of β-amyloid precursor protein in the endoplasmic reticulum/intermediate compartment of NT2N cells. *The Journal of cell biology* 1997;138(3):671-80.

262. Greenfield JP, Tsai J, Gouras GK, et al. Endoplasmic reticulum and trans-Golgi network generate distinct populations of Alzheimer β-amyloid peptides. *Proceedings of the National Academy of Sciences* 1999;96(2):742-47.

263. Thinakaran G, Teplow DB, Siman R, et al. Metabolism of the Swedish Amyloid Precursor Protein Variant in Neuro2a (N2a) Cells EVIDENCE THAT CLEAVAGE AT THE "β-SECRETASE" SITE OCCURS IN THE GOLGI APPARATUS. *Journal of Biological Chemistry* 1996;271(16):9390-97.

264. Vassar R, Bennett BD, Babu-Khan S, et al. Beta-secretase cleavage of Alzheimer's amyloid precursor protein by the transmembrane aspartic protease BACE. *Science* 1999;286.

265. Xu H, Sweeney D, Wang R, et al. Generation of Alzheimer β-amyloid protein in the trans-Golgi network in the apparent absence of vesicle formation. *Proceedings of the National Academy of Sciences* 1997;94(8):3748-52.

266. Yu WH, Cuervo AM, Kumar A, et al. Macroautophagy—a novel β-amyloid peptide-generating pathway activated in Alzheimer's disease. *J Cell Biol* 2005;171(1):87-98.

267. Yu W, Kumar A, Peterhoff C, et al. Autophagic vacuoles are enriched in amyloid precursor protein-secretase activities: implications for β-amyloid peptide over-production and localization in Alzheimer's disease. *The international journal of biochemistry & cell biology* 2004;36(12):2531-40.

268. Takahashi RH, Milner TA, Li F, et al. Intraneuronal Alzheimer Aβ42 accumulates in multivesicular bodies and is associated with synaptic pathology. *The American journal of pathology* 2002;161(5):1869-79.

269. Benzing WC, Mufson EJ, Armstrong DM. Alzheimer's disease-like dystrophic neurites characteristically associated with senile plaques are not found within other neurodegenerative disease unless amyloid β-protein deposition is present. *Brain research* 1993;606(1):10-18.

270. Suzuki K, Terry RD. Fine structural localization of acid phosphatase in senile plaques in Alzheimer's presenile dementia. *Acta neuropathologica* 1967;8(3):276-84.

271. Boland B, Kumar A, Lee S, et al. Autophagy induction and autophagosome clearance in neurons: relationship to autophagic pathology in Alzheimer's disease. *Journal of Neuroscience* 2008;28(27):6926-37.

272. Zweifel SA, Imamura Y, Spaide TC, et al. Prevalence and significance of subretinal drusenoid deposits (reticular pseudodrusen) in age-related macular degeneration. *Ophthalmology* 2010;117(9):1775-81.

273. Terman A, Gustafsson B, Brunk U. Autophagy, organelles and ageing. *The Journal of pathology* 2007;211(2):134-43.

274. Finnemann SC, Leung LW, Rodriguez-Boulan E. The lipofuscin component A2E selectively inhibits phagolysosomal degradation of photoreceptor phospholipid by the retinal pigment epithelium. *Proceedings of the National Academy of Sciences* 2002;99(6):3842-47.

275. Poliakov E, Strunnikova NV, Jiang J-k, et al. Multiple A2E treatments lead to melanization of rod outer segment–challenged ARPE-19 cells. *Molecular vision* 2014;20:285.

276. Kaarniranta K, Salminen A, Haapasalo A, et al. Age-related macular degeneration (AMD): Alzheimer's disease in the eye. *J Alzheimers Dis* 2011.

277. Sundelin S, Wihlmark U, Nilsson SEG, et al. Lipofuscin accumulation in cultured retinal pigment epithelial cells reduces their phagocytic capacity. *Current eye research* 1998;17(8):851-57.

278. Sitte N, Huber M, Grune T, et al. Proteasome inhibition by lipofuscin/ceroid during postmitotic aging of fibroblasts. *The FASEB Journal* 2000;14(11):1490-98.

279. Rodríguez-Muela N, Koga H, García-Ledo L, et al. Balance between autophagic pathways preserves retinal homeostasis. *Aging cell* 2013;12(3):478-88.

280. Nowak JZ. Age-related macular degeneration (AMD): pathogenesis and therapy. *Pharmacological Reports* 2006;58(3):353.

281. Ambati J, Fowler BJ. Mechanisms of age-related macular degeneration. *Neuron* 2012;75(1):26-39.

282. Tanaka Y, Aleksunes LM, Yeager RL, et al. NF-E2-related factor 2 inhibits lipid accumulation and oxidative stress in mice fed a high-fat diet. *Journal of Pharmacology and Experimental Therapeutics* 2008;325(2):655-64.

283. Dunn K, Aotaki-Keen A, Putkey F, et al. ARPE-19, a human retinal pigment epithelial cell line with differentiated properties. *Experimental eye research* 1996;62(2):155-70.

284. Ahmado A, Carr A-J, Vugler AA, et al. Induction of differentiation by pyruvate and DMEM in the human retinal pigment epithelium cell line ARPE-19. *Investigative ophthalmology & visual science* 2011;52(10):7148-59.

285. Bergmann M, Holz F, Kopitz J. Lysosomal stress and lipid peroxidation products induce VEGF-121 and VEGF-165 expression in ARPE-19 cells. *Graefe's archive for clinical and experimental ophthalmology* 2011;249(10):1477-83.

286. Ballinger SW, Van Houten B, Conklin CA, et al. Hydrogen peroxide causes significant mitochondrial DNA damage in human RPE cells. *Experimental eye research* 1999;68(6):765-72.

287. Hall MA, Toshka. Kinetic Studies of Rod Outer Segment Binding and Ingestion by Cultured Rat RPE Cells. *Experimental eye research* 1987;45:907-22.

288. Krohne TU, Stratmann NK, Kopitz J, et al. Effects of lipid peroxidation products on lipofuscinogenesis and autophagy in human retinal pigment epithelial cells. *Experimental eye research* 2010;90(3):465-71.

289. Costes SV, Daelemans D, Cho EH, et al. Automatic and quantitative measurement of protein-protein colocalization in live cells. *Biophysical journal* 2004;86(6):3993-4003.

290. Cardona A, Saalfeld S, Schindelin J, et al. TrakEM2 software for neural circuit reconstruction. *PloS one* 2012;7(6):e38011.

291. White JG, Southgate E, Thomson JN, et al. The structure of the nervous system of the nematode Caenorhabditis elegans: the mind of a worm. *Phil. Trans. R. Soc. Lond* 1986;314:1-340.

292. Goggin P, Zygalakis K, Oreffo R, et al. High-resolution 3D imaging of osteocytes and computational modelling in mechanobiology: insights on bone development, ageing, health and disease. *European cells & materials* 2016;31:264.

293. Sinha D, Valapala M, Shang P, et al. Lysosomes: Regulators of autophagy in the retinal pigmented epithelium. *Experimental eye research* 2016;144:46-53.

294. Kaarniranta K, Sinha D, Blasiak J, et al. Autophagy and heterophagy dysregulation leads to retinal pigment epithelium dysfunction and development of age-related macular degeneration. *Autophagy* 2013;9(7):973-84.

295. Bahr BA, Wisniewski ML, Butler D. Positive lysosomal modulation as a unique strategy to treat age-related protein accumulation diseases. *Rejuvenation Res* 2012;15(2):189-97.

296. Feher J, Kovacs I, Artico M, et al. Mitochondrial alterations of retinal pigment epithelium in age-related macular degeneration. *Neurobiology of aging* 2006;27(7):983-93.

297. Briggman KL, Denk W. Towards neural circuit reconstruction with volume electron microscopy techniques. *Current opinion in neurobiology* 2006;16(5):562-70.

298. Clarke NI, Royle SJ. Correlating light microscopy with serial block face scanning electron microscopy to study mitotic spindle architecture. *Methods in cell biology* 2018;145:29-43.

299. Veleri S, Lazar CH, Chang B, et al. Biology and therapy of inherited retinal degenerative disease: insights from mouse models. *Disease models & mechanisms* 2015;8(2):109-29.

300. Deerinck TJ, Bushong EA, Thor A, et al. NCMIR methods for 3D EM: a new protocol for preparation of biological specimens for serial block face scanning electron microscopy. *Microscopy* 2010:6-8.

301. Telegina DV, Kozhevnikova OS, Bayborodin SI, et al. Contributions of age-related alterations of the retinal pigment epithelium and of glia to the AMD-like pathology in OXYS rats. *Scientific reports* 2017;7:41533.

302. Powner MB, Scott A, Zhu M, et al. Basement membrane changes in capillaries of the ageing human retina. *British Journal of Ophthalmology* 2011;95(9):1316-22.

303. Starnes AC, Huisingh C, MCGWIN G, et al. Multi-nucleate retinal pigment epithelium cells of the human macula exhibit a characteristic and highly specific distribution. *Visual neuroscience* 2016;33.

304. Hollenberg MJ, Lea PJ. High resolution scanning electron microscopy of the retinal pigment epithelium and Bruch's layer. *Investigative ophthalmology & visual science* 1988;29(9):1380-89.

305. Marmor MF, Wolfensberger T. The retinal pigment epithelium. *Function and disease. New York: Oxford* 1998:103-34.

306. Mazzoni F, Safa H, Finnemann SC. Understanding photoreceptor outer segment phagocytosis: Use and utility of RPE cells in culture. *Experimental eye research* 2014;126:51-60.

307. Curcio CA, Messinger JD, Sloan KR, et al. Subretinal drusenoid deposits in non-neovascular age-related macular degeneration: morphology, prevalence, topography, and biogenesis model. *Retina (Philadelphia, Pa.)* 2013;33(2).

308. Russell SR, Mullins RF, Schneider BL, et al. Location, substructure, and composition of basal laminar drusen compared with drusen associated with aging and age-related macular degeneration. *American journal of ophthalmology* 2000;129(2):205-14.

309. Green WR, McDonnell PJ, Yeo JH. Pathologic features of senile macular degeneratlon. *Ophthalmology* 1985;92(5):615-27.

310. Sarks S, Cherepanoff S, Killingsworth M, et al. Relationship of basal laminar deposit and membranous debris to the clinical presentation of early age-related macular degeneration. *Investigative ophthalmology & visual science* 2007;48(3):968-77.

311. Al-Hussaini H, Schneiders M, Lundh P, et al. Drusen are associated with local and distant disruptions to human retinal pigment epithelium cells. *Exp Eye Res* 2009;88(3):610-2.

312. Ramrattan RS, van der Schaft TL, Mooy CM, et al. Morphometric analysis of Bruch's membrane, the choriocapillaris, and the choroid in aging. *Investigative ophthalmology & visual science* 1994;35(6):2857-64.

313. Espinosa-Heidmann DG, Suner IJ, Catanuto P, et al. Cigarette smoke–related oxidants and the development of sub-RPE deposits in an experimental animal model of dry AMD. *Investigative ophthalmology & visual science* 2006;47(2):729-37.

314. Oh Y, Oh I, Morimoto J, et al. Osteopontin has a crucial role in osteoclast-like multinucleated giant cell formation. *Journal of cellular biochemistry* 2014;115(3):585-95.

315. Park JK, Askin F. Osteoclast-like multinucleated giant cells in sinonasal inflammation of granulomatosis with polyangiitis (Wegener's granulomatosis). *Clin. Exp. Rheumatol* 2013;31:S28-S31.

316. Hornik TC, Neniskyte U, Brown GC. Inflammation induces multinucleation of Microglia via PKC inhibition of cytokinesis, generating highly phagocytic multinucleated giant cells. *Journal of neurochemistry* 2014;128(5):650-61.

317. Woldringh C, Huls P, Vischer N. Volume growth of daughter and parent cells during the cell cycle of Saccharomyces cerevisiae a/alpha as determined by image cytometry. *Journal of bacteriology* 1993;175(10):3174-81.

318. Chen H-C, Zhu Y-T, Chen S-Y, et al. Wnt signaling induces epithelial–mesenchymal transition with proliferation in ARPE-19 cells upon loss of contact inhibition. *Laboratory Investigation* 2012;92(5):676.

319. Saika S, Yamanaka O, Nishikawa-Ishida I, et al. Effect of Smad7 Gene Overexpression on Transforming Growth Factor β–Induced Retinal Pigment Fibrosis in a Proliferative Vitreoretinopathy Mouse Model. *Archives of ophthalmology* 2007;125(5):647-54.

320. Ebina M, Takahashi T, Chiba T, et al. Cellular hypertrophy and hyperplasia of airway smooth muscle underlying bronchial asthma. *Am Rev Respir Dis* 1993;148(720):6.

321. Wang Y, Huang S, Sah VP, et al. Cardiac muscle cell hypertrophy and apoptosis induced by distinct members of the p38 mitogen-activated protein kinase family. *Journal of Biological Chemistry* 1998;273(4):2161-68.

322. Brunelle JK, Bell EL, Quesada NM, et al. Oxygen sensing requires mitochondrial ROS but not oxidative phosphorylation. *Cell metabolism* 2005;1(6):409-14.

323. Guzy RD, Hoyos B, Robin E, et al. Mitochondrial complex III is required for hypoxia-induced ROS production and cellular oxygen sensing. *Cell metabolism* 2005;1(6):401-08.

324. Scherz-Shouval R, Shvets E, Fass E, et al. Reactive oxygen species are essential for autophagy and specifically regulate the activity of Atg4. *The EMBO journal* 2007;26(7):1749-60.

325. Bulua AC, Simon A, Maddipati R, et al. Mitochondrial reactive oxygen species promote production of proinflammatory cytokines and are elevated in TNFR1-associated periodic syndrome (TRAPS). *Journal of Experimental Medicine* 2011;208(3):519-33.

326. Winkler BS, Boulton ME, Gottsch JD, et al. Oxidative damage and age-related macular degeneration. *Molecular vision* 1999;5:32.

327. Jager RD, Mieler WF, Miller JW. Age-related macular degeneration. *New England Journal of Medicine* 2008;358(24):2606-17.

328. Jensen P. Antimycin-insensitive oxidation of succinate and reduced nicotinamide-adenine dinucleotide in electron-transport particles I. pH dependency and hydrogen peroxide formation. *Biochimica et Biophysica Acta (BBA)-Enzymology and Biological Oxidation* 1966;122(2):157-66.

329. Ershov AV, Bazan NG. Photoreceptor phagocytosis selectively activates PPARγ expression in retinal pigment epithelial cells. *Journal of neuroscience research* 2000;60(3):328-37.

330. Taylor HR, West S, Muñoz B, et al. The long-term effects of visible light on the eye. *Archives of ophthalmology* 1992;110(1):99-104.

331. Taylor HR, Munoz B, West S, et al. Visible light and risk of age-related macular degeneration. *Transactions of the American Ophthalmological Society* 1990;88:163.

332. Bienert GP, Møller AL, Kristiansen KA, et al. Specific aquaporins facilitate the diffusion of hydrogen peroxide across membranes. *Journal of Biological Chemistry* 2007;282(2):1183-92.

333. Azad MB, Chen Y, Gibson SB. Regulation of autophagy by reactive oxygen species (ROS): implications for cancer progression and treatment. *Antioxidants & redox signaling* 2009;11(4):777-90.

334. Johansson I, Monsen VT, Pettersen K, et al. The marine n-3 PUFA DHA evokes cytoprotection against oxidative stress and protein misfolding by inducing autophagy and NFE2L2 in human retinal pigment epithelial cells. *Autophagy* 2015;11(9):1636-51.

335. Wang AL, Lukas TJ, Yuan M, et al. Autophagy, exosomes and drusen formation in age-related macular degeneration. *Autophagy* 2009;5(4):563-64.

336. Handa JT. How does the macula protect itself from oxidative stress? *Molecular aspects of medicine* 2012;33(4):418-35.

337. Braun S, Hanselmann C, Gassmann MG, et al. Nrf2 transcription factor, a novel target of keratinocyte growth factor action which regulates gene expression and inflammation in the healing skin wound. *Molecular and cellular biology* 2002;22(15):5492-505.

338. Li J, Stein TD, Johnson JA. Genetic dissection of systemic autoimmune disease in Nrf2-deficient mice. *Physiological genomics* 2004;18(3):261-72.

339. Chou MY, Hartvigsen K, Hansen L, et al. Oxidation-specific epitopes are important targets of innate immunity. *Journal of internal medicine* 2008;263(5):479-88.

340. Gu X, Meer SG, Miyagi M, et al. Carboxyethylpyrrole protein adducts and autoantibodies, biomarkers for age-related macular degeneration. *Journal of Biological Chemistry* 2003.

341. Crabb JW, Miyagi M, Gu X, et al. Drusen proteome analysis: an approach to the etiology of age-related macular degeneration. *Proceedings of the National Academy of Sciences* 2002;99(23):14682-87.

342. Hollyfield JG, Bonilha VL, Rayborn ME, et al. Oxidative damage–induced inflammation initiates age-related macular degeneration. *Nature medicine* 2008;14(2):194.

343. Rangasamy T, Cho CY, Thimmulappa RK, et al. Genetic ablation of Nrf2 enhances susceptibility to cigarette smoke–induced emphysema in mice. *The Journal of clinical investigation* 2004;114(9):1248-59.

344. Smith C, Hansch C. The relative toxicity of compounds in mainstream cigarette smoke condensate. *Food and Chemical Toxicology* 2000;38(7):637-46.

345. Cross CE, O'NEIL CA, Reznick AZ, et al. Cigarette Smoke Oxidation of Human Plasma Constituents a. *Annals of the New York Academy of Sciences* 1993;686(1):72-89.

346. Lykkesfeldt J, Christen S, Wallock LM, et al. Ascorbate is depleted by smoking and repleted by moderate supplementation: a study in male smokers and nonsmokers with matched dietary antioxidant intakes–. *The American journal of clinical nutrition* 2000;71(2):530-36.

347. O'Neill CA, Halliwell B, Davis P, et al. Aldehyde-induced protein modifications in human plasma: protection by glutathione and dihydrolipoic acid. *The Journal of laboratory and clinical medicine* 1994;124(3):359-70.

348. Uranga RM, Bruce-Keller AJ, Morrison CD, et al. Intersection between metabolic dysfunction, high fat diet consumption, and brain aging. *Journal of neurochemistry* 2010;114(2):344-61.

349. Salas IH, Weerasekera A, Ahmed T, et al. High fat diet treatment impairs hippocampal long-term potentiation without alterations of the core neuropathological features of Alzheimer disease. *Neurobiology of disease* 2018;113:82-96.

350. Hogg RE, Woodside JV, McGrath A, et al. Mediterranean diet score and its association with age-related macular degeneration: the European eye study. *Ophthalmology* 2017;124(1):82-89.

351. Merle BM, Silver RE, Rosner B, et al. Adherence to a Mediterranean diet, genetic susceptibility, and progression to advanced macular degeneration: a prospective cohort study–3. *The American journal of clinical nutrition* 2015;102(5):1196-206.

352. Curcio CA. Antecedents of soft drusen, the specific deposits of age-related macular degeneration, in the biology of human macula. *Investigative ophthalmology & visual science* 2018;59(4):AMD182-AMD94.

353. Yuzefovych LV, Musiyenko SI, Wilson GL, et al. Mitochondrial DNA damage and dysfunction, and oxidative stress are associated with endoplasmic reticulum stress, protein degradation and apoptosis in high fat diet-induced insulin resistance mice. *PloS one* 2013;8(1):e54059.

354. Furukawa S, Fujita T, Shimabukuro M, et al. Increased oxidative stress in obesity and its impact on metabolic syndrome. *The Journal of clinical investigation* 2017;114(12):1752-61.

355. Lee J, Ellis JM, Wolfgang MJ. Adipose fatty acid oxidation is required for thermogenesis and potentiates oxidative stress-induced inflammation. *Cell reports* 2015;10(2):266-79.

356. Speakman JR. Use of high-fat diets to study rodent obesity as a model of human obesity. *Int J Obes (Lond), doi* 2019;10.

357. Rudolf M, Curcio CA. Esterified cholesterol is highly localized to Bruch's membrane, as revealed by lipid histochemistry in wholemounts of human choroid. *Journal of Histochemistry & Cytochemistry* 2009;57(8):731-39.

358. Sakaguchi H, Miyagi M, Shadrach KG, et al. Clusterin is present in drusen in age-related macular degeneration. *Experimental eye research* 2002;74(4):547.

359. Oh SB, Kim MS, Park S, et al. Clusterin contributes to early stage of Alzheimer's disease pathogenesis. *Brain Pathol* 2018.

360. Hoffmann S, Friedrichs U, Eichler W, et al. Advanced glycation end products induce choroidal endothelial cell proliferation, matrix metalloproteinase-2 and VEGF upregulation in vitro. *Graefe's archive for clinical and experimental ophthalmology* 2002;240(12):996-1002.

361. Christensen DR, Brown FE, Cree AJ, et al. Sorsby fundus dystrophy–A review of pathology and disease mechanisms. *Experimental eye research* 2017;165:35-46.

362. Kim S, Sadda S, Humayun M, et al. Morphometric analysis of the macula in eyes with geographic atrophy due to age-related macular degeneration. *Retina* 2002;22(4):464-70.

363. Curcio CA, Medeiros NE, Millican CL. Photoreceptor loss in age-related macular degeneration. *Investigative ophthalmology & visual science* 1996;37(7):1236-49.

364. Sadigh S, Cideciyan AV, Sumaroka A, et al. Abnormal thickening as well as thinning of the photoreceptor layer in intermediate age-related macular degeneration. *Investigative ophthalmology & visual science* 2013;54(3):1603-12.

365. Hartmann KI, Gomez ML, Bartsch D-U, et al. Effect of change in drusen evolution on photoreceptor inner segment/outer segment junction. *Retina (Philadelphia, Pa.)* 2012;32(8):1492.

366. Jacobson SG, Aleman TS, Cideciyan AV, et al. Human cone photoreceptor dependence on RPE65 isomerase. *Proceedings of the National Academy of Sciences* 2007;104(38):15123-28.

367. Chui TY, Song H, Clark CA, et al. Cone photoreceptor packing density and the outer nuclear layer thickness in healthy subjects. *Investigative ophthalmology & visual science* 2012;53(7):3545-53.

368. Sung KR, Wollstein G, Bilonick RA, et al. Effects of age on optical coherence tomography measurements of healthy retinal nerve fiber layer, macula, and optic nerve head. *Ophthalmology* 2009;116(6):1119-24.

369. Jacobson SG, Cideciyan AV. Treatment possibilities for retinitis pigmentosa. *New England Journal of Medicine* 2010;363(17):1669-71.

370. Kishan AU, Modjtahedi BS, Martins EN, et al. Lipids and age-related macular degeneration. *Survey of ophthalmology* 2011;56(3):195-213.

371. Demirkaya N, van Dijk HW, van Schuppen SM, et al. Effect of age on individual retinal layer thickness in normal eyes as measured with spectral-domain optical coherence tomography. *Investigative ophthalmology & visual science* 2013;54(7):4934-40.

372. Karampelas M, Sim DA, Keane PA, et al. Evaluation of retinal pigment epithelium–Bruch's membrane complex thickness in dry age-related macular degeneration using optical coherence tomography. *British Journal of Ophthalmology* 2013:bjophthalmol-2013-303219.

373. Bressler NM, Munoz B, Maguire MG, et al. Five-year incidence and disappearance of drusen and retinal pigment epithelial abnormalities: Waterman study. *Archives of ophthalmology* 1995;113(3):301-08.

374. Bressler NM, Silva JC, Bressler SB, et al. Clinicopathologic correlation of drusen and retinal pigment epithelial abnormalities in age-related macular degeneration. *Retina (Philadelphia, Pa.)* 1994;14(2):130-42.

375. Rogala J, Zangerl B, Assaad N, et al. In vivo quantification of retinal changes associated with drusen in age-related macular degeneration. *Investigative ophthalmology & visual science* 2015;56(3):1689-700.

376. Schuman SG, Koreishi AF, Farsiu S, et al. Photoreceptor layer thinning over drusen in eyes with age-related macular degeneration imaged in vivo with spectral-domain optical coherence tomography. *Ophthalmology* 2009;116(3):488-96. e2.

377. Acton JH, Smith RT, Hood DC, et al. Relationship between retinal layer thickness and the visual field in early age-related macular degeneration. *Investigative ophthalmology & visual science* 2012;53(12):7618-24.

378. Weber BH, Vogt G, Pruett RC, et al. Mutations in the tissue inhibitor of metalloproteinases-3 (TIMP3) in patients with Sorsby's fundus dystrophy. *Nature genetics* 1994;8(4):352.

379. Fariss RN, Apte SS, Luthert PJ, et al. Accumulation of tissue inhibitor of metalloproteinases-3 in human eyes with Sorsby's fundus dystrophy or retinitis pigmentosa. *British Journal of Ophthalmology* 1998;82(11):1329-34.

380. Felbor U, Doepner D, Schneider U, et al. Evaluation of the gene encoding the tissue inhibitor of metalloproteinases-3 in various maculopathies. *Investigative ophthalmology & visual science* 1997;38(6):1054-59.

381. De La Paz M, Pericak-Vance MA, Lennon F, et al. Exclusion of TIMP3 as a candidate locus in age-related macular degeneration. *Investigative ophthalmology & visual science* 1997;38(6):1060-65.

382. Kamei M, Hollyfield JG. TIMP-3 in Bruch's membrane: changes during aging and in age-related macular degeneration. *Investigative ophthalmology & visual science* 1999;40(10):2367-75.

383. Spraul CW, Lang GE, Grossniklaus HE, et al. Histologic and morphometric analysis of the choroid, Bruch's membrane, and retinal pigment epithelium in postmortem eyes with age-related macular degeneration and histologic examination of surgically excised choroidal neovascular membranes. *Survey of ophthalmology* 1999;44:S10-S32.

384. Spraul CW, Lang GE, Grossniklaus HE. Morphometric analysis of the choroid, Bruch's membrane, and retinal pigment epithelium in eyes with age-related macular degeneration. *Investigative ophthalmology & visual science* 1996;37(13):2724-35.

385. Bird A, Marshall J. Retinal pigment epithelial detachments in the elderly. *Transactions of the ophthalmological societies of the United Kingdom* 1986;105:674-82.

386. Fernandez-Godino R, Pierce EA, Garland DL. Extracellular matrix alterations and deposit formation in AMD *Retinal Degenerative Diseases*: Springer; 2016 p53-58.

387. Hu X, Plomp AS, van Soest S, et al. Pseudoxanthoma elasticum: a clinical, histopathological, and molecular update. *Survey of ophthalmology* 2003;48(4):424-38.

388. Chong NV, Keonin J, Luthert PJ, et al. Decreased thickness and integrity of the macular elastic layer of Bruch's membrane correspond to the distribution of lesions associated with age-related macular degeneration. *The American journal of pathology* 2005;166(1):241-51.

389. Beattie JR, Pawlak AM, Boulton ME, et al. Multiplex analysis of age-related protein and lipid modifications in human Bruch's membrane. *The FASEB Journal* 2010;24(12):4816-24.

390. Curcio CA, Johnson M. Structure, function, and pathology of Bruch's membrane. *Elastic* 2012;146(152):210-13.

391. Priore LVD, Geng L, Tezel TH, et al. Extracellular matrix ligands promote RPE attachment to inner Bruch's membrane. *Current eye research* 2002;25(2):79-89.

392. Stitt AW. AGEs and diabetic retinopathy. *Investigative ophthalmology & visual science* 2010;51(10):4867-74.

393. Cannizzaro L, Rossoni G, Savi F, et al. Regulatory landscape of AGE-RAGE-oxidative stress axis and its modulation by PPARγ activation in high fructose diet-induced metabolic syndrome. *Nutrition & metabolism* 2017;14(1):5.

394. Boulton M, Docchio F, Dayhaw-Barker P, et al. Age-related changes in the morphology, absorption and fluorescence of melanosomes and lipofuscin granules of the retinal pigment epithelium. *Vision research* 1990;30(9):1291-303.

395. Ferrington DA, Sinha D, Kaarniranta K. Defects in retinal pigment epithelial cell proteolysis and the pathology associated with age-related macular degeneration. *Progress in retinal and eye research* 2016;51:69-89.

396. Wang AL, Lukas TJ, Yuan M, et al. Autophagy and exosomes in the aged retinal pigment epithelium: possible relevance to drusen formation and age-related macular degeneration. *PloS one* 2009;4(1):e4160.

397. Anderson DM, Ablonczy Z, Koutalos Y, et al. Bis (monoacylglycero) phosphate lipids in the retinal pigment epithelium implicate lysosomal/endosomal dysfunction in a model of stargardt disease and human retinas. *Scientific reports* 2017;7(1):17352.

398. Bhattacharya S, Yin J, Winborn CS, et al. Prominin-1 is a novel regulator of autophagy in the human retinal pigment epithelium. *Investigative ophthalmology & visual science* 2017;58(4):2366-87.

399. Tan LX, Toops KA, Lakkaraju A. Protective responses to sublytic complement in the retinal pigment epithelium. *Proceedings of the National Academy of Sciences* 2016;113(31):8789-94.

400. Wavre-Shapton ST, Tolmachova T, da Silva ML, et al. Conditional ablation of the choroideremia gene causes age-related changes in mouse retinal pigment epithelium. *PloS one* 2013;8(2):e57769.

401. Young RW, Bok D. Participation of the retinal pigment epithelium in the rod outer segment renewal process. *The Journal of cell biology* 1969;42(2):392-403.

402. Lakkaraju A, Finnemann SC, Rodriguez-Boulan E. The lipofuscin fluorophore A2E perturbs cholesterol metabolism in retinal pigment epithelial cells. *Proceedings of the National Academy of Sciences* 2007;104(26):11026-31.

403. Las G, Sereda S, Wikstrom JD, et al. Fatty acids suppress autophagic turnover in β-cells. *Journal of Biological Chemistry* 2011:jbc. M111. 242412.

404. Koga H, Kaushik S, Cuervo AM. Altered lipid content inhibits autophagic vesicular fusion. *The FASEB Journal* 2010;24(8):3052-65.

405. Guha S, Liu J, Baltazar G, et al. Rescue of compromised lysosomes enhances degradation of photoreceptor outer segments and reduces lipofuscin-like autofluorescence in retinal pigmented epithelial cells *Retinal Degenerative Diseases*: Springer; 2014 p105-11.

406. Bergmann M, Schutt F, Holz F, et al. Inhibition of the ATP-driven proton pump in RPE lysosomes by the major lipofuscin fluorophore A2-E may contribute to the pathogenesis of age-related macular degeneration. *The FASEB Journal* 2004;18(3):562-64.

407. Guha S, Baltazar GC, Coffey EE, et al. Lysosomal alkalinization, lipid oxidation, and reduced phagosome clearance triggered by activation of the P2X7 receptor. *Faseb j* 2013;27(11):4500-9.

408. Mitter SK, Song C, Qi X, et al. Dysregulated autophagy in the RPE is associated with increased susceptibility to oxidative stress and AMD. *Autophagy* 2014;10(11):1989-2005.

409. Feeney-Burns L, Hilderbrand E, Eldridge S. Aging human RPE: morphometric analysis of macular, equatorial, and peripheral cells. *Investigative ophthalmology & visual science* 1984;25(2):195-200.

410. Rózanowska M, Jarvis-Evans J, Korytowski W, et al. Blue light-induced reactivity of retinal age pigment in vitro generation of oxygen-reactive species. *Journal of Biological Chemistry* 1995;270(32):18825-30.

411. Tung YT, Wang BJ, Hu MK, et al. Autophagy: a double-edged sword in Alzheimer's disease. *J Biosci* 2012;37.

412. Wang G, Mao Z. Chaperone-mediated autophagy: roles in neurodegeneration. *Transl Neurodegener* 2014;3.

413. Hu J, Bok D. A cell culture medium that supports the differentiation of human retinal pigment epithelium into functionally polarized monolayers. *Mol Vis* 2001;7(1):14-19.

414. Toops KA, Tan LX, Lakkaraju A. A detailed three-step protocol for live imaging of intracellular traffic in polarized primary porcine RPE monolayers. *Experimental eye research* 2014;124:74-85.

415. Maminishkis A, Chen S, Jalickee S, et al. Confluent monolayers of cultured human fetal retinal pigment epithelium exhibit morphology and physiology of native tissue. *Invest Ophthalmol Vis Sci* 2006;47(8):3612-24.

416. Ablonczy Z, Dahrouj M, Tang PH, et al. Human retinal pigment epithelium cells as functional models for the RPE in vivo. *Investigative ophthalmology & visual science* 2011;52(12):8614-20.

417. Blenkinsop TA, Salero E, Stern JH, et al. The culture and maintenance of functional retinal pigment epithelial monolayers from adult human eye. *Epithelial Cell Culture Protocols: Second Edition* 2013:45-65.

418. Johnson LV, Forest DL, Banna CD, et al. Cell culture model that mimics drusen formation and triggers complement activation associated with age-related macular degeneration. *Proceedings of the National Academy of Sciences* 2011;108(45):18277-82.

419. Lynn SA, Keeling E, Dewing JM, et al. A convenient protocol for establishing a human cell culture model of the outer retina. *F1000Res* 2018;7:1107.

420. Yuan N, Song L, Zhang S, et al. Bafilomycin A1 targets both autophagy and apoptosis pathways in pediatric B-cell acute lymphoblastic leukemia. *Haematologica* 2015;100.

421. Wu YC, Wu WK, Li Y, et al. Inhibition of macroautophagy by bafilomycin A1 lowers proliferation and induces apoptosis in colon cancer cells. *Biochem Biophys Res Commun* 2009;382.

422. Pivtoraiko VN, Harrington AJ, Mader BJ, et al. Low-dose bafilomycin attenuates neuronal cell death associated with autophagy-lysosome pathway dysfunction. *Journal of neurochemistry* 2010;114(4):1193-204.

423. Kim MH, Chung J, Chung SM, et al. Hydrogen peroxide-induced cell death in a human retinal pigment epithelial cell line, ARPE-19. *Korean Journal of Ophthalmology* 2003;17(1):19-28.

424. Piippo N, Korkmaz A, Hytti M, et al. Decline in cellular clearance systems induces inflammasome signaling in human ARPE-19 cells. *Biochimica et Biophysica Acta (BBA)-Molecular Cell Research* 2014;1843(12):3038-46.

425. Kaczara P, Sarna T, Burke JM. Dynamics of H2O2 availability to ARPE-19 cultures in models of oxidative stress. *Free Radical Biology and Medicine* 2010;48(8):1064-70.

426. Halliwell B, Clement MV, Long LH. Hydrogen peroxide in the human body. *FEBS letters* 2000;486(1):10-13.

427. Bucci C, Thomsen P, Nicoziani P, et al. Rab7: a key to lysosome biogenesis. *Molecular biology of the cell* 2000;11(2):467-80.

428. Humphries IV WH, Szymanski CJ, Payne CK. Endo-lysosomal vesicles positive for Rab7 and LAMP1 are terminal vesicles for the transport of dextran. *PloS one* 2011;6(10):e26626.

429. Finnemann SC, Nandrot EF. MerTK activation during RPE phagocytosis in vivo requires αVβ5 integrin *Retinal Degenerative Diseases*: Springer; 2006 p499-503.

430. Gottardi CJ, Arpin M, Fanning AS, et al. The junction-associated protein, zonula occludens-1, localizes to the nucleus before the maturation and during the remodeling of cell-cell contacts. *Proceedings of the National Academy of Sciences* 1996;93(20):10779-84.

431. Bright NA, Davis LJ, Luzio JP. Endolysosomes Are the Principal Intracellular Sites of Acid Hydrolase Activity. *Curr Biol* 2016;26(17):2233-45.

432. Klionsky DJ, Abdelmohsen K, Abe A, et al. Guidelines for the use and interpretation of assays for monitoring autophagy. *Autophagy* 2016;12(1):1-222.

433. Codogno P, Mehrpour M, Proikas-Cezanne T. Canonical and non-canonical autophagy: variations on a common theme of self-eating? *Nature reviews Molecular cell biology* 2012;13(1):7.

434. Scarlatti F, Maffei R, Beau I, et al. Non-canonical autophagy: an exception or an underestimated form of autophagy? *Autophagy* 2008;4(8):1083-85.

435. Lim C-Y, Zoncu R. The lysosome as a command-and-control center for cellular metabolism. *J Cell Biol* 2016;214(6):653-64.

436. Luzio JP, Hackmann Y, Dieckmann NM, et al. The biogenesis of lysosomes and lysosome-related organelles. *Cold Spring Harbor perspectives in biology* 2014;6(9):a016840.

437. Lynn SA, Ward G, Keeling E, et al. Ex-vivo models of the Retinal Pigment Epithelium (RPE) in long-term culture faithfully recapitulate key structural and physiological features of native RPE. *Tissue and Cell* 2017;49(4):447-60.

438. Essner E, Gorrin GM, Griewski RA. Localization of lysosomal enzymes in retinal pigment epithelium of rats with inherited retinal dystrophy. *Invest Ophthalmol Vis Sci* 1978;17(3):278-88.

439. Jung T, Bader N, Grune T. Lipofuscin: formation, distribution, and metabolic consequences. *Annals of the New York Academy of Sciences* 2007;1119(1):97-111.

440. Kaarniranta K, Hyttinen J, Ryhanen T, et al. Mechanisms of protein aggregation in the retinal pigment epithelial cells. *Front Biosci (Elite Ed)* 2010;2:1374-84.

441. Hyttinen JM, Amadio M, Viiri J, et al. Clearance of misfolded and aggregated proteins by aggrephagy and implications for aggregation diseases. *Ageing research reviews* 2014;18:16-28.

442. Cataldo A, Petanceska S, Terio N, et al. A-beta localization to abnormal endosomes coincides with early increases in soluble A-beta in Alzheimer's disease brain. *Neurobiol Aging* 2004;25:1263-72.

443. Kaur G, Tan LX, Rathnasamy G, et al. Aberrant early endosome biogenesis mediates complement activation in the retinal pigment epithelium in models of macular degeneration. *Proceedings of the National Academy of Sciences* 2018;115(36):9014-19.

444. Kim J-Y, Zhao H, Martinez J, et al. Noncanonical autophagy promotes the visual cycle. *Cell* 2013;154(2):365-76.

445. Liu J, Copland DA, Theodoropoulou S, et al. Impairing autophagy in retinal pigment epithelium leads to inflammasome activation and enhanced macrophage-mediated angiogenesis. *Scientific reports* 2016;6:20639.

446. Hu X, Crick SL, Bu G, et al. Amyloid seeds formed by cellular uptake, concentration, and aggregation of the amyloid-beta peptide. *Proceedings of the National Academy of Sciences* 2009;106(48):20324-29.

447. Kaarniranta K, Tokarz P, Koskela A, et al. Autophagy regulates death of retinal pigment epithelium cells in age-related macular degeneration. *Cell Biology and Toxicology* 2017;33(2):113-28.